OCS Study
MMS 2005-008

Coastal Marine Institute

Visibility and Atmospheric Dispersion Capability over the Northern Gulf of Mexico

Estimations and Observations of Boundary Layer Parameters

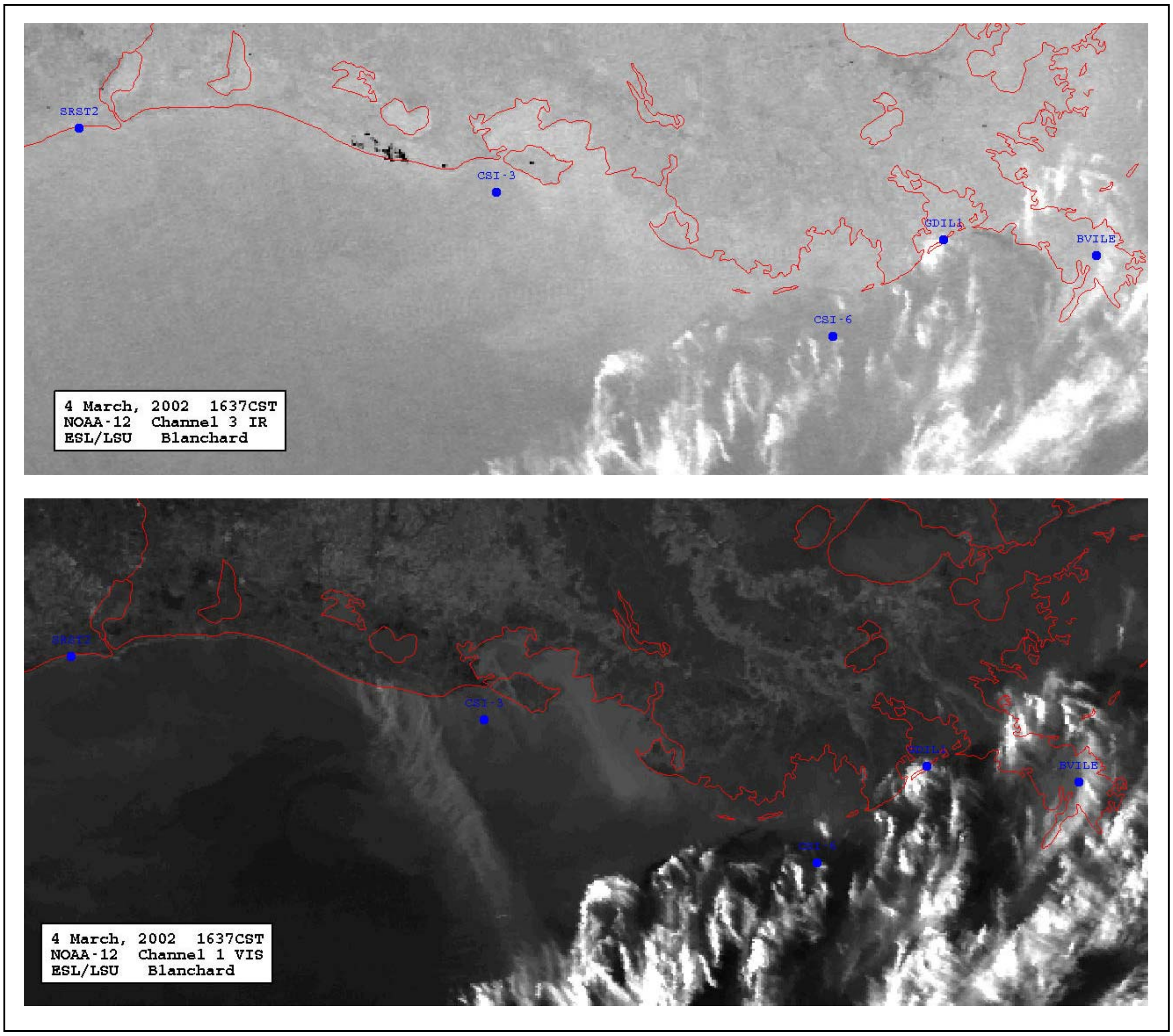

U.S. Department of the Interior
Minerals Management Service
Gulf of Mexico OCS Region

Cooperative Agreement
Coastal Marine Institute
Louisiana State University

OCS Study
MMS 2005-008

Coastal Marine Institute

Visibility and Atmospheric Dispersion Capability over the Northern Gulf of Mexico

Estimations and Observations of Boundary Layer Parameters

Authors

S.A. Hsu
B.W. Blanchard

March 2005

Prepared under MMS Contract
1435-01-99-CA-30951-17810
by
Coastal Marine Institute
Louisiana State University
Baton Rouge, Louisiana 70803

Published by

U.S. Department of the Interior
Minerals Management Service
Gulf of Mexico OCS Region

Cooperative Agreement
Coastal Marine Institute
Louisiana State University

DISCLAIMER

This report was prepared under contract between the Minerals Management Service (MMS) and the Coastal Studies Institute, Louisiana State University. This report has been technically reviewed by the MMS, and it has been approved for publication. Approval does not signify that the contents necessarily reflect the views and policies of the MMS, nor does mention of trade names or commercial products constitute endorsement or recommendation for use. It is, however, exempt from review and compliance with the MMS editorial standards.

REPORT AVAILABILITY

Extra copies of this report may be obtained from the Public Information Office (Mail Stop 5034) at the following address:

U.S. Department of the Interior
Minerals Management Service
Gulf of Mexioc OCS Region
Public Information Office (MS 5034)
1201 Elmwood Park Boulevard
New Orleans, Louisiana 70123-2394

Telephone: (504)736-2519 or
1-800-200-GULF

CITATION

Suggested citation:

Hsu, S. A. and B. W. Blanchard. 2005. Visibility and atmospheric dispersion capability over the northern Gulf of Mexico: Estimations and observations of boundary layer parameters: Final Report. U.S. Dept. of the Interior, Minerals Management Service, Gulf of Mexico OCS Region, New Orleans, LA. OCS Study MMS 2005-008. 184 pp.

ABOUT THE COVER

NOAA-12 satellite imagery for 4 March 2002 1637 CST reveals the locations of coastal marsh fires in southwest Louisiana and the resulting plumes extending southward over the shelf waters (courtesy of the Earth Scan Lab, LSU).

ABSTRACT

Two visibility and meteorological stations were made operational in the Louisiana coastal waters beginning in November 2001. An hourly data record is being archived, and near-real time information is made available over the internet. Simplified formulas are derived for the offshore atmospheric boundary layer which require only easily obtainable input parameters. With these formulations, monthly mean variations of stability, mixing height, and ventilation factor (an indicator of dispersion capability) are provided for the northern Gulf of Mexico. A method for determining whether fog or haze conditions are observed at a monitoring station is given. Using this algorithm, the effects of fog and haze at three coastal stations are discussed. Several periods of reduced visibility at our primary monitoring station are examined using pertinent weather maps and satellite observations. It is shown that naturally occurring fog conditions are by far the most common cause of reduced visibility along the Louisiana coast. Haze can be observed each month; however, the total duration is small and the extent to which it reduces visibility is usually much less than that due to fog. Plumes from inland (near-coast) areas can affect the OCS region.

TABLE OF CONTENTS

LIST OF FIGURES

LIST OF TABLES

I. EXECUTIVE SUMMARY

In 1999, the Environmental Protection Agency (EPA) promulgated new regulations for protecting and improving visibility in the national parks and wilderness areas (the Regional Haze regulations). EPA regulations regarding the viewing of scenic vistas in locations such as the Breton Island National Wilderness Area have focused new attention on visibility impacts of pollutant emissions. The Minerals Management Service (MMS), which oversees offshore activity including air quality aspects, has funded several studies associated with these issues in the Gulf of Mexico region. This Final Report presents the activities and findings of one such project designed to investigate visibility and mixing height over the Gulf of Mexico.

In the marine environment, visibility can be affected by sea spray, hence wind and wave measurements are needed. Visibility sensors were thus deployed on two instrumented platforms in the Louisiana shelf waters (see Fig. 1) and an hourly archive of pertinent meteorological and oceanographic data was accumulated. The hourly reports were also made available in near-real time over the internet.

Visibility is directly related to the distribution of aerosols, particulates, and pollutants, which is largely determined by the mixed layer properties. Routinely available measurements were employed to develop air-sea interaction formulas describing stability characteristics and mixing height over the Gulf. These parameters are essential inputs for air quality modeling efforts. Monthly average data from National Data Buoy Center (NDBC) offshore buoys and Coastal-Marine Automated Network (C-MAN) stations is used to illustrate spatial variations in the Gulf region.

Definitions of haze and fog are applied to the data from several stations to determine the potential frequency of occurrence of these phenomena. Seasonal variations are presented, along with the distribution of severely restricted visibility conditions.

Several low visibility episodes have been identified during our measurement period. Meteorological conditions, and satellite imagery when available, associated with these events are discussed. It will be shown that significant reductions in Louisiana coastal and offshore visibility are almost entirely due to transient natural conditions (fog). Episodes of haze are generally short-lived and affect visibility much less. Offshore haze can result from plume drift generated by coastal sources. Neutral and unstable conditions dominate over the Gulf. Spatial and temporal variations of the mixed layer height result, with an average computed height of only 445 m at our measurement station. When combined with low average wind speeds (ventilation factor), areas of potentially low atmospheric dispersion capabilities occur, particularly in late summer.

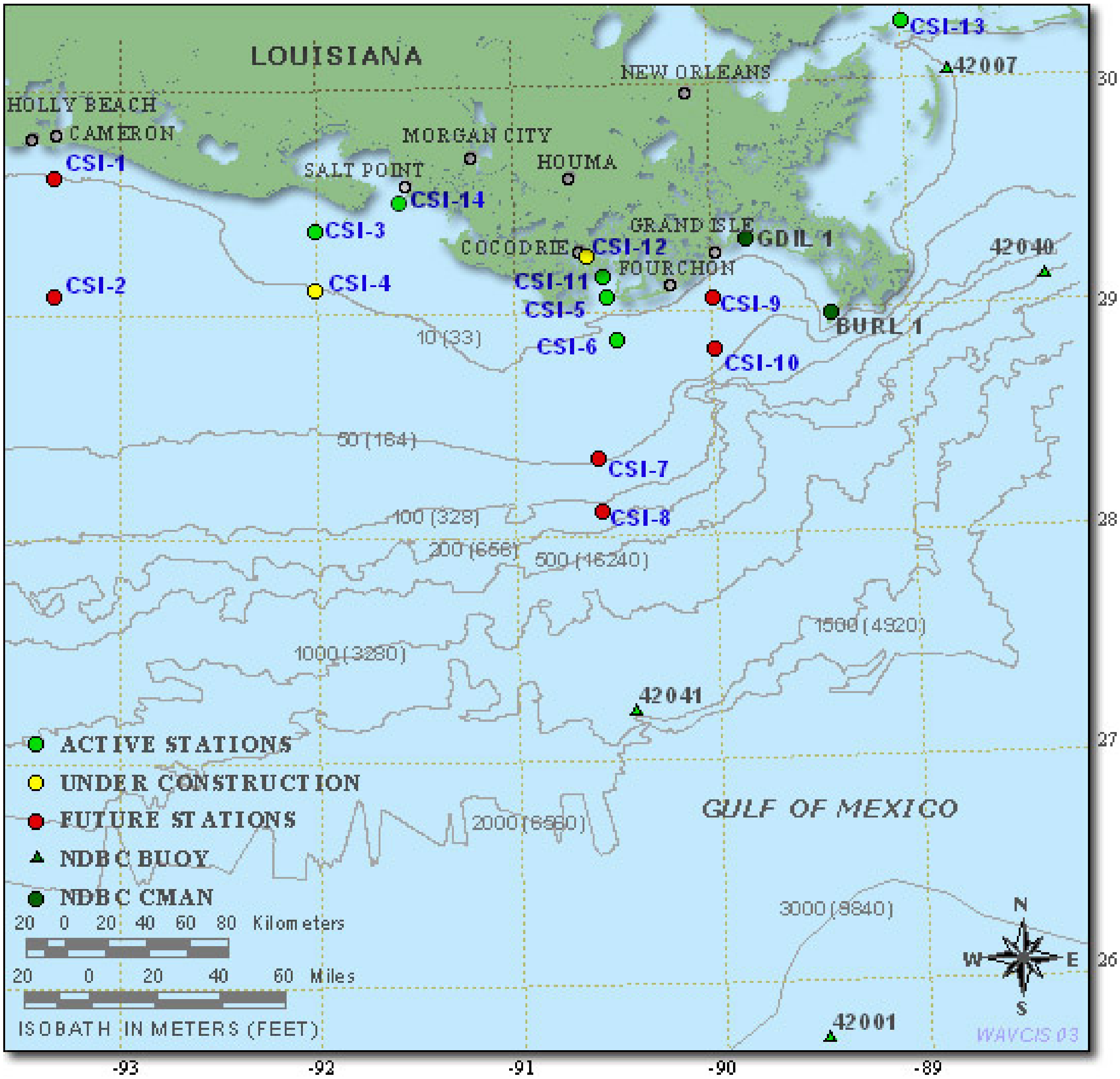

Figure 1. Locations of the NDBC and WAVCIS instrumented platforms in the northern Gulf of Mexico. For this study, platforms CSI-3 and CSI-6 were equipped with visibility sensors (map courtesy of WAVCIS webpage).

II. FIELD PROGRAM

In order to study characteristics of the atmospheric boundary layer and visibility over the Louisiana coastal waters, we proposed to deploy two surface stations; one near shore and the other closer to the shelf break. Under a separate program (WAVCIS, WAVe Current Information System), the Coastal Studies Institute, Louisiana State University, is constructing a network of instrumented platforms in the OCS region (see Fig. 1). Both oceanographic and meteorological parameters are recorded hourly at these stations and transmitted to LSU for quality control and archiving. The data are then made available in near-real time via the web at www.wavcis.lsu.edu (detailed information about this program can be found at the website). Two WAVCIS stations were eventually utilized for our visibility measurements.

The first was near-shore at 92°03.68' 29°26.47' (south of Marsh Island, WAVCIS CSI-3) in late October 2001. Unfortunately, several logistic and contractual obstacles delayed the construction of the deeper water platform for some time. In late June 2003, the second visibility station came on line at WAVCIS CSI-6, located at 90°29' 28°52' (south of Terrebonne Bay). For this study, we integrated a Belfort Model 6100 visibility sensor and a Rotronics Model MP101A relative humidity/air temperature probe into the existing WAVCIS sensor suite.

The Belfort Model 6100 is designed to measure visibility conditions over a range of 0 - 10 miles. Visibility is detected using widely accepted principles of forward scattering. A high-output infrared LED transmitter projects light into a sample volume, and light scattered in a forward direction is collected by the receiver. The light source is modulated to provide excellent rejection of background noise and natural variations in background light intensity. The sensor outputs an analog signal which is proportional to visibility. Accuracy is +/- 10%. If measured visibility falls below 100', then the accuracy is fixed at 10'. The Rotronics MP101A is commonly used in remote weather stations and ocean buoys. Sensor accuracy at 25°C is +/- 1.5% and +/- 0.2°C.

WAVCIS platforms CSI-3 and CSI-6 are shown in Fig. 2. For CSI-3, the anemometer, air temperature/humidity sensor, visibility sensor, and pressure sensor are mounted at 23.4 m, 23 m, 21.9 m, and 13.3 m asl, respectively. They are similarly mounted on CSI-6 at heights 37.4 m, 37 m, 35.9 m, and 16.3 m, respectively. The sensors are sampled at 1 Hz for a 10-minute period at the beginning of each hour. As can be seen from Fig. 2, open space on production platforms is usually very limited. Best efforts were made to mount the sensors in a location providing clear air from all directions.

For each hourly record, standard meteorological formulas (see, e.g., Hsu, 1988) were applied to derive a dew-point temperature as follows:

The saturation vapor pressure, e_s, was obtained from the air temperature by

$$e_s = 6.1078 * e^{(2.302 * 7.5 * T_{air} / (237.3 + T_{air}))} \qquad \textbf{(1)}$$

By definition, relative humidity is the ratio of actual vapor pressure to saturation vapor pressure, or

$$\mathrm{RH} = \frac{e}{e_s} \qquad \textbf{(2)}$$

Therefore, vapor pressure e is

$$e = \frac{\mathrm{RH}}{100} * e_s \qquad \textbf{(3)}$$

A simple program was written to estimate a wet-bulb temperature from the measured air temperature and relative humidity by referencing tables from Weast et al. (1964). If the measured air temperature or the estimated wet-bulb temperature were below zero, then the dew-point temperature was given by

$$T_{dew} = \frac{261.4 \log\left(\frac{e}{6.1078}\right)}{9.321 - \log\left(\frac{e}{6.1078}\right)} \qquad \textbf{(4)}$$

otherwise

$$T_{dew} = \frac{237.3 \log\left(\frac{e}{6.1078}\right)}{7.5 - \log\left(\frac{e}{6.1078}\right)} \qquad \textbf{(5)}$$

Tables 1 and 2 list the data return rates for CSI-3 and CSI-6, respectively. With the exception of May and October 2002, monthly records were generally better than 95% complete. Missing data was mostly due to station maintenance or sensor failure. Note that these measurements are continuing as of this publication, and can still be accessed through the WAVCIS website.

Monthly time series of measured parameters for the period of November 2001 through October 2003 are presented in Figs. 3 to 58.

Figure 2. WAVCIS platforms CSI-3 (top) and CSI-6 (bottom) (courtesy of the WAVCIS program).

Table 1.
Data Return Rate (%) for Station WAVCIS CSI-3 (Shaded Months < 75% Complete)

Month	Visibility	T_{air}	Relative Humidity
2001			
November	99	99	99
December	99	100	99
2002			
January	97	97	97
February	79	79	79
March	100	100	100
April	100	100	100
May	70	70	70
June	98	98	98
July	97	97	97
August	98	98	98
September	95	95	95
October	97	97	71
November	99	99	78
December	99	99	99
2003			
January	97	97	97
February	98	98	98
March	93	93	93
April	80	99	99
May	100	100	100
June	99	99	99
July	100	100	100
August	92	99	99
September	99	99	99
October	100	100	100

Table 2.
Data Return Rate (%) for Station WAVCIS CSI-6 (Shaded Months < 75% Complete)

Month	Visibility	T_{air}	Relative Humidity
2003			
July	0	99	0
August	100	100	99
September	99	99	99
October	100	100	95

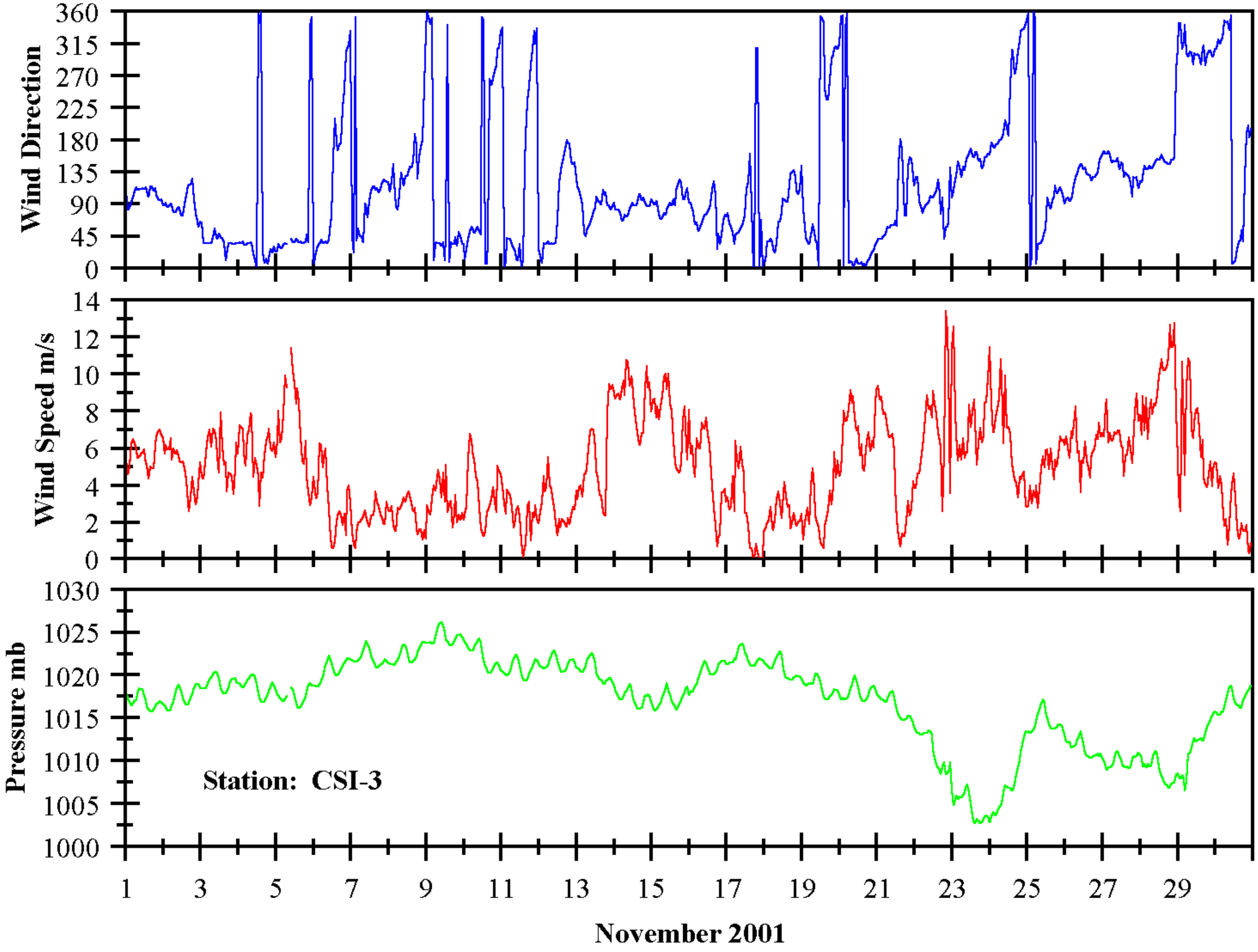

Figure 3. November 2001 hourly meteorological record from station CSI-3.

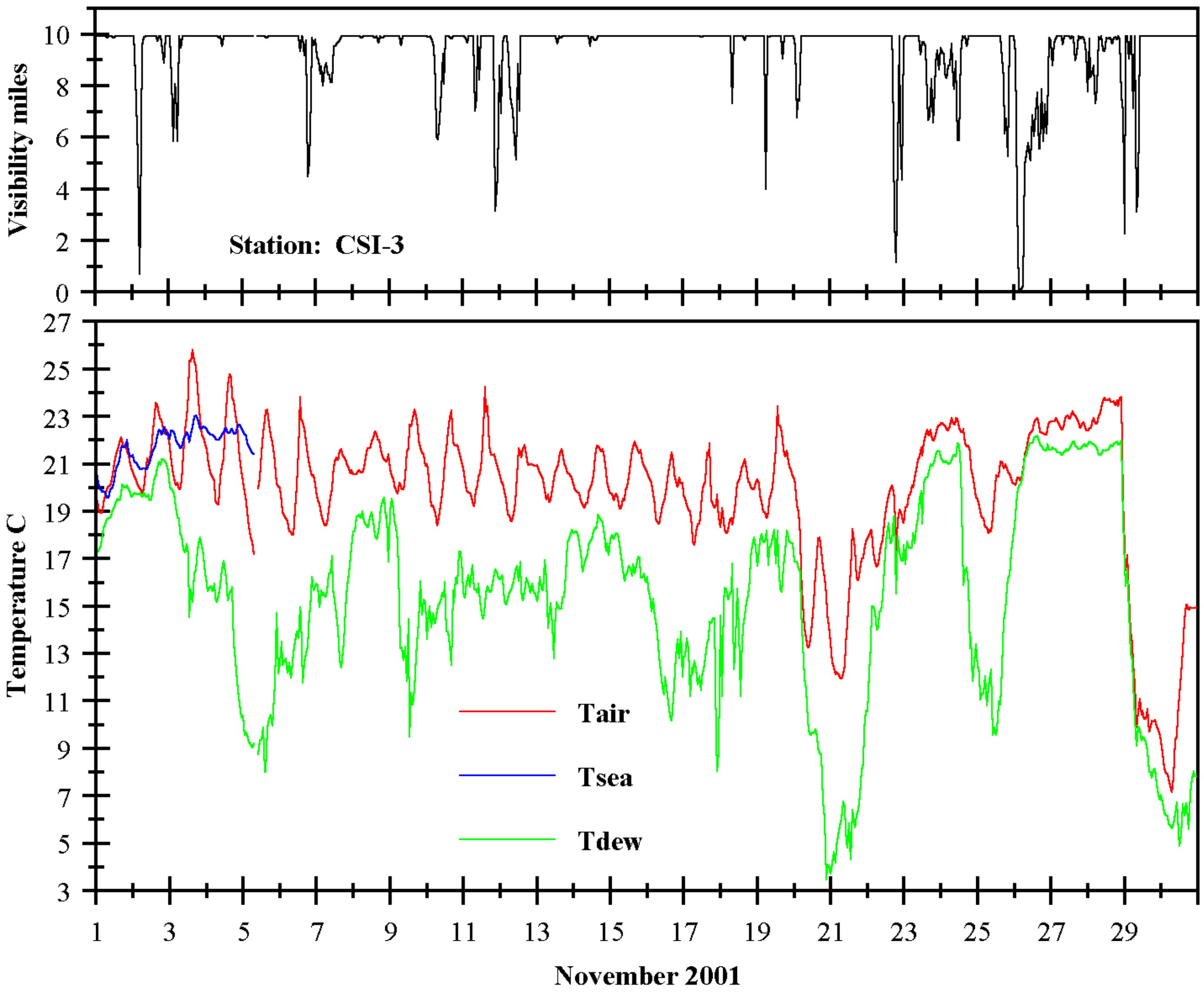

Figure 4. November 2001 hourly visibility and temperature records for station CSI-3.

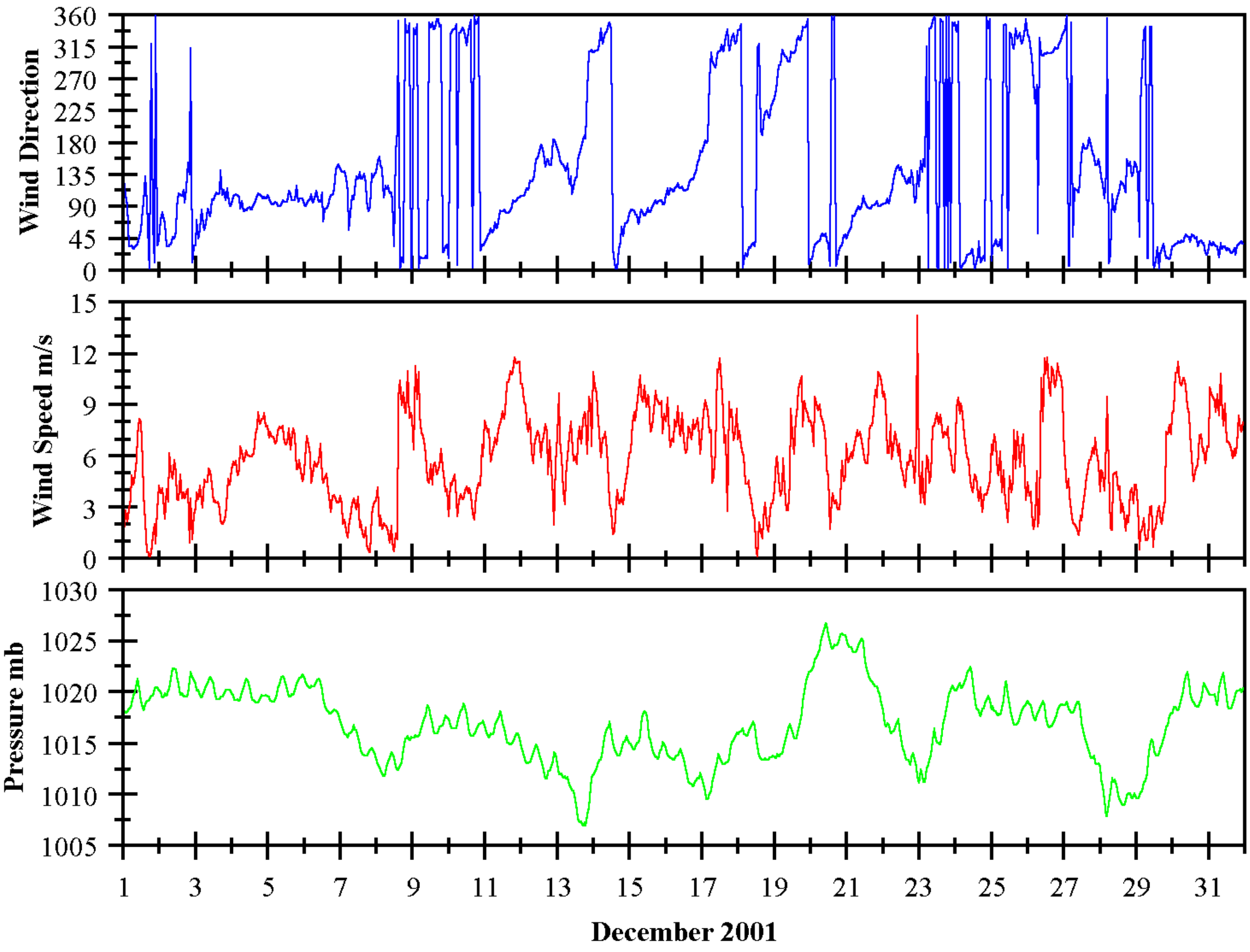

Figure 5. December 2001 hourly meteorological record for station CSI-3.

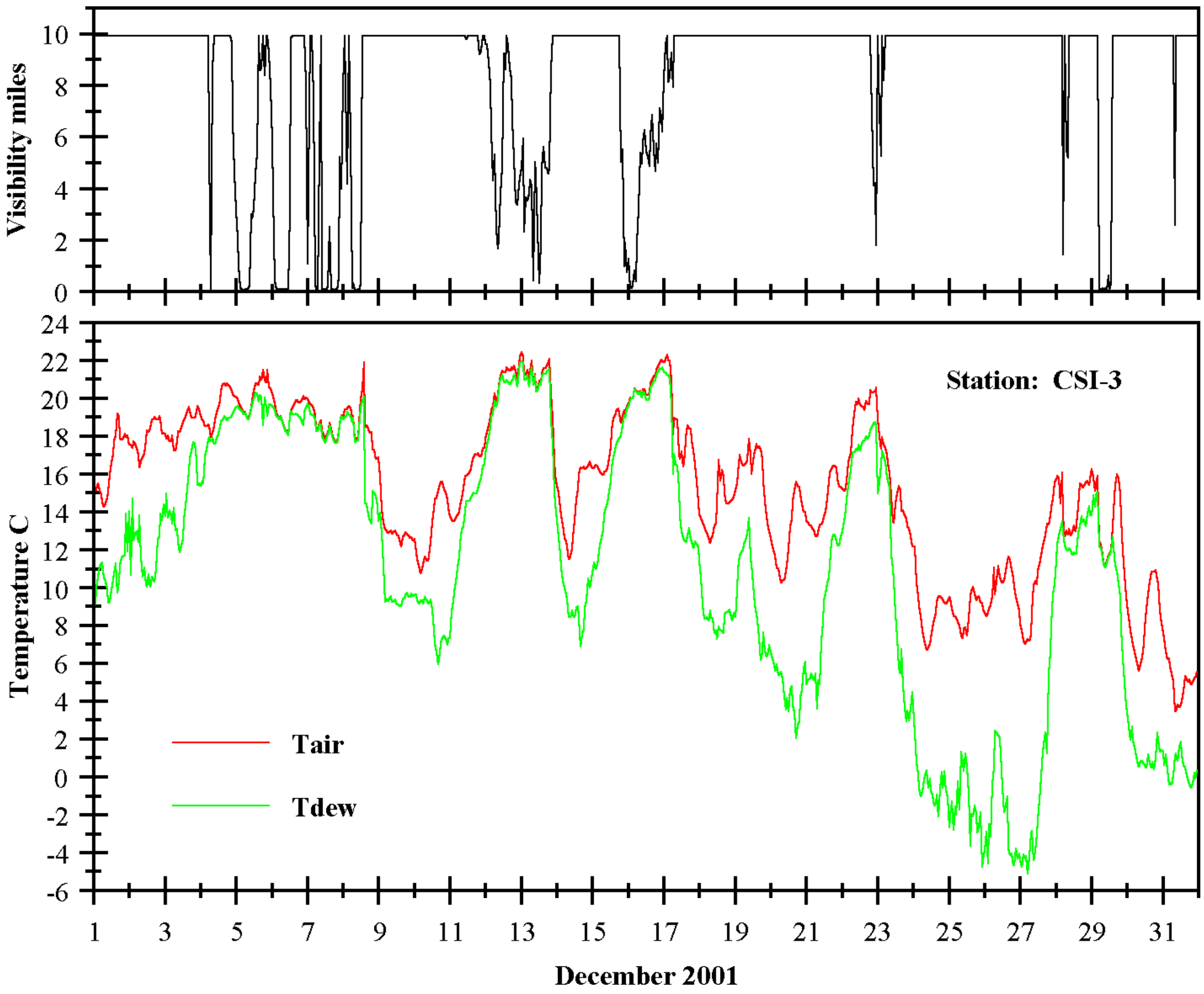

Figure 6. December 2001 hourly visibility and temperature records for station CSI-3.

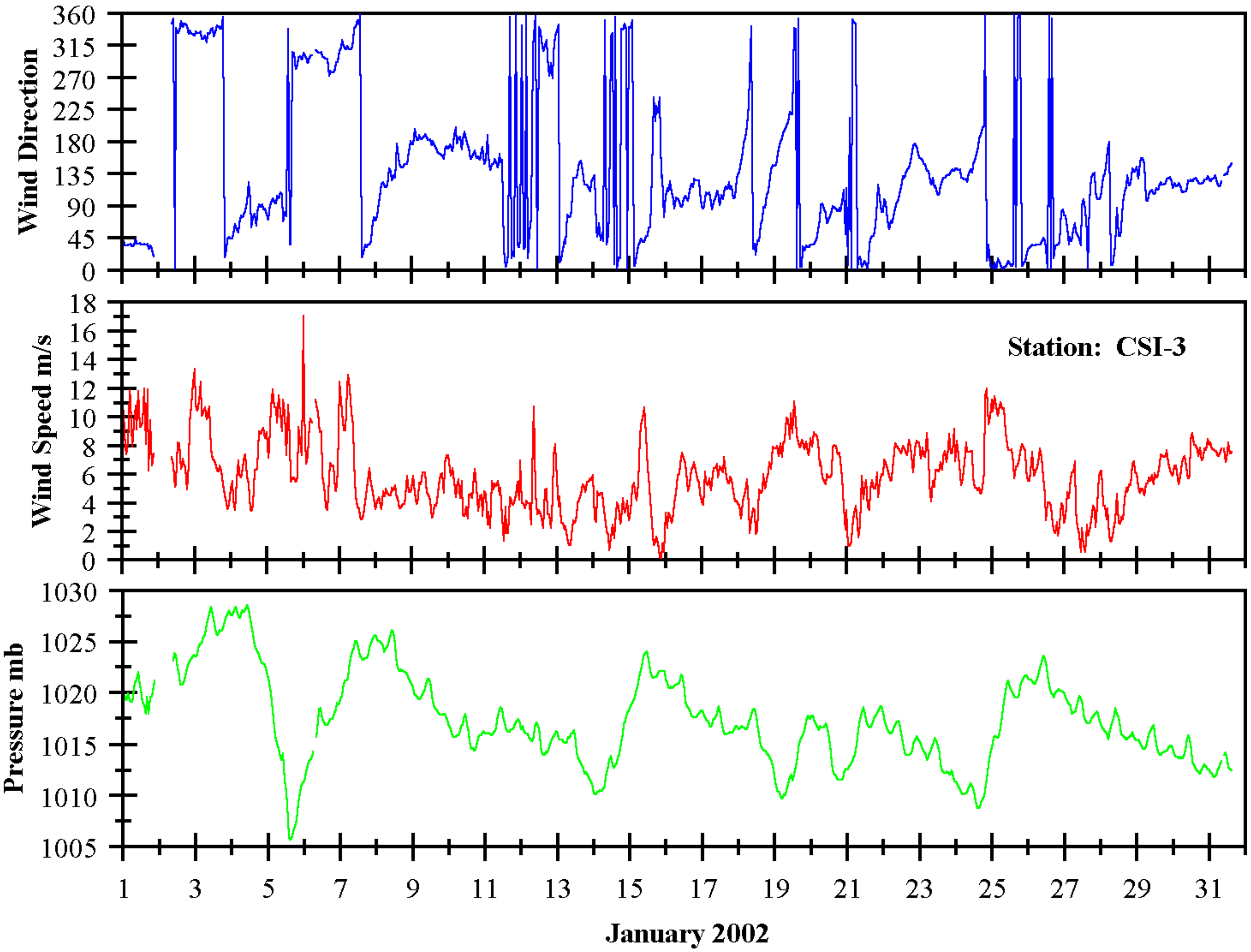

Figure 7. January 2002 hourly meteorological records for station CSI-3.

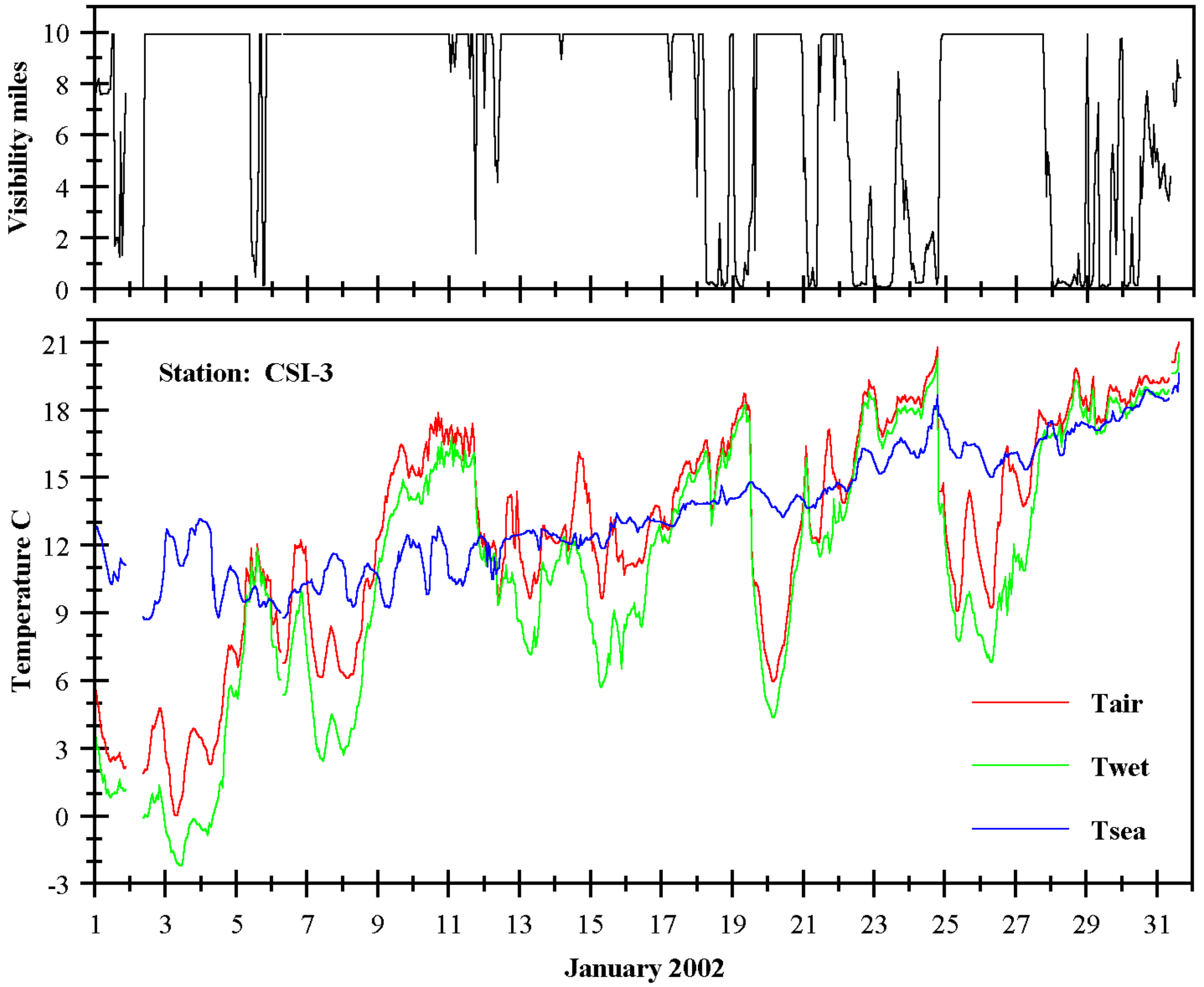

Figure 8. January 2002 hourly visibility and temperature records for station CSI-3.

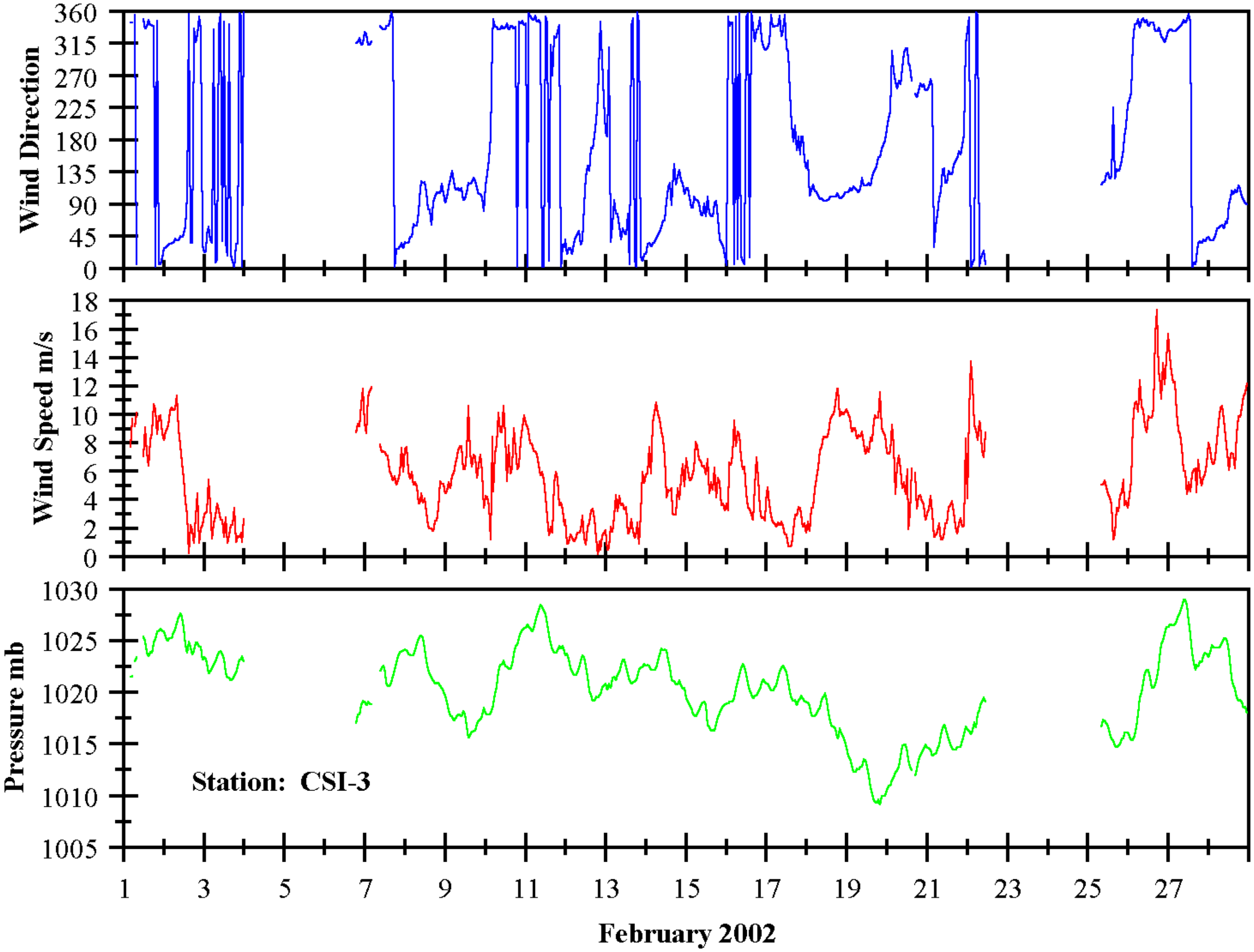

Figure 9. February 2002 hourly meteorological records for station CSI-3.

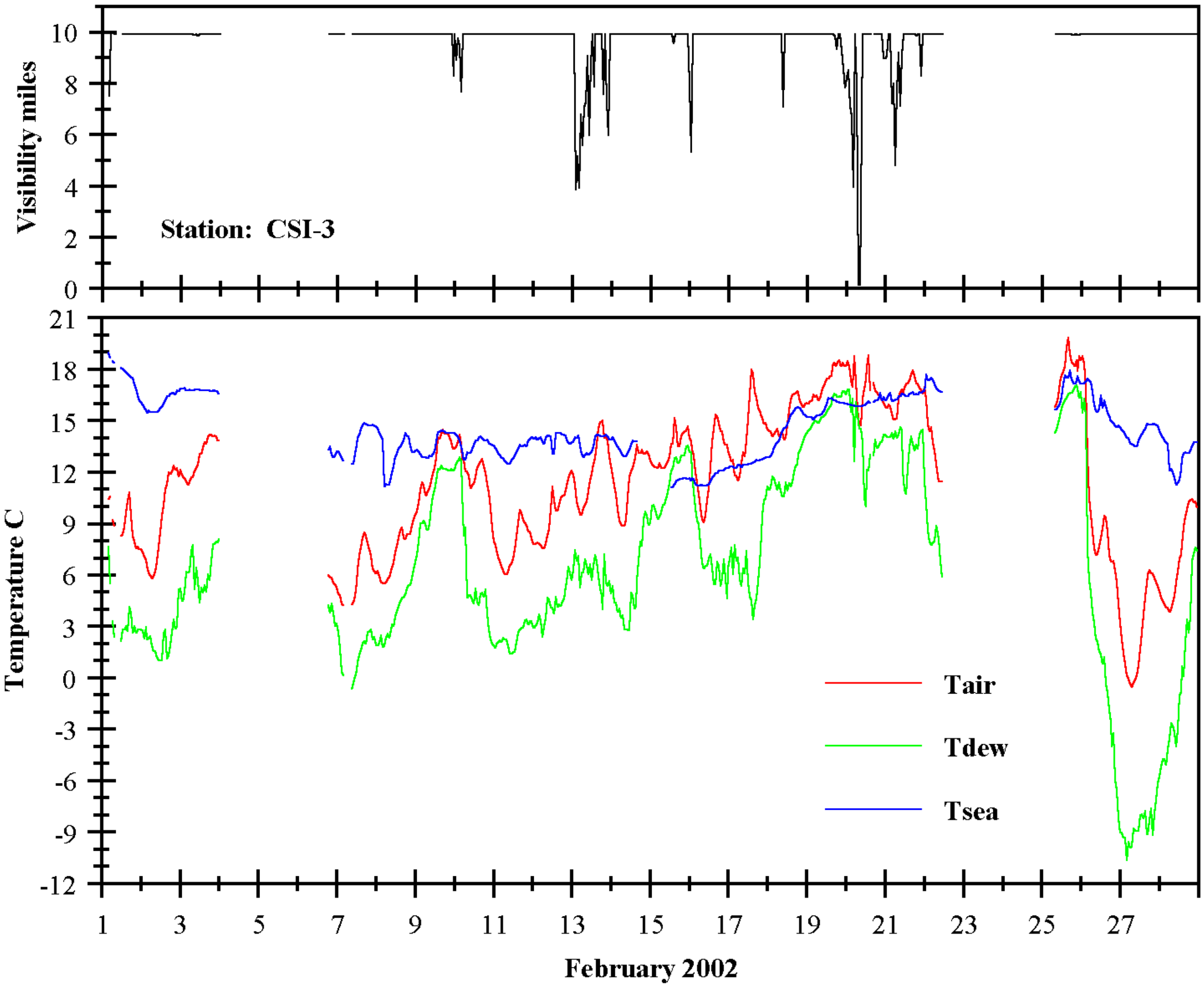

Figure 10. February 2002 hourly visibility and temperature records for station CSI-3.

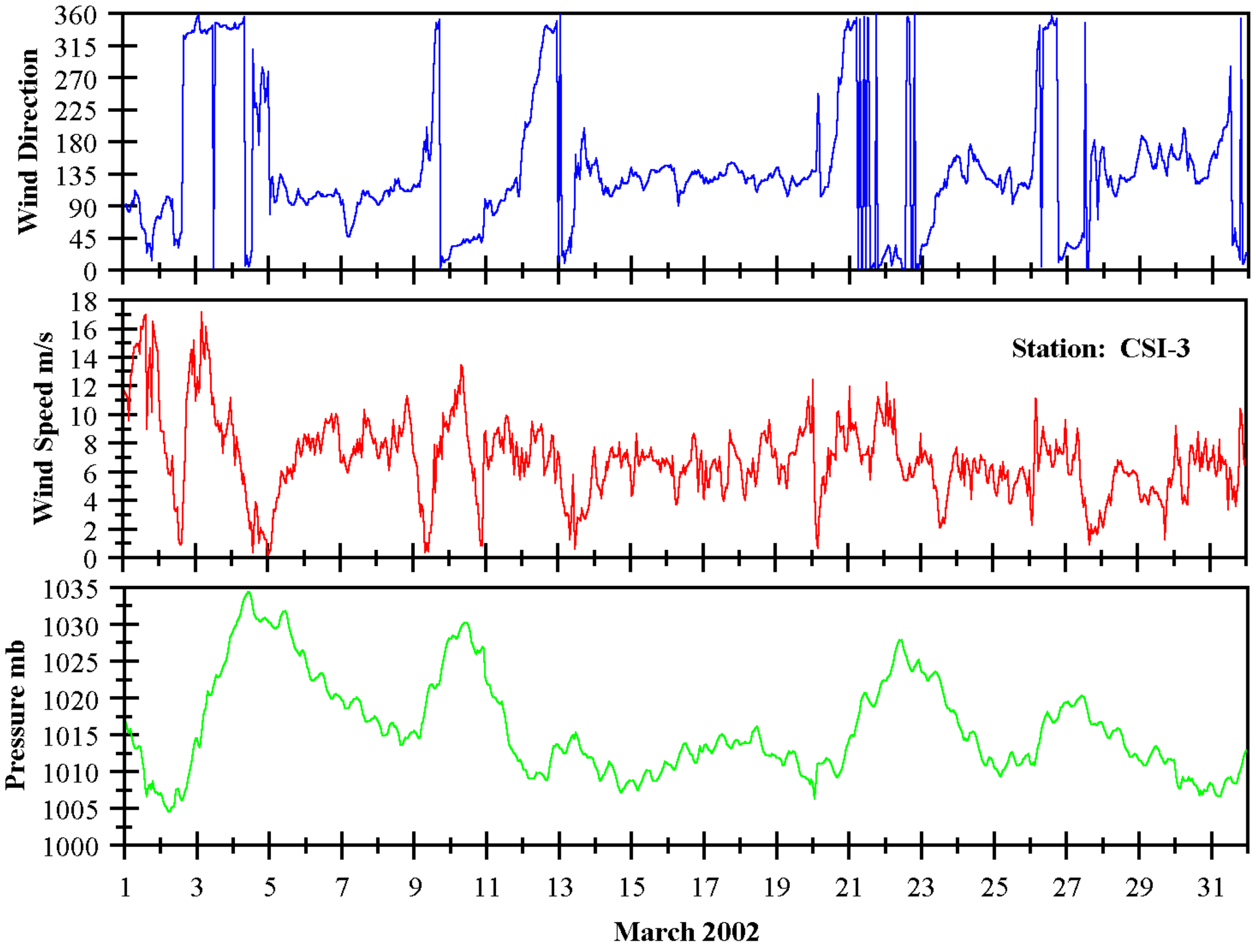

Figure 11. March 2002 hourly meteorological records for station CSI-3.

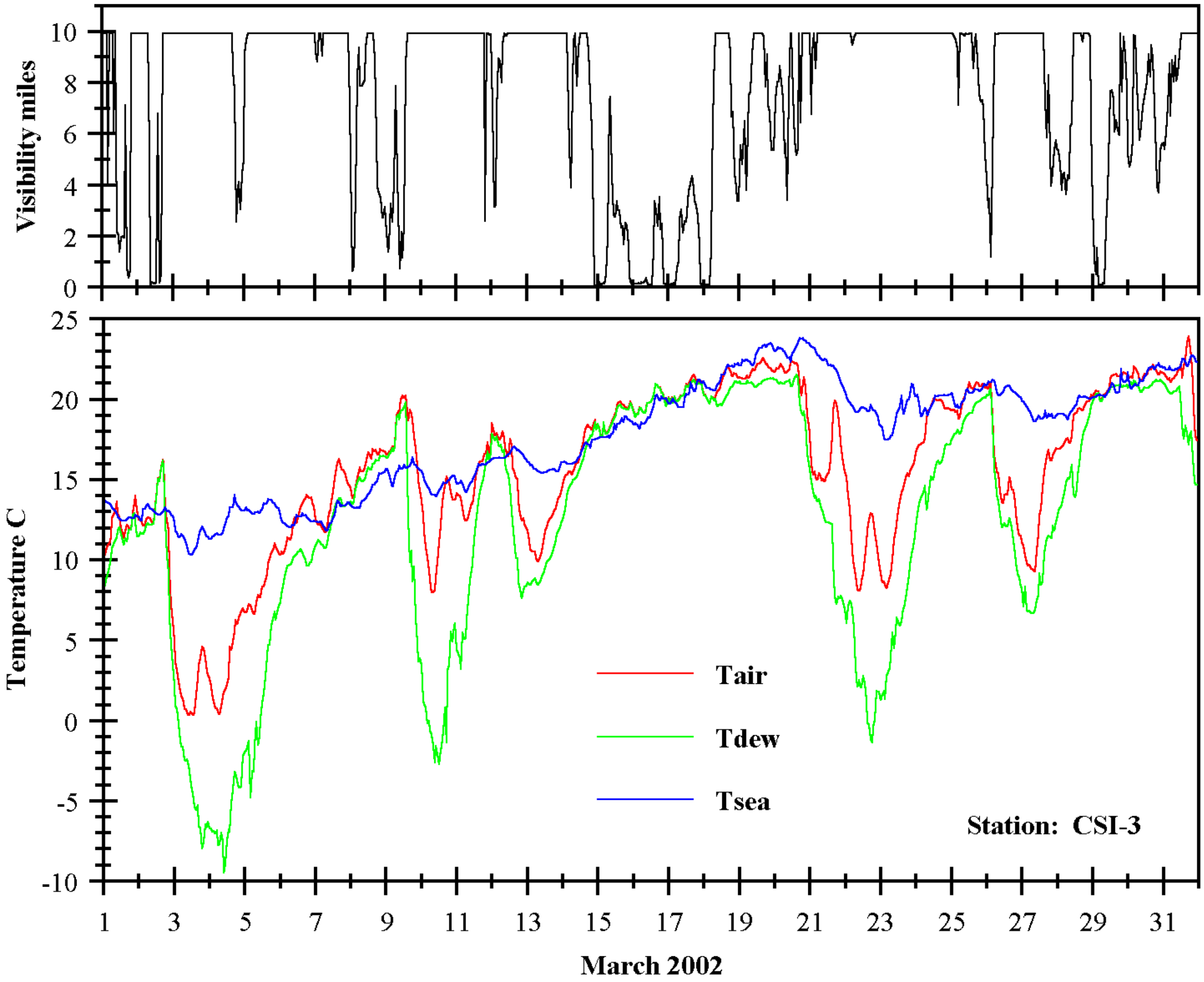

Figure 12. March 2002 hourly visibility and temperature records for station CSI-3.

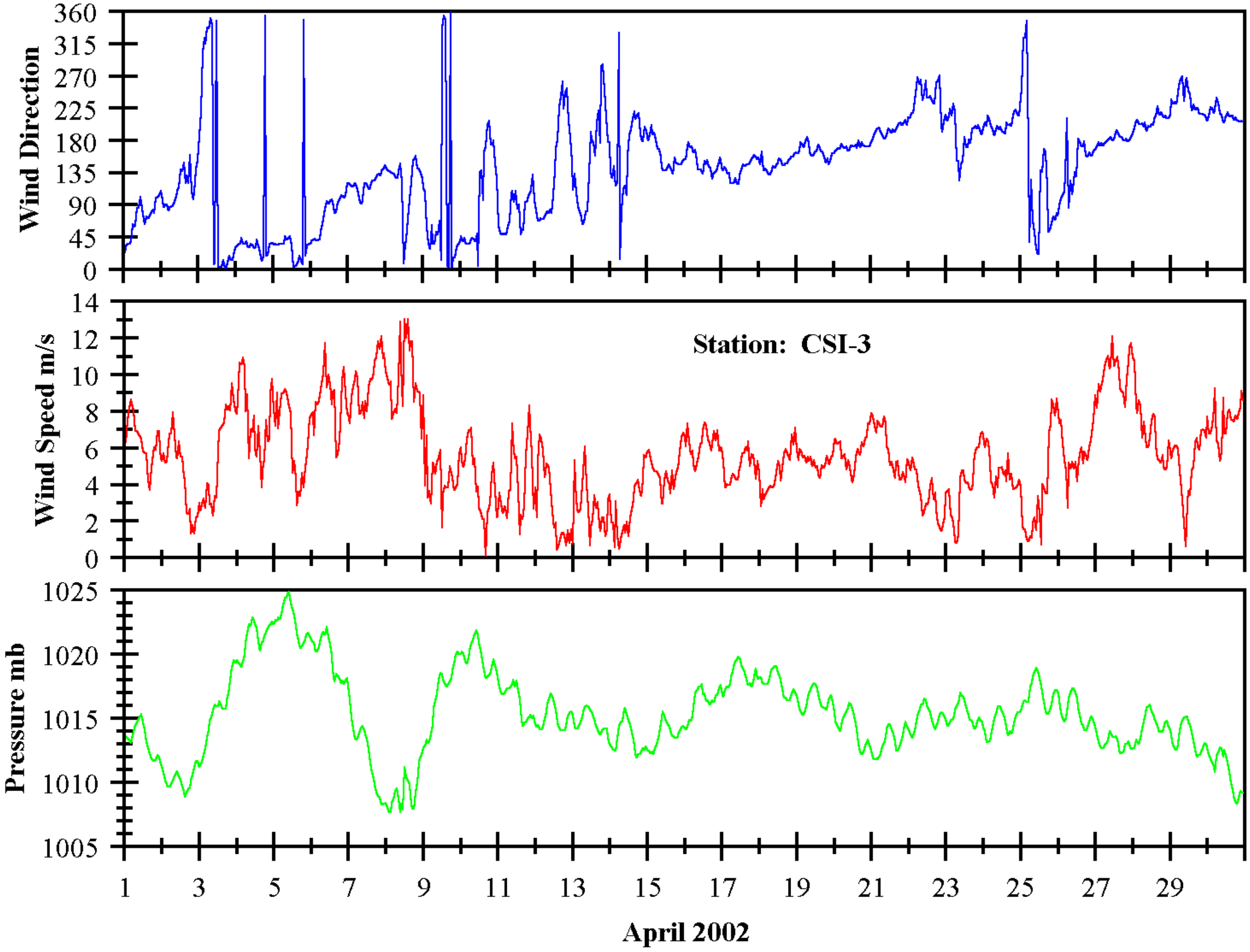

Figure 13. April 2002 hourly meteorological records for station CSI-3.

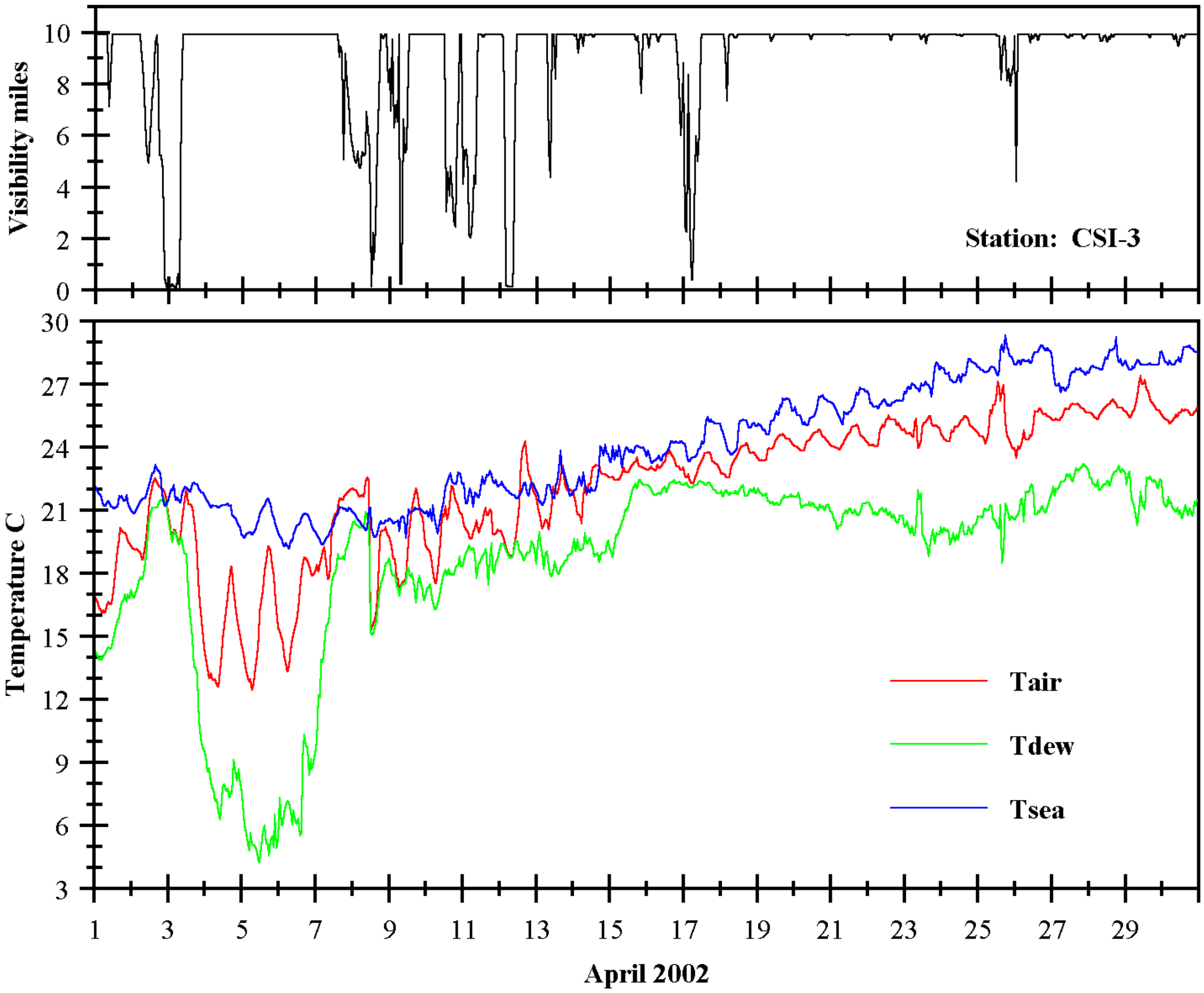

Figure 14. April 2002 hourly visibility and temperature records for station CSI-3.

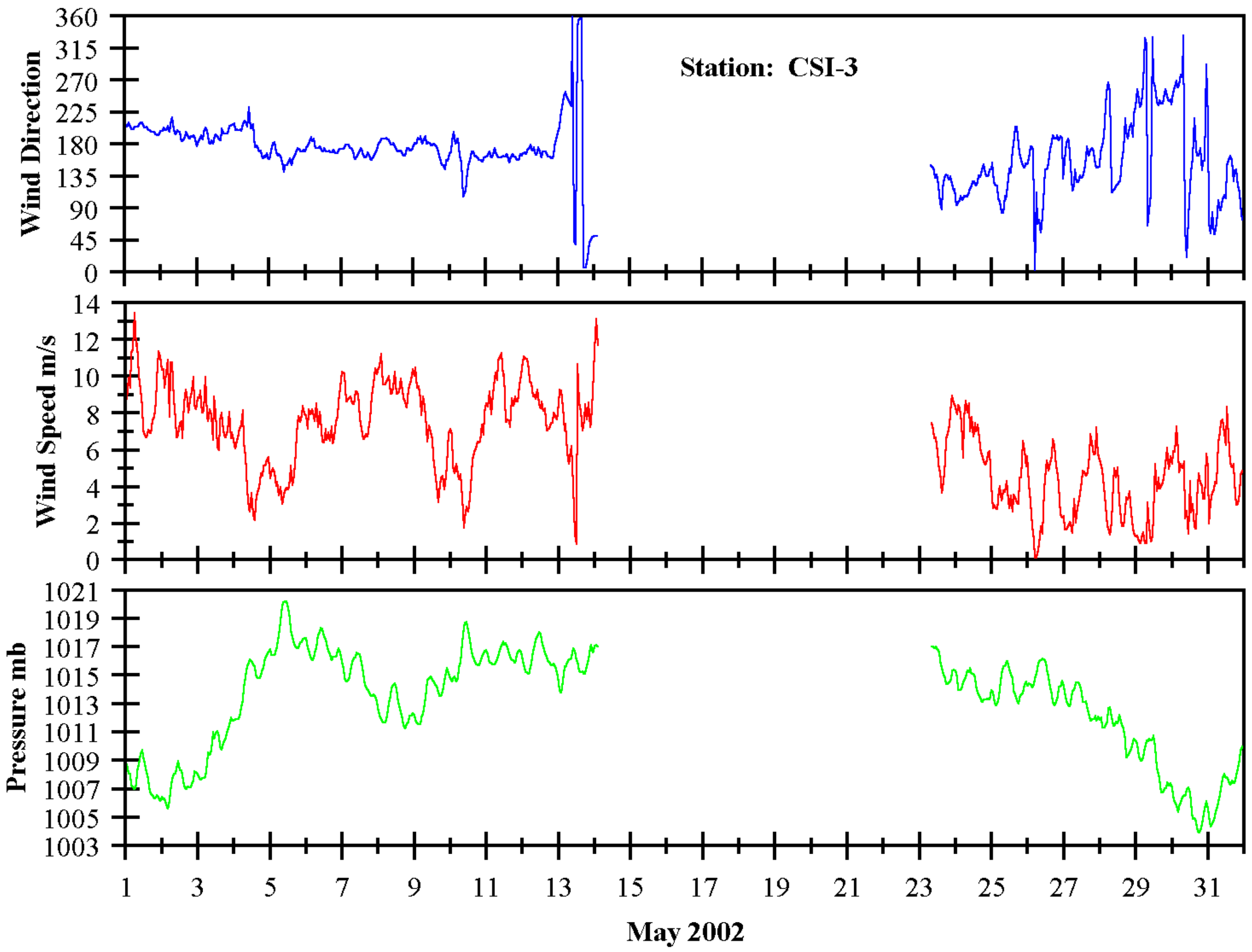

Figure 15. May 2002 hourly meteorological records for station CSI-3.

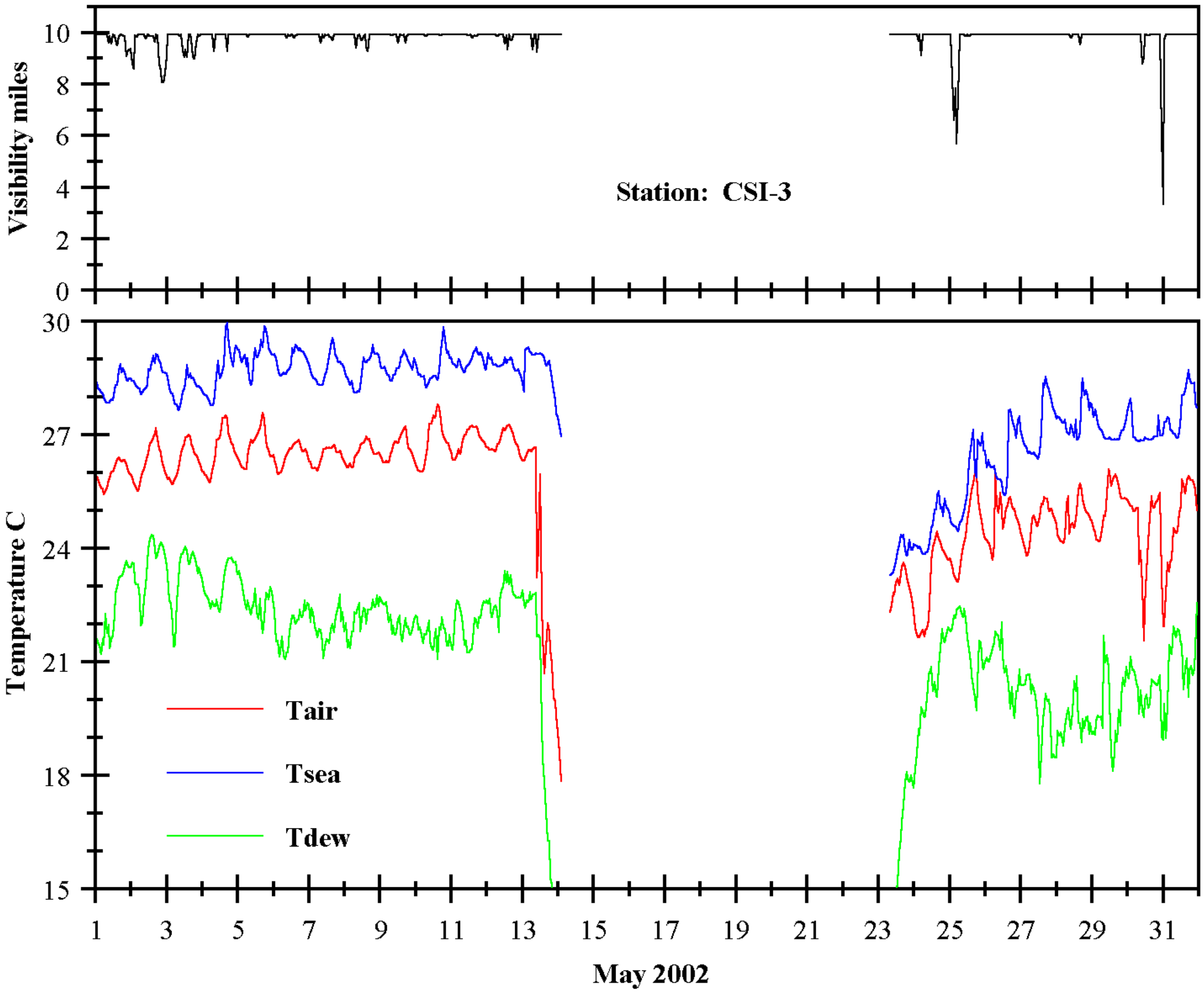

Figure 16. May 2002 hourly visibility and temperature records for station CSI-3.

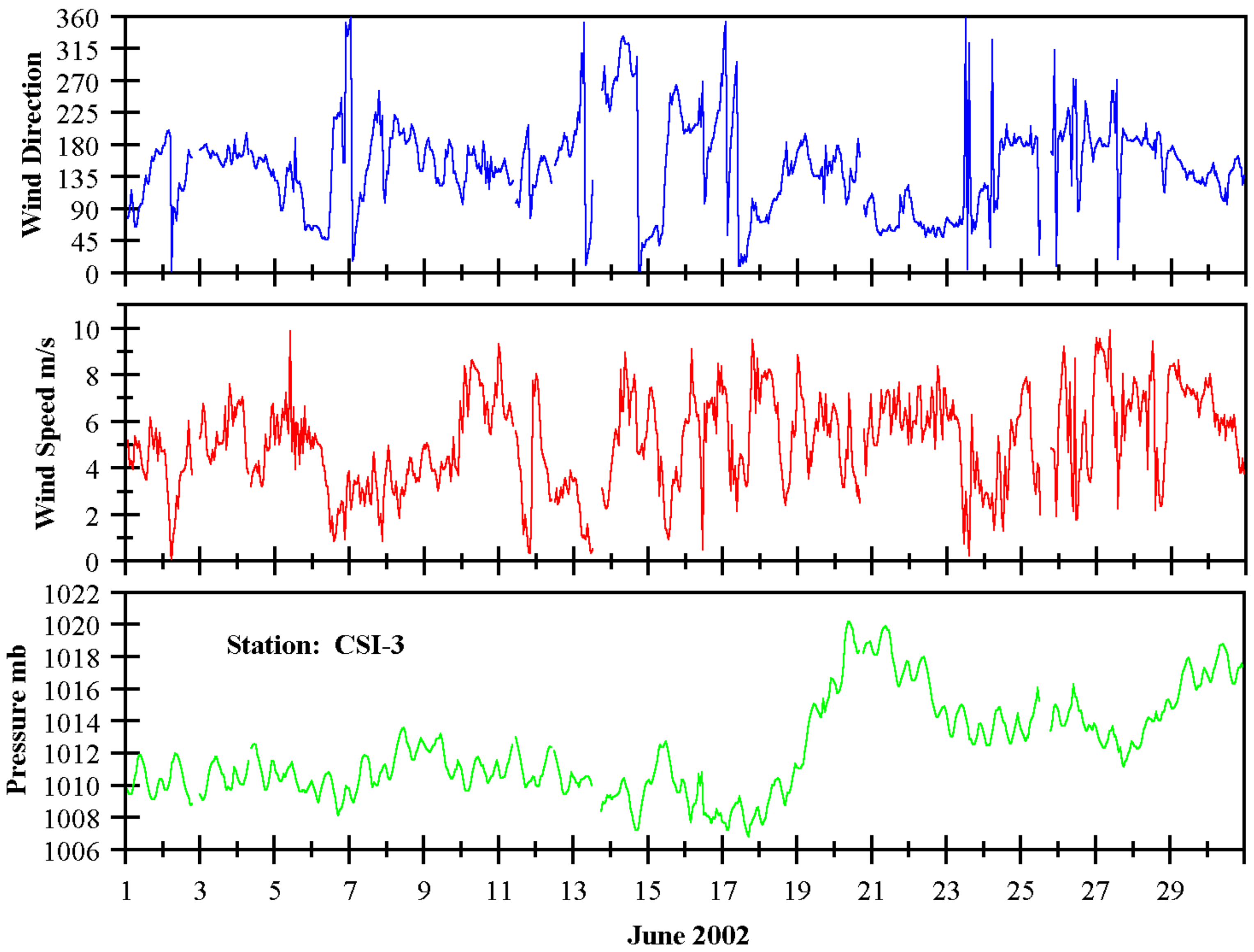

Figure 17. June 2002 hourly meteorological records for station CSI-3.

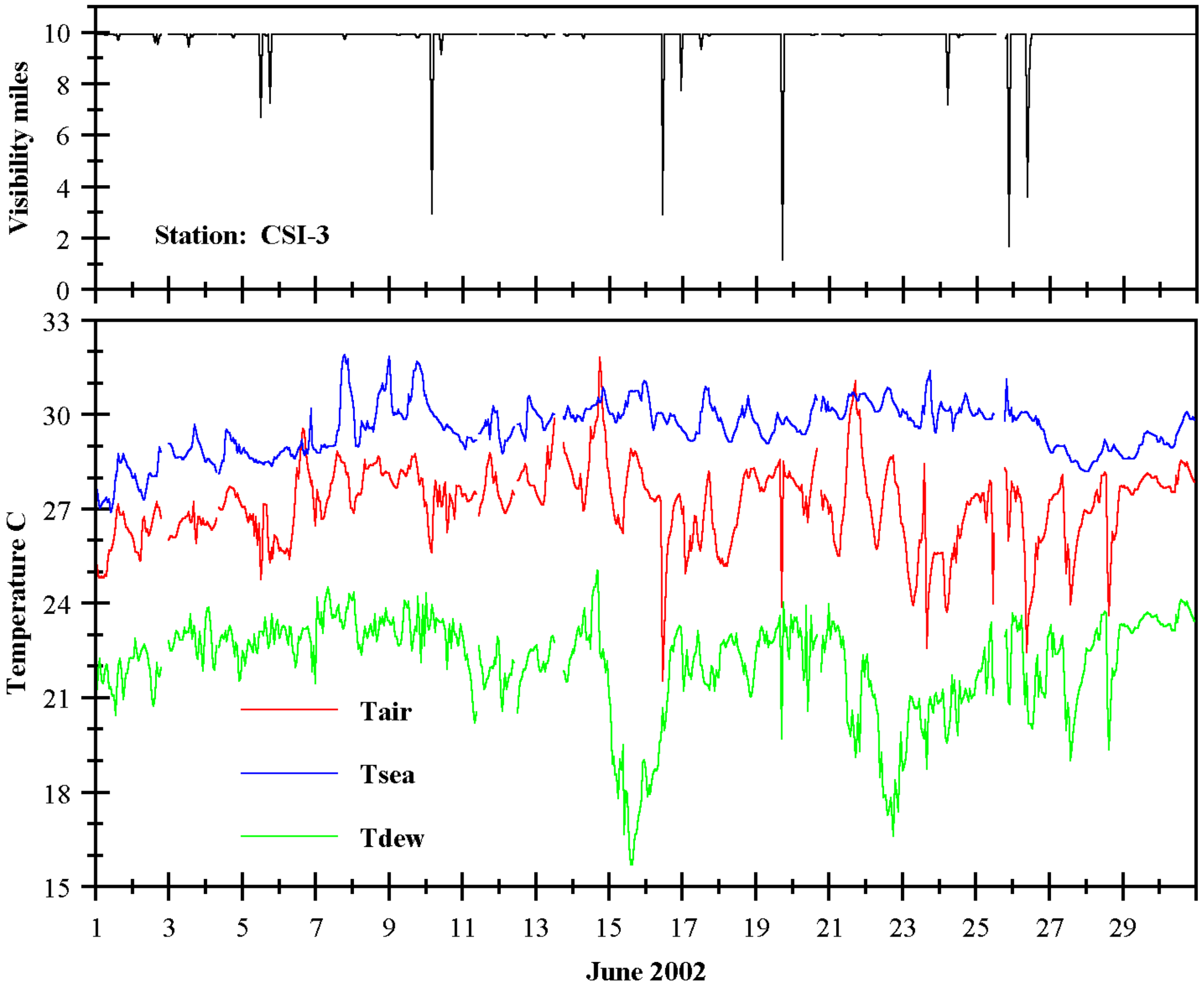

Figure 18. June 2002 hourly visibility and temperature records for station CSI-3.

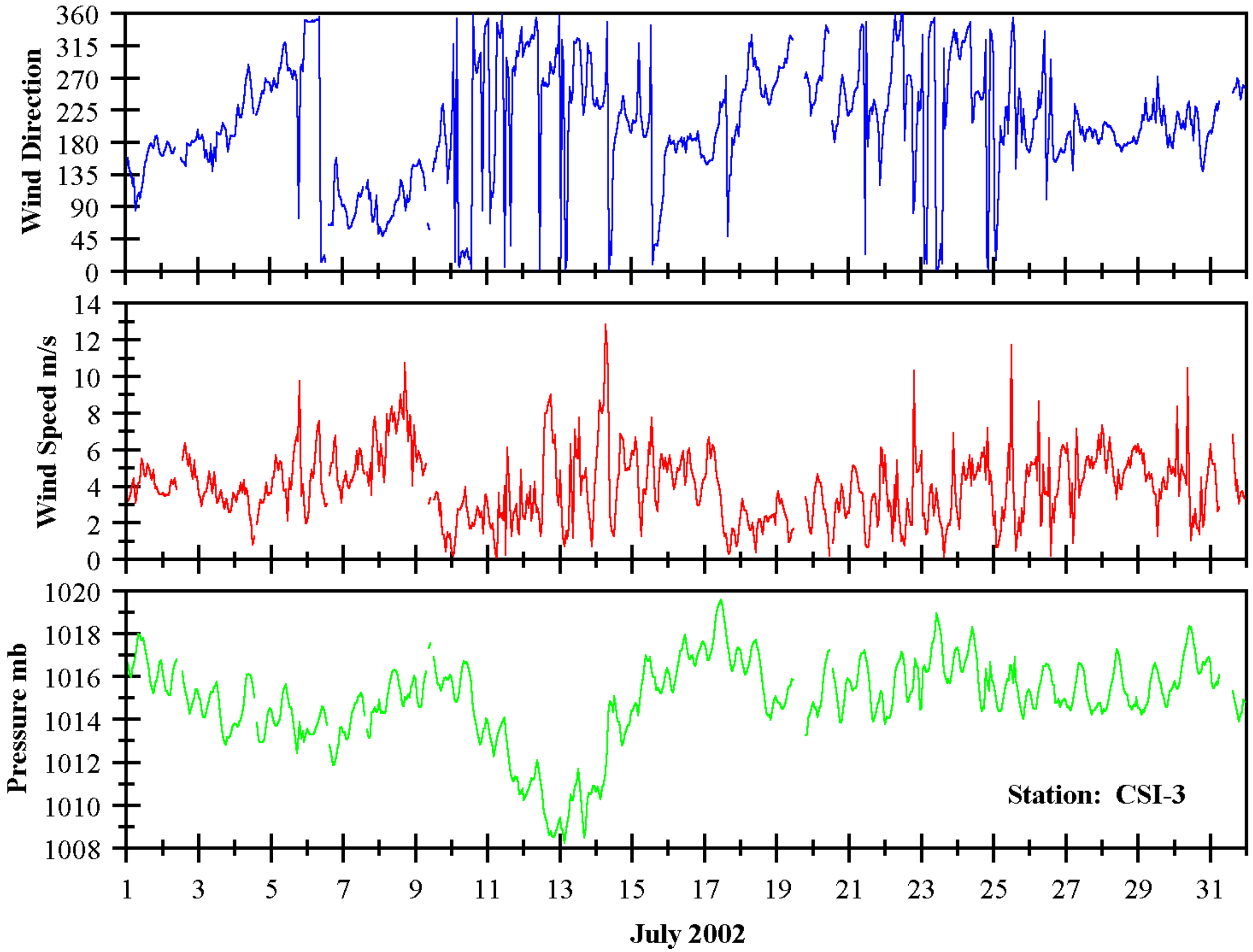

Figure 19. July 2002 hourly meteorological records for station CSI-3.

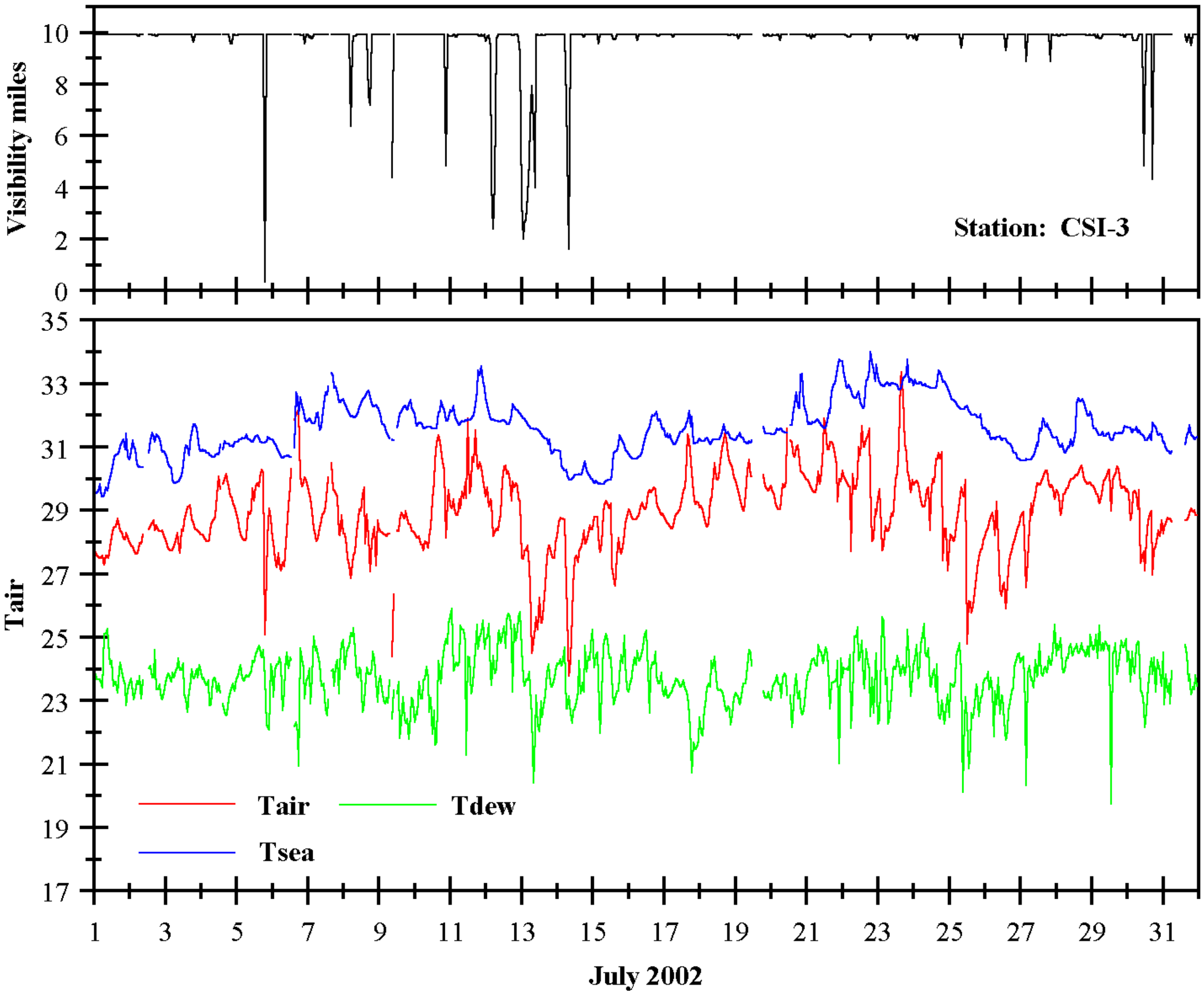

Figure 20. July 2002 hourly visibility and temperature records for station CSI-3.

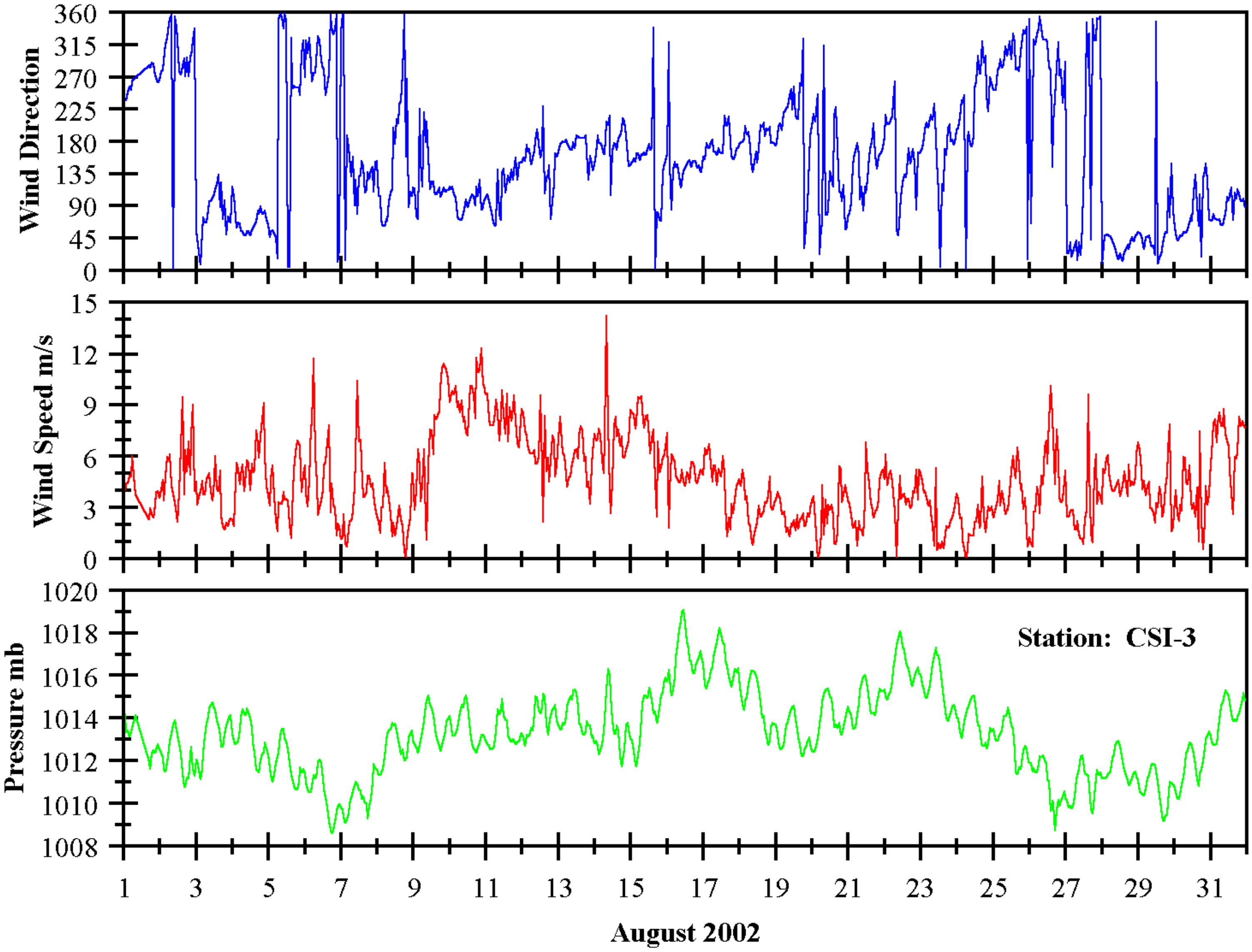

Figure 21. August 2002 hourly meteorological records for station CSI-3.

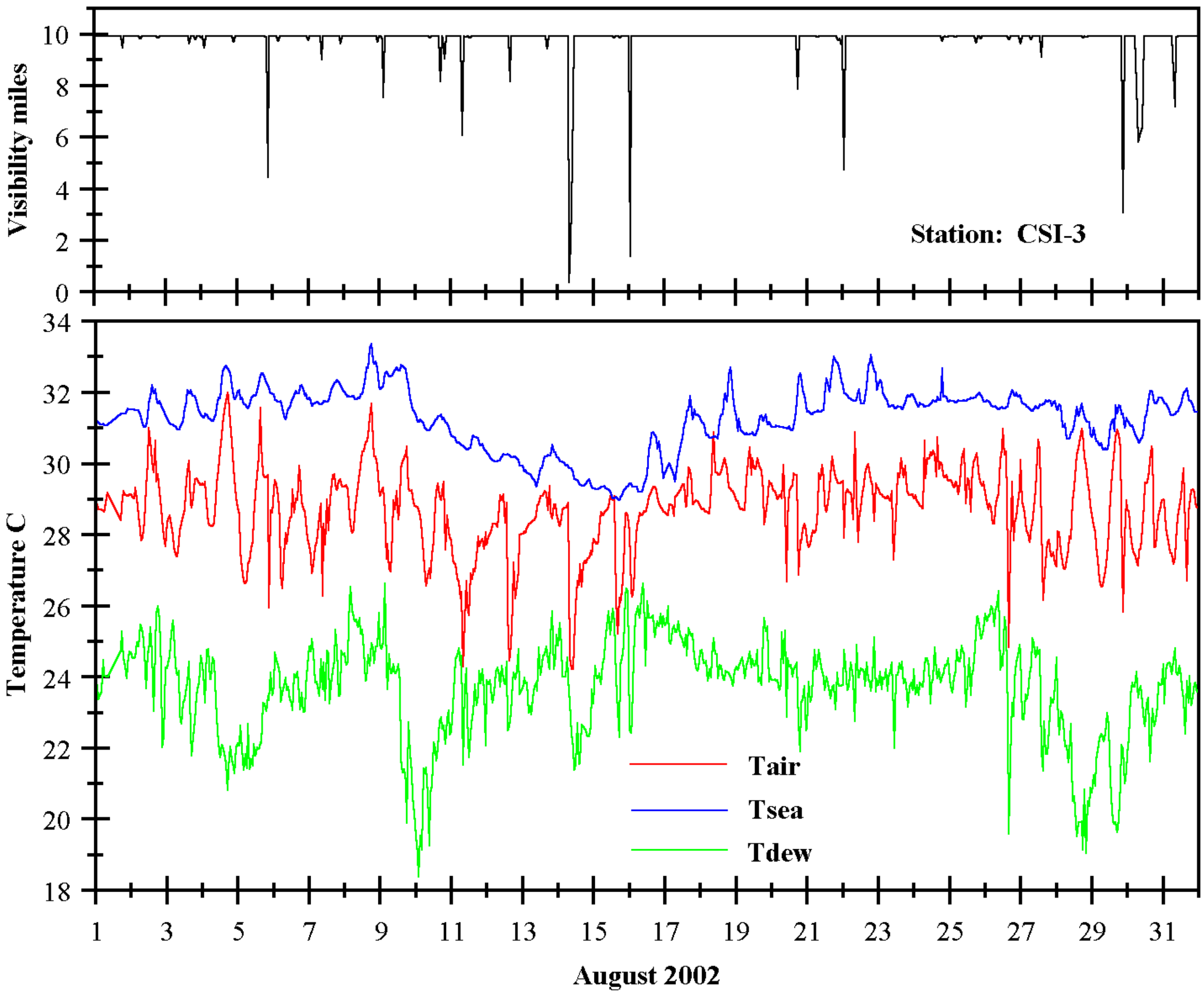

Figure 22. August 2002 hourly visibility and temperature records for station CSI-3.

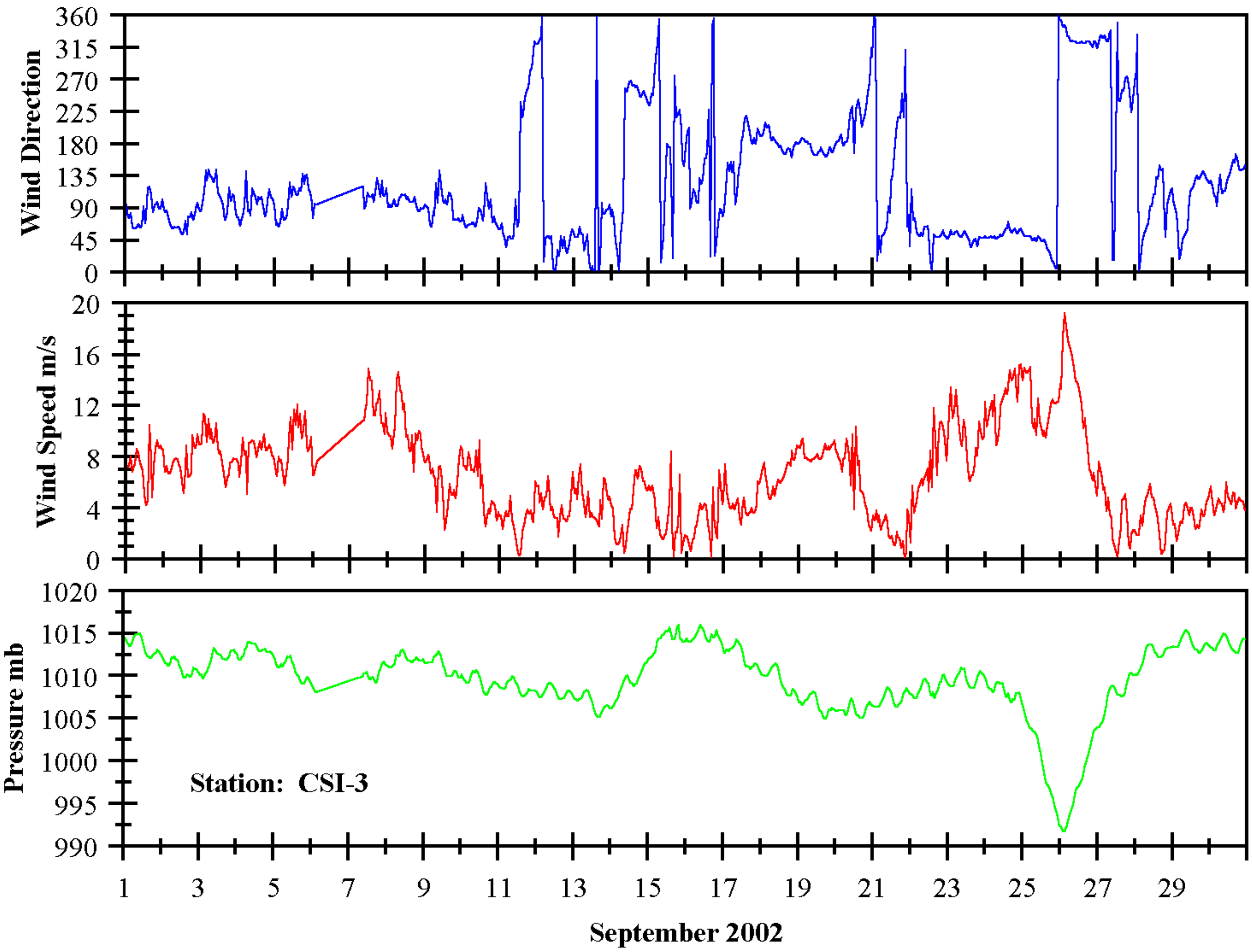

Figure 23. September 2002 hourly meteorological records for station CSI-3.

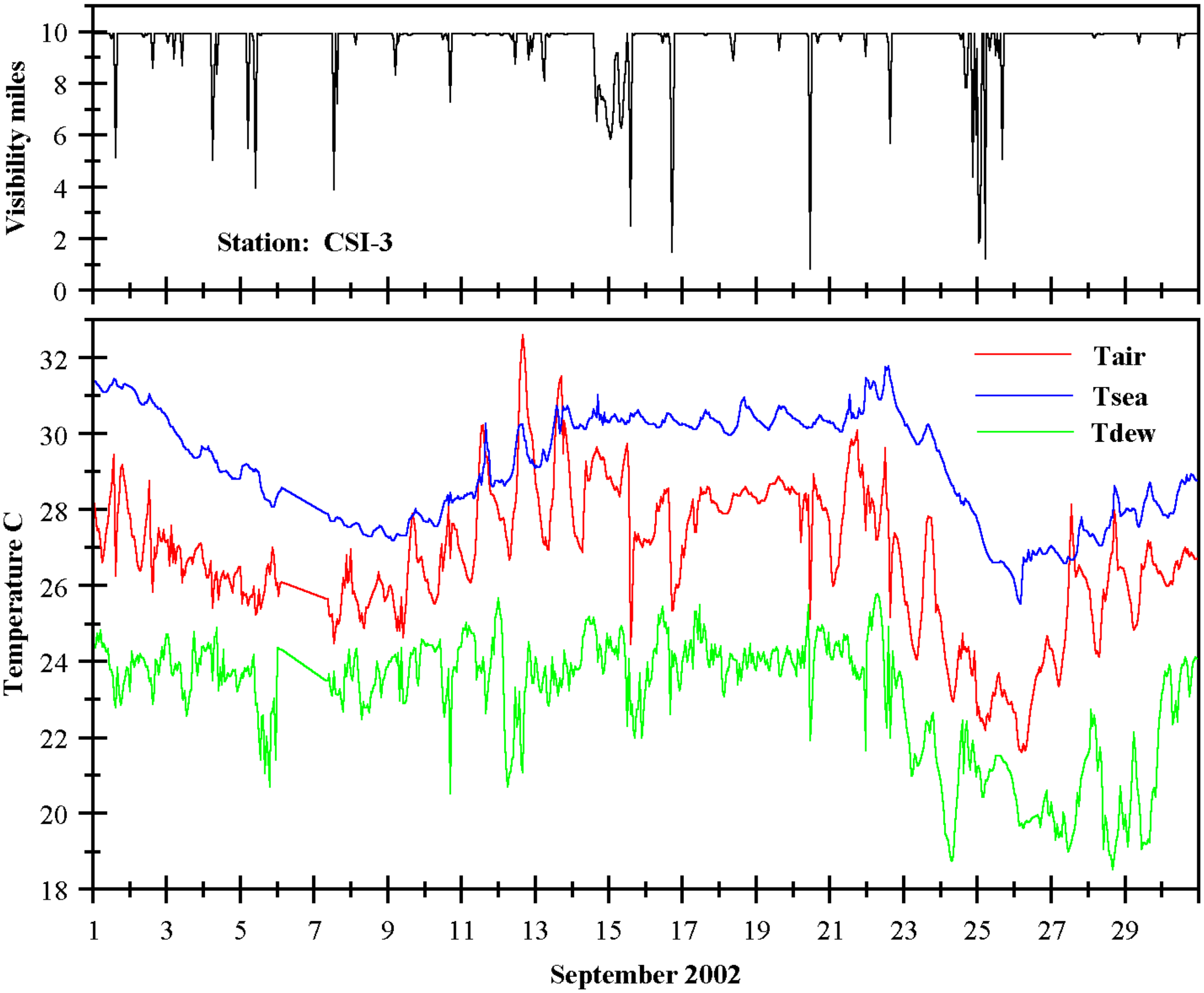

Figure 24. September 2002 hourly visibility and temperature records for station CSI-3.

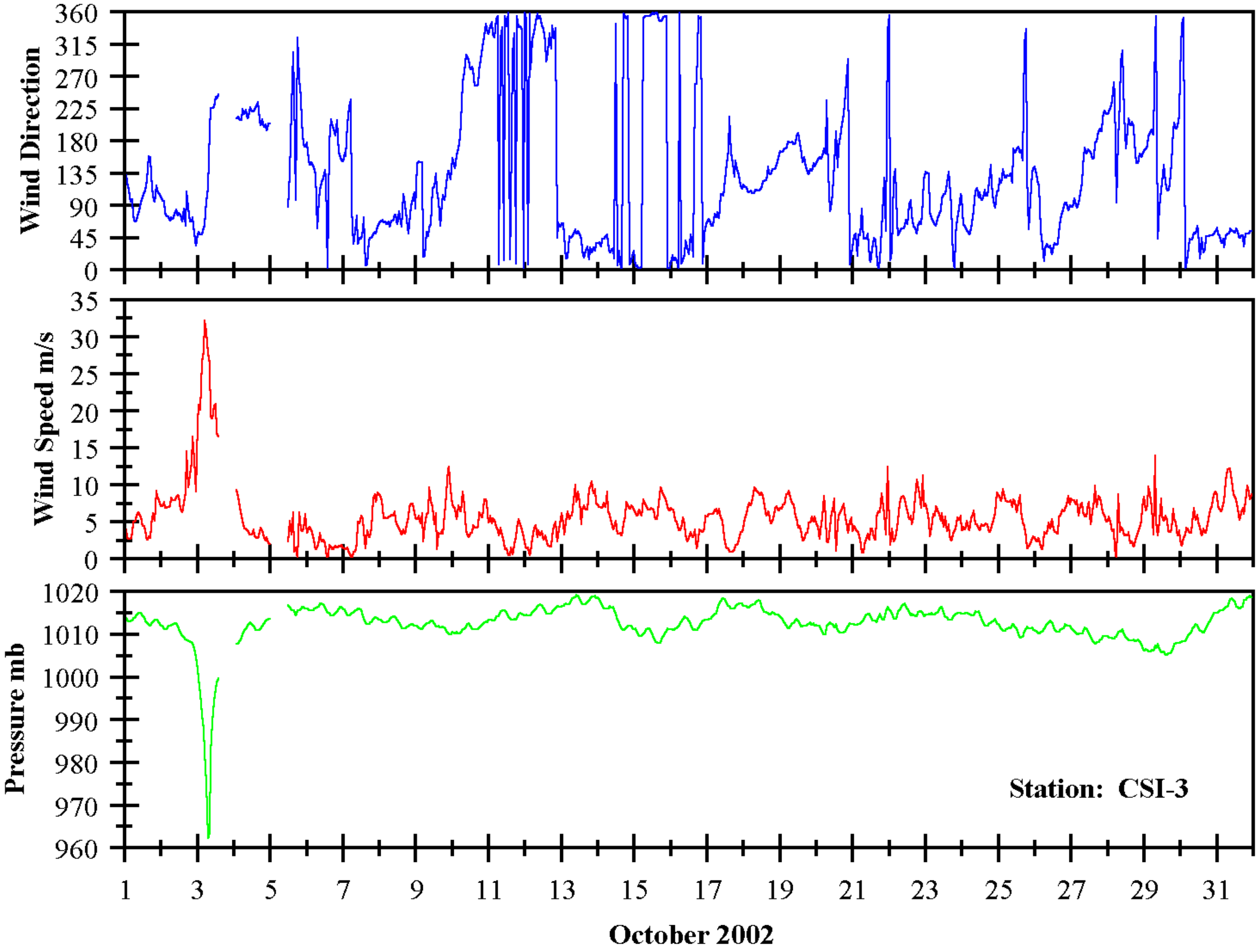

Figure 25. October 2002 hourly meteorological records for station CSI-3.

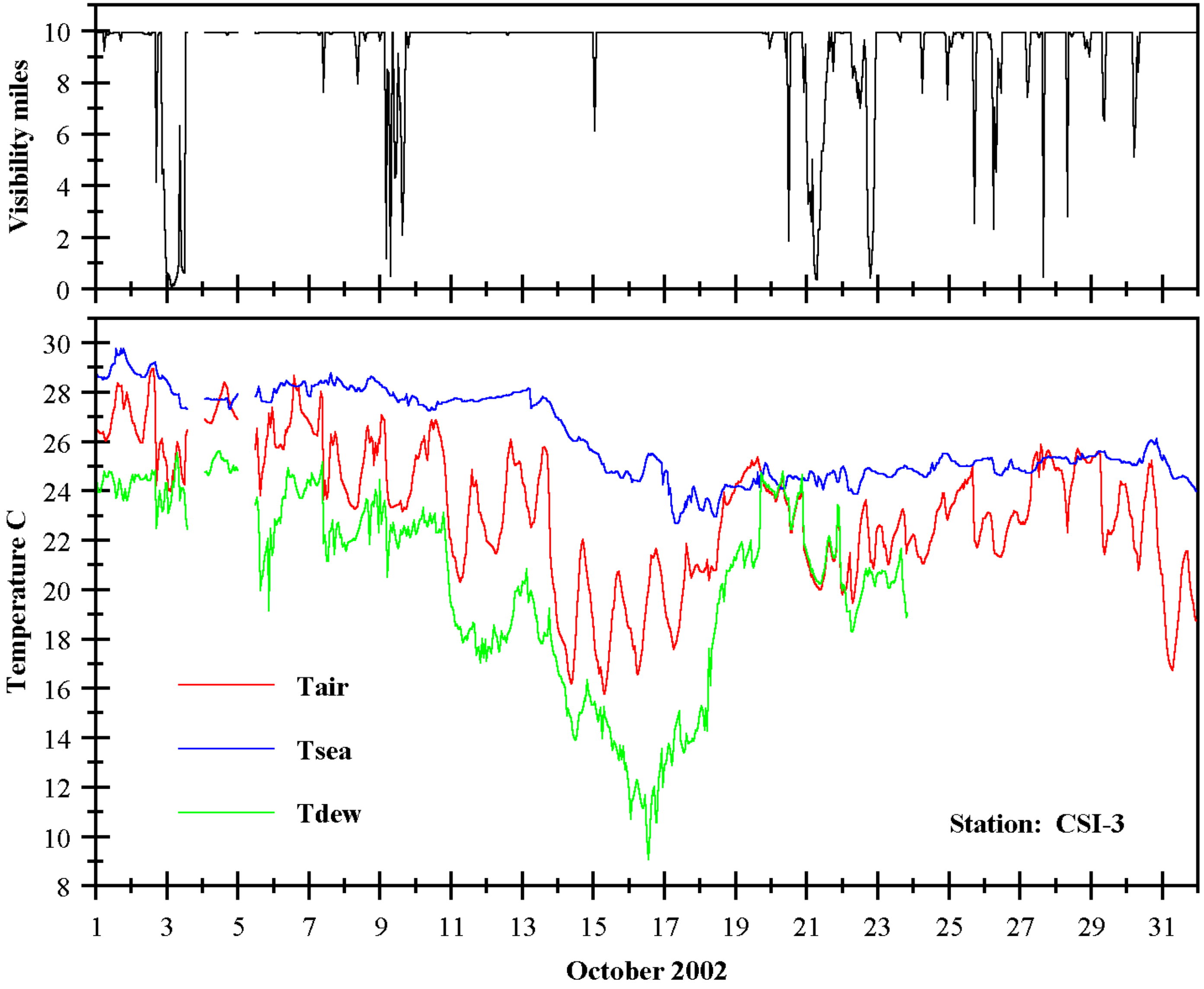

Figure 26. October 2002 hourly visibility and temperature records for station CSI-3.

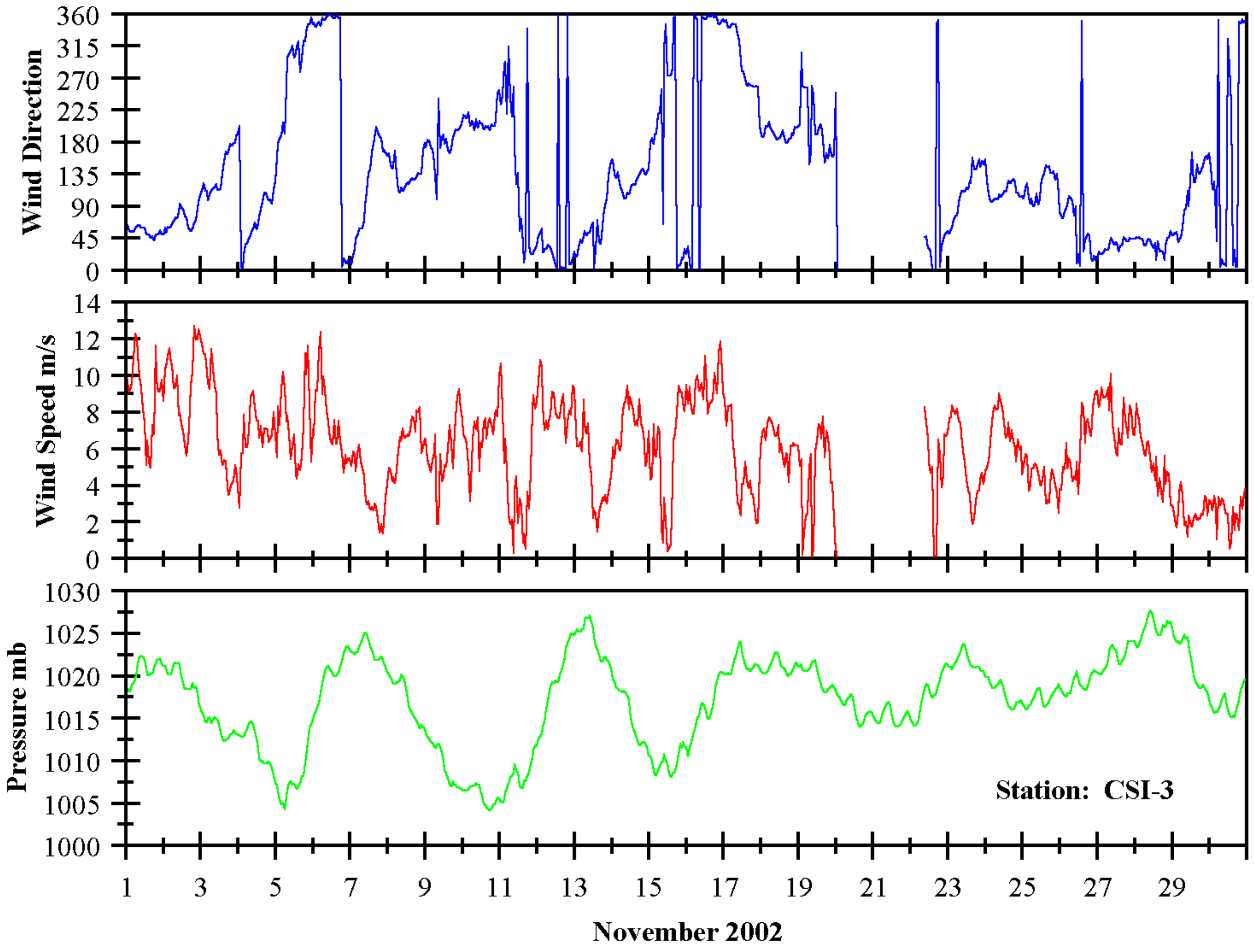

Figure 27. November 2002 hourly meteorological records for station CSI-3.

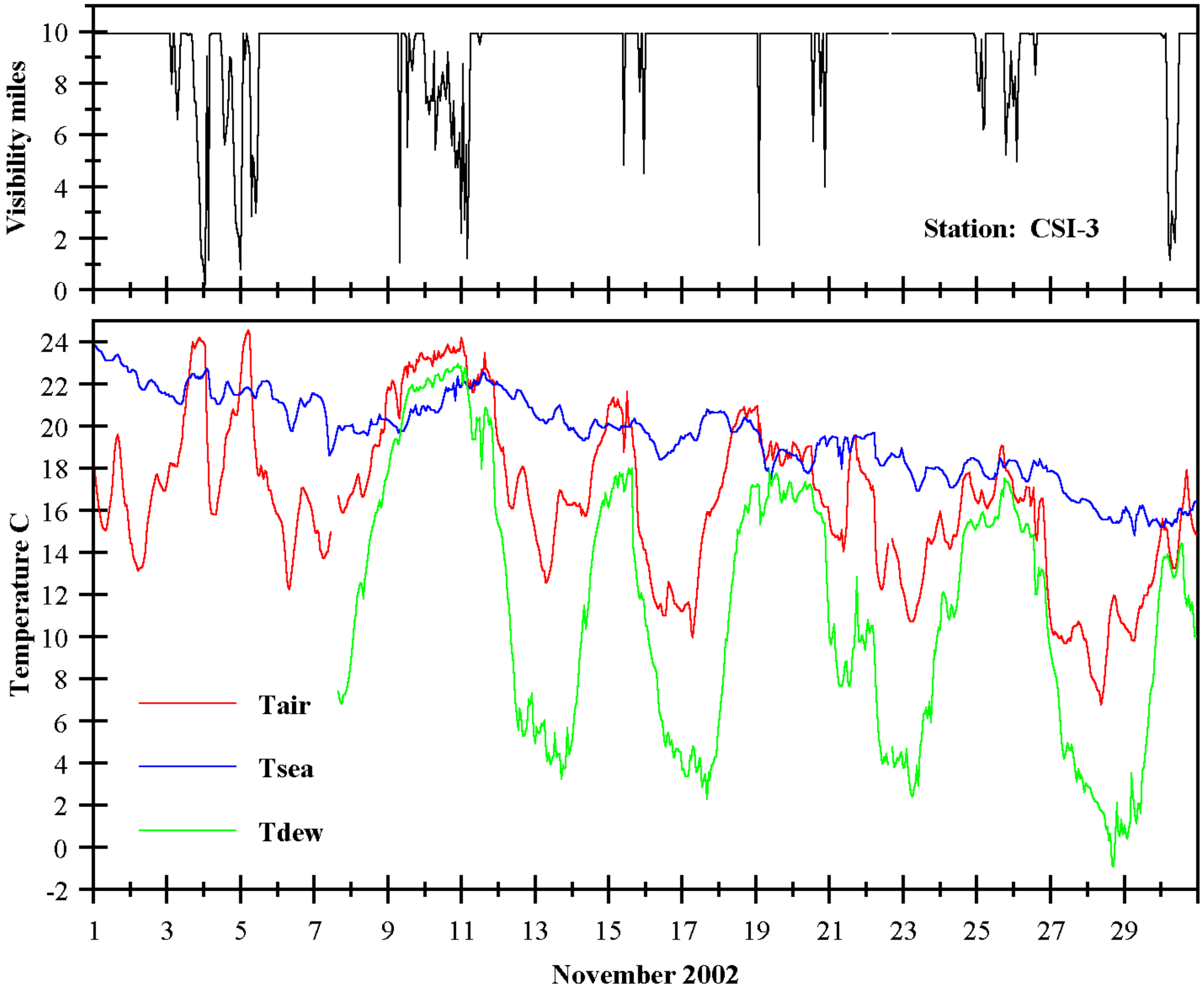

Figure 28. November 2002 hourly visibility and temperature records for station CSI-3.

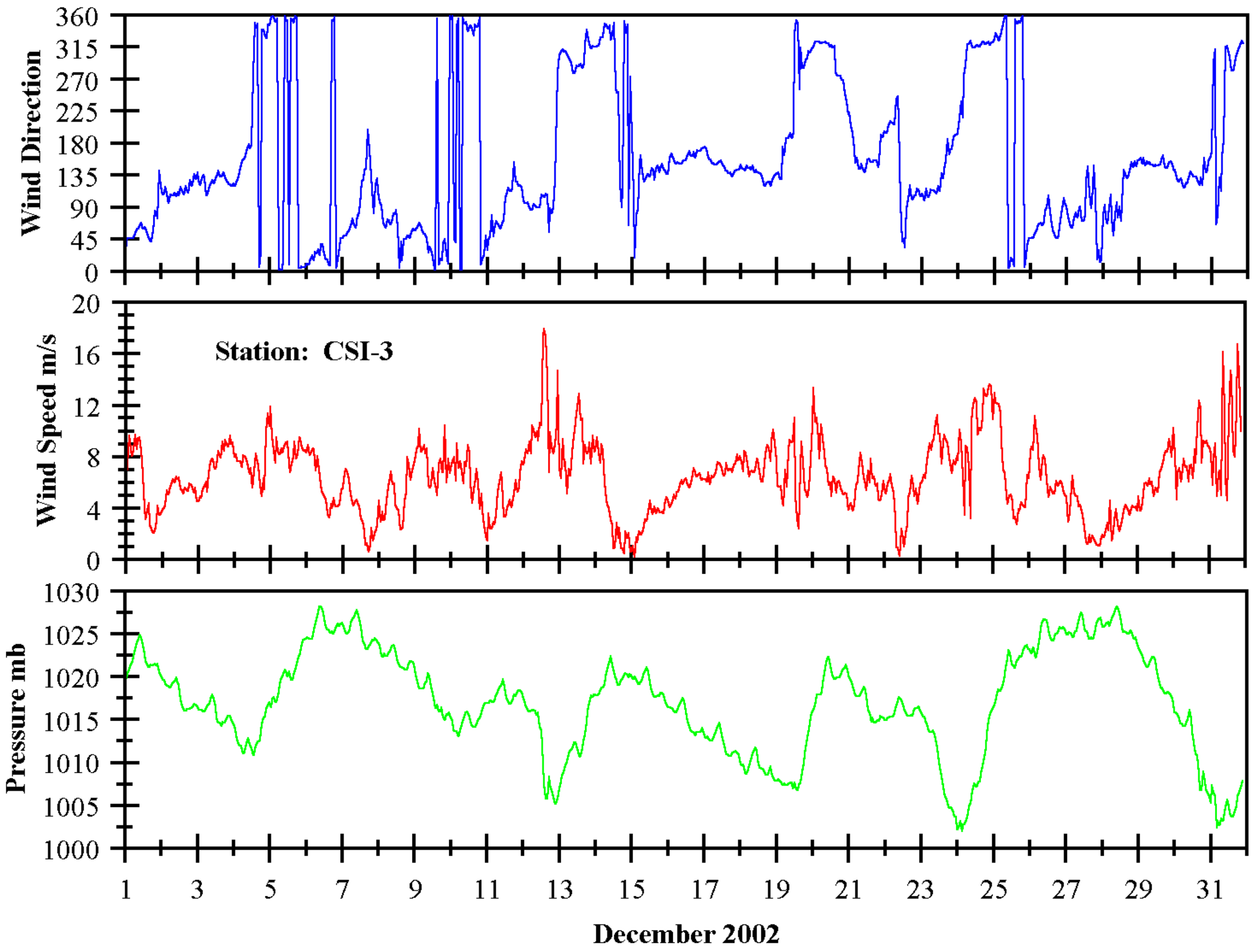

Figure 29. December 2002 hourly meteorological records for station CSI-3.

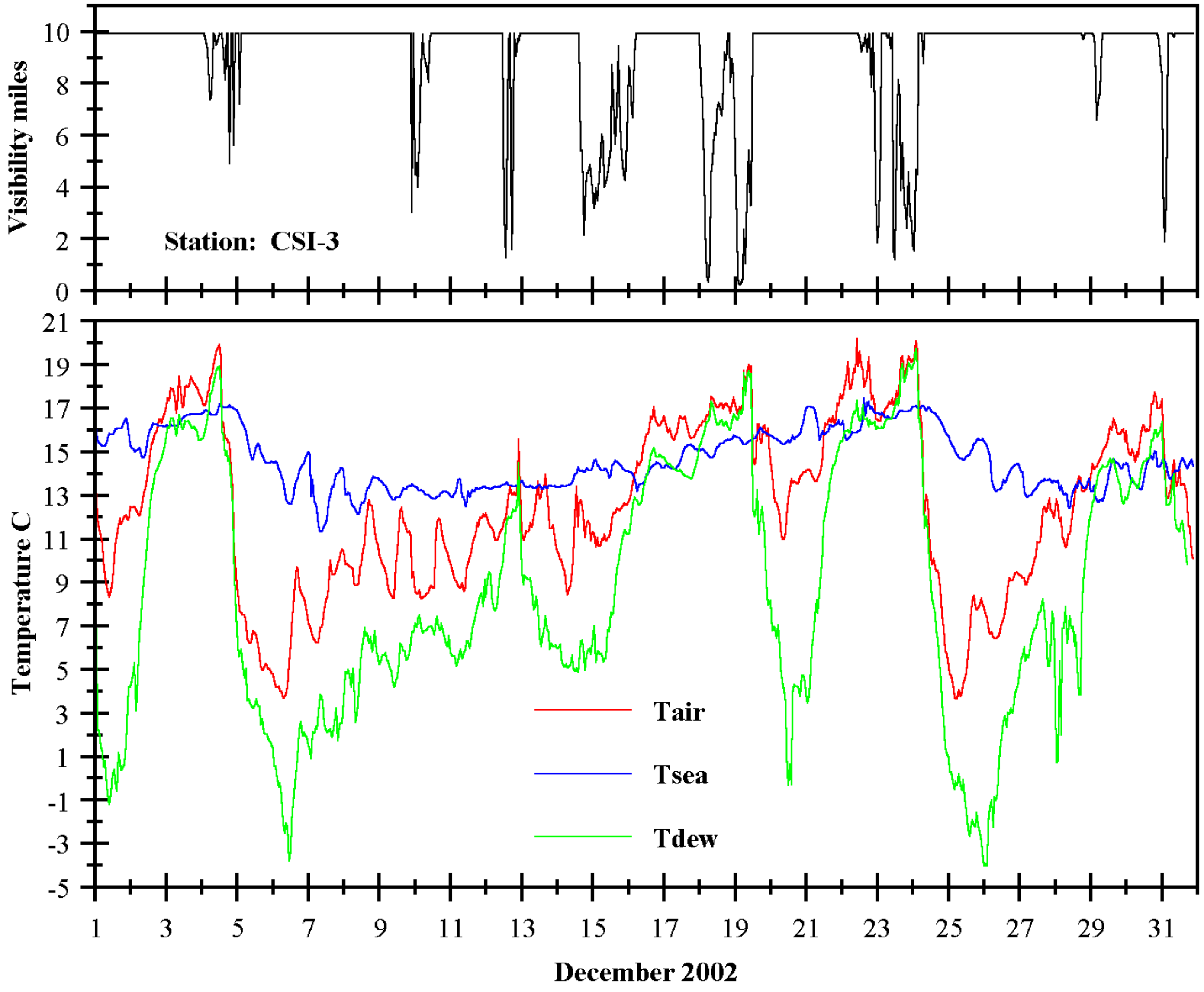

Figure 30. December 2002 hourly visibility and temperature records for station CSI-3.

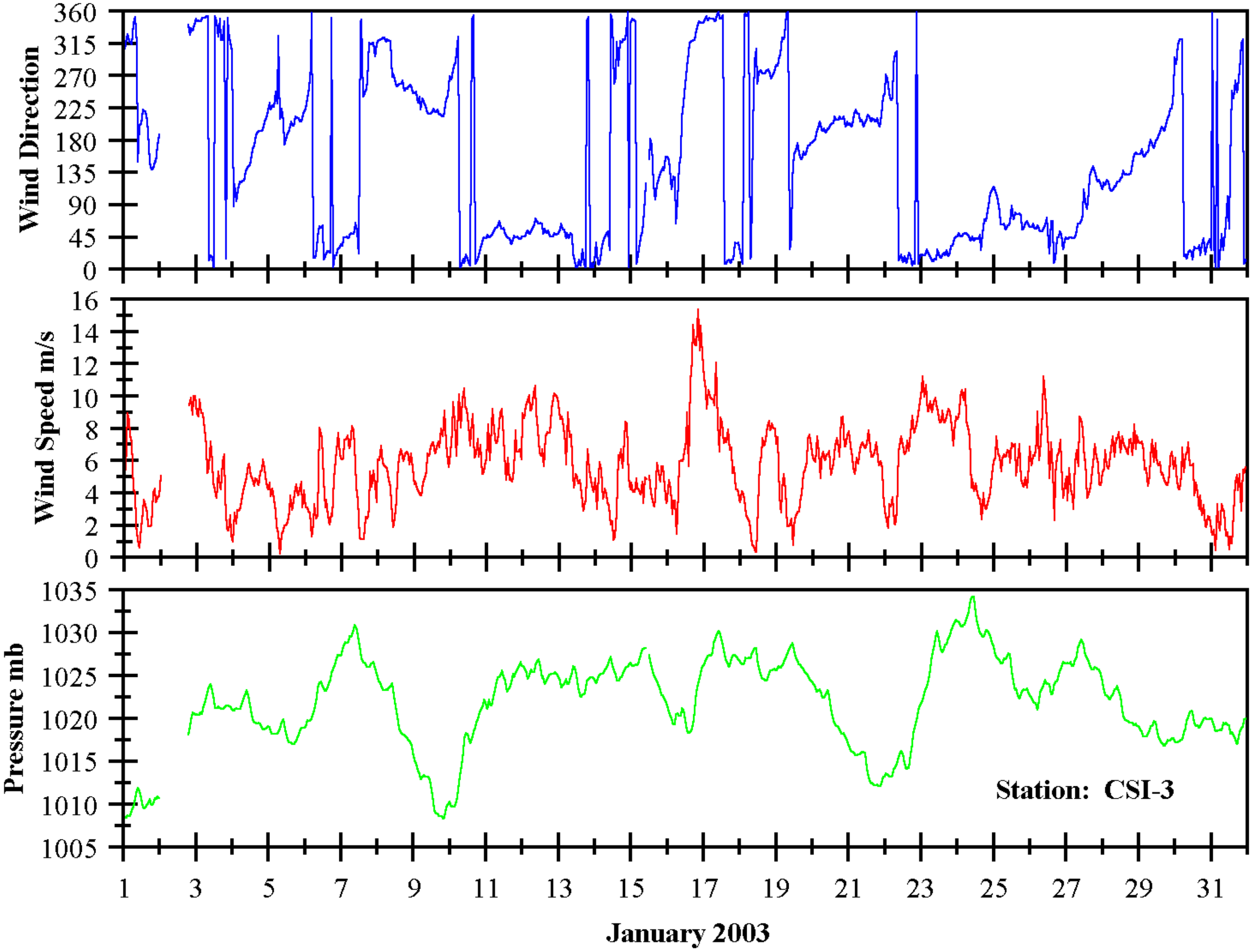

Figure 31. January 2003 hourly meteorological records for station CSI-3.

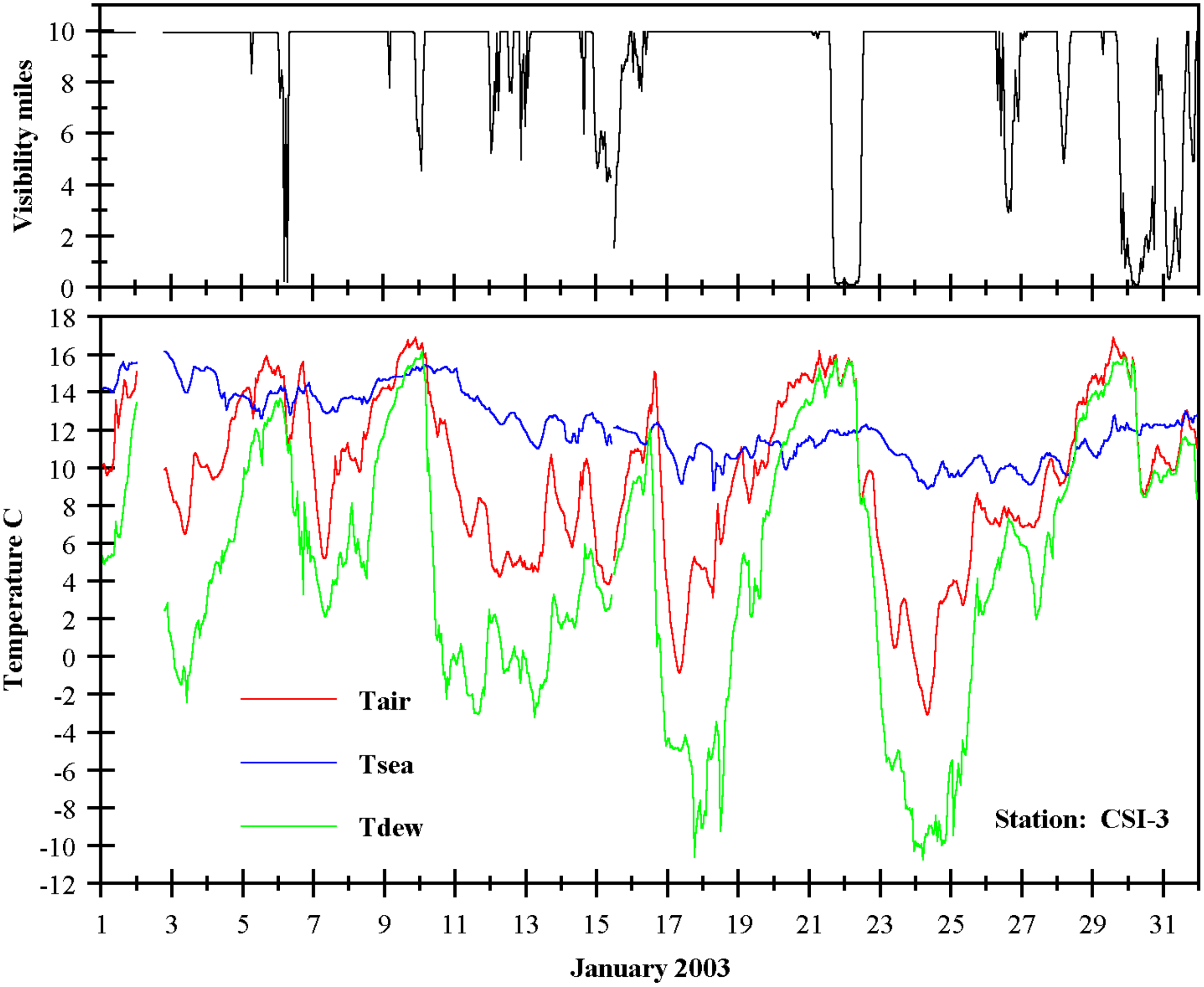

Figure 32. January 2003 hourly visibility and temperature records for station CSI-3.

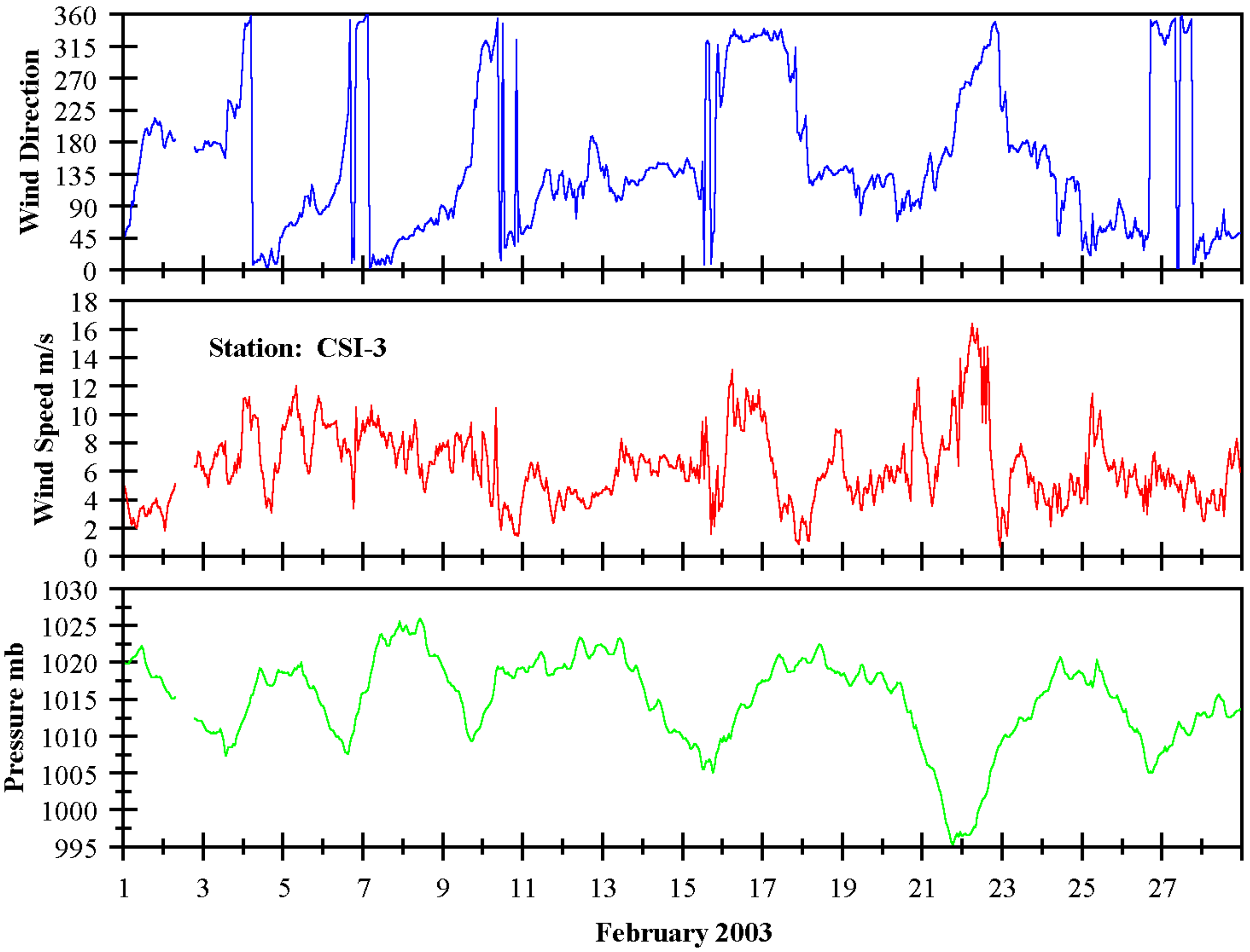

Figure 33. February 2003 hourly meteorological records for station CSI-3.

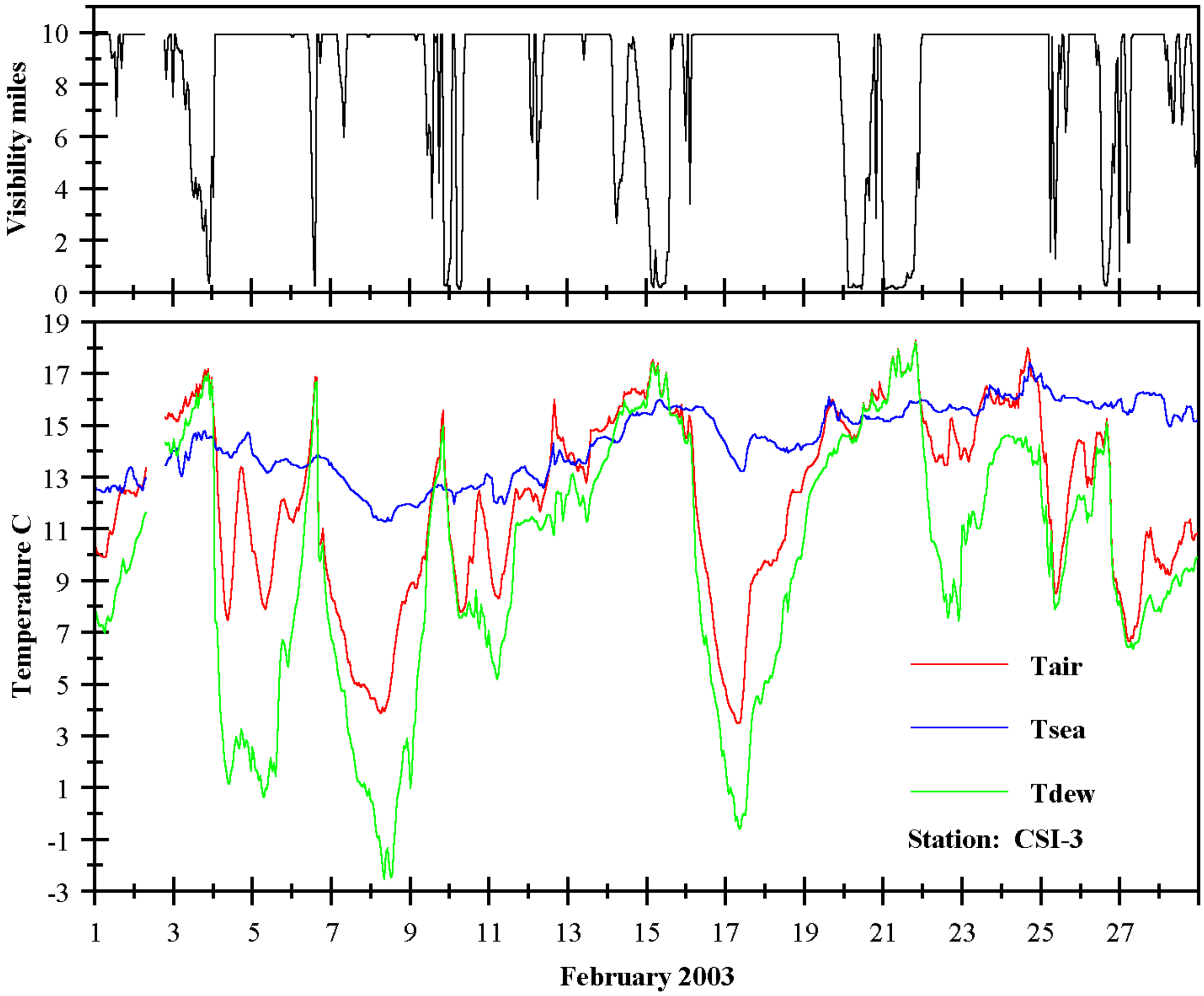

Figure 34. February 2003 hourly visibility and temperature records for station CSI-3.

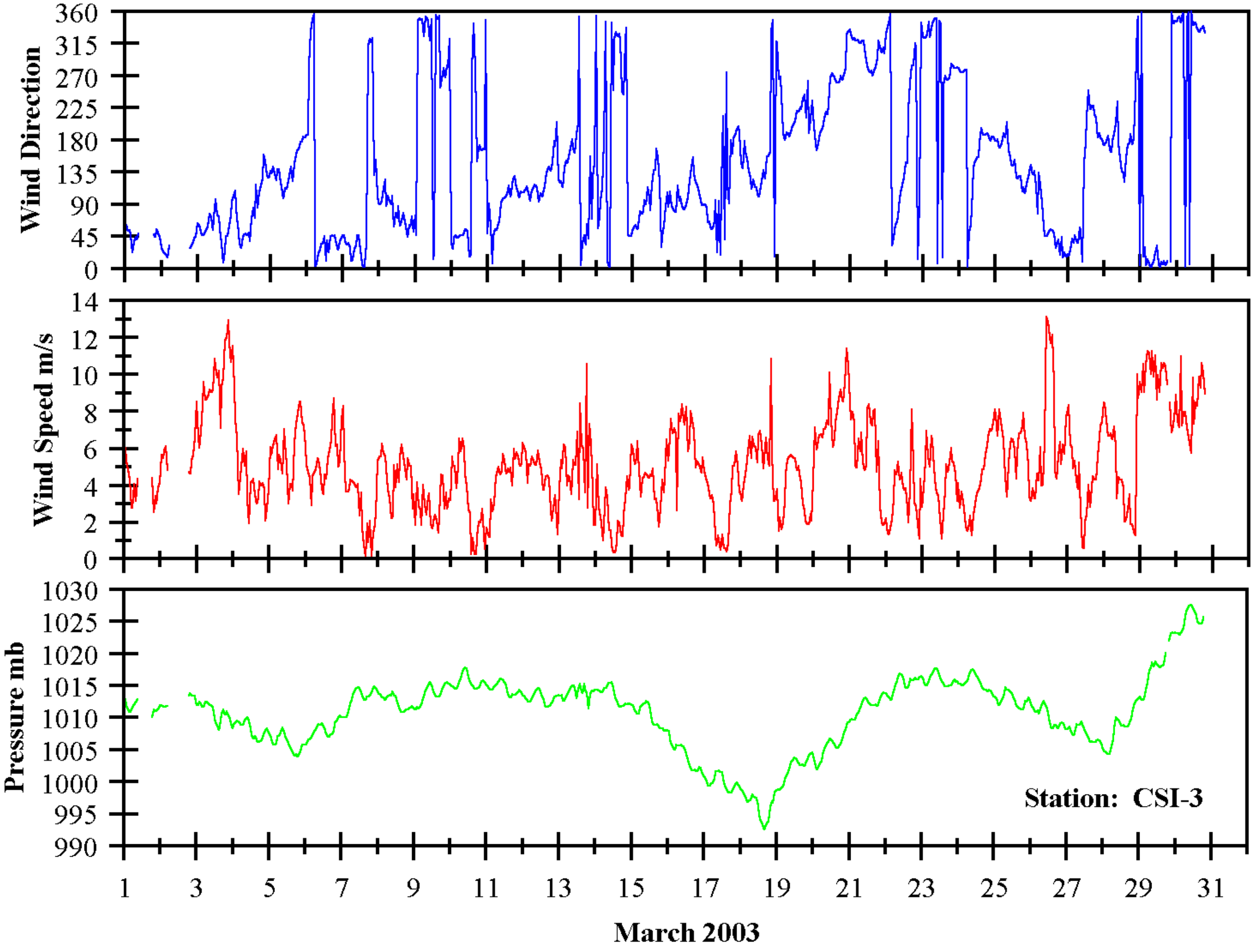

Figure 35. March 2003 hourly meteorological records for station CSI-3.

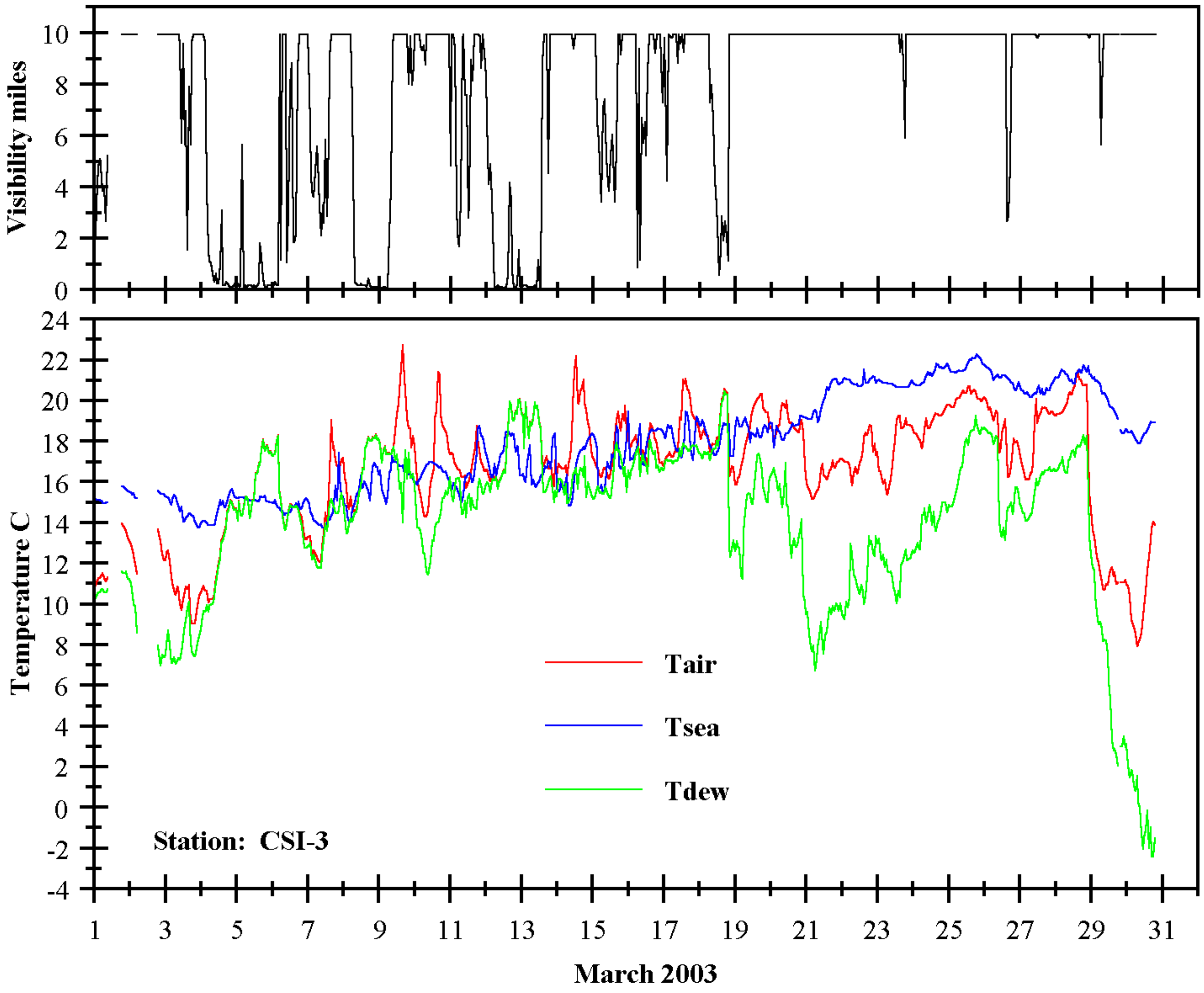

Figure 36. March 2003 hourly visibility and temperature records for station CSI-3.

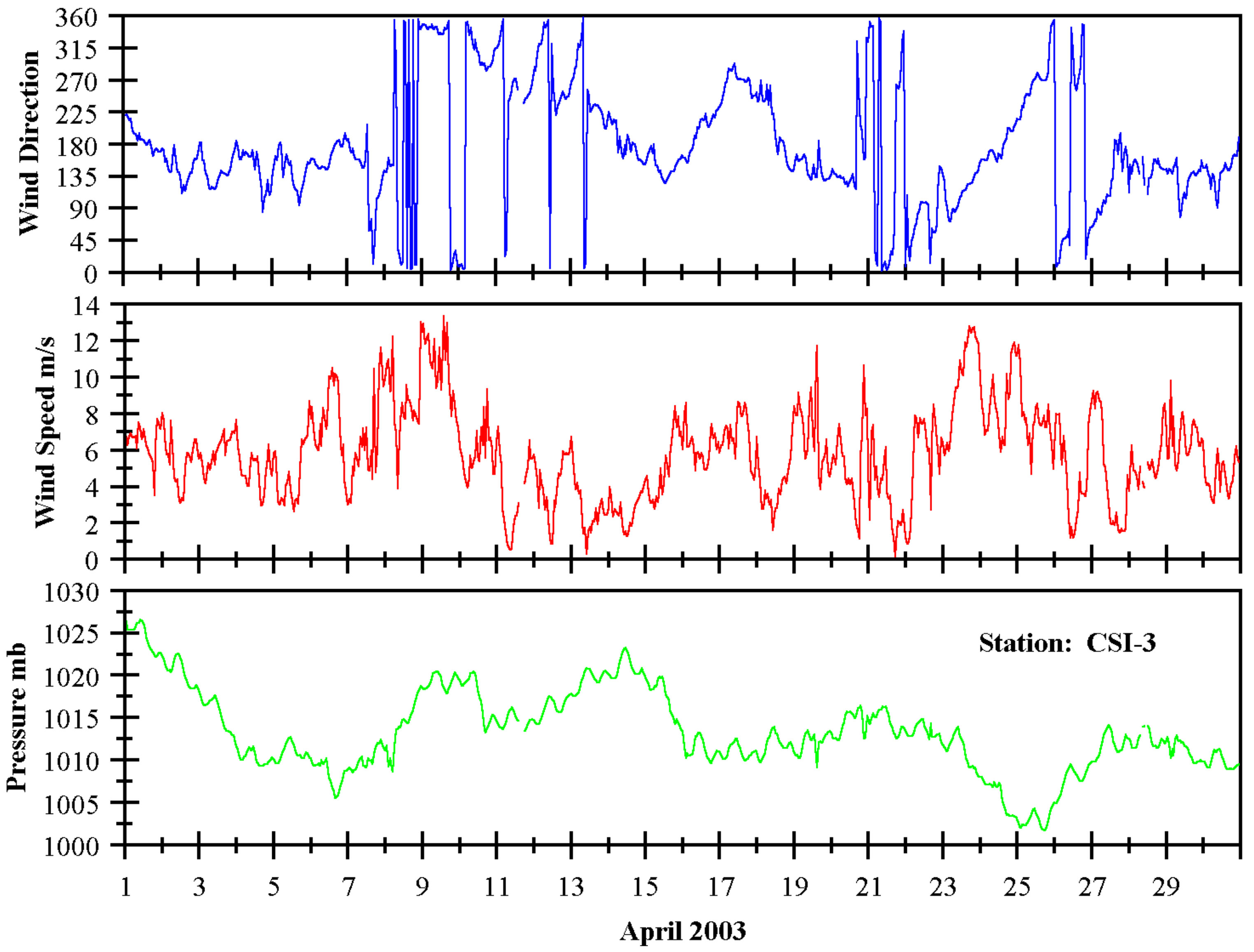

Figure 37. April 2003 hourly meteorological records for station CSI-3.

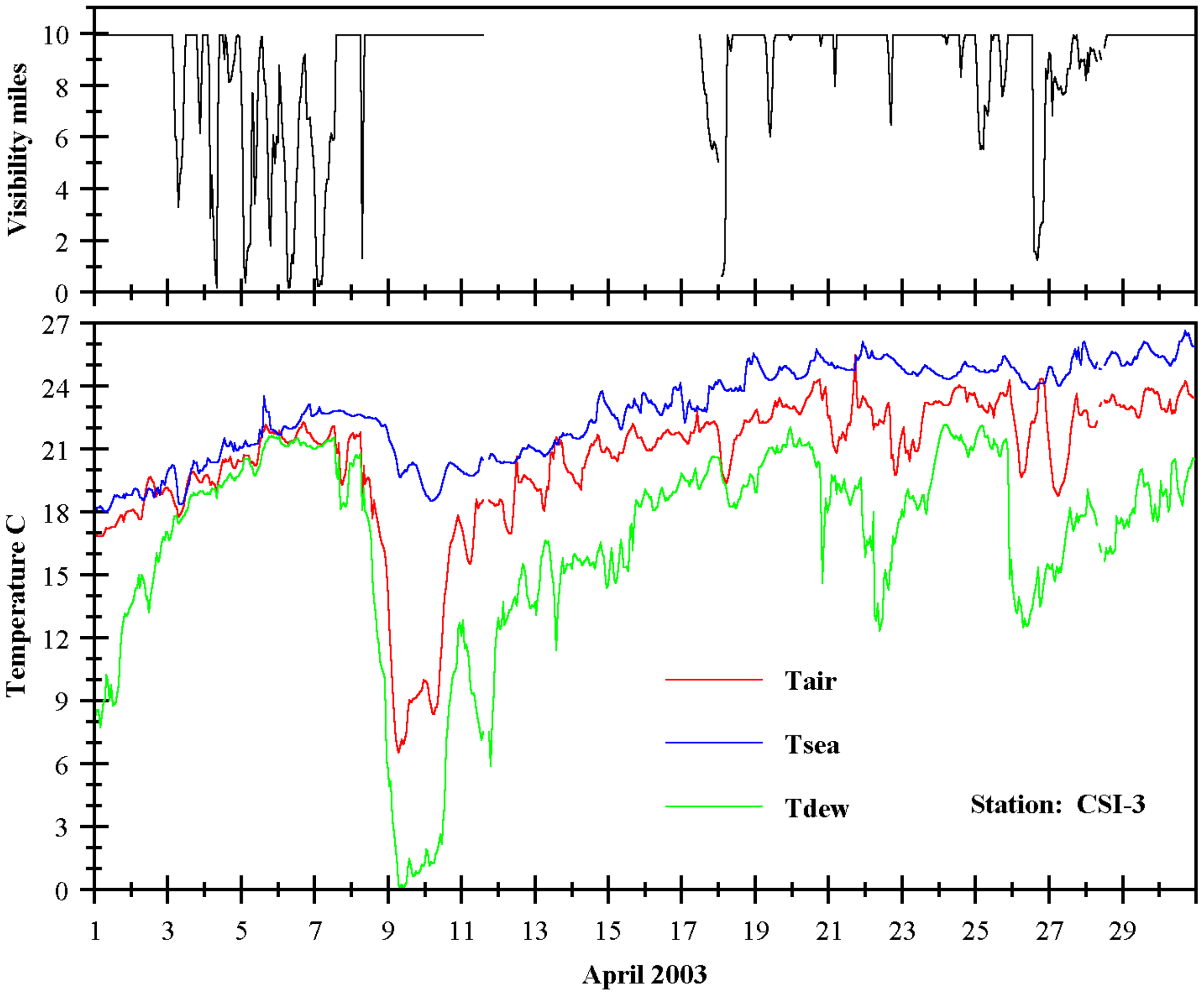

Figure 38. April 2003 hourly visibility and temperature records for station CSI-3.

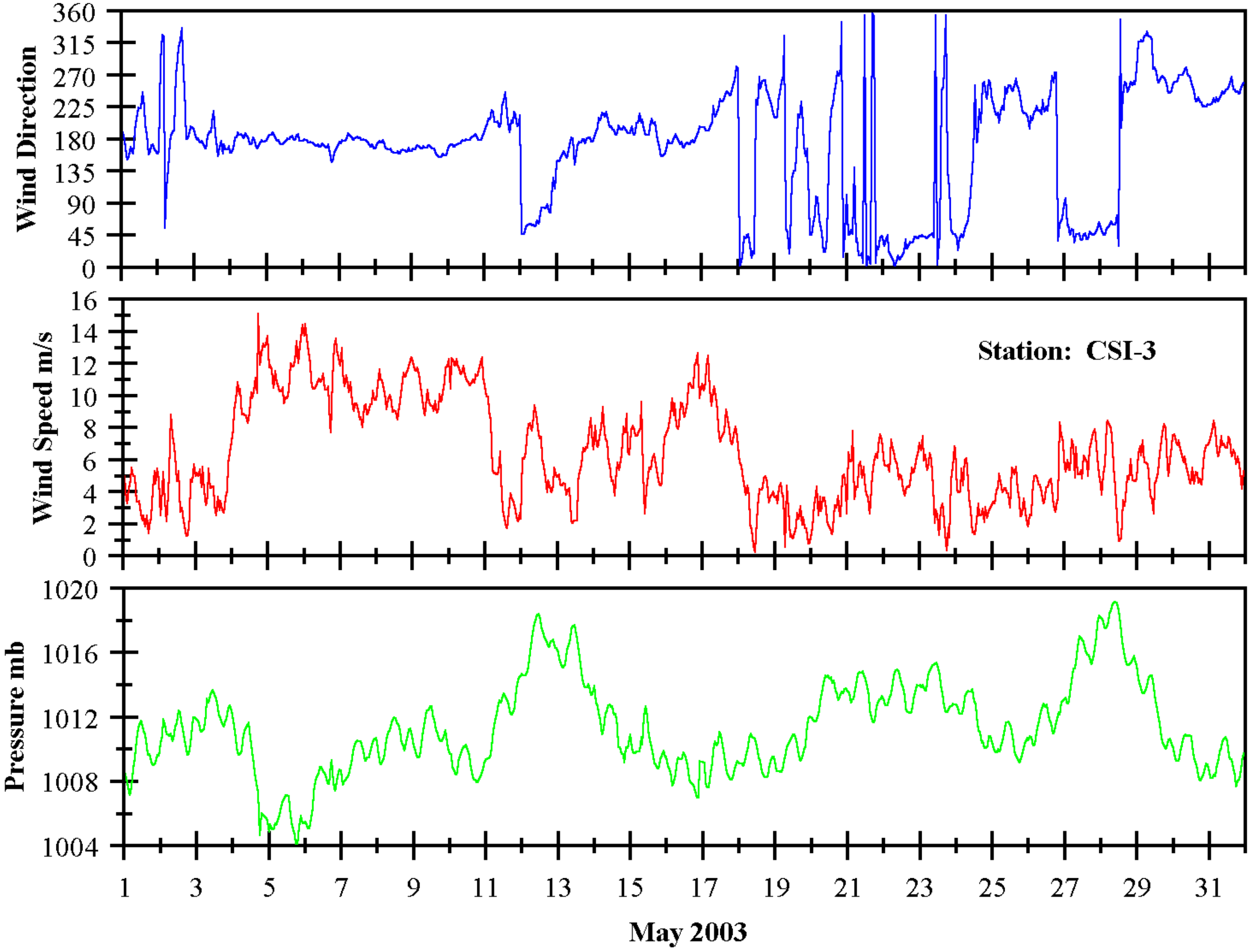

Figure 39. May 2003 hourly meteorological records for station CSI-3.

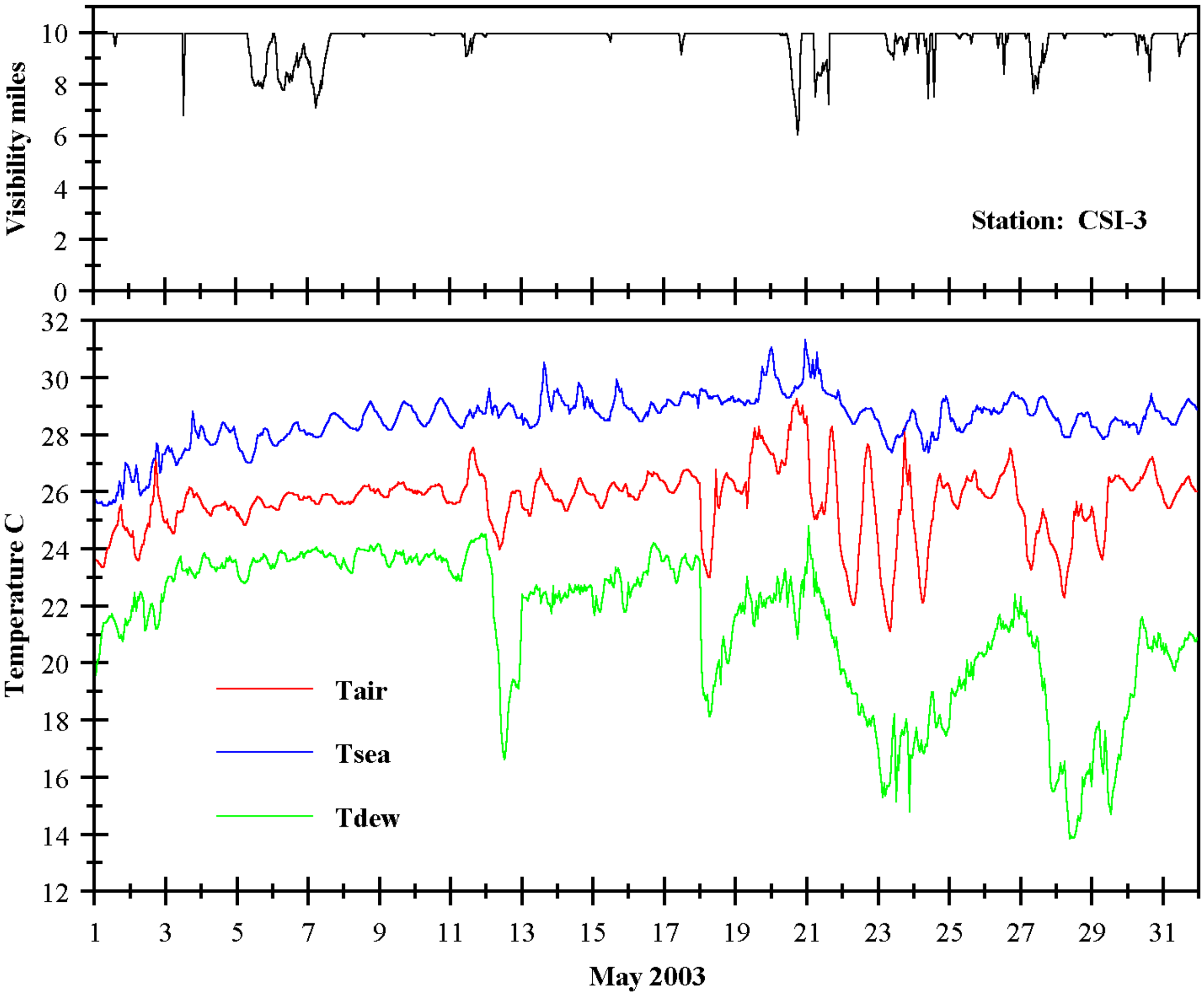

Figure 40. May 2003 hourly visibility and temperature records for station CSI-3.

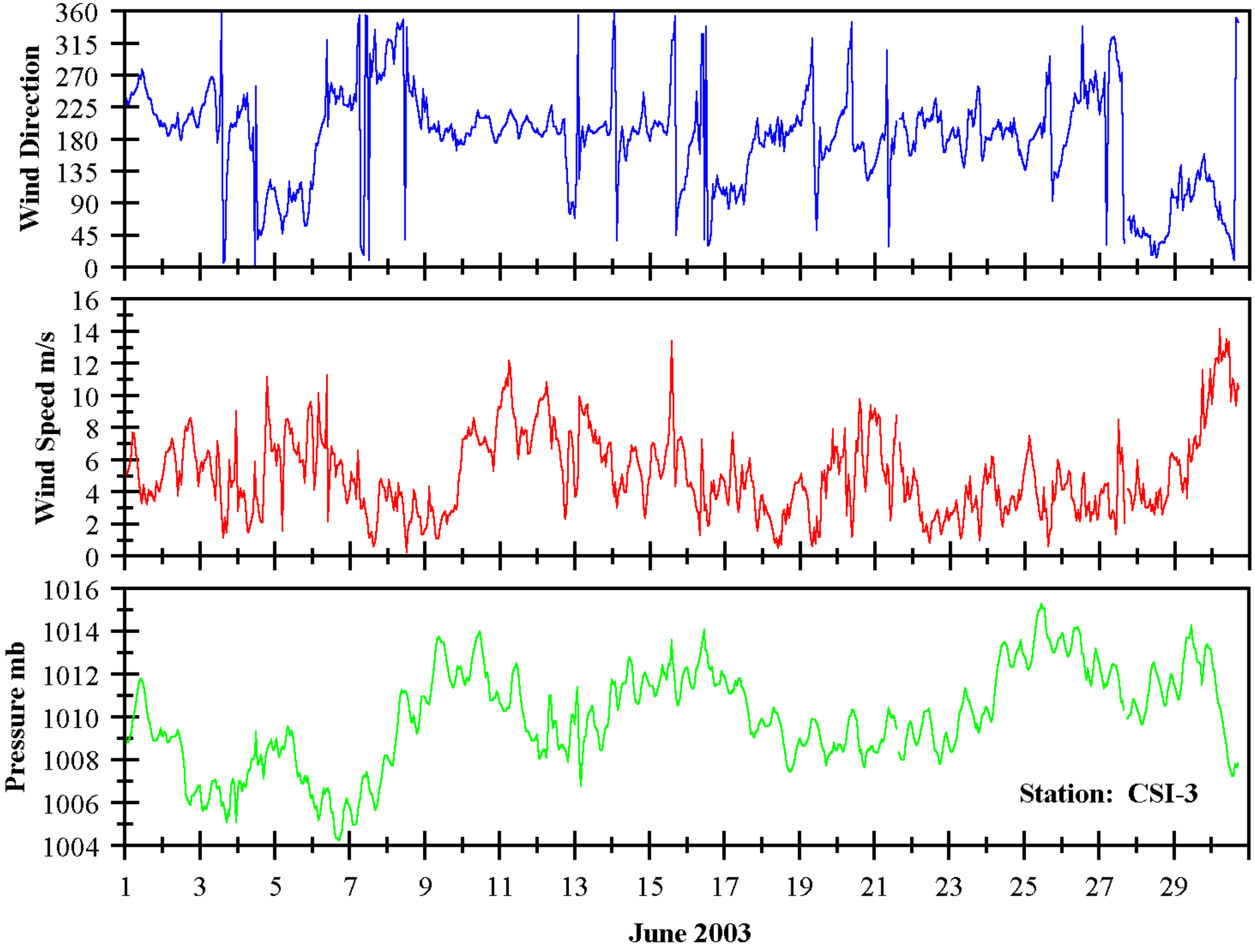

Figure 41. June 2003 hourly meteorological records for station CSI-3.

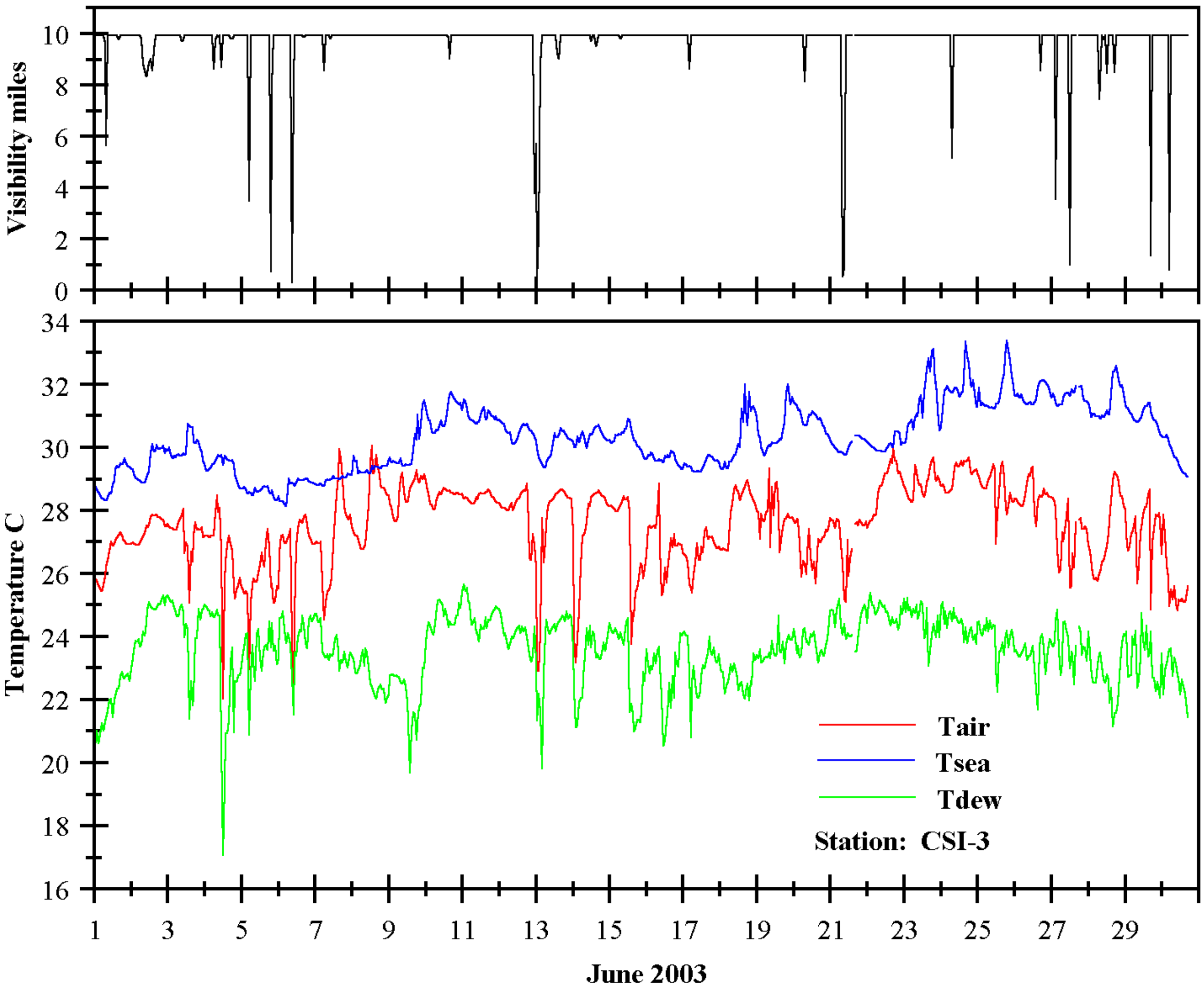

Figure 42. June 2003 hourly visibility and temperature records for station CSI-3.

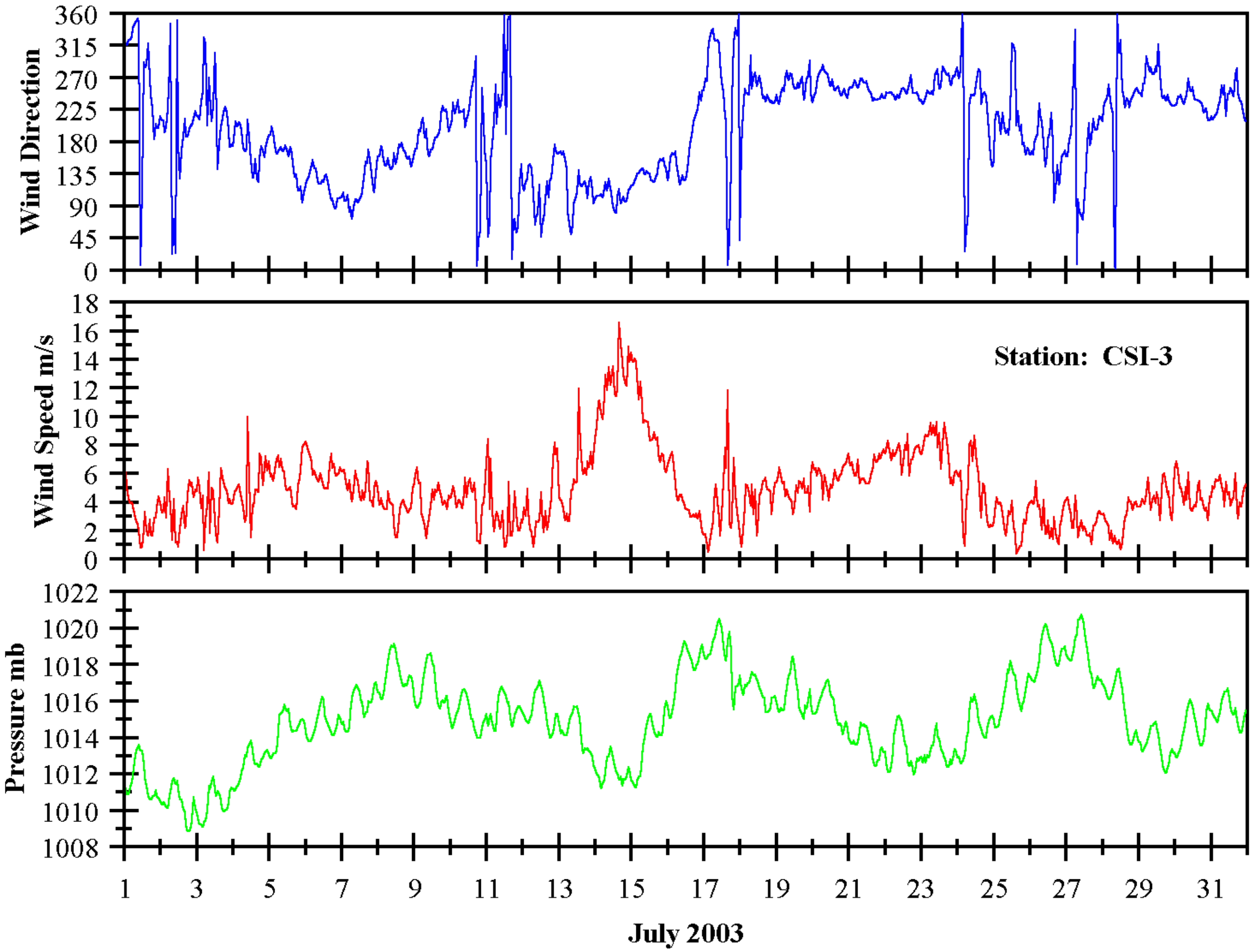

Figure 43. July 2003 hourly meteorological records for station CSI-3.

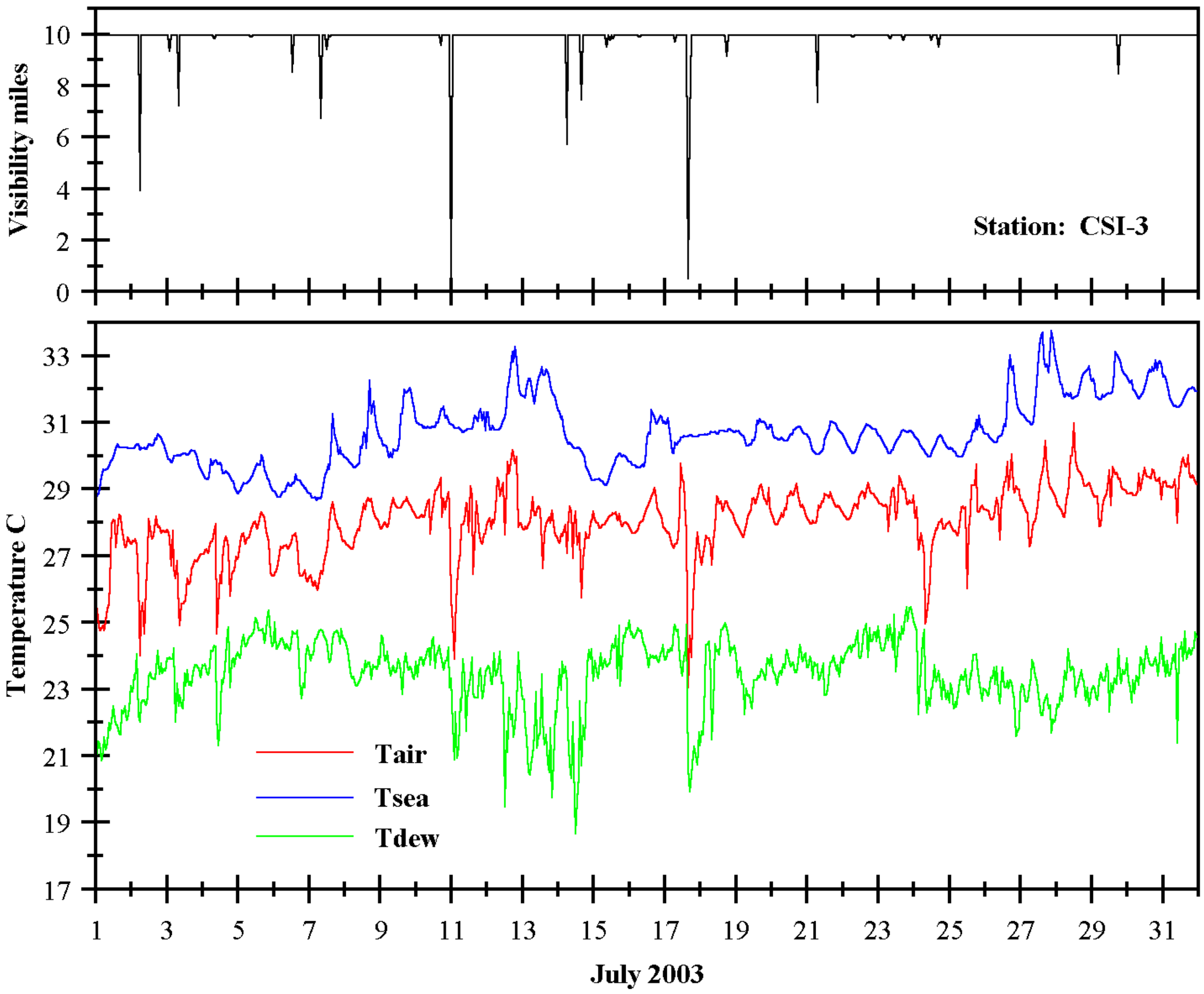

Figure 44. July 2003 hourly visibility and temperature records for station CSI-3.

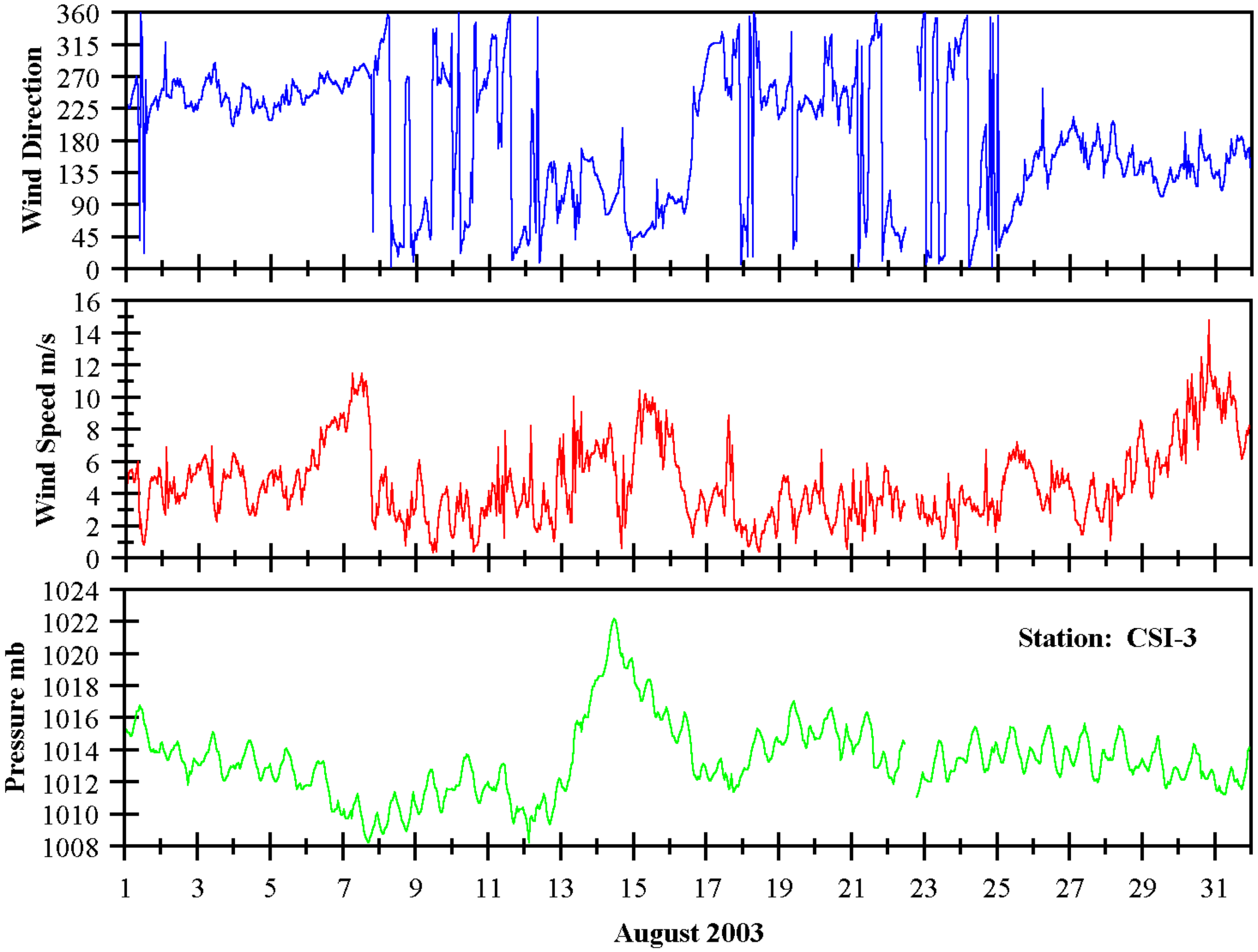

Figure 45. August 2003 hourly meteorological records for station CSI-3.

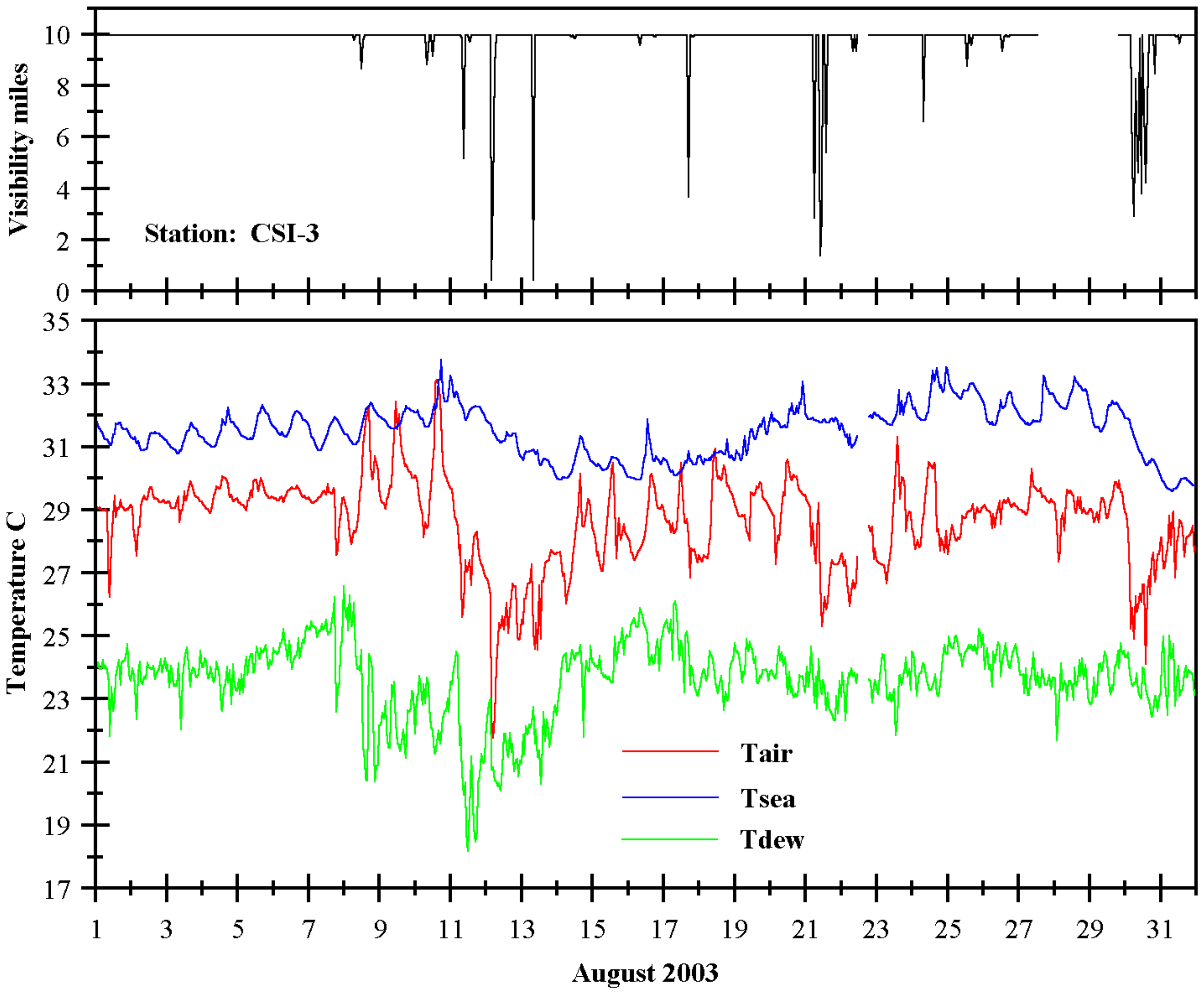

Figure 46. August 2003 hourly visibility and temperature records for station CSI-3.

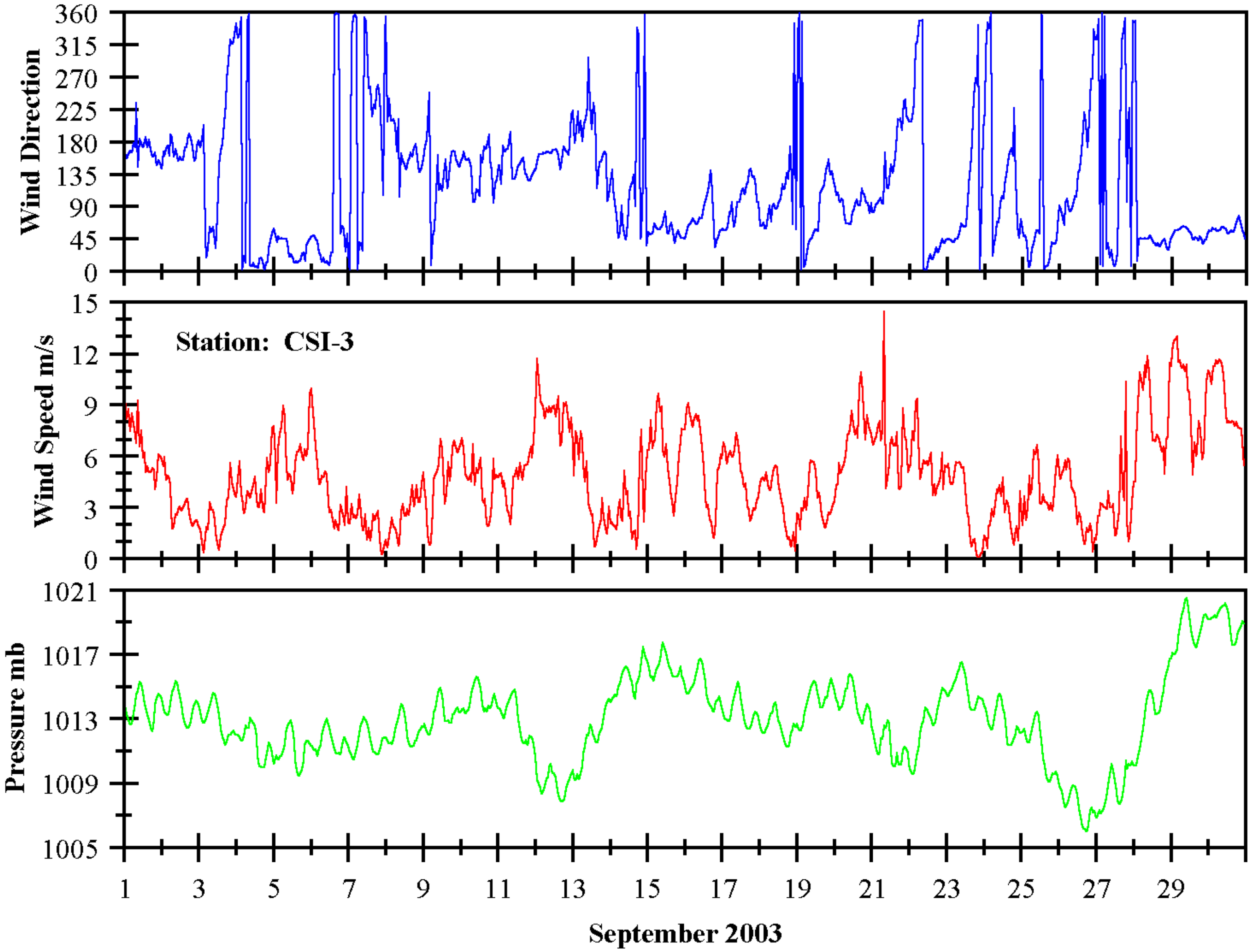

Figure 47. September 2003 hourly meteorological records for station CSI-3.

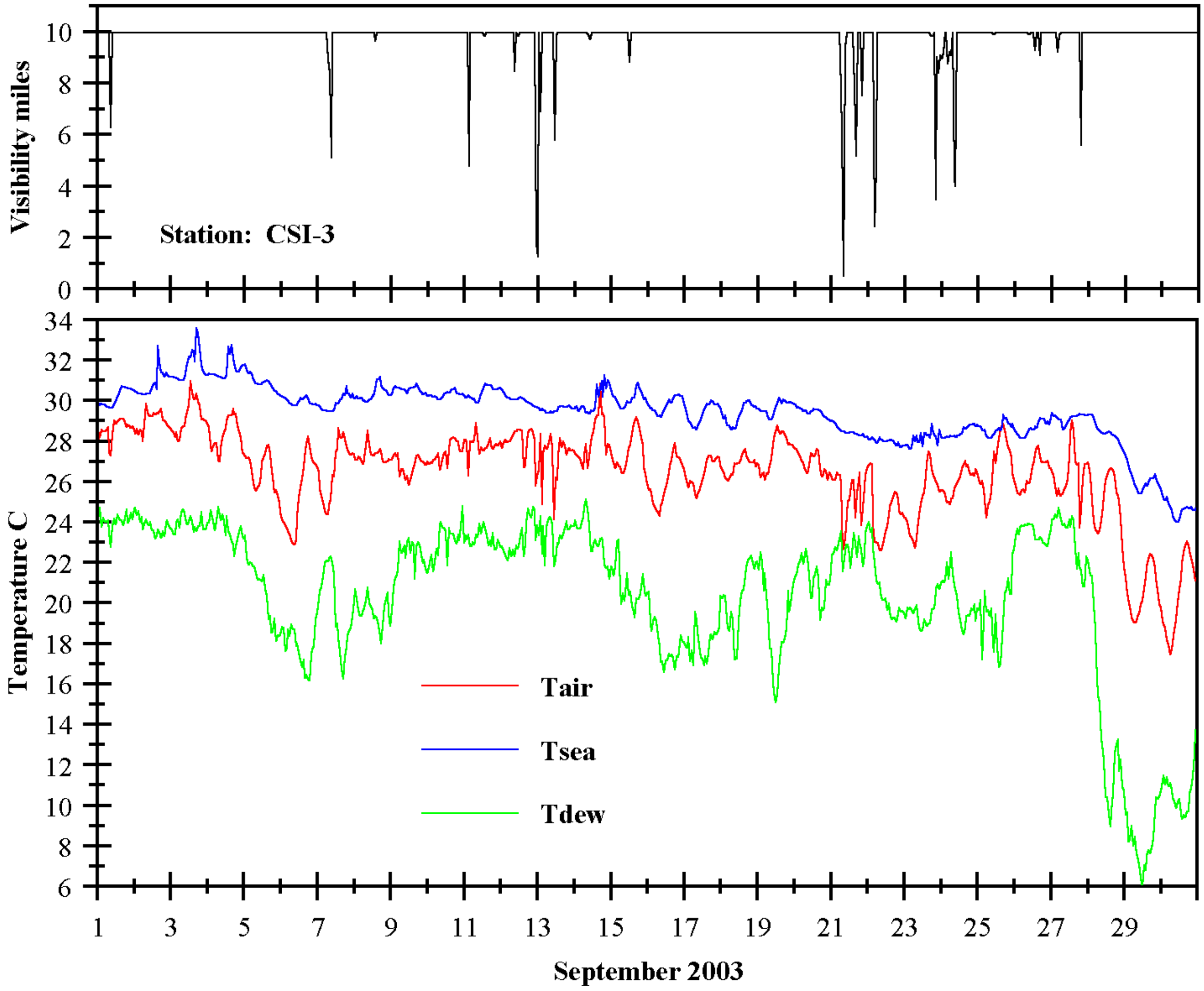

Figure 48. September 2003 hourly visibility and temperature records for station CSI-3.

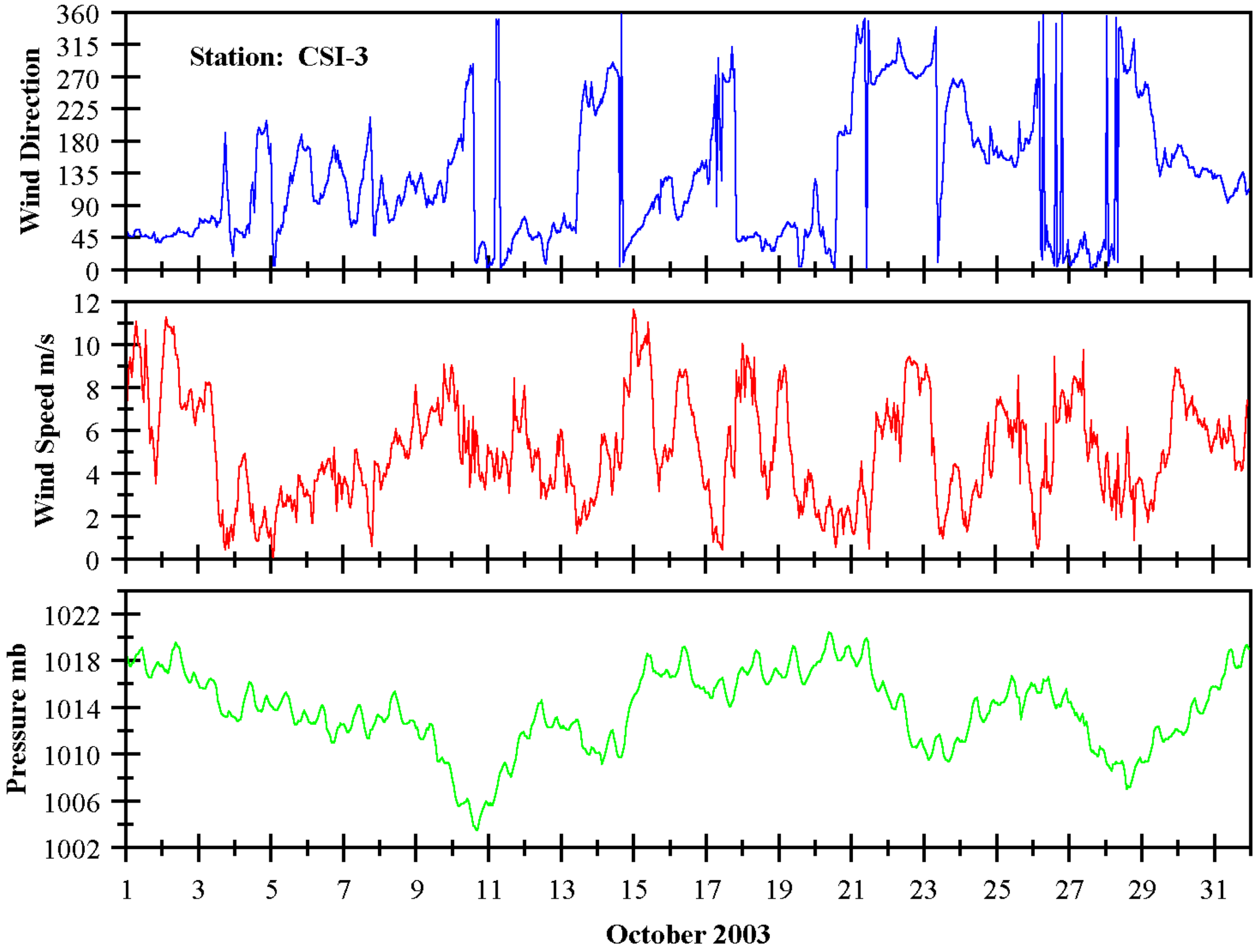

Figure 49. October 2003 hourly meteorological records for station CSI-3.

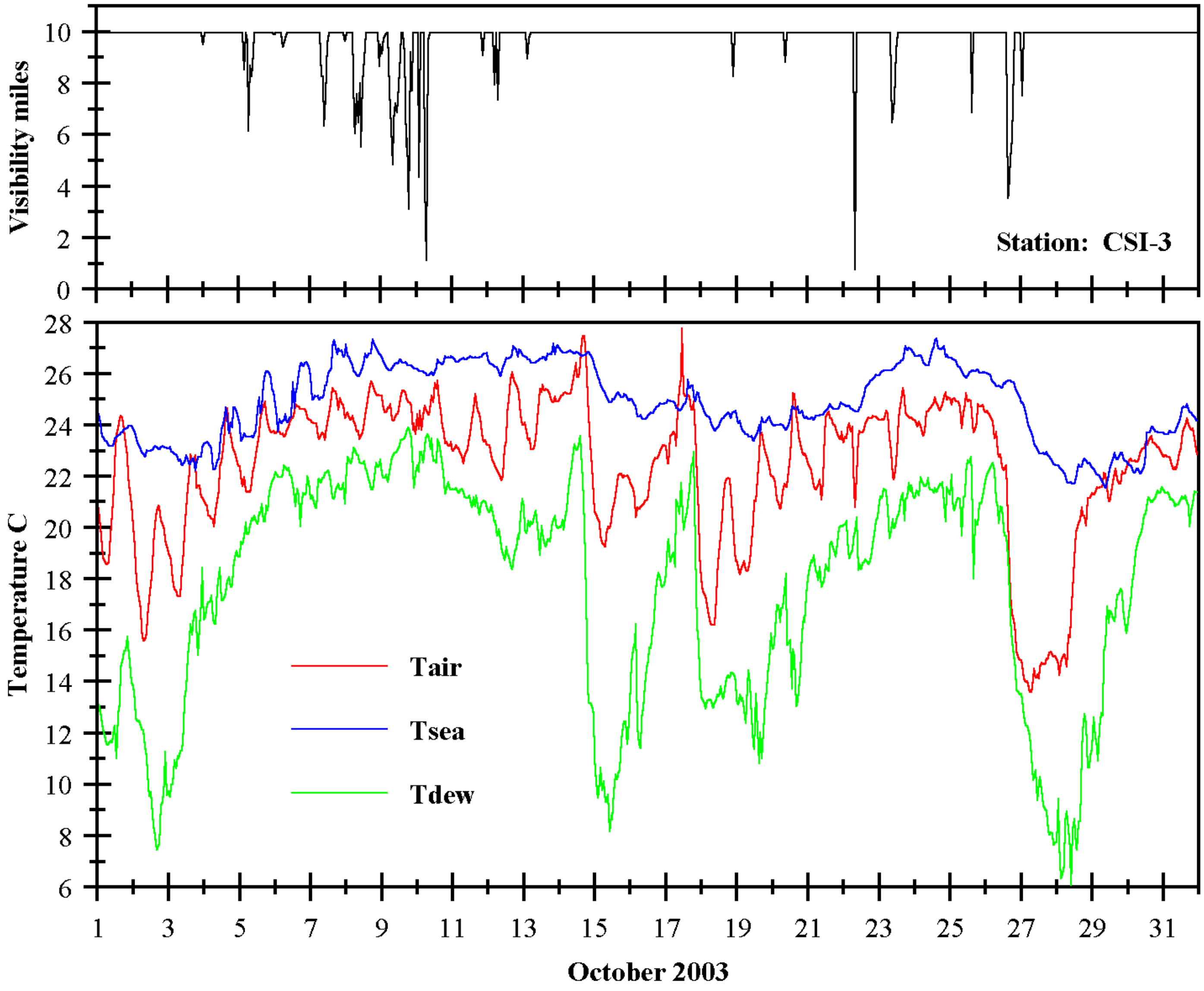

Figure 50. October 2003 hourly visibility and temperature records for station CSI-3.

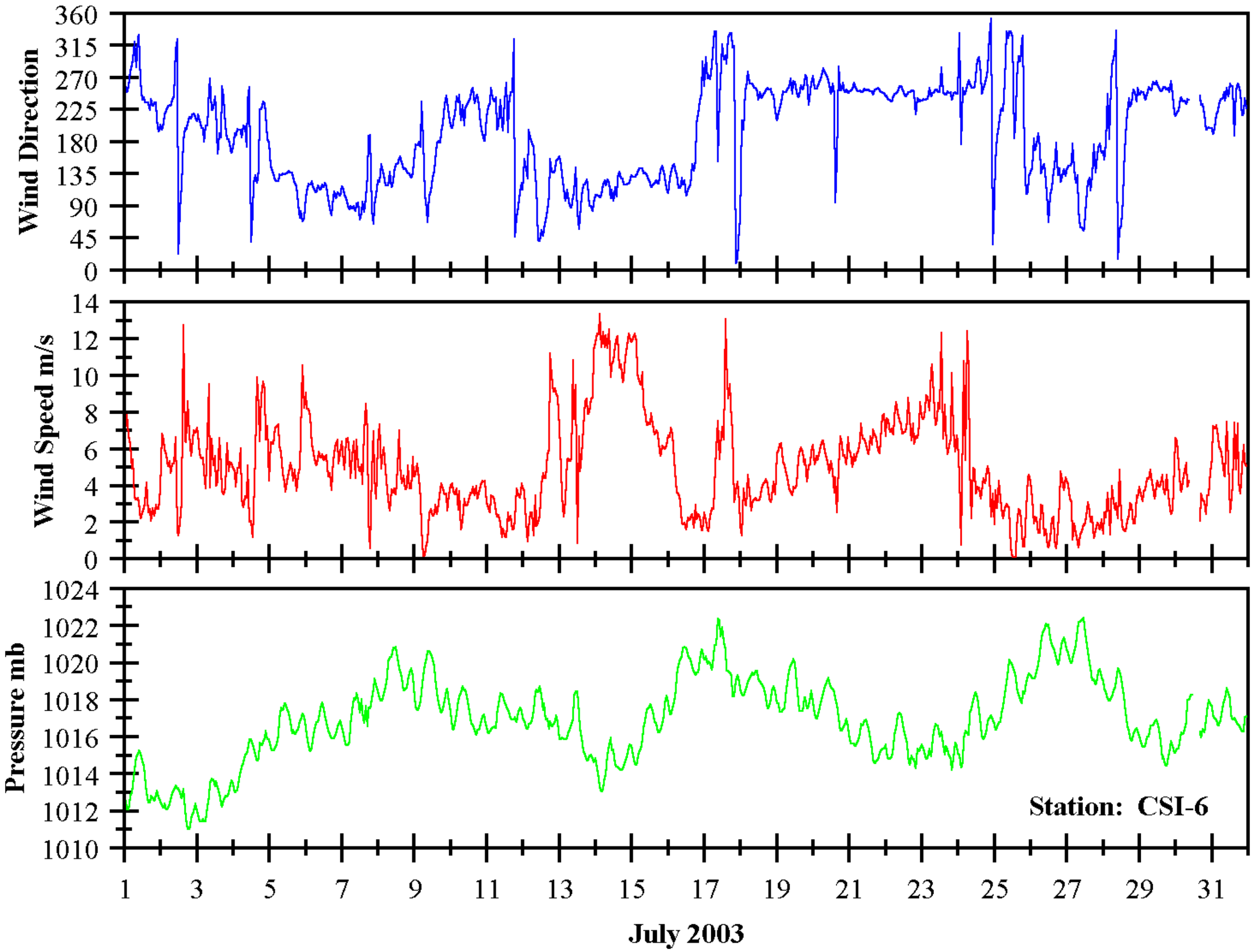

Figure 51. July 2003 hourly meteorological records for station CSI-6.

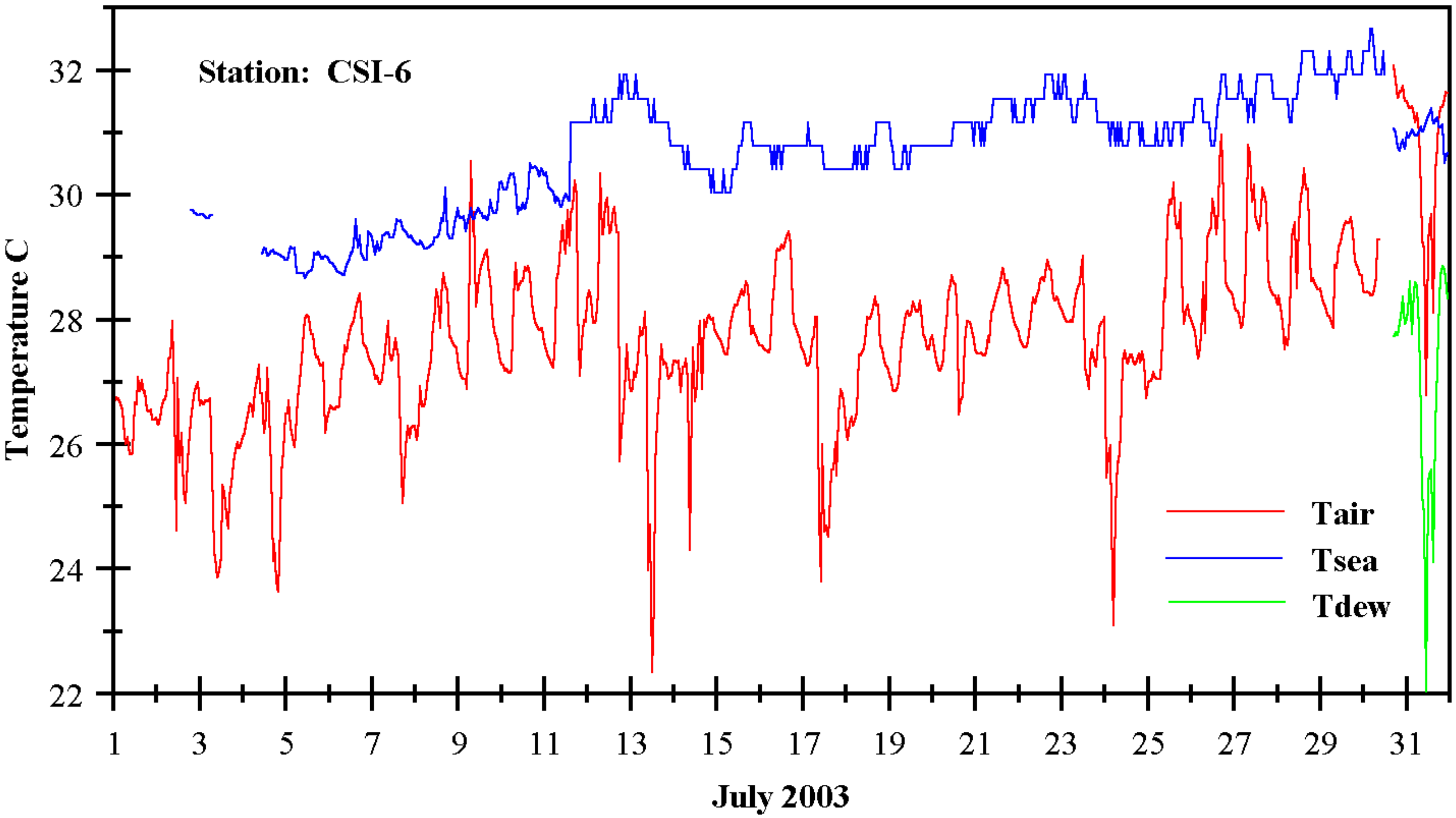

Figure 52. July 2003 hourly temperature records for station CSI-6.

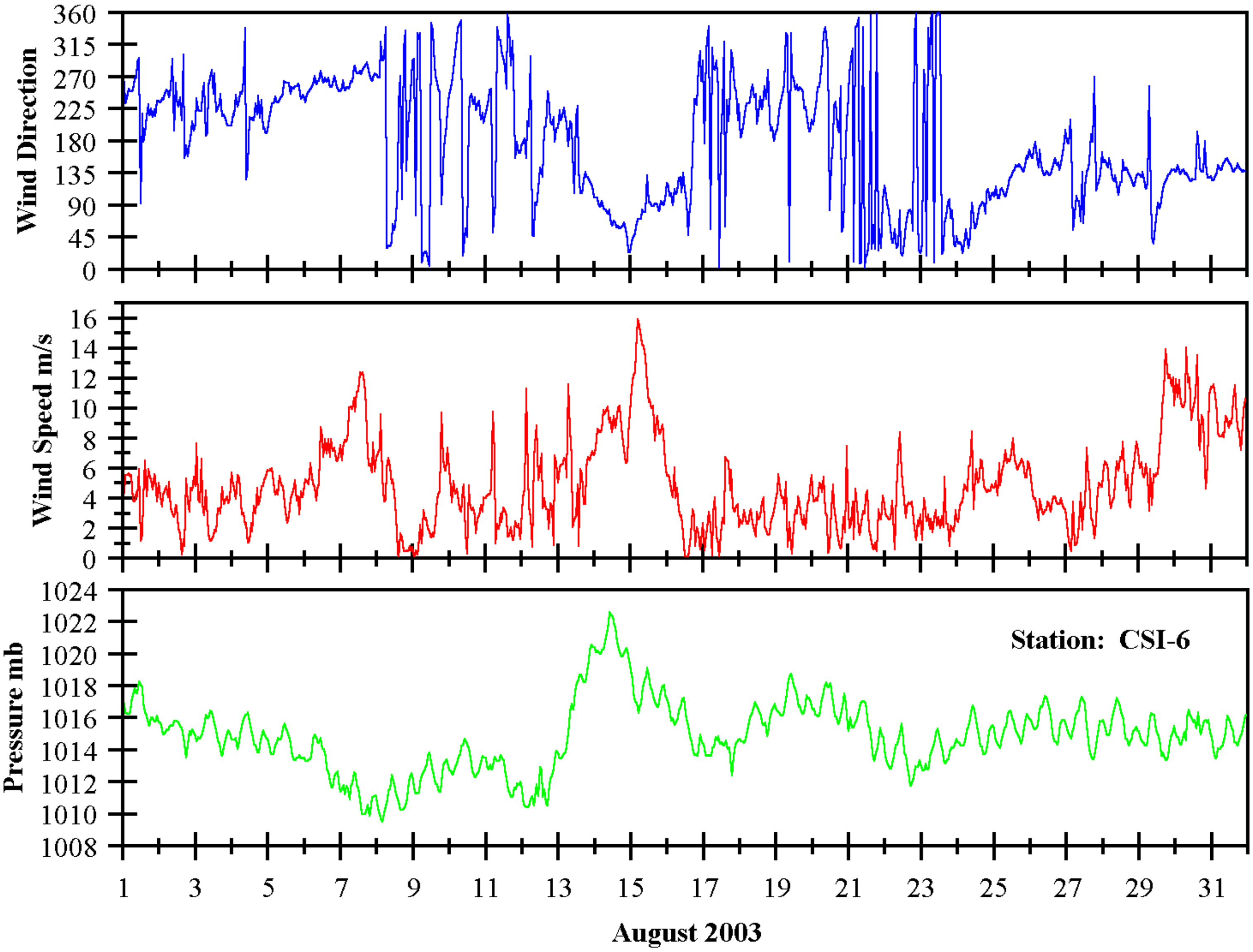

Figure 53. August 2003 hourly meteorological records for station CSI-6.

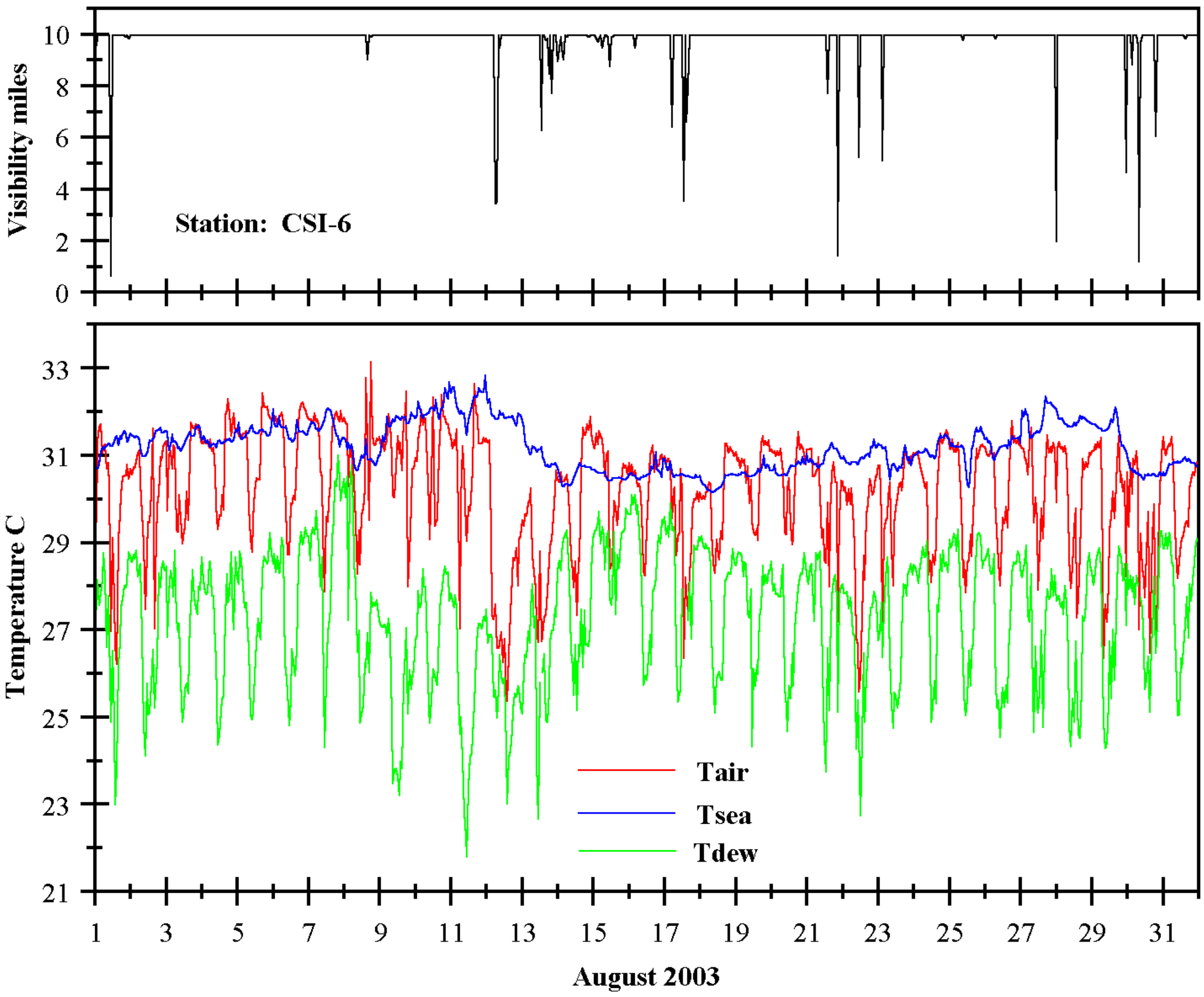

Figure 54. August 2003 hourly visibility and temperature records for station CSI-6.

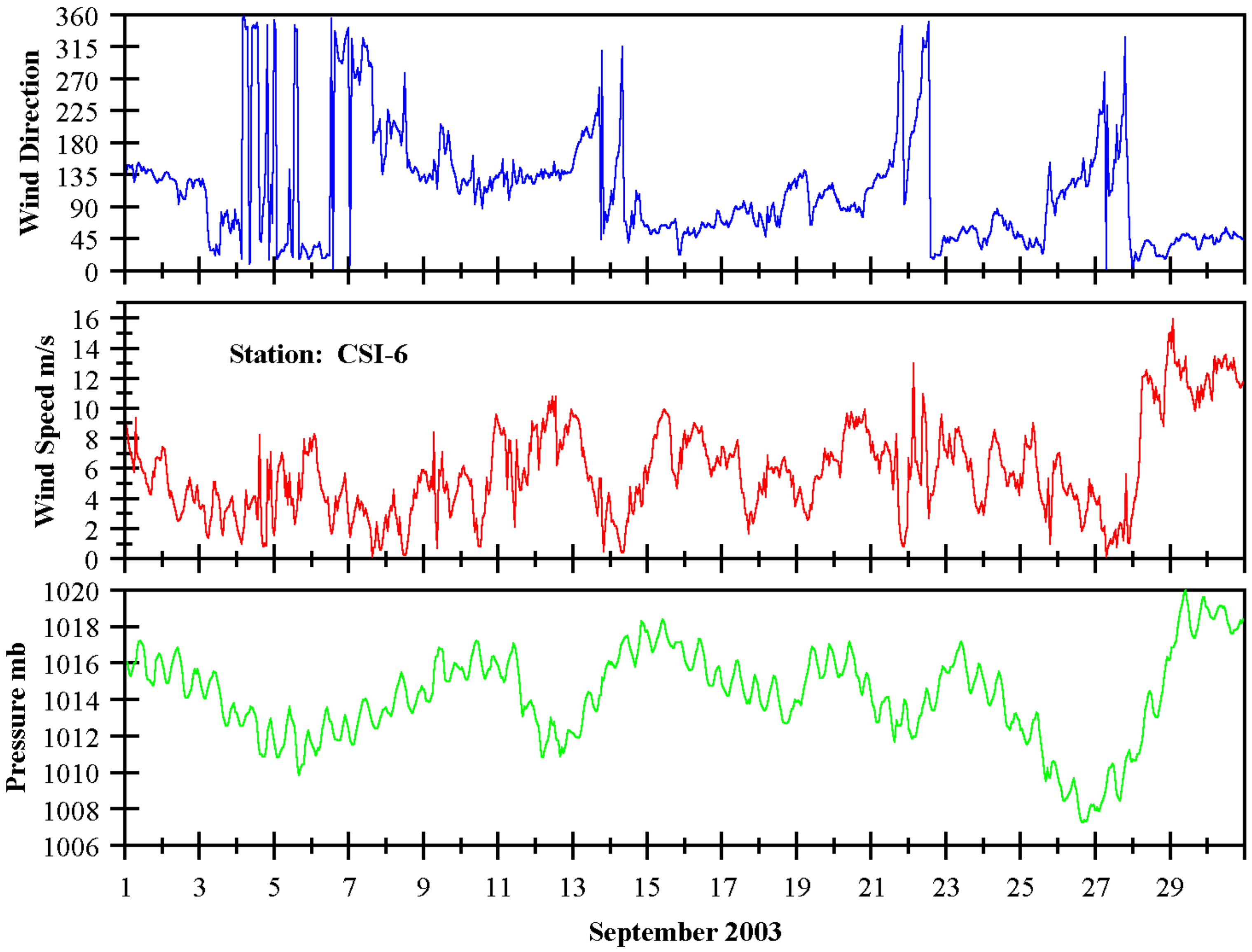

Figure 55. September 2003 hourly meteorological records for station CSI-6.

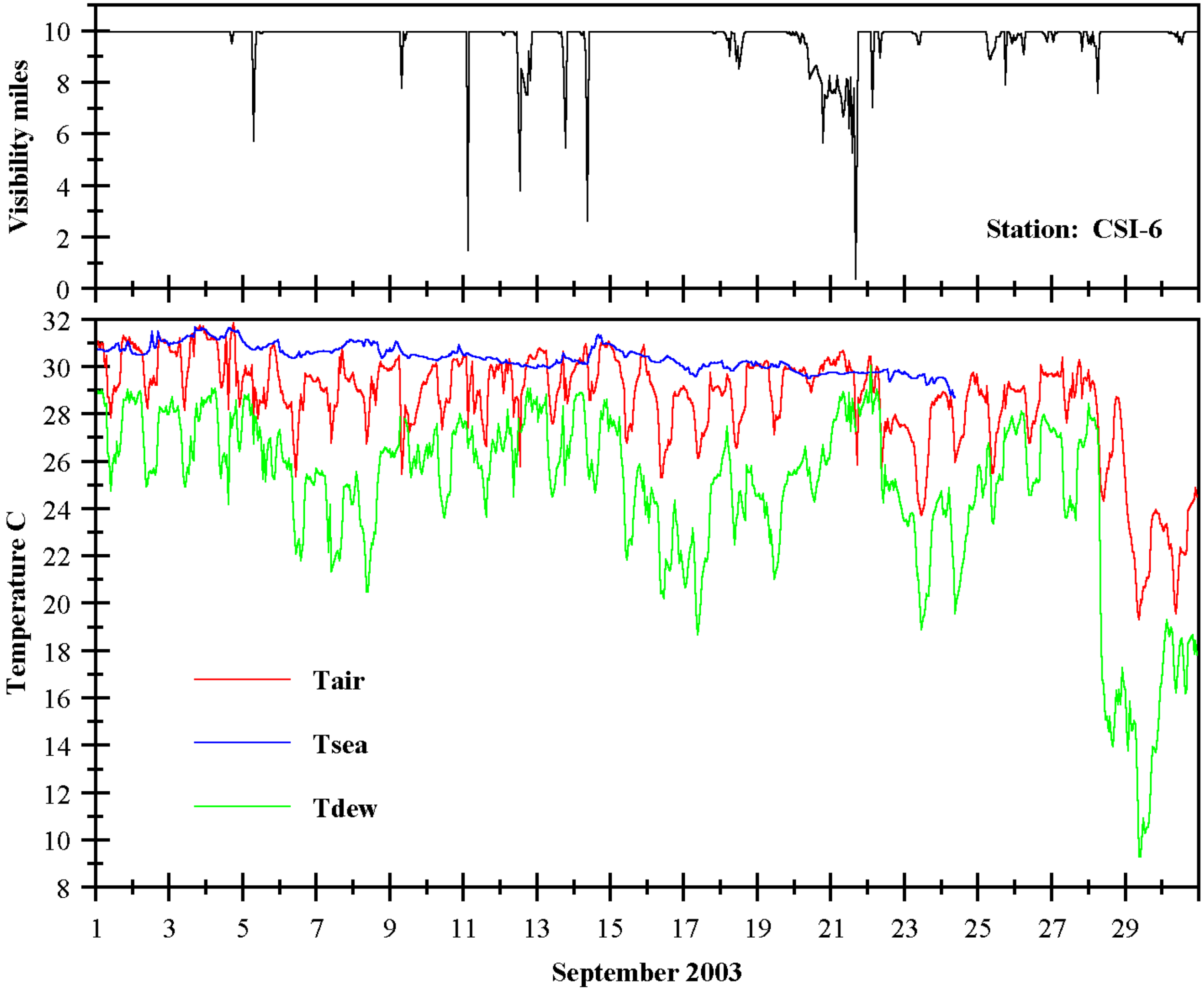

Figure 56. September 2003 hourly visibility and temperature records for station CSI-6.

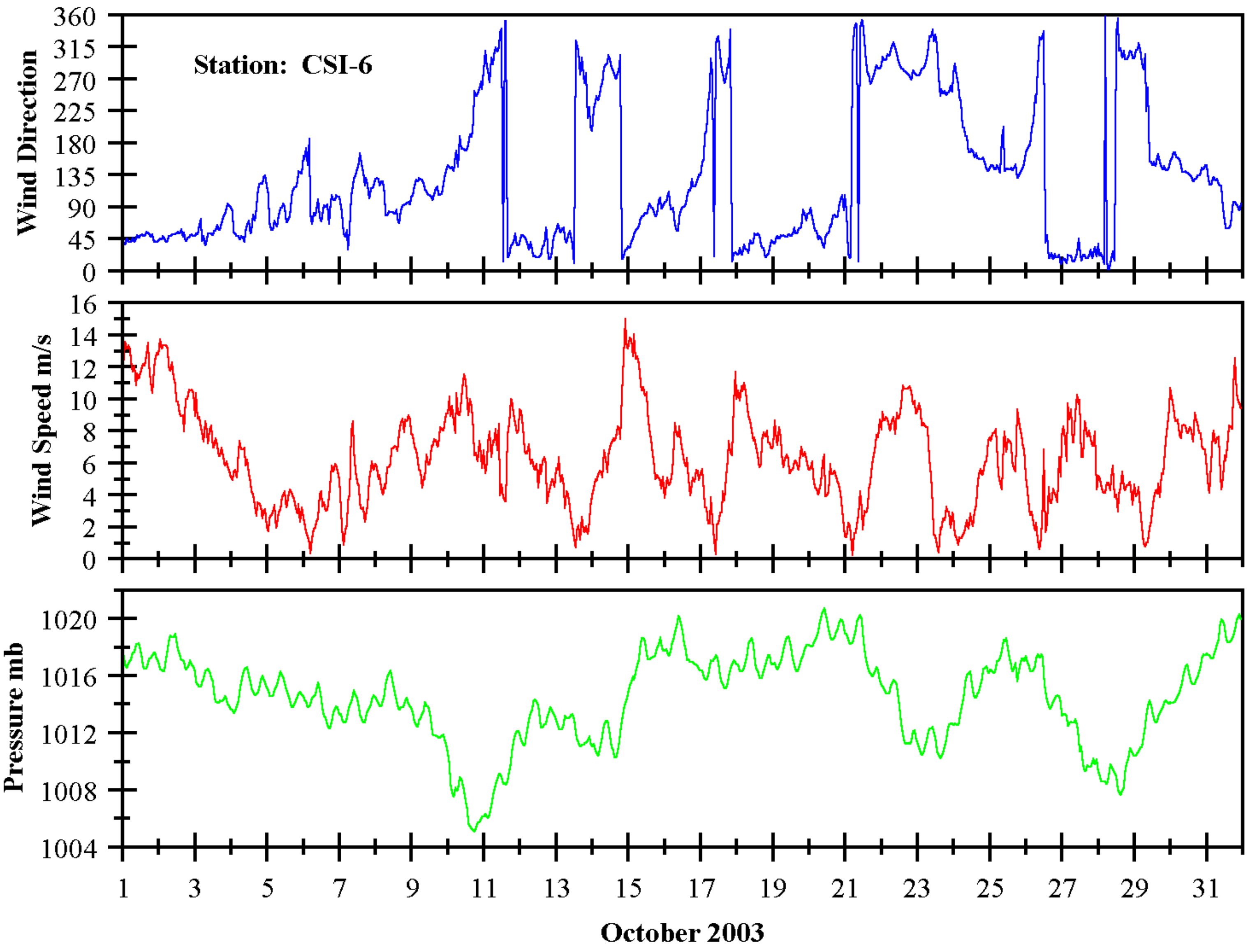

Figure 57. October 2003 hourly meteorological records for station CSI-6.

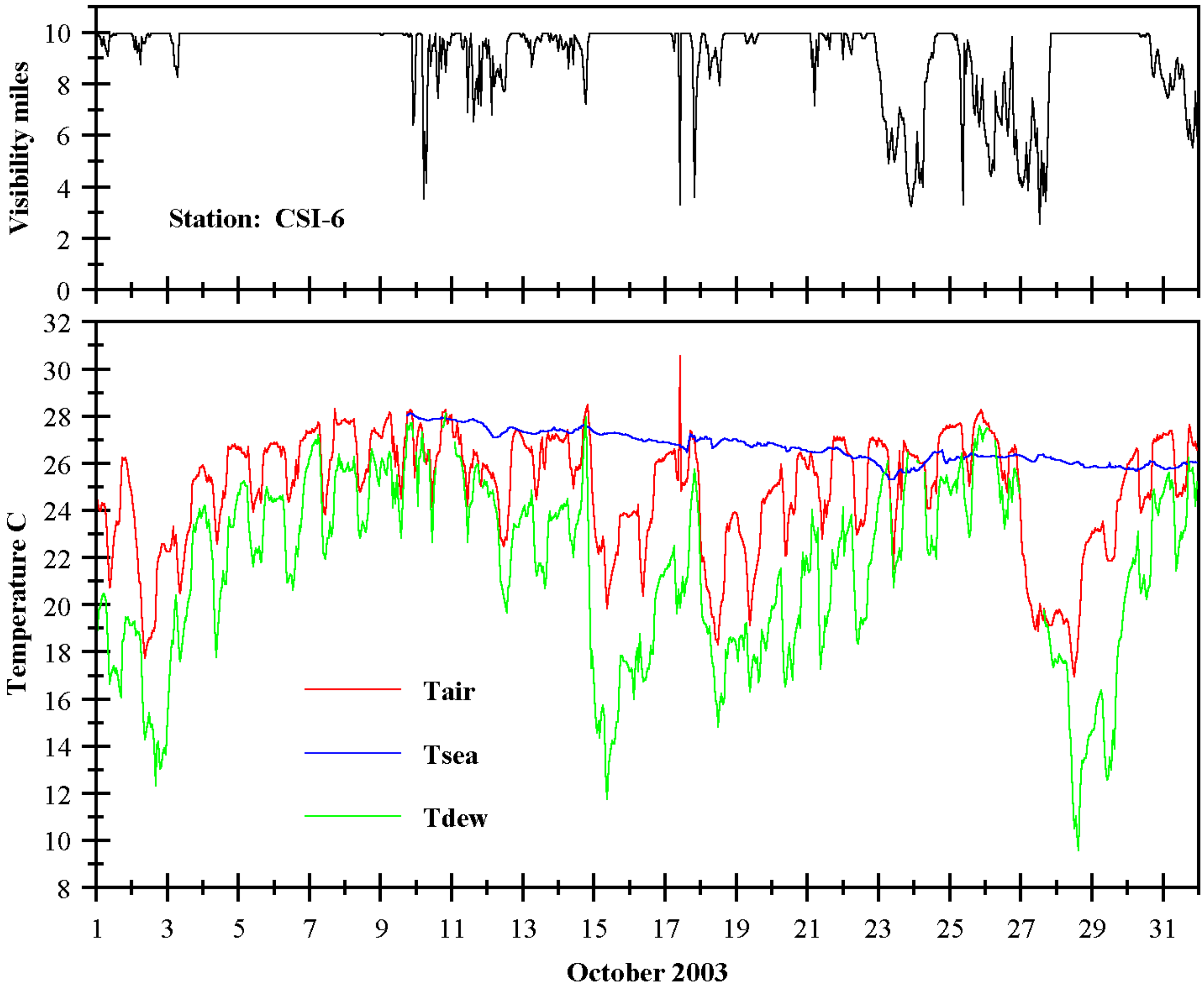

Figure 58. October 2003 hourly visibility and temperature records for station CSI-6.

III. Scientific Methodology

Visibility is defined as the greatest distance from an observer that a permanent object of known characteristics can be seen and identified by unaided, normal eye. Obviously, the best way to describe the surface visibility over the Gulf of Mexico is to measure it directly. Although we have established two offshore measurement stations as proposed, we need to use a surrogate approach to expand the study area over regions of the Gulf under U.S. jurisdiction. For this purpose, we employ the ventilation factor. This index rates the atmospheric dispersion capability, and is defined as the product of the wind speed and mixing height.

Because the mixing height is a function of atmospheric stability, we must first characterize the stability classification over the Gulf.

A. Overwater Stability Determination

In order to determine the impact of offshore and onshore emissions from joint sources on the air quality of coastal regions, Hanna et al. (1984) proposed and evaluated their Offshore and Coastal Dispersion (OCD) Model. In that model, overwater stability classes are required. Hanna et al. recommended the following relationship between the Monin-Obukhov (MO) length L_v (defined using the virtual temperature) and stability classes:

	Stability Class
$-10\text{ m} \le L_v < -5\text{ m}$	B
$-25\text{ m} \le L_v < -10\text{ m}$	C
$\lvert L_v \rvert > 25\text{ m}$	D
$10\text{ m} < L_v \le 25\text{ m}$	E
$5\text{ m} < L_v \le 10\text{ m}$	F

Determination of MO length to compute the stability class requires both wind shear and heat flux. Since these parameters are not normally observed, the stability length is first formulated to use routinely measured wind speed and air-sea temperature difference (Hsu, 1992). In order to take the humidity effect into account, the Bowen ratio is included in the formulation as follows.

In the atmospheric boundary layer the buoyancy length scale, L, or MO length, is a fundamental parameter that characterizes the "stability" of the surface layer (Panofsky and Dutton, 1984). L describes the relative importance between the buoyancy effect (or thermal turbulence) and the wind shear (or mechanical turbulence) (see Panofsky and Dutton, 1984) such that

$$L = -\frac{u_*^3 \rho C_p T}{\kappa g H \left(1 + \frac{0.07}{B}\right)} \qquad (6)$$

where u_* is the friction velocity, ρ is the air density, C_p is the specific heat capacity at constant air pressure, T is the absolute air temperature at the reference height, κ is the von Karman constant, g is the gravitational acceleration, H is the vertical heat flux, and B is the Bowen ratio of sensible to latent heat flux. The parameters u_*, B, and also the cloudiness are not normally measured in the marine environment. According to Arya (1999), the primary advantages of Pasquill's stability classification scheme as used in the OCD model are its simplicity and its requirement of only routinely available information from surface meteorological stations, such as mean surface wind speed, solar radiation, and cloudiness. Therefore, our purpose is to provide a practical way to estimate L using routinely recorded overwater measurements.

At the air-sea interface, according to Hsu (1988), we have

$$\tau = \rho\, u_*^2 = \rho\, C_d\, U_{10}^2 \qquad \textbf{(7)}$$

and

$$H = \rho\, C_p\, C_T \left(T_{sea} - T_{air}\right) U_{10} \qquad \textbf{(8)}$$

where τ is the shearing stress, C_d is the drag coefficient, C_T is the sensible heat flux coefficient, T_{sea} and T_{air} (in °C) are sea and air temperatures, respectively; and U_{10} (in m s^{-1}) is the wind speed at 10 m above the surface.

Substituting Eqs. (7) and (8) into (6), we obtain

$$\frac{z}{L} = -\frac{\kappa\, g\, z\, C_T \left(T_{sea} - T_{air}\right)\left(1 + \frac{0.07}{B}\right)}{\left(T_{air} + 273.16\right) U_z^2\, C_d^{3/2}} \qquad \textbf{(9)}$$

where z is a reference height normally set to 10 m.

According to Hsu (1999)

$$B = 0.146\left(T_{sea} - T_{air}\right)^{0.49} \qquad \textbf{(10)}$$

Data from the geographical regions of the Equatorial Atlantic and East China Sea were used to derive Eq. (10). Because the resulting correlation coefficient was 0.94, it is employed for this study as a first approximation. In a following section, we will show that slightly different relationships are found in the Gulf region.

Now, if we group the measured parameters from routine ship or buoy observations, i.e., T_{sea}, T_{air}, and U_z, we get

$$\frac{z}{L} = \kappa\, C_T\, C_d^{-3/2}\, R_b = A\, R_b \qquad \textbf{(11)}$$

where A needs to be determined from pertinent field measurements, and R_b is the bulk Richardson number.

According to Smith (1980), $C_T = 1.10 * 10^{-3}$ under unstable (or $T_{sea} > T_{air}$) conditions and $0.83 * 10^{-3}$ under stable (or $T_{air} > T_{sea}$) conditions; hence A is expected to be different for unstable vs. stable conditions. Also, under unstable conditions

$$R_b = -\frac{g\, z\left(T_{sea} - T_{air}\right)\left(1 + \frac{0.07}{B}\right)}{\left(T_{air} + 273.16\right) U_z^2} \qquad \textbf{(12)}$$

and under stable

$$R_b = \frac{g\, z\left(T_{sea} - T_{air}\right)}{\left(T_{air} + 273.16\right) U_z^2} \qquad \textbf{(13)}$$

Note that when $T_{sea} < T_{air}$, evaporation is suppressed and assumed here to be less active so that the water vapor correction term (1 + 0.07/B) is dropped.

To identify the coefficients for Eq. (11), pertinent data sets provided by Hwang and Shemdin (1988) and Donelan et al. (1997) with T_{air}, T_{sea}, U_{10}, and z/L measurements were incorporated in the analysis. Our results are shown in Fig. 59. If one accepts these high R^2 values, Fig. 59 should be useful operationally. Now, substituting the proper value of "A" for unstable and stable conditions respectively, we have

$$\frac{z}{L} = 10.2\, R_b \qquad \textbf{(14)}$$

with $R^2 = 0.87$ for unstable condition, and

$$\frac{z}{L} = 6.3\, R_b \qquad \textbf{(15)}$$

with $R^2 = 0.97$ for stable condition. Furthermore, by substituting Eq. (12) into (14) and rearranging, one gets

$$L = -\frac{\left(T_{air} + 273.2\right) U_z^2}{100\left(T_{sea} - T_{air}\right)\left(1 + \frac{0.07}{B}\right)} \qquad \textbf{(16)}$$

for unstable conditions. Similarly, substituting Eq. (13) into (15), we have

$$L = \frac{\left(T_{air} + 273.2\right) U_z^2}{62\left(T_{air} - T_{sea}\right)} \qquad \textbf{(17)}$$

for stable conditions.

Eqs. (16) and (17) are our proposed method to determine overwater L using routine measurements of wind and air and sea temperatures.

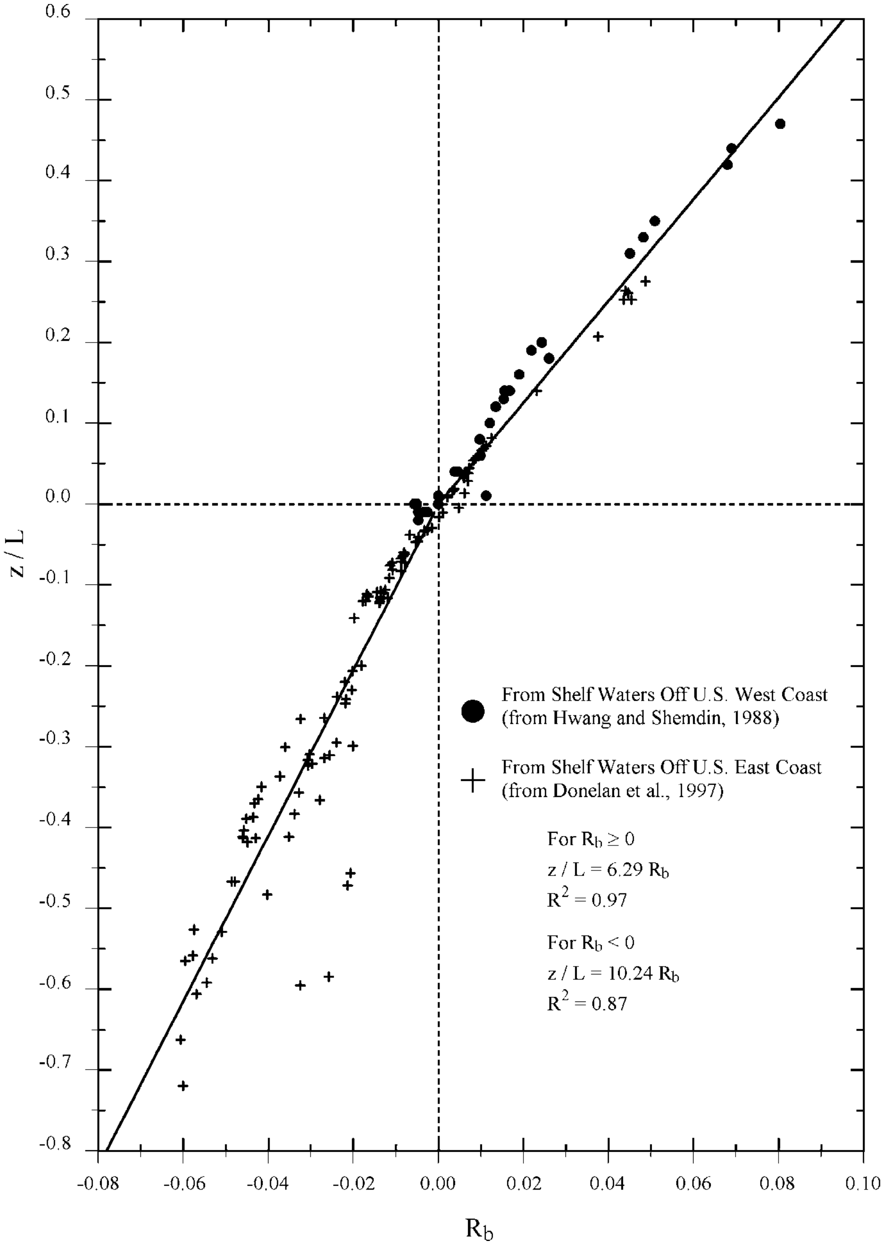

Figure 59. An overwater relationship between z/L and R_b (see text for details).

B. Bowen Ratio Variations Over the Gulf of Mexico

The ratio of the sensible heat flux to the latent heat flux is commonly referred to as the Bowen ratio (see, e.g., Roll, 1965) and takes the form

$$B = \frac{H_s}{H_l} = \frac{C_p\, C_T \left(T_{sea} - T_{air}\right)}{L_T\, C_E \left(q_{sea} - q_{air}\right)} \qquad \textbf{(18)}$$

where the specific humidity, q_{sea}, is related to the saturation vapor pressure, e_{sea}, through (Hsu, 1988)

$$q_{sea} = 0.62\left(\frac{e_{sea}}{P}\right) \qquad \textbf{(19)}$$

and

$$e_{sea} = 6.1078 * 10^{\left[\,7.5 T_{sea} / \left(237.3 + T_{sea}\right)\right]} \qquad \textbf{(20)}$$

For the specific humidity and saturation vapor pressure of the air, the dew point temperature (T_{dew}) replaces T_{sea} in Eqs. (19) and (20).

The Bowen ratio has been found to vary widely in the marine environment. Using surface data recorded during a strong cold air outbreak over the Gulf of Mexico in 1996, Hsu (1998) demonstrated that a compelling linear correlation between the vapor pressure difference and sea-air temperature difference does exist. With this result, and from Eq. (18), it was also shown that B can be related to the sea-air temperature difference alone as

$$B = a\left(T_{sea} - T_{air}\right)^{b} \qquad \textbf{(21)}$$

Hourly data from several NDBC stations were used to derive values of a and b over the Gulf of Mexico, which varied from 0.077 to 0.078 and 0.67 to 0.71, respectively. Hsu (1999) went on to further verify Eq. (21) using data from a tropical ocean location and a cold air outbreak region, ultimately deriving Eq. (10). This equation has since been advocated for use by Hsu and Blanchard (2003) in marine atmospheric boundary layer applications.

While very high correlations were established, relatively small data sets were used in formulating Eq. (10). Furthermore, Hsu (1998) showed several variations for Eq. (21) with a distinct difference between coastal and deep Gulf stations. The purpose of this analysis task is to investigate the spatial and temporal variations of Eq. (21) over the Gulf using long term records from available buoy, Coastal Marine Automated Network (C-MAN) stations, and our WAVCIS platform.

Records from two C-MAN stations (GDIL1 and DPIA1), WAVCIS platform CSI-3, and 11 moored buoys (42001, 42002, 42003, 42041, 42019,42020, 42036, 42039, 42040, 42007, and 42035), ranging from the deep Gulf to near shore, were used (see Figs. 1 and 65 and Table 4 for locations). The period of record was 1999 through 2002, and was selected primarily for two reasons. First, hourly dew point temperatures generally became routine at most stations during 1999 with the following exceptions: 42003, year 2000; 42019, year 2000; 42020, year 2000; 42041, year 2002; and DPIA1, 2002. The complete year of 2002 from WAVCIS CSI-3 was used.

Second, by using a multi-year record, any bias introduced into the data due to ENSO effects should be minimized. ENSO (El Nino / Southern Oscillation) is the term for the coupled ocean-atmosphere interactions in the tropical Pacific characterized by episodes of anomously high sea surface temperatures in the equatorial and tropical eastern Pacific; associated with large-scale swings in surface air pressure between the western and eastern Pacific. ENSO is the most prominent source of interannual variability in weather and climate around the world (Geer, 1996). El Nino and La Nina are the extremes of the ENSO cycle, and can produce large shifts in the usual weather patterns. For the southeastern U.S. and the Gulf of Mexico region, this can mean cooler, wetter winters (El Nino), or warmer, drier winters (La Nina). According to the NOAA Climate Diagnostics Center (2004) and the Climatic Prediction Center, 1999 experienced weak to moderate La Nina conditions which continued through most of 2000 (the third quarter being Neutral) until the second quarter of 2001, after which more Neutral conditions prevailed. Weak El Nino began in the second quarter of 2002 and strengthened slightly through the years end.

The only data editing performed was to remove every hourly record which was missing any of the pertinent parameters: wind speed, pressure, or sea- air- or dew-point temperatures. Finally, since we were only considering unstable conditions, a subset was created containing only records in which $T_{sea} > T_{air}$. For each hour, the Bowen ratio was computed using Eqs. (18) through (20) with $C_T = 1.13 * 10^{-3}$ (Large and Pond, 1982); $C_p = 1004$ J kg^{-1}; $C_E = 1.12 * 10^{-3}$ (Smith, 1988); and $L_T = 2.5 * 10^6$ J kg^{-1} (Hsu, 1988). Note that the wind speed parameter cancels out in Eq. (18); hence sensor height corrections for the various platforms was not necessary.

The resulting unstable data sets were analyzed in two ways. A relationship between the Bowen ratio and sea-air temperature difference was derived for each station for the entire period of record. Since this usually included over 20,000 data points, the data was reduced into about 20 classes with a range of 0.5 to 0.8°C. For each Class, a mean and standard deviation of the Bowen ratio was computed, and then the power curve (Eq. 21) fit to the data. The unstable data sets were also further separated into monthly sets, and Eq. (21) fit to the smaller record.

Monthly analysis at each station yielded a family of curves similar to those shown in Figs. 60 and 61. This was not an unanticipated result, particularly for the coastal and near shore stations. Fall and winter frontal passages over this region bring colder and much drier continental air over the shelf waters. The large sea-air temperature differences, as well as those between q_{sea} and q_{air} (due to low dew point temperatures), produce a wide range of sensible and latent heat fluxes. This effect diminishes later in the season as the shelf waters cool. In summer, much smaller gradients are observed as conditions become more homogeneous. Nevertheless, the seasonal variations of the mean Bowen ratio are significant, as much as 2 to 3 times in magnitude at the near shore stations. This distribution extends even over the deep Gulf stations, although the variations are considerably smaller.

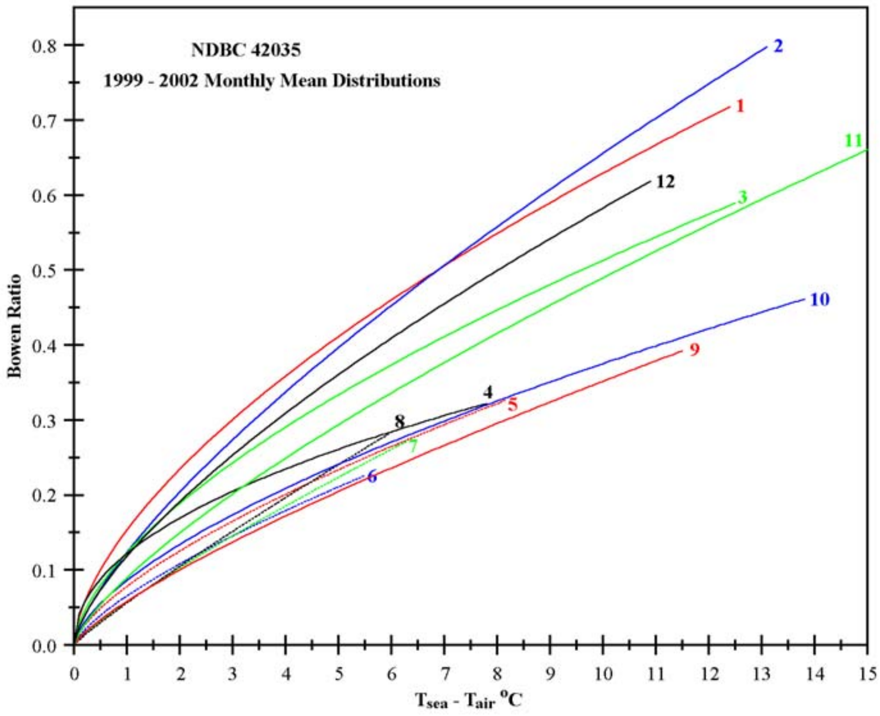

Figure 60. Seasonal distribution of Bowen ratio vs. temperature difference for buoy 42035 in the coastal waters.

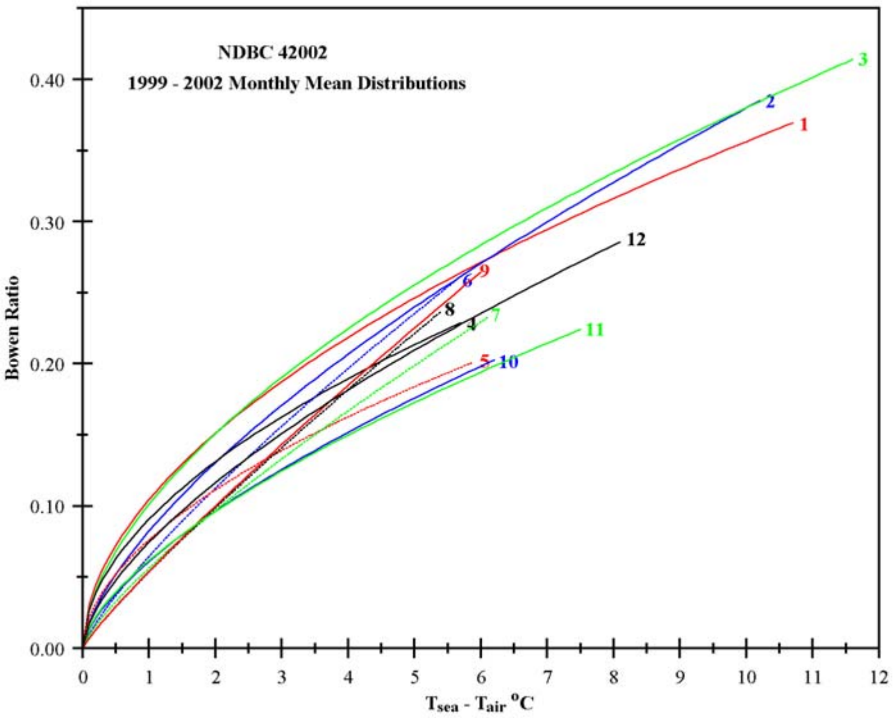

Figure 61. Seasonal distribution of Bowen ratio vs. temperature difference for buoy 42002 in the deep Gulf waters.

Extremely high correlation coefficients were obtained for the relationships derived from most of the classified data sets. Somewhat poorer values were produced at DPIA1 and the WAVCIS station, however only one year of data was available at these locations. Figs. 62 and 63 show examples of the near coast and deep Gulf, respectively. Clearly, much higher Bowen ratios and greater temperature differences generally occur near shore than over the deep Gulf, and these characteristics are thus described by different relationships.

The various stations were then grouped into four categories - deep Gulf (buoys 42001, 42002, 42003, and 42041); shelf break region (buoys 42019, 42020, 42036, 42039, and 42040); shelf waters (buoys 42007 and 42035, WAVCIS CSI-3); and coastal (C-MAN GDIL1 and DPIA1). Very similar relationships were found amongst the stations in each group. Little difference was noted between the coastal stations and those in the adjacent shelf waters, hence these regions were combined.

Our final result is shown in Fig. 64. A mean relationship was derived from the stations within each region of coastal waters, shelf break, and deep Gulf. The relationship provided by Hsu (1999) and Hsu and Blanchard (2003) is also depicted. Each region is found to exhibit a unique relationship, with much higher ratios observed in the coastal region decreasing as one moves offshore. The relationship proposed by Hsu and Blanchard (2003) appears best suited to the coastal region, completely overestimating conditions over the deep Gulf and shelf waters over most of the sea-air temperature difference range. However, since it has been verified in such diverse geographic locations, it remains the recommended formula for operational use.

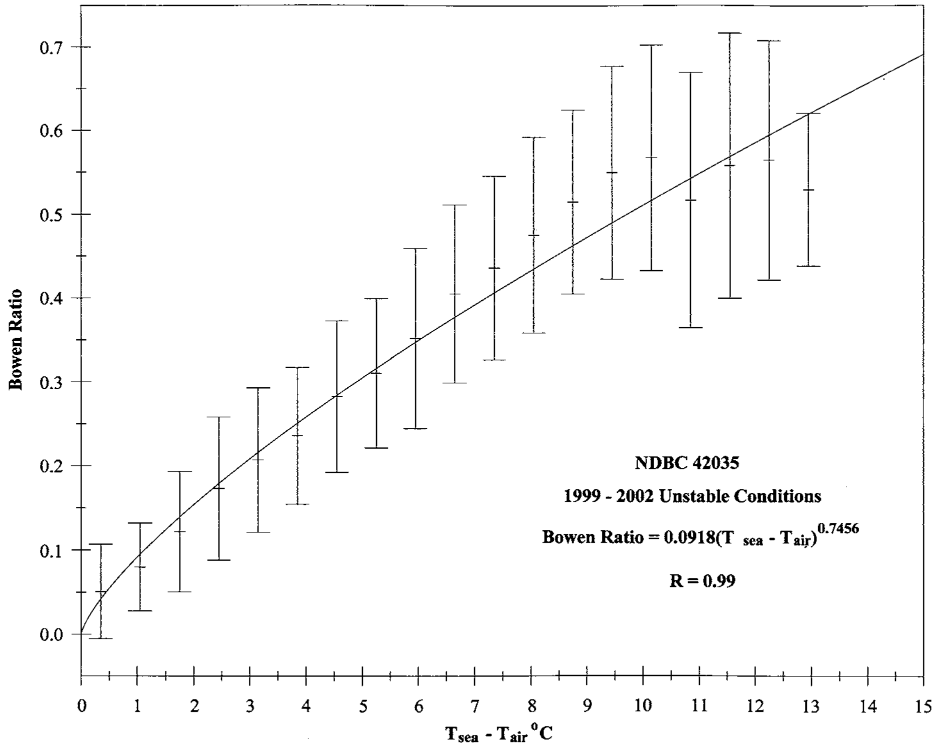

Figure 62. Mean and standard deviation of Bowen ratio vs. temperature difference for classified data from buoy 42035 in the Gulf coastal waters.

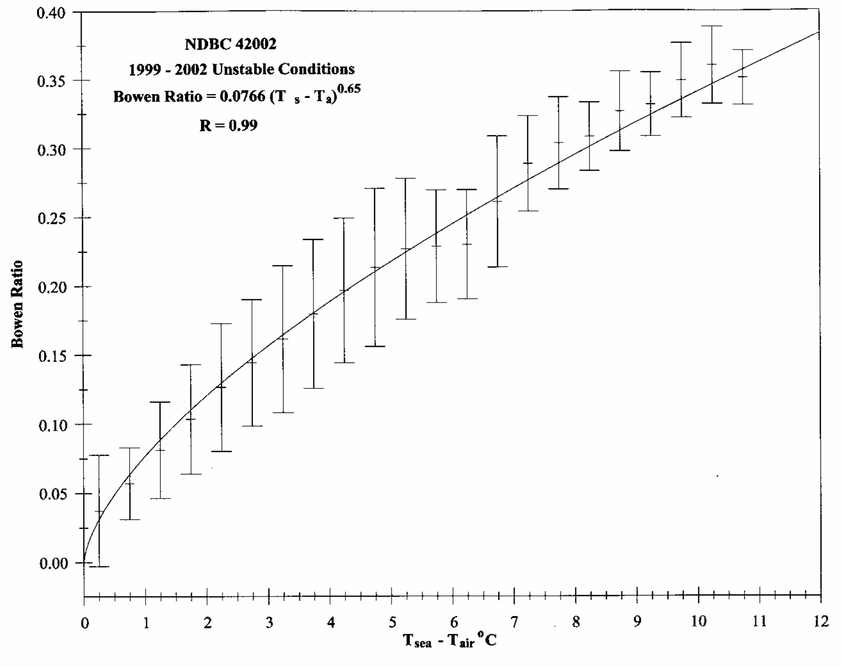

Figure 63. Mean and standard deviation of Bowen ratio vs. temperature difference for classified data from buoy 42002 in the deep Gulf waters.

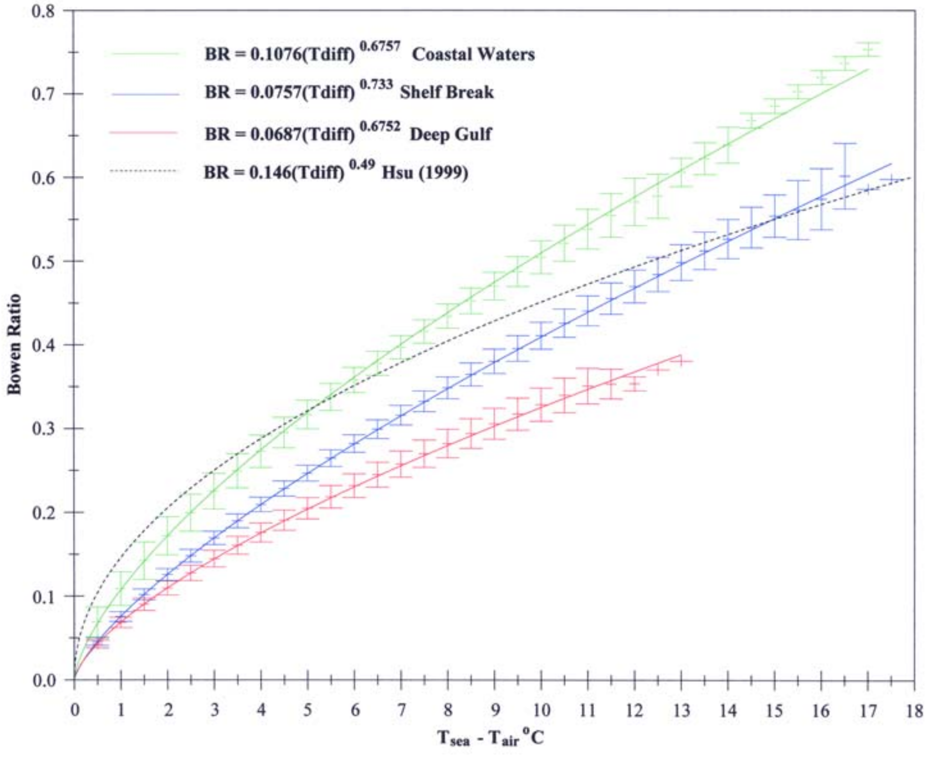

Figure 64. Derived relationships between the Bowen ratio and sea-air temperature difference from the coast to the deep Gulf waters. Dotted line is Eq. (10) as proposed by Hsu (1999) and Hsu and Blanchard (2003).

C. Overwater Mixing Heights and Ventilation Factor

Due to potential evaporation, the air over the water is usually moister than that over land, and the top of the marine boundary layer is often times capped by clouds (see, e.g., Garratt, 1992). On the basis of analysis of vertical soundings by research aircraft, rawinsondings, and radar wind profilers and Radio Acoustic Sounding Systems (RASS), it has been shown by Garratt (1992) that the mixing height h = LCL, the lifting condensation level, under cumulus cloud conditions (where LCL = cloud base). The height of the LCL may be estimated by (see Hsu, 1998)

$$H_{LCL} = 125\left(T_{air} - T_{dew}\right) \qquad \textbf{(22)}$$

where H_{LCL} is in meters and the dewpoint depression at the sea surface in degrees Celcius.

If T_{dew} is not available, it may be estimated by (Hsu, 1988, p. 21)

$$T_{dew} = \frac{237.3\log_{10}\left(\frac{e_{air}}{6.1078}\right)}{7.5 - \log_{10}\left(\frac{e_{air}}{6.1078}\right)} \qquad \textbf{(23)}$$

From Hsu (1998)

$$e_{air} = \frac{1}{0.62} P\, q_{air} \qquad \textbf{(24)}$$

and for operational applications (Hsu, 1998, Fig. 3)

$$\left(q_{sea} - q_{air}\right) = 5.68 + 0.37\left(T_{sea} - T_{air}\right) \qquad \textbf{(25)}$$

where q_{sea} and e_{sea} are given by Eqs. (19) and (20), respectively.

Since both T_{sea} and T_{air} can be obtained routinely by buoys, ships, and satellites, Eq. (22) can be used to estimate the mixing height if fair weather cumulus clouds are present.

On the eastern and Gulf coasts of the U.S., as well as over the East China Sea, cold air outbreaks are common in the winter season. Under these conditions, according to Hsu (1997), the mixing height, Z_i, is convectively unstable that

$$Z_i = 369 + 6004\left(\overline{w'\theta_v'}\right)_0 \qquad \textbf{(26)}$$

where Z_i is in meters and $\left(\overline{w'\theta_v'}\right)_0$ is the buoyancy flux in meters per second Kelvin.

For operational applications, the buoyancy flux at the sea surface is found to be

$$\left(\overline{w'\theta_v'}\right)_0 = C_T\, U_{10} \left(T_{sea} - T_{air}\right)\left(1 + \frac{0.07}{B}\right) \qquad \textbf{(27)}$$

where $C_T = 1.1 * 10^{-3}$ under unstable conditions (Smith, 1980) and B is the Bowen ratio provided in Eq. (10).

During certain periods, the sea-surface temperature is less than the air temperature. Therefore, the boundary layer is said to be stable. The mixing height under stable conditions, h_{stable}, is (see Garratt, 1992)

$$h_{stable} = c^* \sqrt{\frac{u_* L}{f}} \qquad \textbf{(28)}$$

where f if the Coriolis parameter. From limited measurements under stable conditions, the coefficient c^* is found to be 0.11 as shown by Hsu and Blanchard (2003). Certainly, more field experiments are needed to further substantiate Eq. (28) and the value of c^*.

Finally, the ventilation factor is given by the product of the computed mixed height and the wind speed measured by offshore buoys and platforms. The ventilation factor is related to pollution dispersion capacity as shown in Table 3.

Table 3.
Pollution dispersion forecast categories related to atmospheric ventilation (product of wind speed and mixing depth) (after Eagleman, 1996, based on the air pollution dispersal index used by the State of Colorado Department of Health in Denver).

Pollution dispersion	Ventilation (m^2 / sec)
Bad	0 - 2000
Fair	2001 - 4000
Good	4001 - 6000
Excellent	6001 or more

IV. APPLICATIONS

As discussed in the previous section, spatial and temporal variations of the mixed layer over the Gulf of Mexico region are a function of the prevailing atmospheric stability. In this analysis, monthly mean values were obtained for pertinent NDBC C-MAN and buoy stations in the Gulf (see Fig. 65 and Table 4 for approximate locations). Parameters included air and sea temperatures, dew point temperatures, and average wind speeds. Table 4 includes the stations and the period of record for each parameter used here. Note that the dew point records are generally of much shorter duration. For our CSI-3 platform, monthly averages were computed.

From sea-air temperature differences, mean L values were derived using Eqs. (16) and (17). Setting $z = 10$ m, z/L values were found to determine whether the stability was unstable ($z/L < -0.4$), neutral ($|z/L| < 0.4$), or stable ($z/L > 0.4$). Mixed height values were then computed using Eqs. (26), (22), and (28) for unstable, neutral, or stable, respectively. Finally, from the mean wind speed values, an estimated ventilation factor for each station was found. If a station reported insufficient or missing data so that a monthly mean was not available, then mixing height and ventilation factor were not computed. Note that no correction was made for anemometer height. The results are shown in Figs. 66 through 89.

The seasonal progression of air and sea temperatures is clear, with cool shelf waters gradually warming in the springtime to near homogeneous conditions by late summer. In the fall, the cycle repeats as returning cold fronts again chill the shallower shelf.

Slightly unstable ($z/L < 0$) conditions are found at almost every station throughout the year. Stability Class D (or neutral) prevails; in the summer months several of the C-MAN stations achieve Class C (free convective). Buoys in the northeastern Gulf also approach Class C in the winter months, with buoy 42040 surpassing the mark in December.

Mean mixed heights over the open Gulf typically range between 400 - 800 m, with higher values over the deeper waters. Areas of low ventilation factor index (hence, poor dispersion capability) are seen almost every month, mostly along the coastal areas. In the winter months, the low ventilation factor is mainly due to lower mean mixed heights, while in summer light average winds are the dominant factor.

Table 4.
Locations and pertinent periods of record for coastal and offshore stations used in this report.

Station	Type	Location Lat N Lon W	Air Temperature	Sea Temperature	Dew Temperature	Wind Speed
BVILE	ASOS	29.20 84.24				
BUSL1	C-MAN	27.88 90.90	1/91 - 4/93	1/91 - 12/93		1/91 - 12/93
CSI-3	WAVCIS	29.44 92.06	11/01 - 10/03	11/01 - 10/03	11/01 - 10/03	11/01 - 10/03
CSI-6	WAVCIS	28.87 90.48				
DPIA1	C-MAN	30.25 88.07	1/87 - 12/01	1/87 - 12/98	2/97 - 7/97	1/87 - 12/01
DRYF1	C-MAN	24.64 82.86	12/92 - 12/01	12/92 - 12/01		12/92 - 12/01
GBCL1	C-MAN	27.80 93.10	9/89 - 9/92	9/89 - 9/92		9/89 - 9/92
GDIL1	C-MAN	29.27 89.96	12/84 - 12/01	12/84 - 12/01	5/89 - 12/01	12/84 - 12/01
LONF1	C-MAN	24.84 80.86	11/92 - 12/01	11/92 - 12/01		11/92 - 12/01
MLRF1	C-MAN	25.01 80.38	12/87 - 12/01	12/87 - 12/01		12/87 - 12/01
MPCL1	C-MAN	29.40 88.60	2/88 - 7/92	2/88 - 7/92		2/88 - 7/92
PTAT2	C-MAN	27.83 97.05	3/84 - 12/01	10/89 - 12/01	4/97 - 12/01	3/84 - 12/01
SANF1	C-MAN	24.46 81.88	1/91 - 12/01	5/91 - 12/01		1/91 - 12/01
SMKF1	C-MAN	24.63 81.11	2/88 - 12/01	2/88 - 12/01	3/97 - 12/01	2/88 - 12/01
SRST1	C-MAN	29.67 94.05	2/84 - 12/01		4/97 - 12/01	2/84 - 12/01
VENF1	C-MAN	27.07 82.45	1/94 - 12/01	1/94 - 12/01	4/97 - 12/01	1/94 - 12/01
42001	Buoy	25.84 89.66	8/75 - 12/01	8/75 - 12/01	8/75 - 12/01	8/75 - 12/01
42002	Buoy	25.17 94.42	6/73 - 12/01	9/76 - 12/01	6/73 - 12/01	6/73 - 12/01
42003	Buoy	26.01 85.91	11/76 - 12/01	11/76 - 12/01	6/00 - 12/01	11/76 - 12/01
42005	Buoy	30.00 85.90	12/78 - 5/80	12/78 - 5/80		12/78 - 5/80
42007	Buoy	30.09 88.77	1/81 - 12/01	1/81 - 12/01	12/98 - 12/01	1/81 - 12/01
42008	Buoy	28.70 95.30	10/80 - 7/84	10/80 - 11/83		10/80 - 7/84
42019	Buoy	27.91 95.36	5/90 - 12/01	5/90 - 12/01	5/93 - 12/01	5/90 - 12/01
42020	Buoy	26.95 96.70	5/90 - 12/01	5/90 - 12/01	12/98 - 12/01	5/90 - 12/01
42035	Buoy	29.25 94.41	5/93 - 12/01	5/93 - 12/01	8/98 - 12/01	5/93 - 12/01
42036	Buoy	28.51 84.51	1/94 - 12/01	1/94 - 12/01	11/98 - 12/01	1/94 - 12/01
42039	Buoy	28.80 86.06	12/95 - 12/01	12/95 - 12/01	5/97 - 12/01	12/95 - 12/01
42040	Buoy	29.21 88.20	12/95 - 12/01	12/95 - 12/01	12/95 - 12/01	12/95 - 12/01
42041	Buoy	27.50 90.46				

*ASOS - Automated Surface Observing System (NOAA / FAA) - Boothville, LA (BVILE)

WAVCIS - Wave Current Information System (LSU)

C-MAN - Coastal-Marine Automated Network (NDBC) - Bullwinkle, LA (BUSL1), Dauphin Island, AL (DPIA1), Dry Tortugas, FL (DRYF1), Garden Banks, LA (GBCL1), Grand Isle, LA (GDIL1), Long Key, FL (LONF1), Molasses Reef, FL (MLRF1), Main Pass, LA (MPCL1), Port Aransas, TX (PTAT2), Sand Key, FL (SANF1), Sombrero Key, FL (SMKF1), Sabine, TX (SRST2), and Venice, FL (VENF1)

Buoy - offshore moored stations (NDBC)

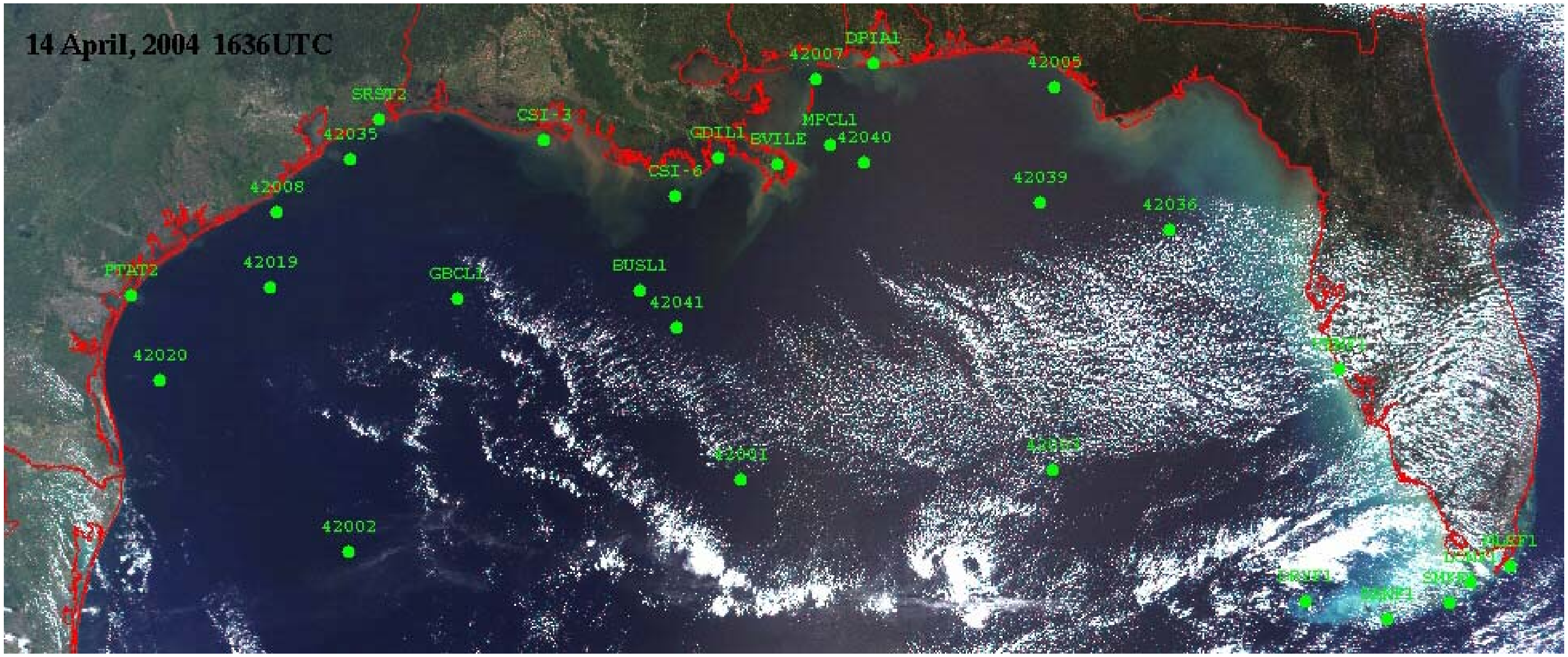

Figure 65. Approximate locations of National Data Buoy Center Coastal-Marine Automated Network and offshore buoys along with WAVCIS platforms CSI-3 and CSI-6 superimposed on a MODIS satellite image.

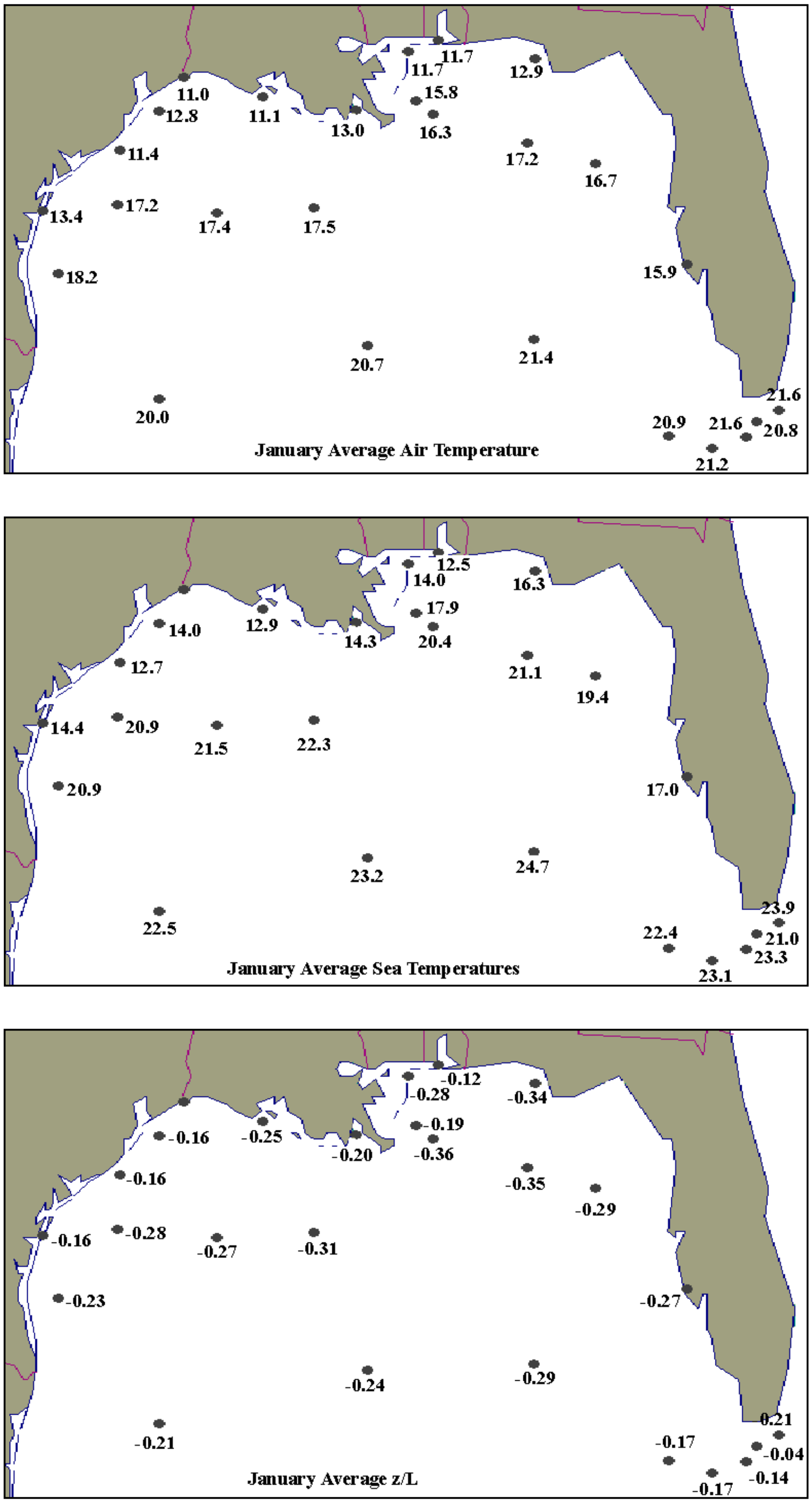

Figure 66. January monthly mean values of air temperature, sea temperature, and stability (z/L).

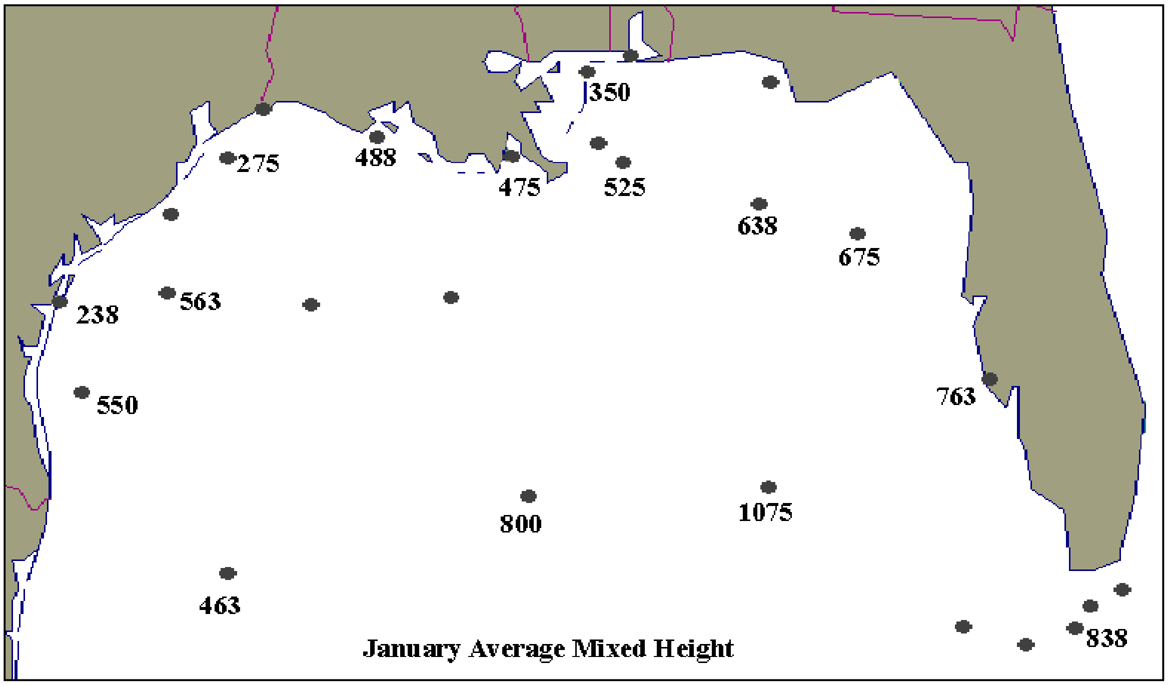

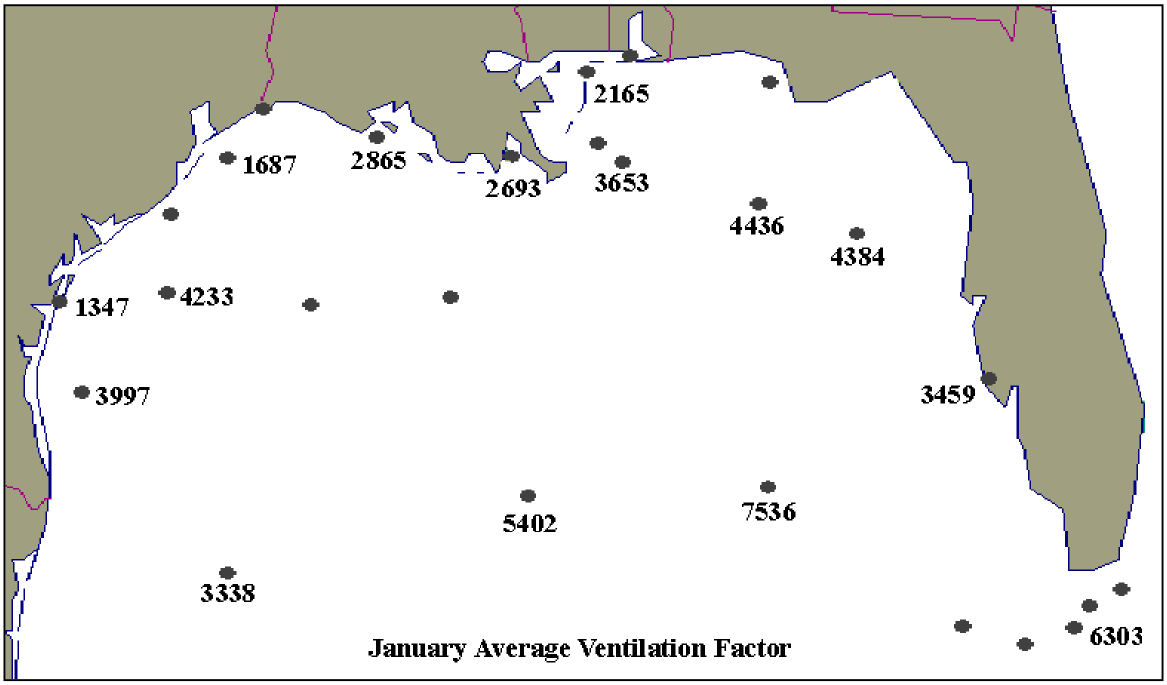

Figure 67. January monthly mean mixed heights (m) and ventilation factor index.

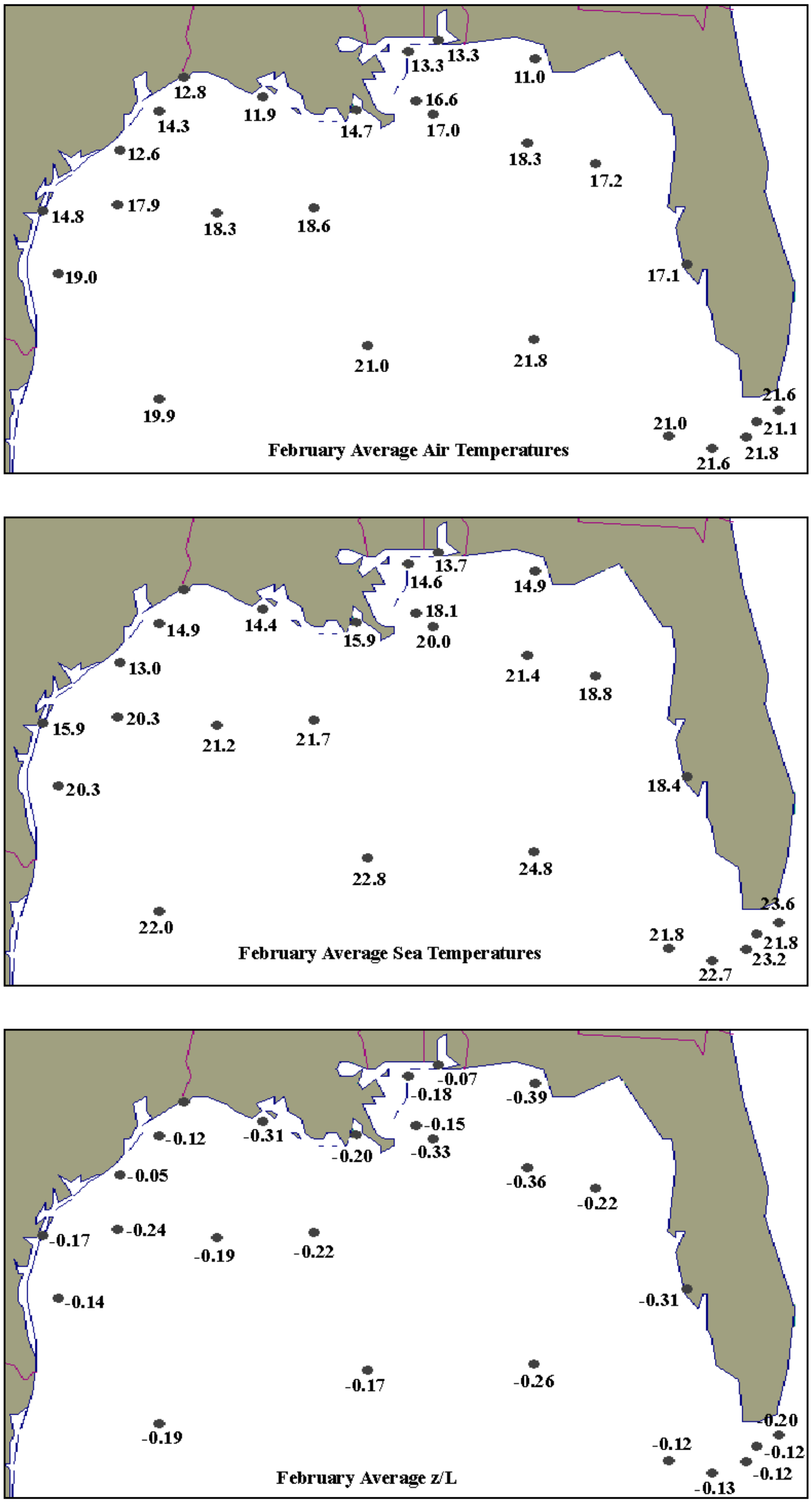

Figure 68. February monthly mean air temperature, sea temperature, and stability (z/L).

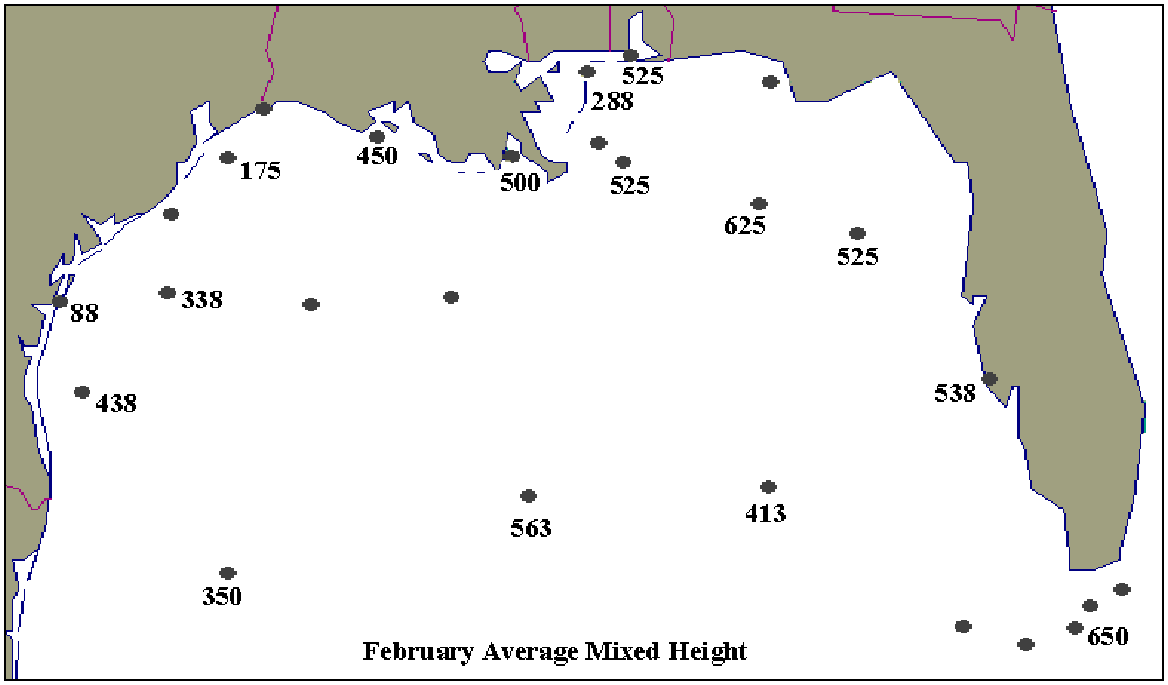

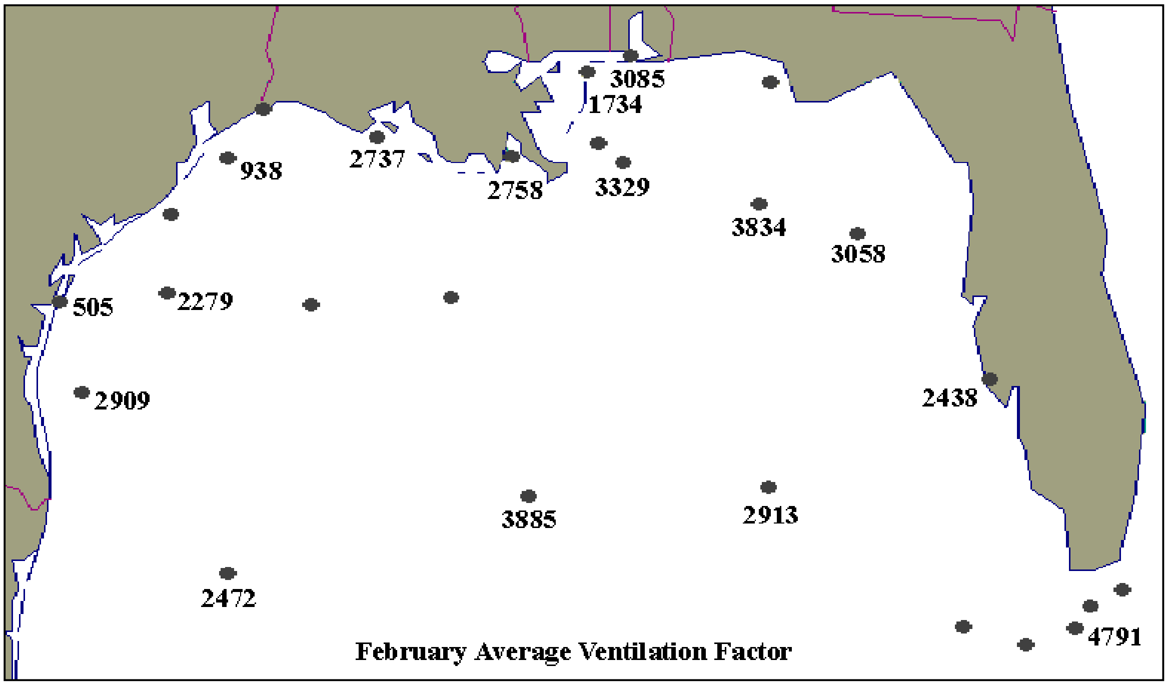

Figure 69. February monthly mean mixed heights (m) and ventilation factor index.

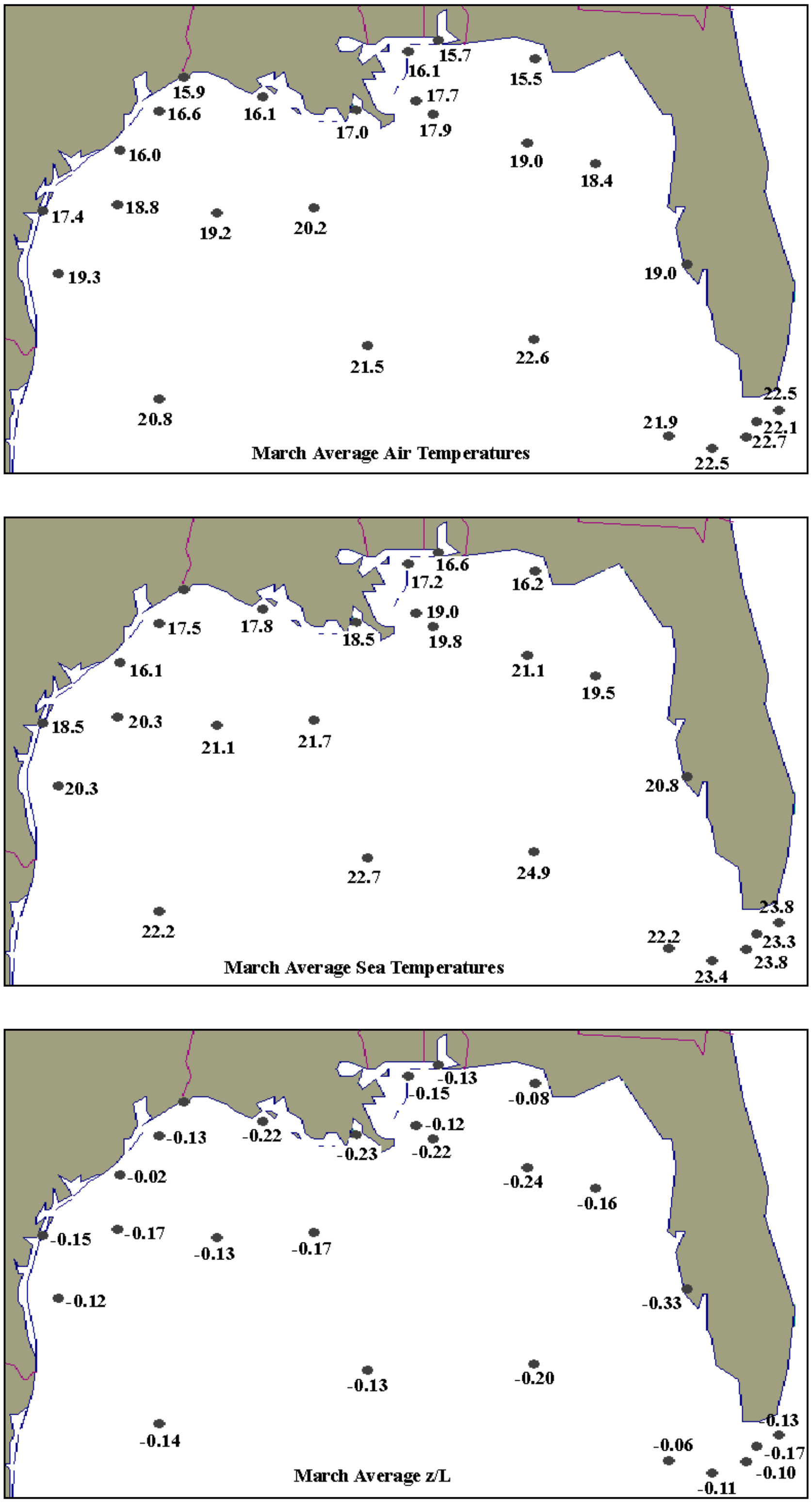

Figure 70. March monthly mean air temperature, sea temperature, and stability (z/L).

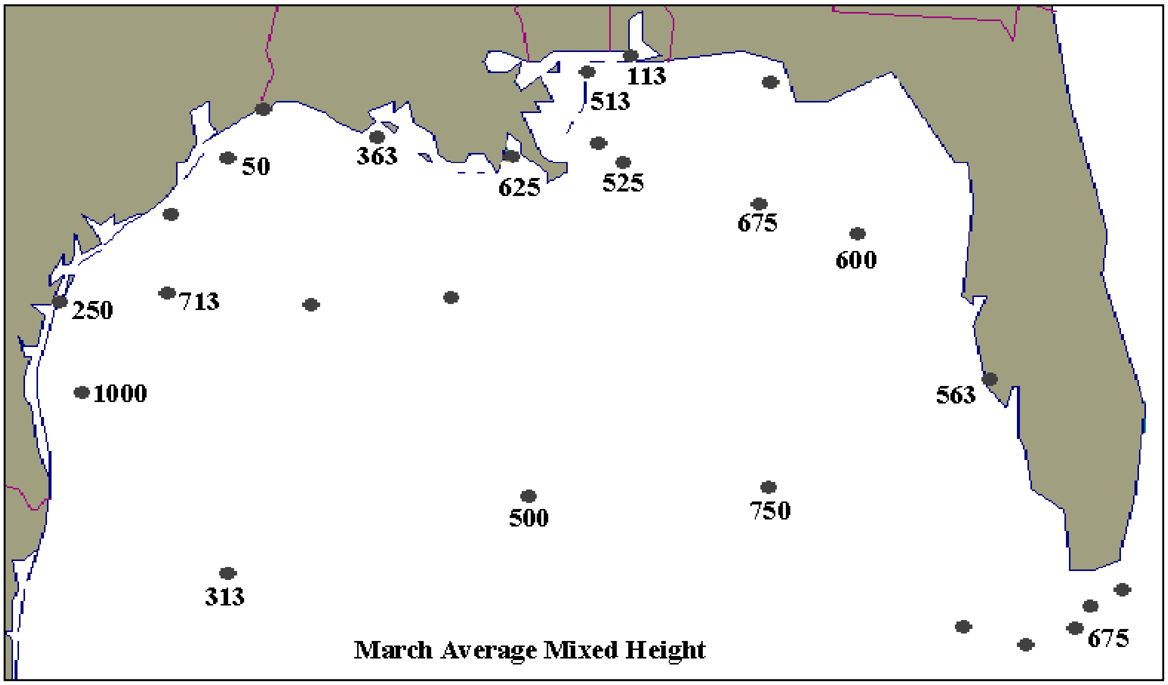

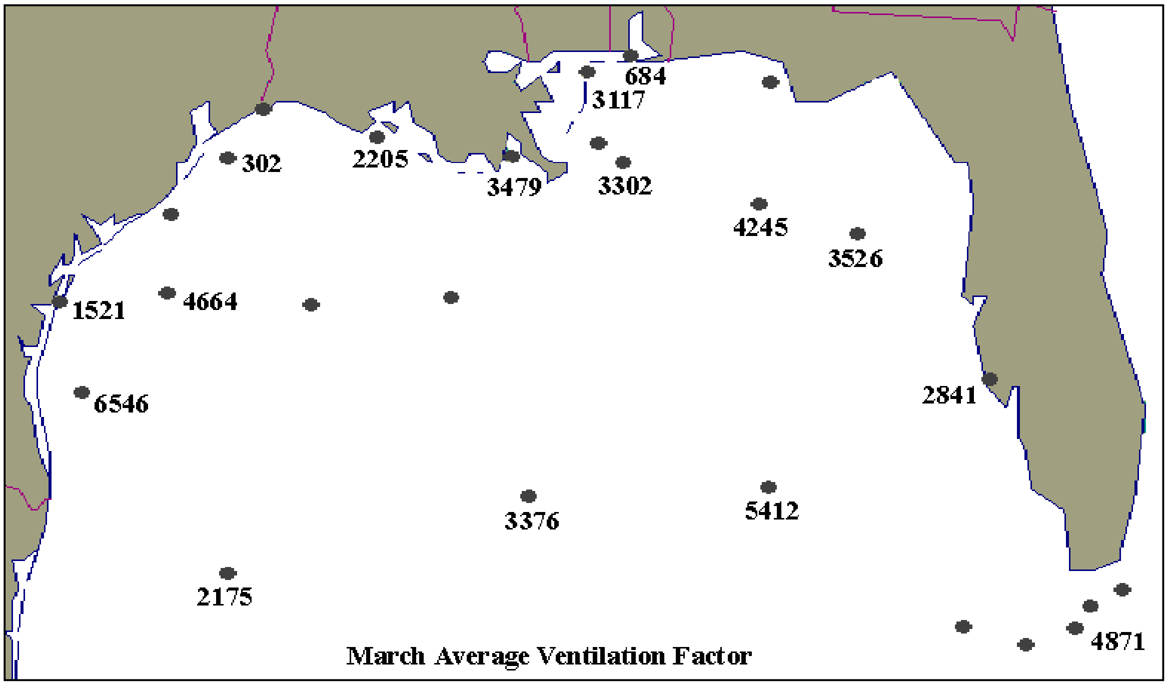

Figure 71. March monthly mean mixed height (m) and ventilation factor index.

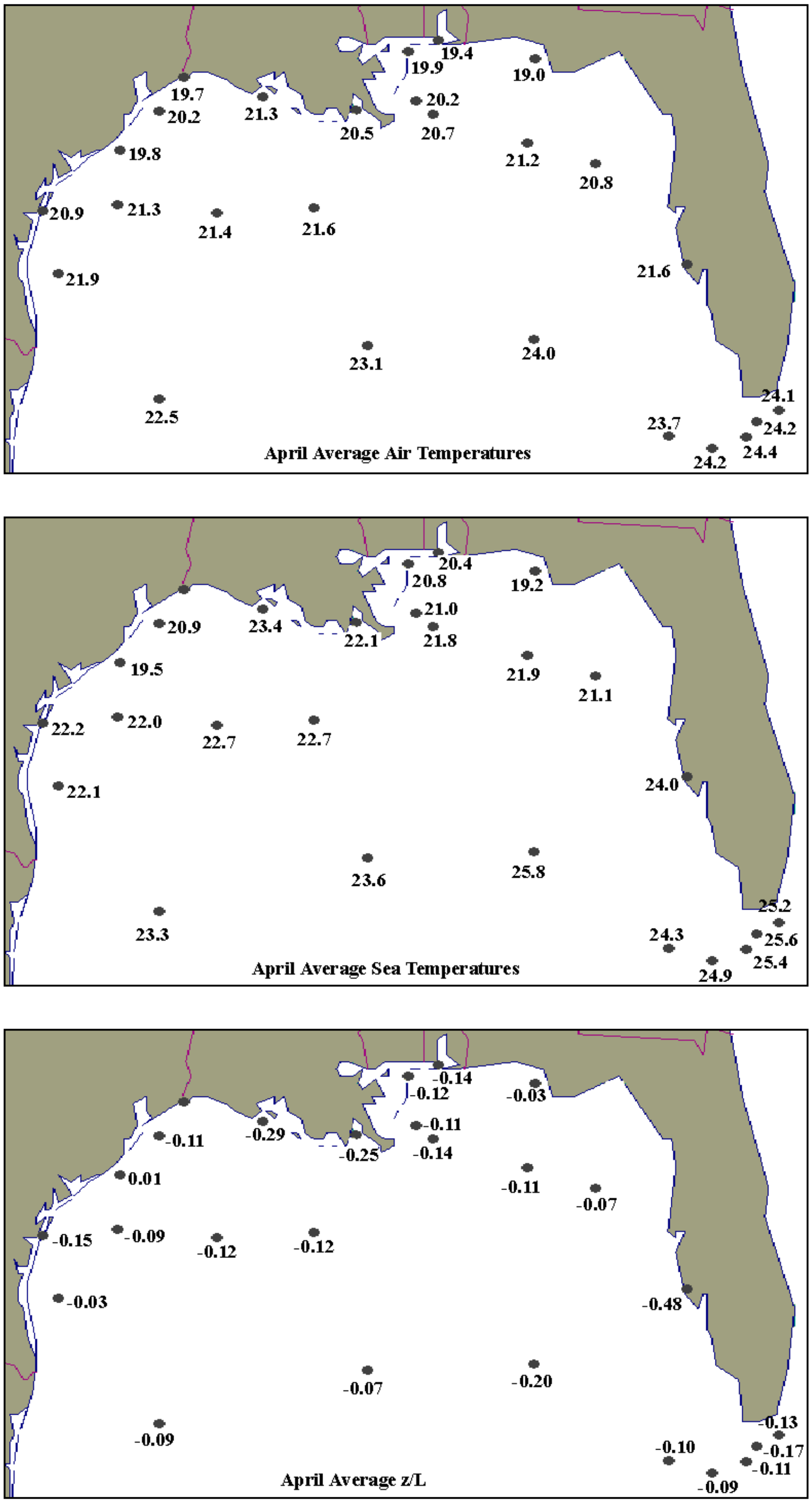

Figure 72. April monthly mean air temperature, sea temperature, and stability (z/L).

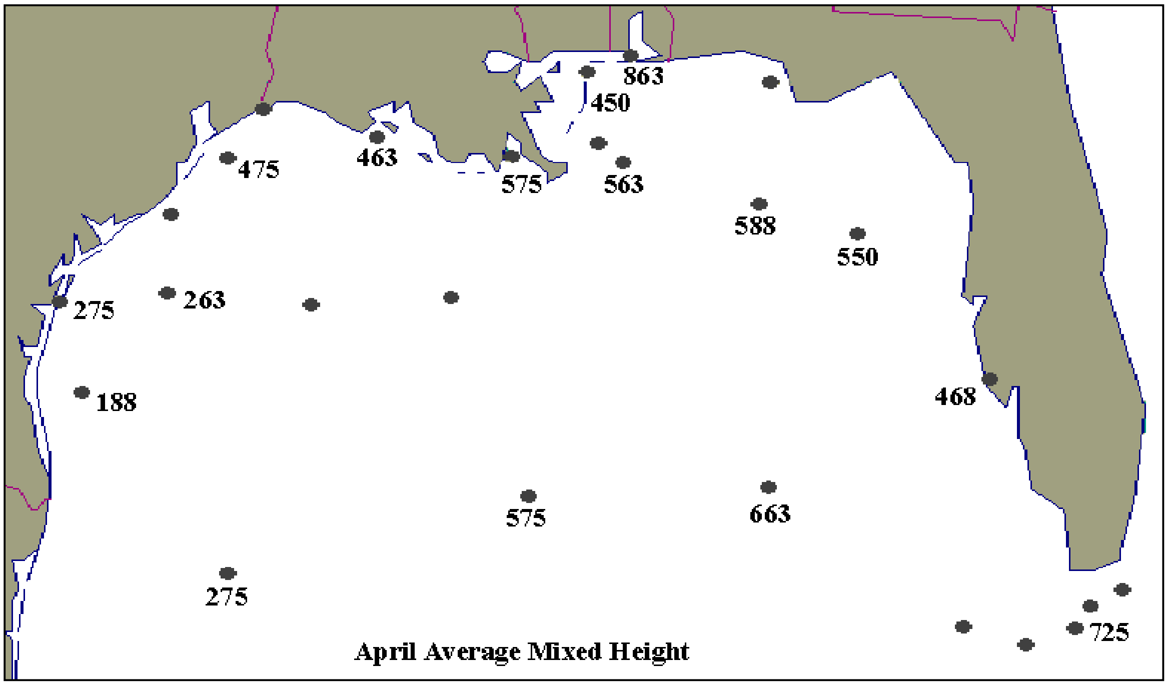

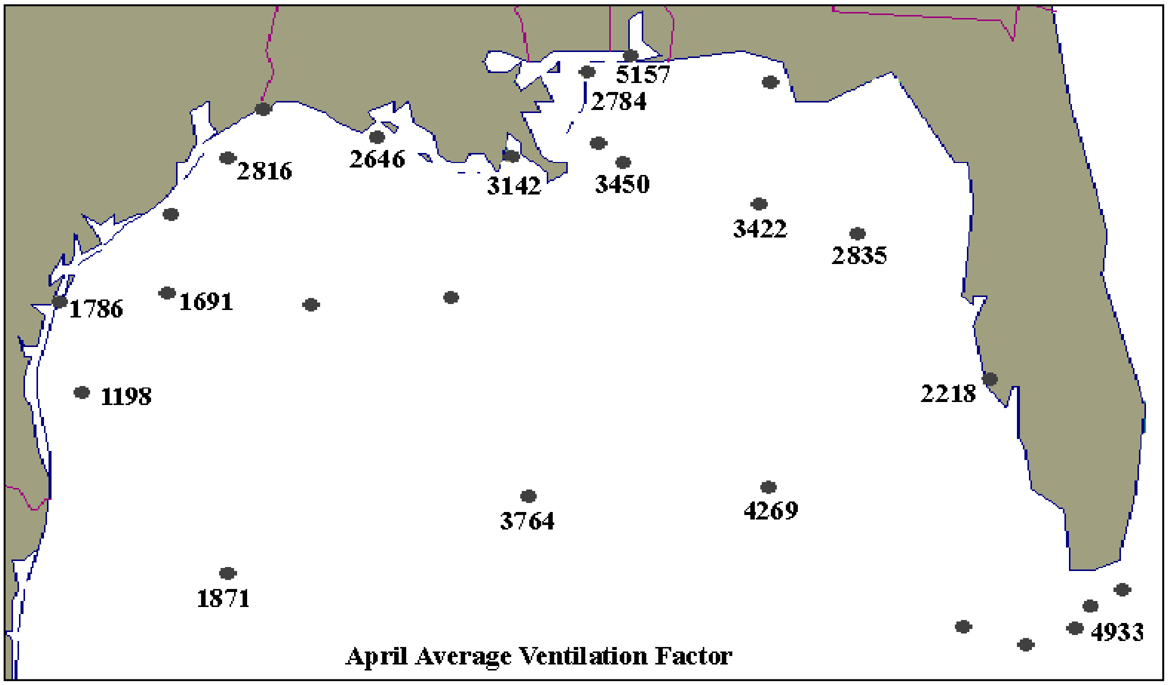

Figure 73. April monthly mean mixed height (m) and ventilation factor index.

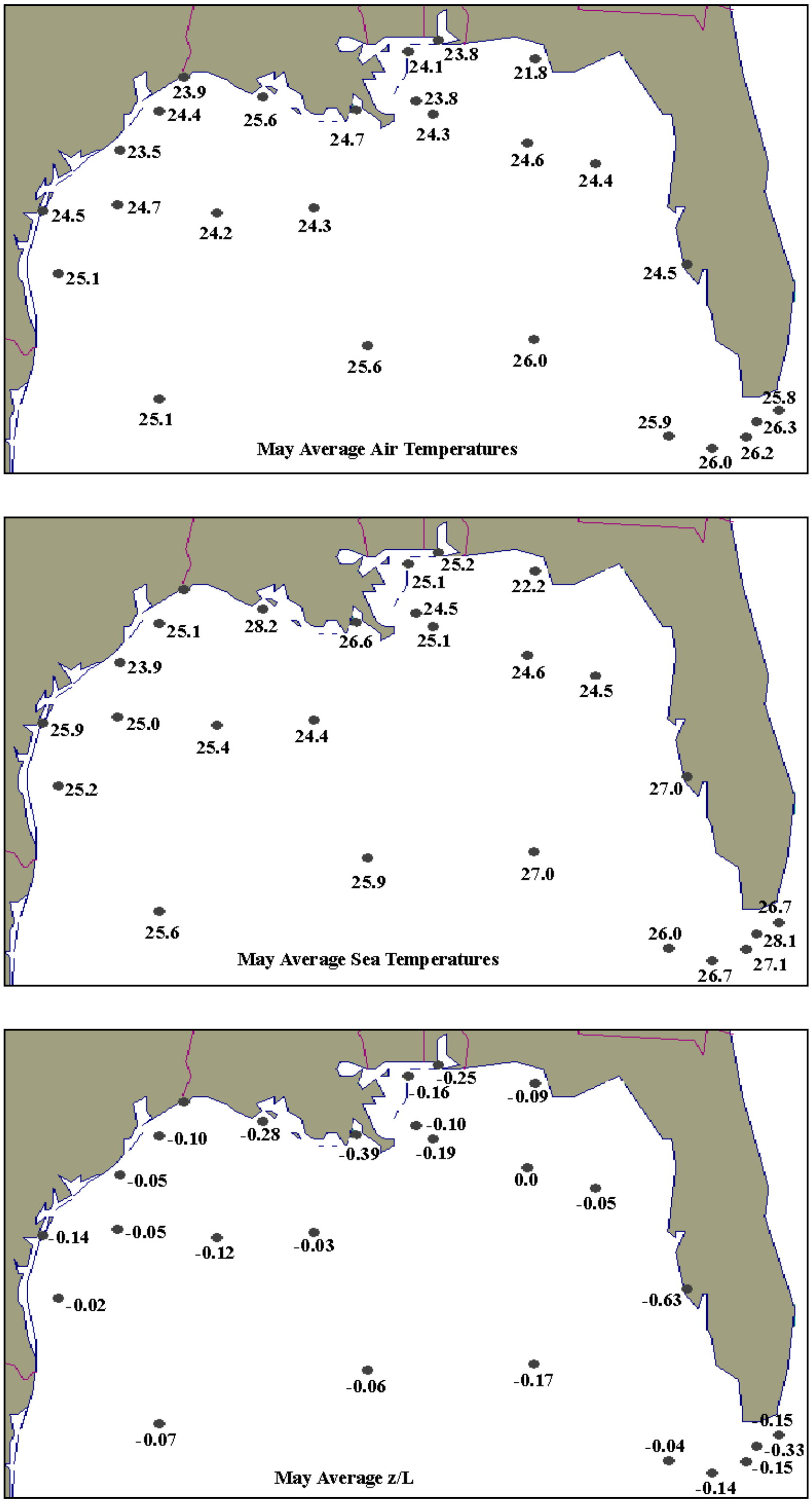

Figure 74. May monthly mean air temperature, sea temperature, and stability (z/L).

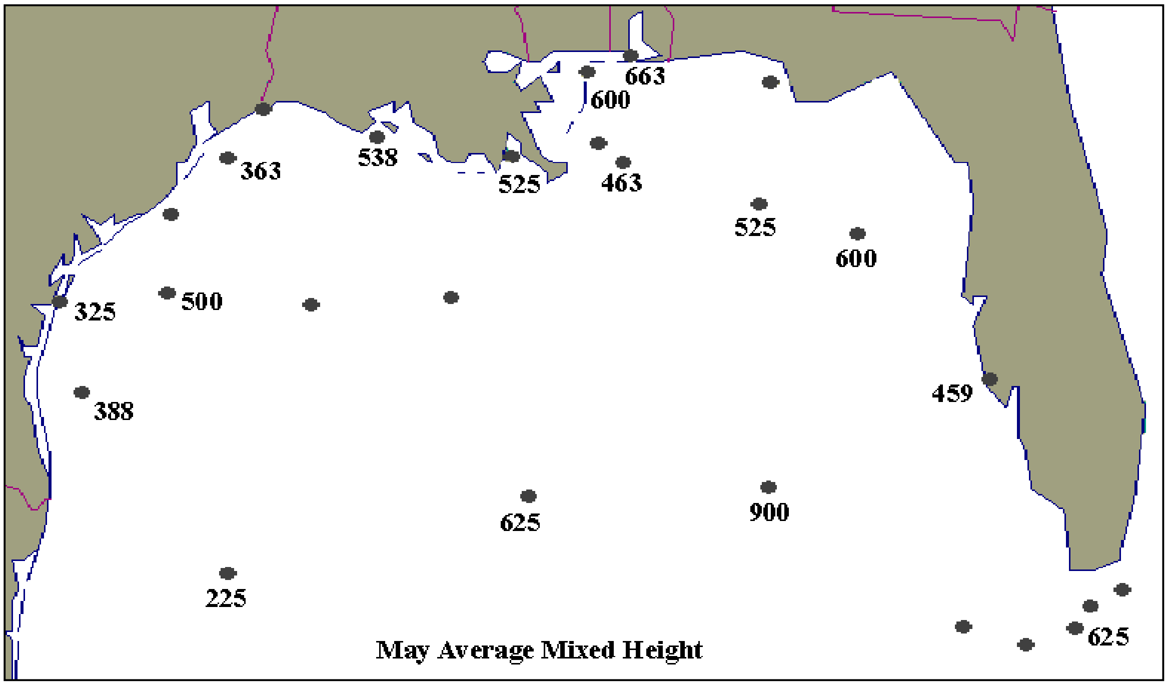

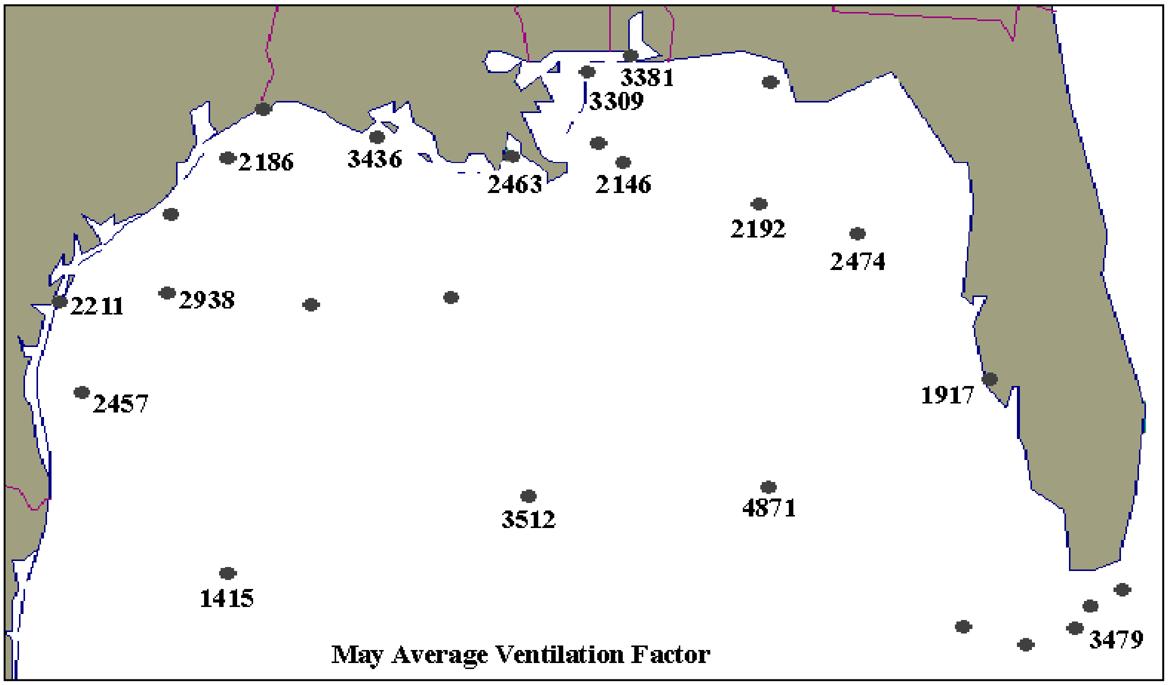

Figure 75. May monthly mean mixed height (m) and ventilation factor index.

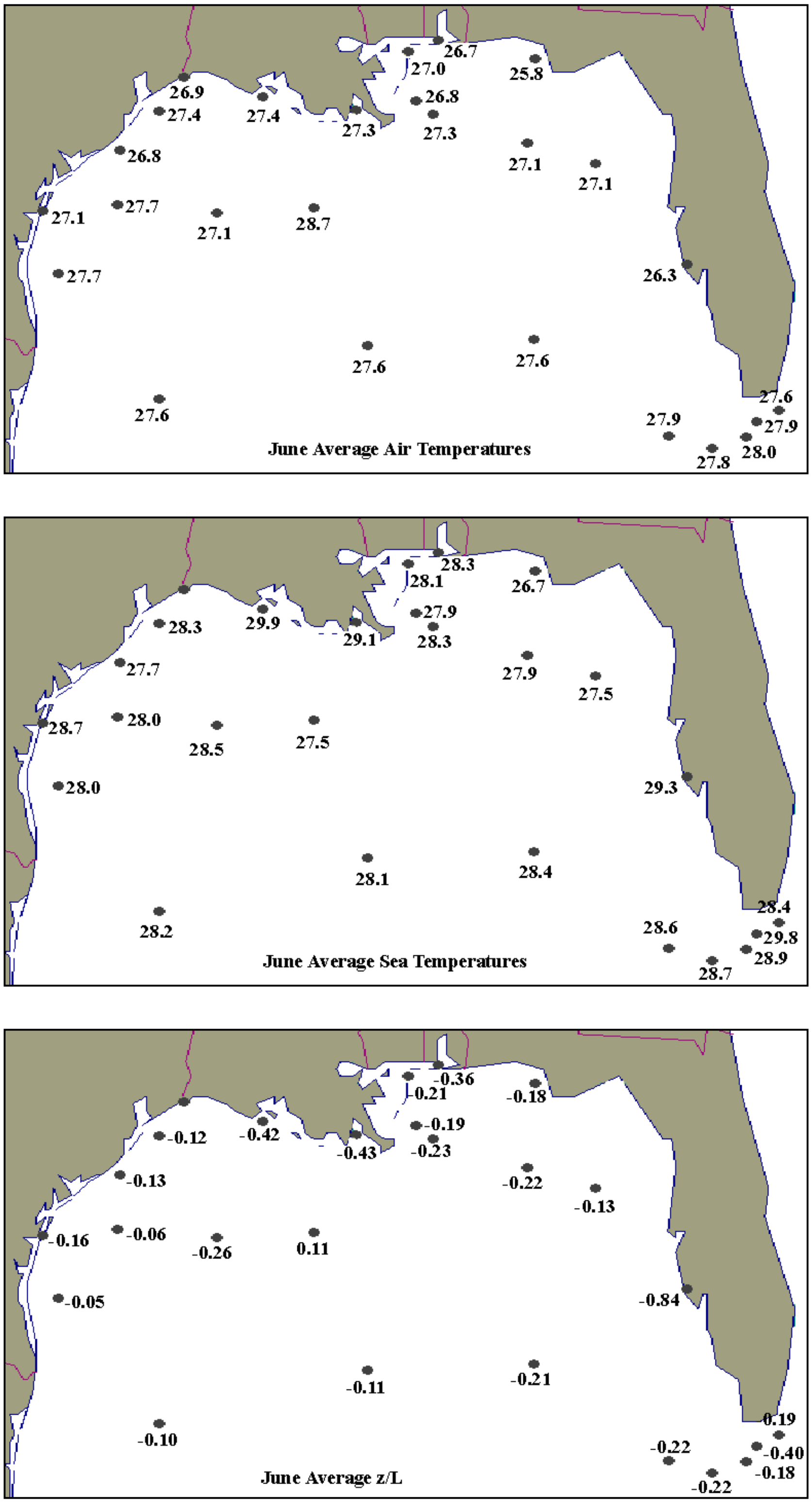

Figure 76. June monthly mean air temperature, sea temperature, and stability (z/L).

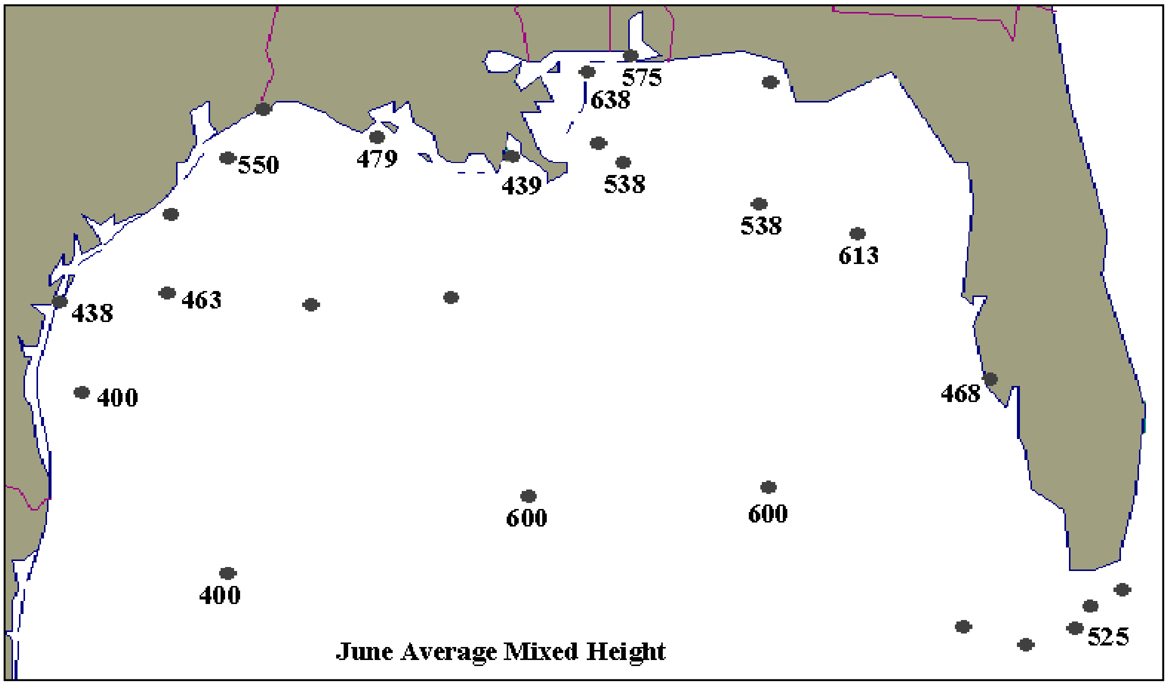

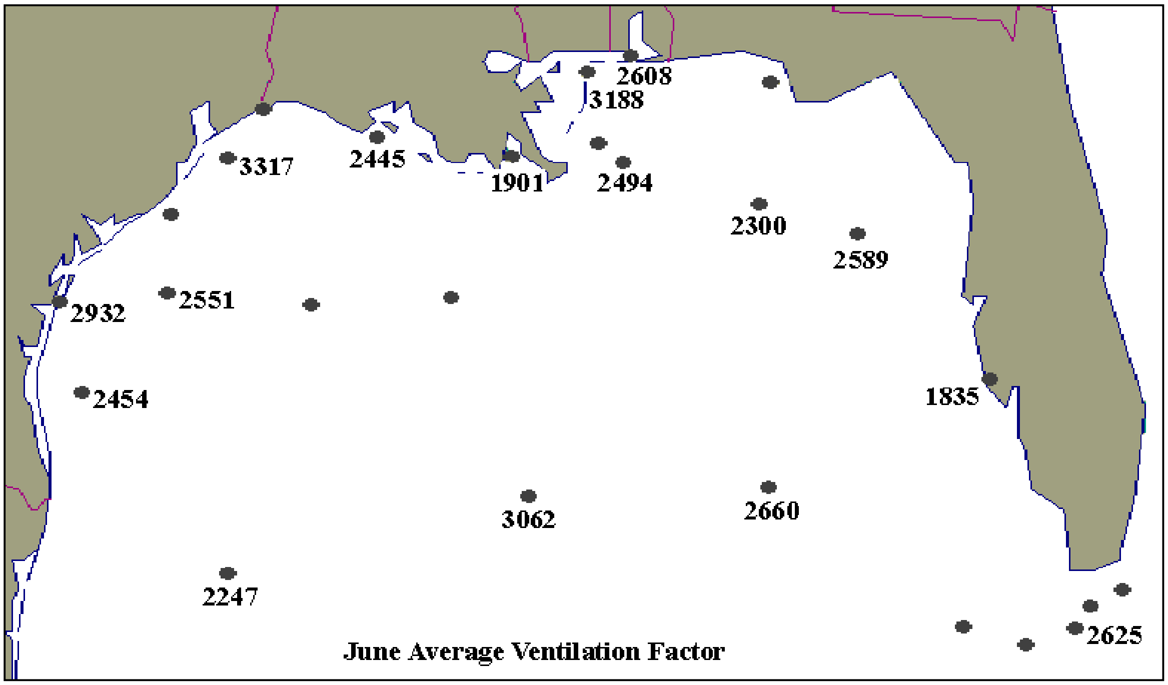

Figure 77. June monthly mean mixed height (m) and ventilation factor index.

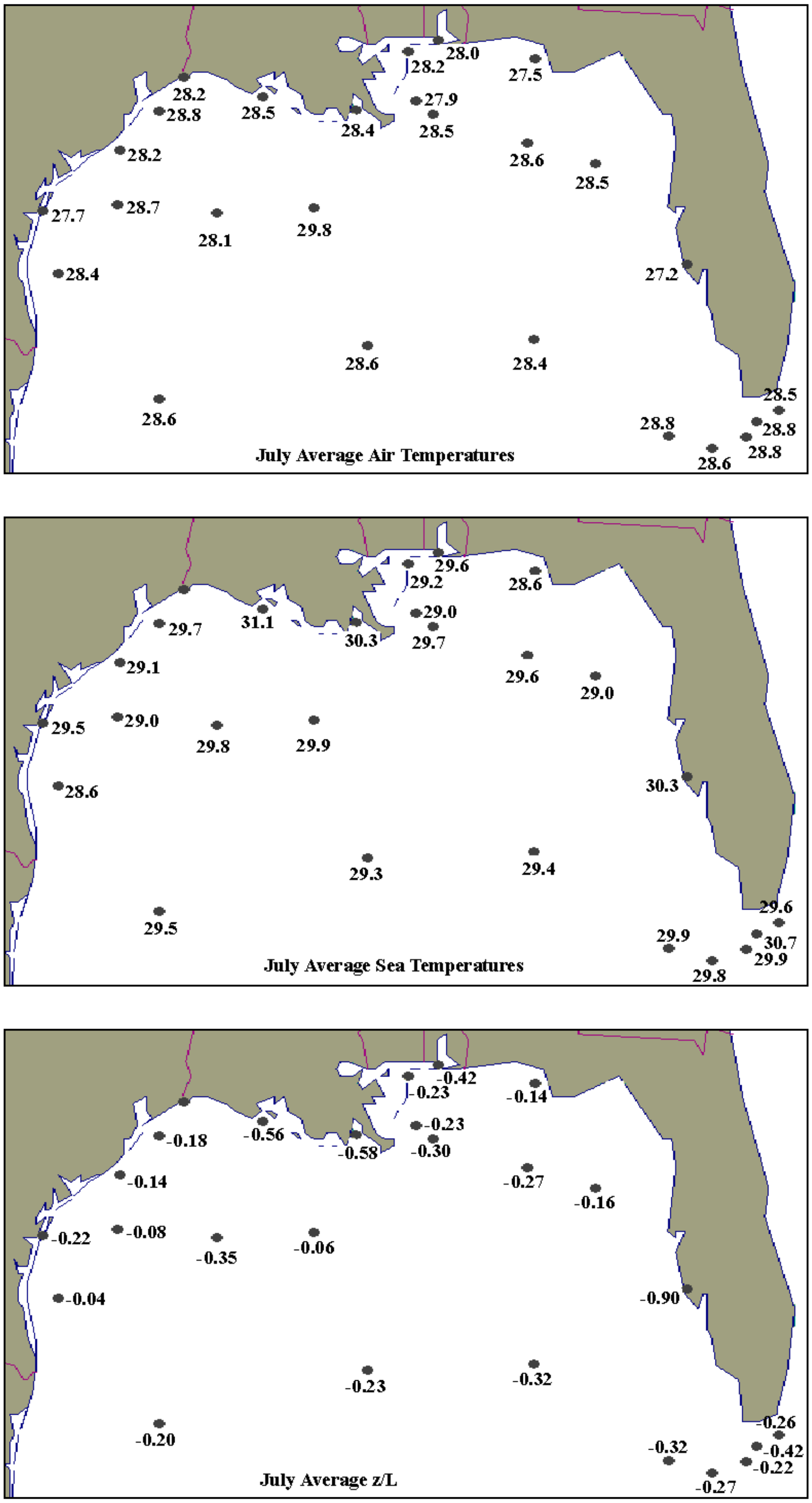

Figure 78. July monthly mean air temperature, sea temperature, and stability (z/L).

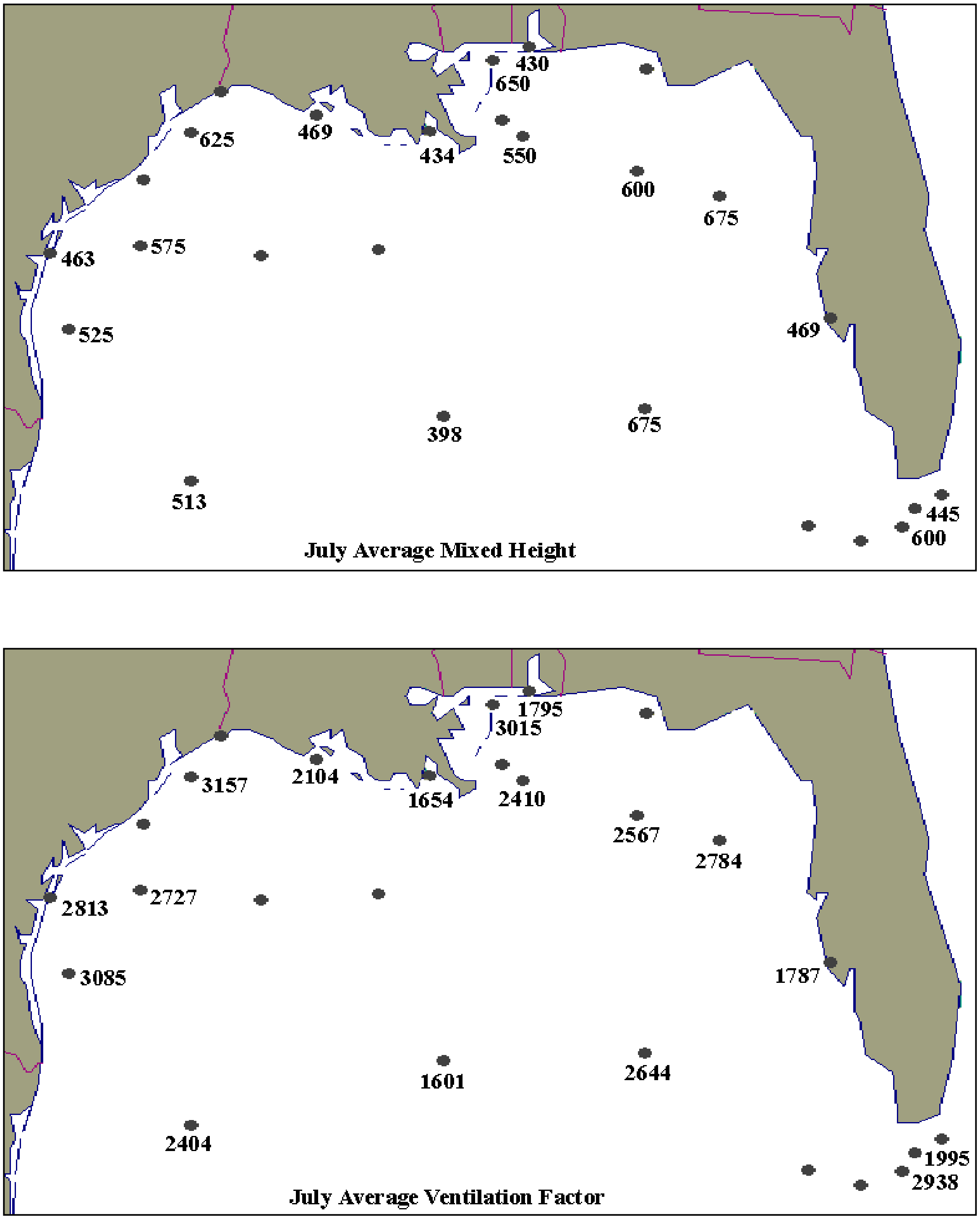
July Average Mixed Height

July Average Ventilation Factor

Figure 79. July monthly mean mixed height (m) and ventilation factor index.

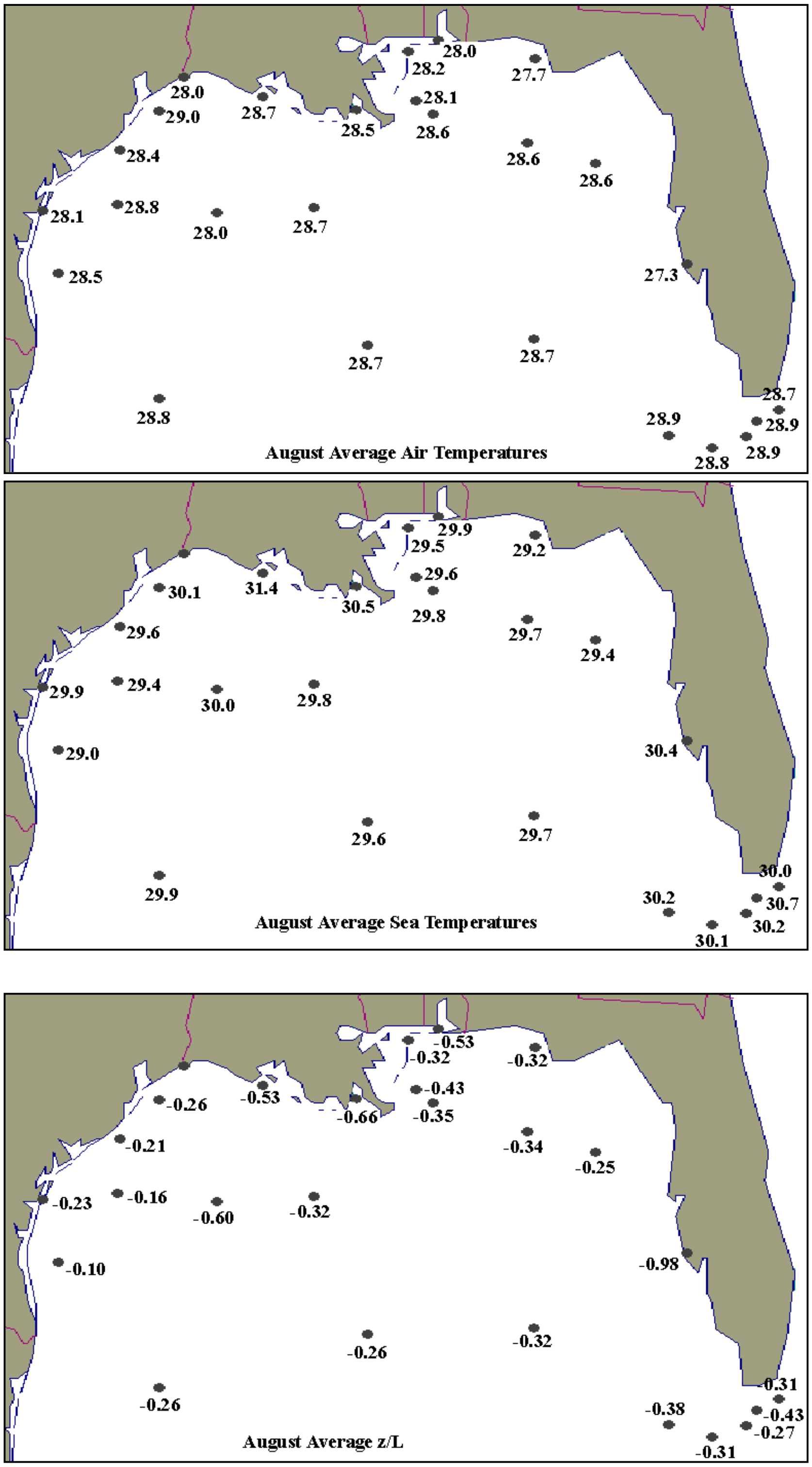

Figure 80. August monthly mean air temperature, sea temperature, and stability (z/L).

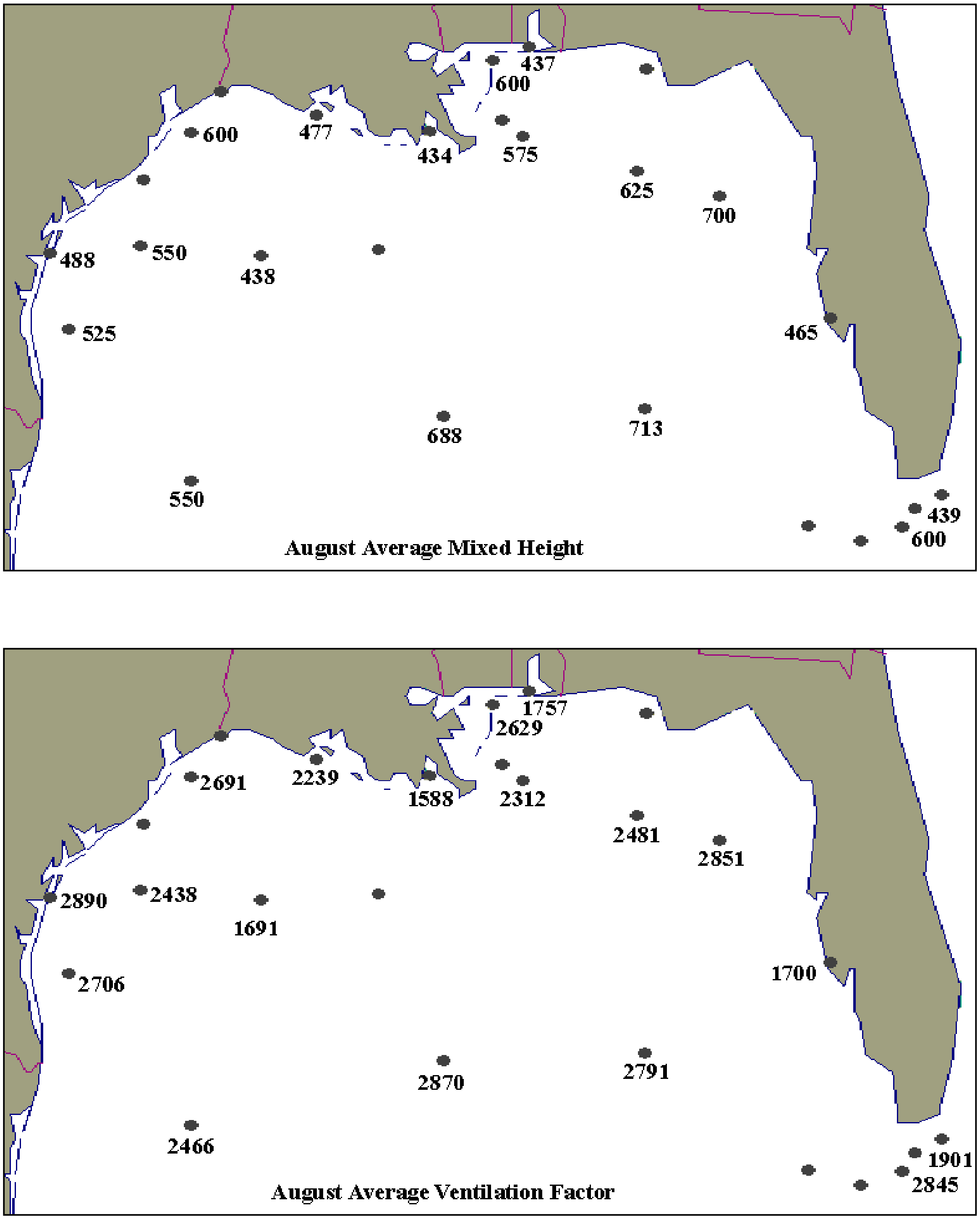

Figure 81. August monthly mean mixed height (m) and ventilation factor index.

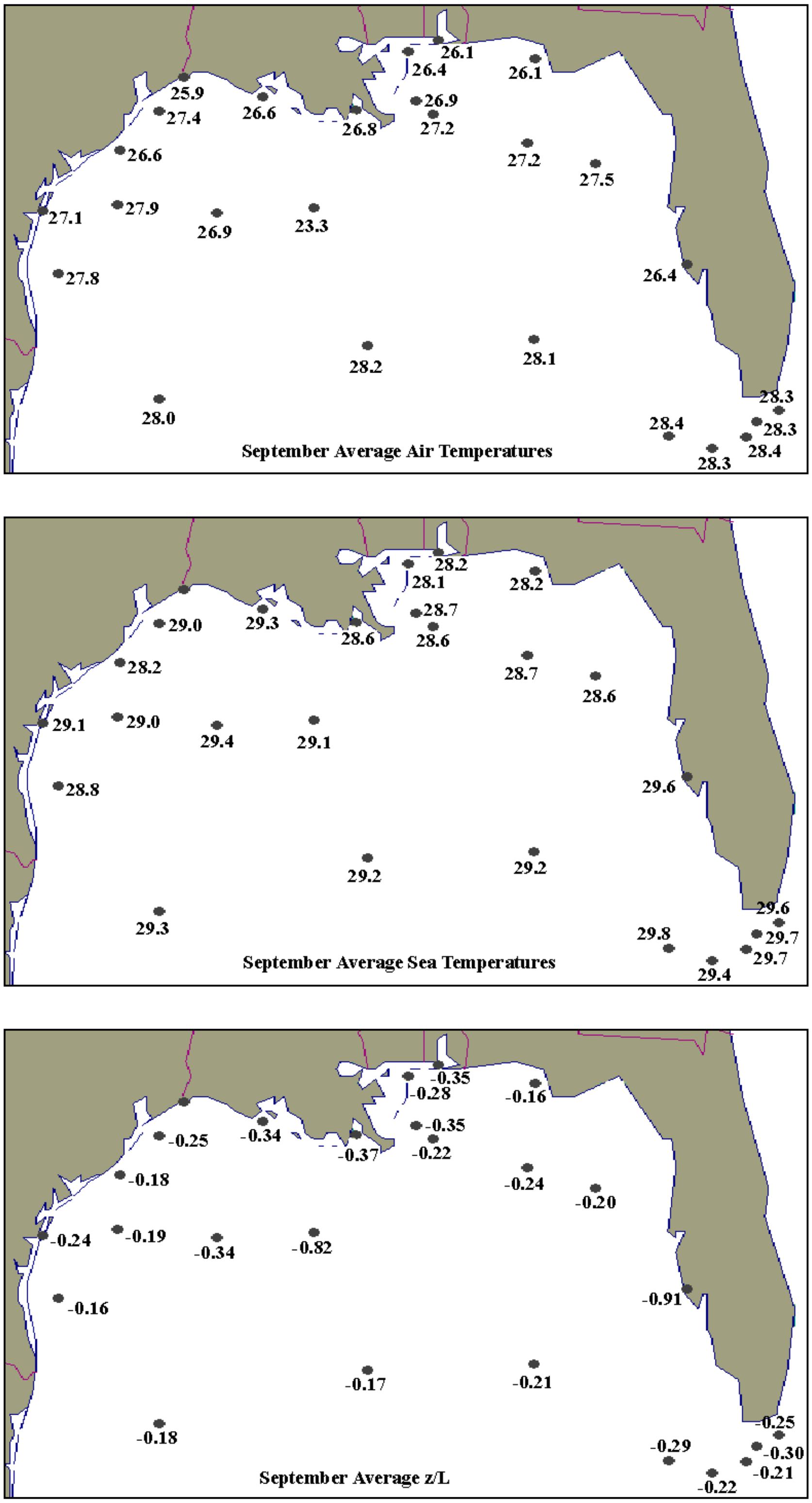

Figure 82. September monthly mean air temperature, sea temperature, and stability (z/L).

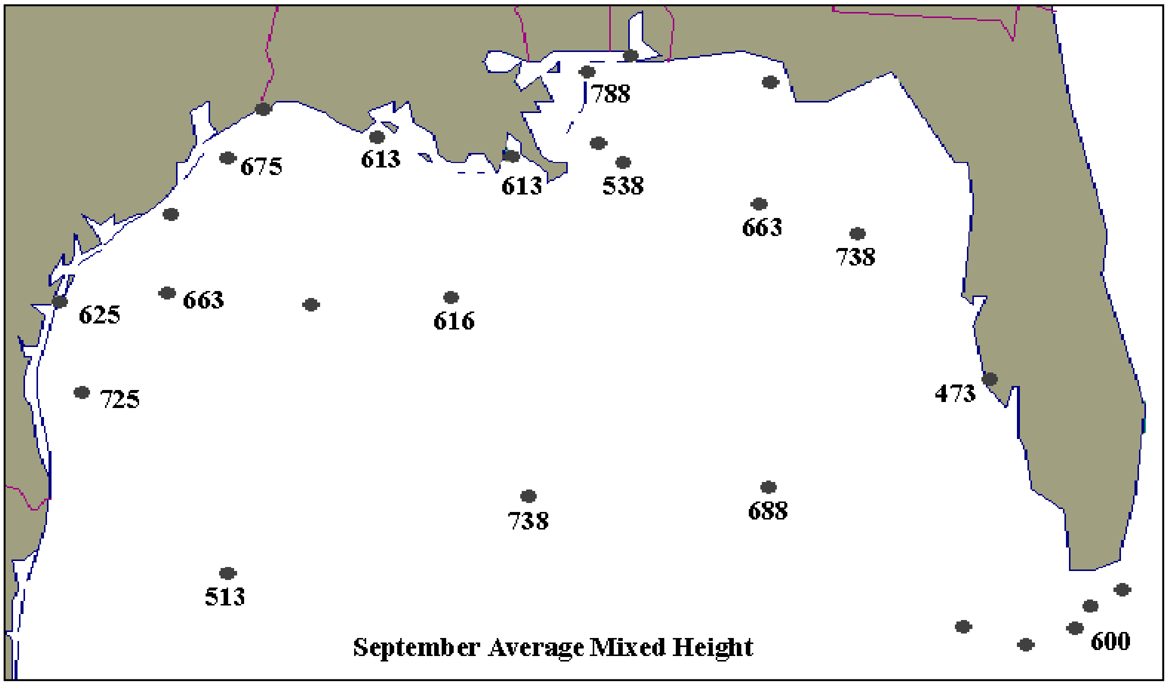

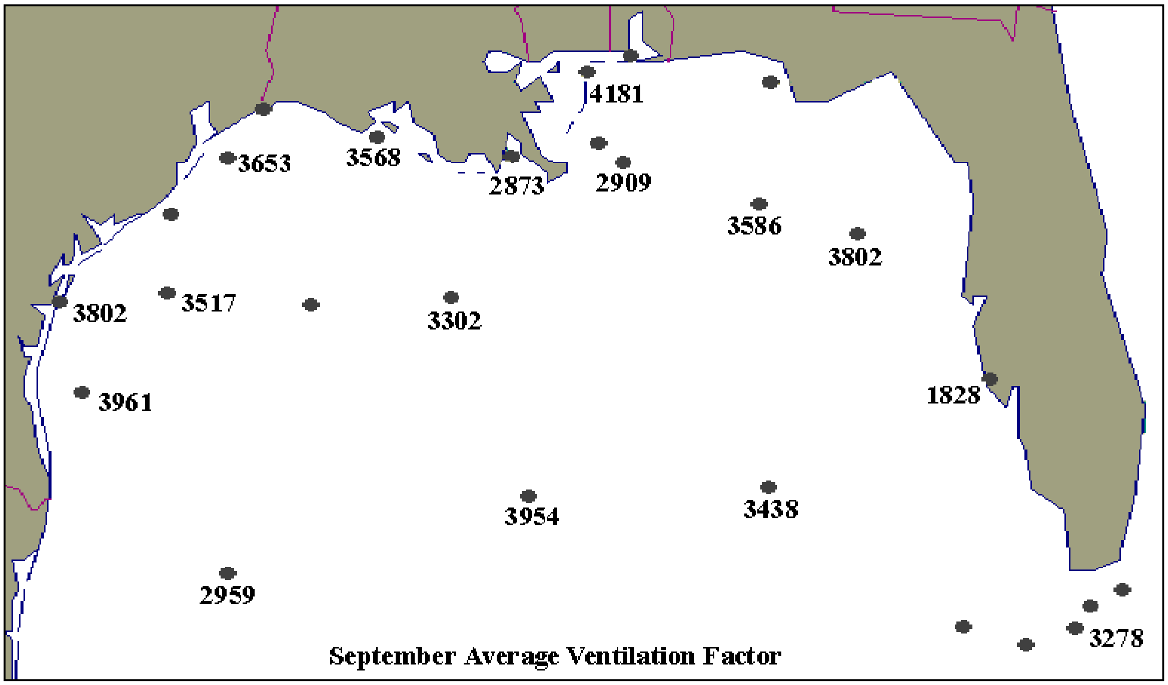

Figure 83. September monthly mean mixed height (m) and ventilation factor index.

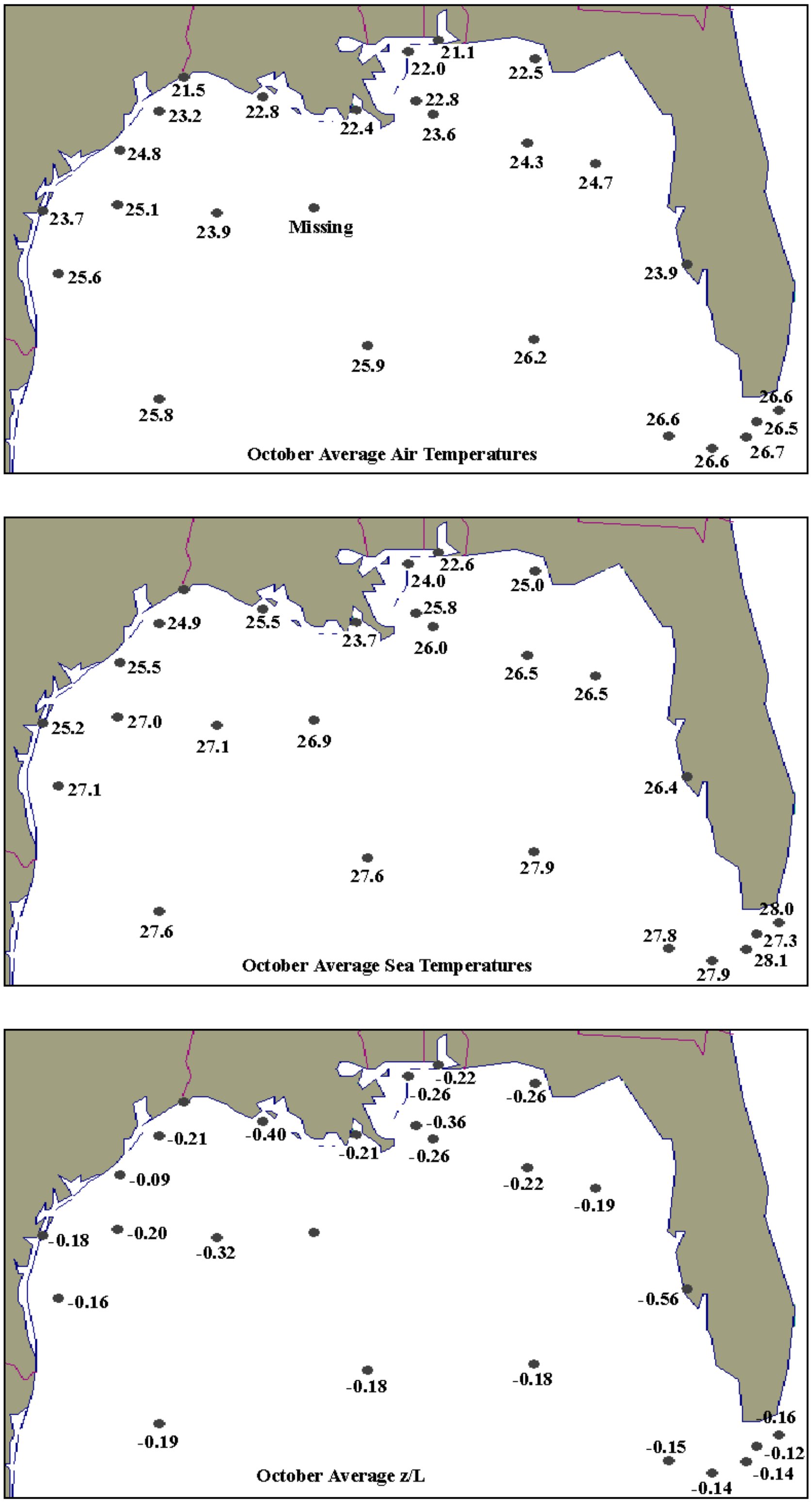

Figure 84. October monthly mean air temperature, sea temperature, and stability (z/L).

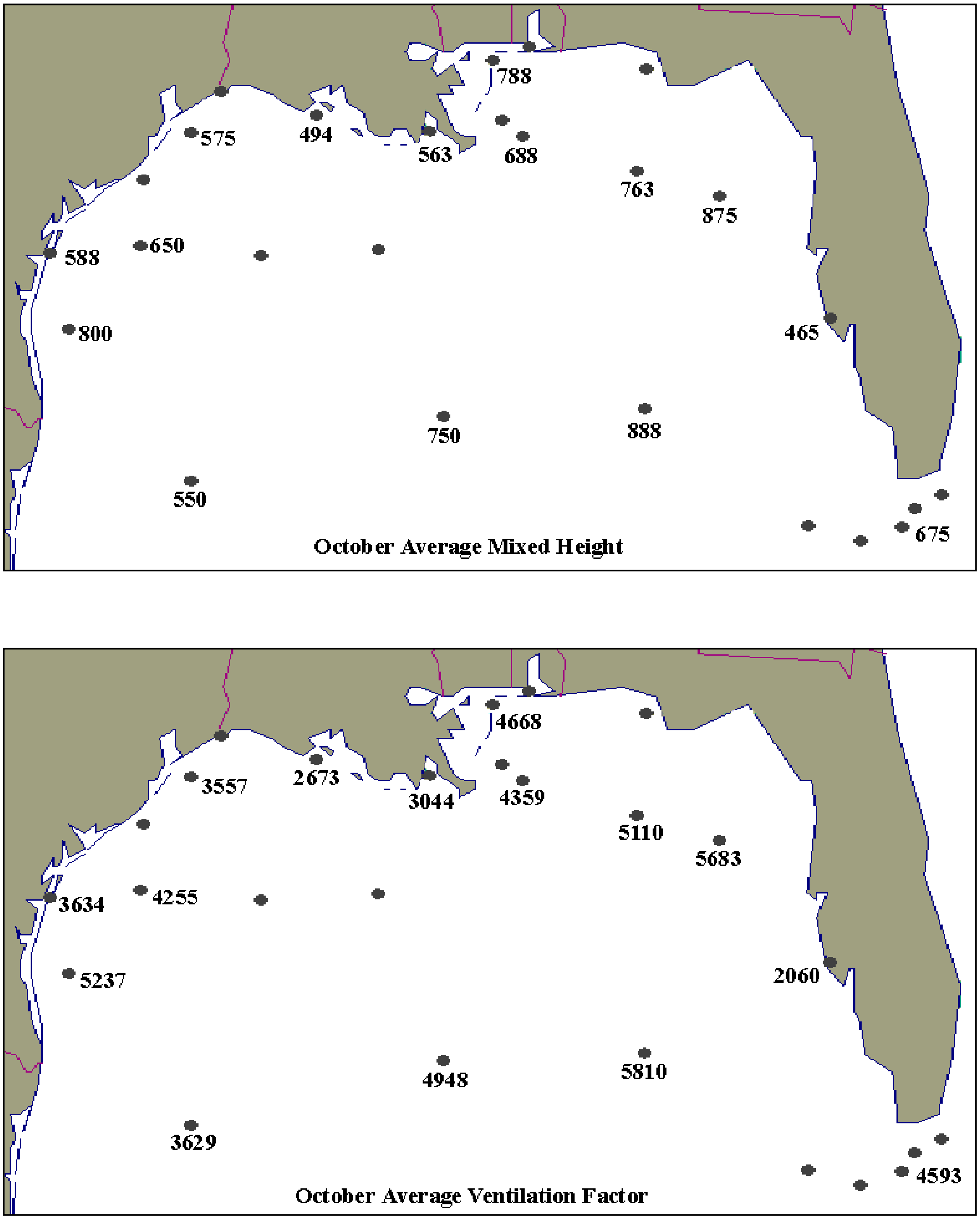

Figure 85. October monthly mean mixing height (m) and ventilation factor index.

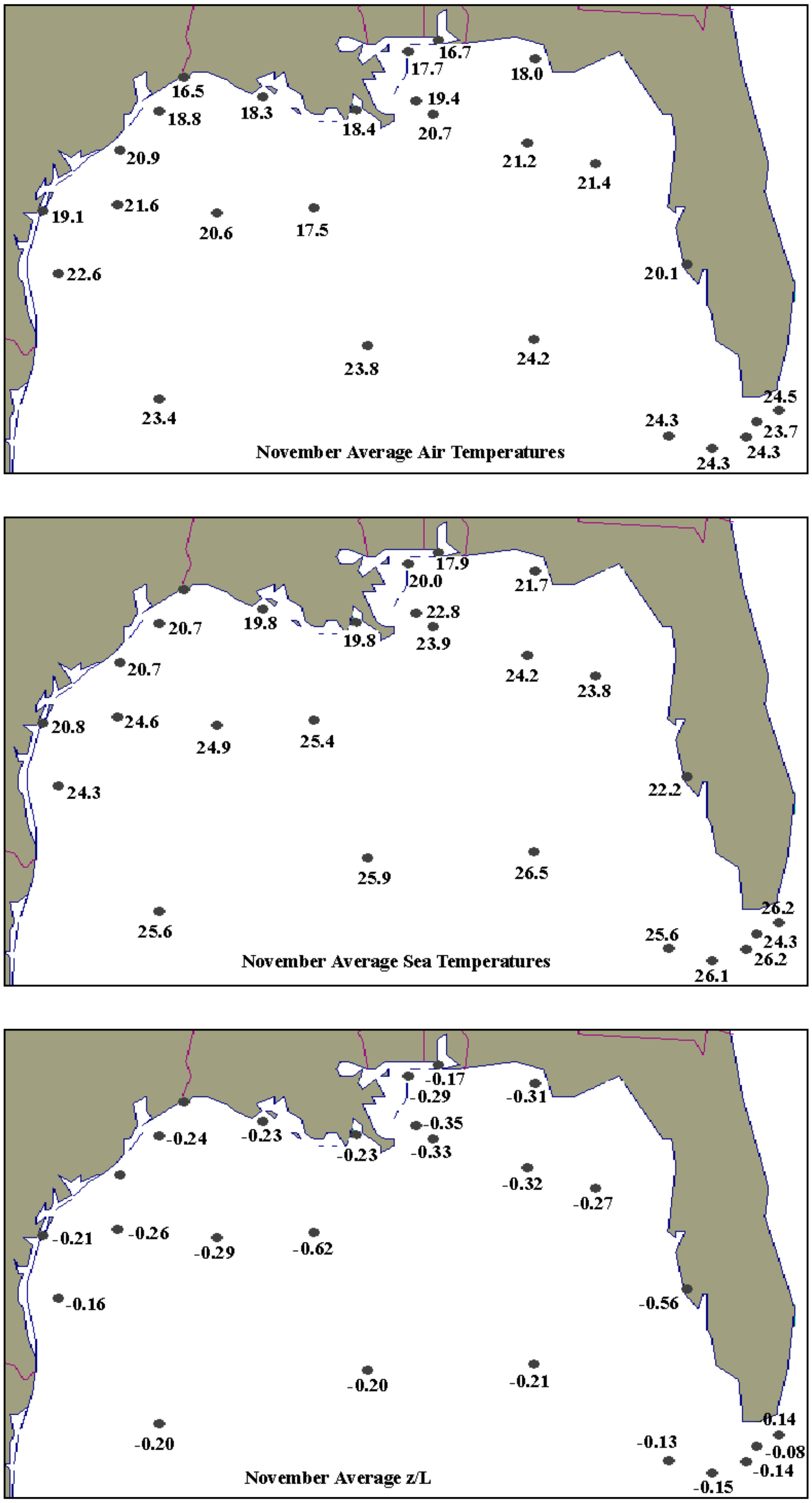

Figure 86. November monthly mean air temperature, sea temperature, and stability (z/L).

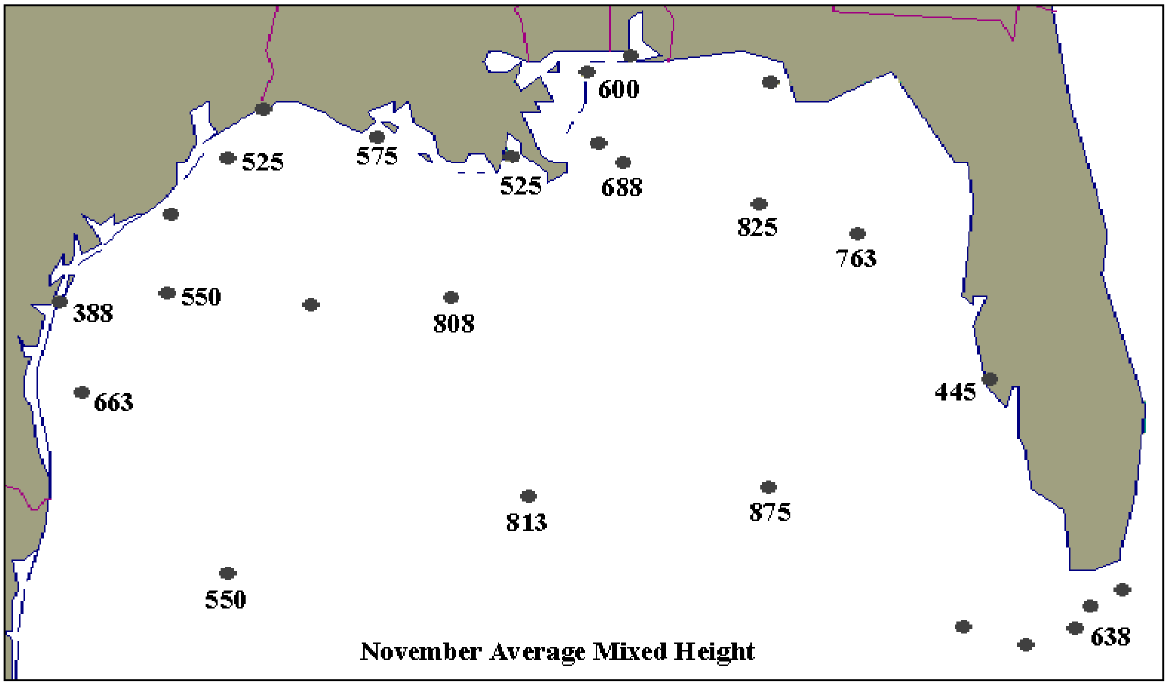

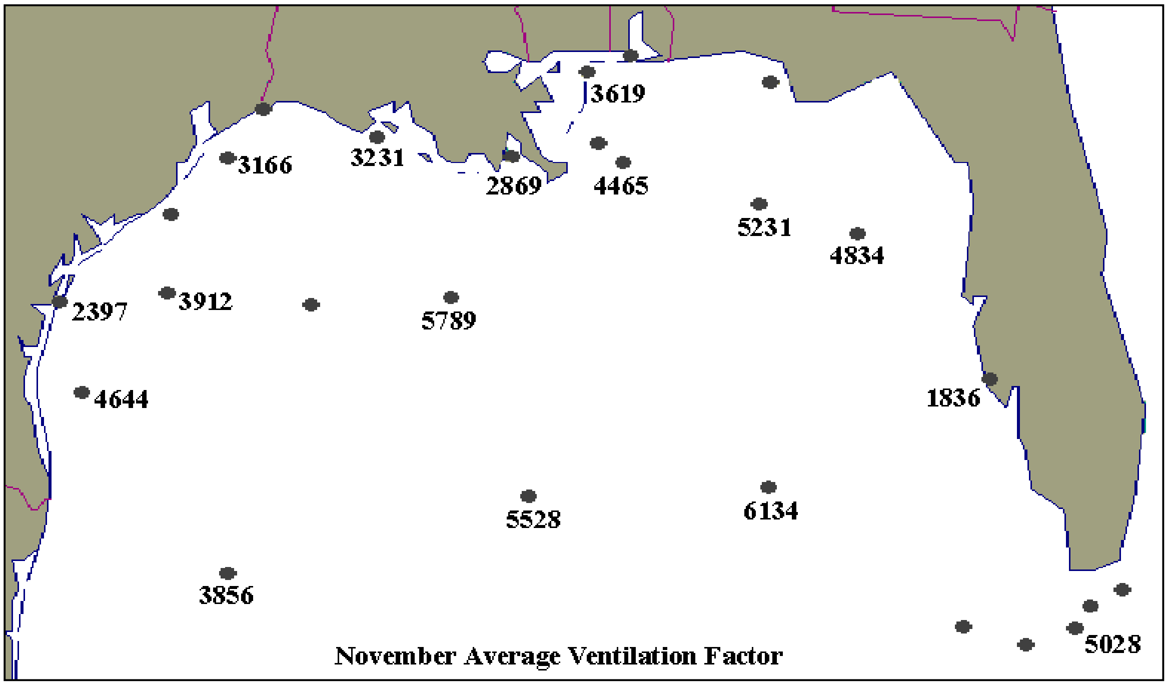

Figure 87. November monthly mean mixed height (m) and ventilation factor index.

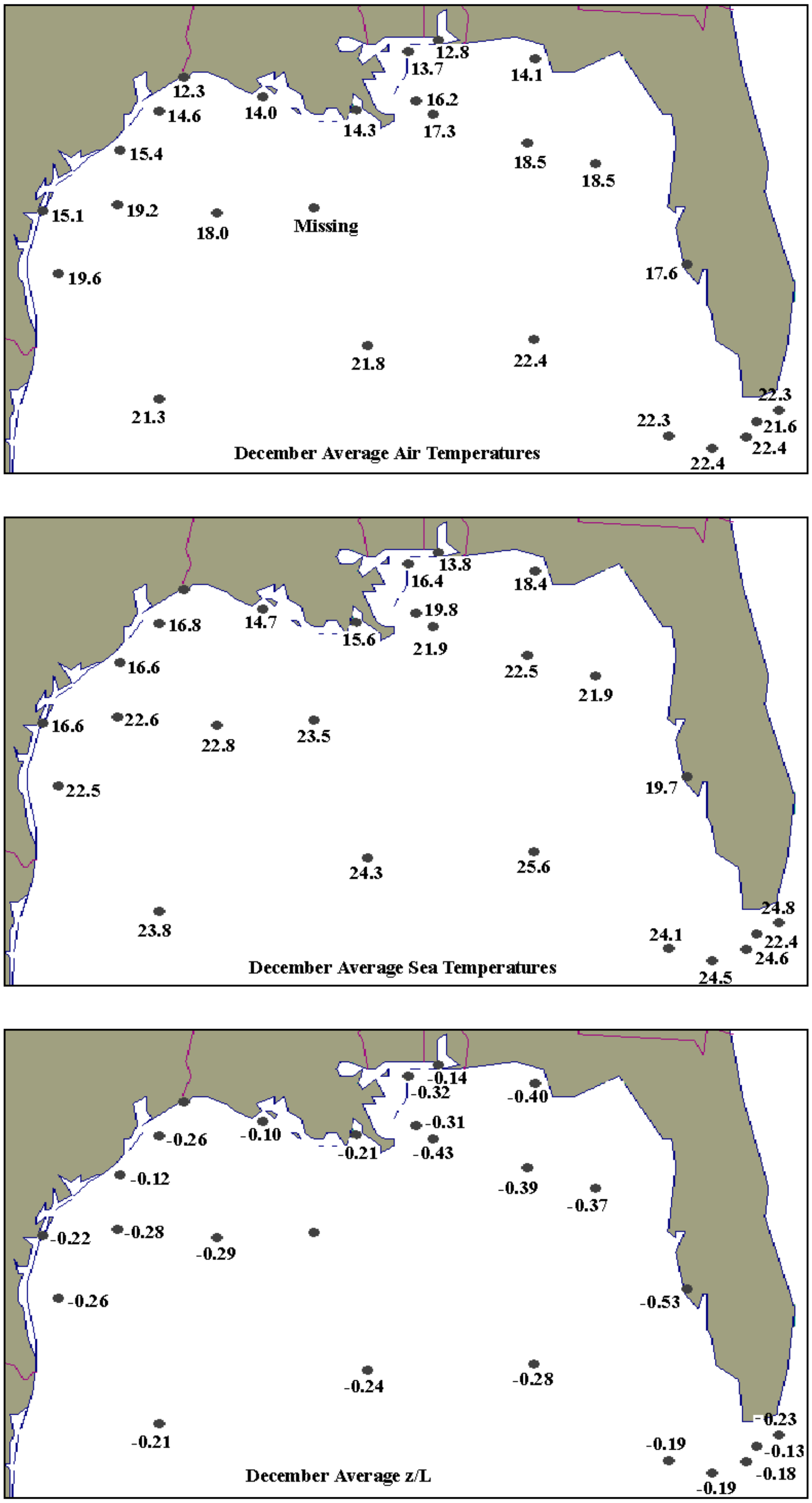

Figure 88. December monthly mean air temperature, sea temperature, and stability (z/L).

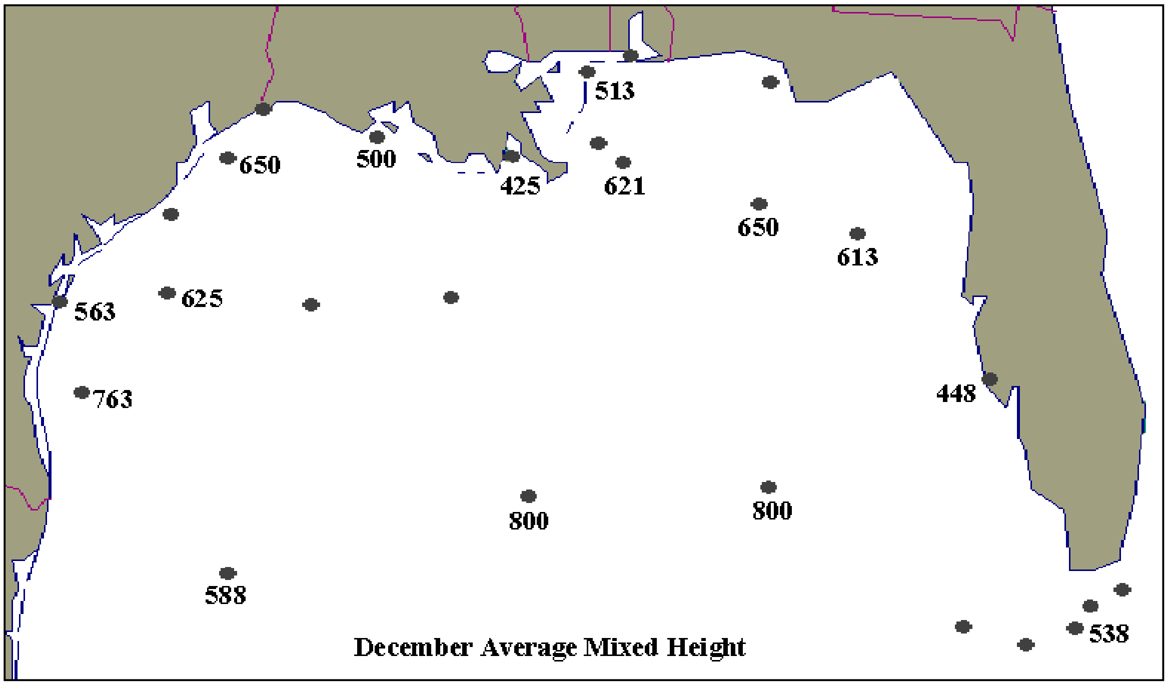

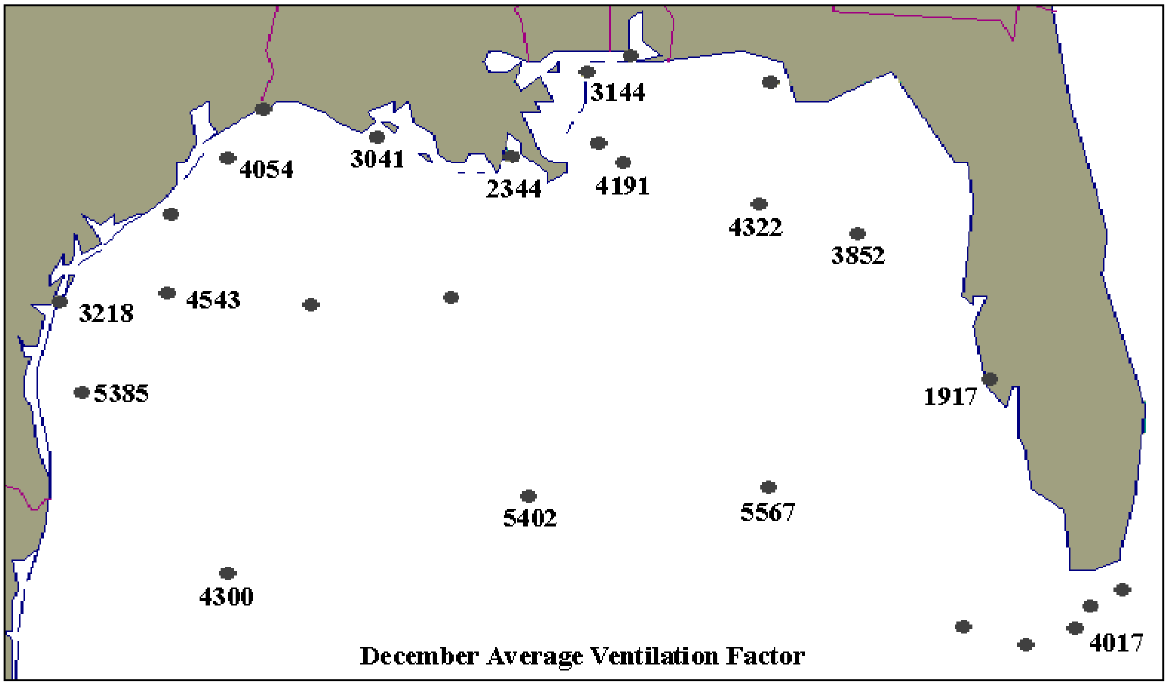

Figure 89. December monthly mean mixing height (m) and ventilation factor index.

With the deployment of our second visibility station on WAVCIS platform CSI-6, we were able to record three months of simultaneous measurements during August through October 2003. Our two stations are added to NDBC station GDIL1, 42041, and 42001 here to create a "line" extending from the coast across the shelf to the deep Gulf.

Table 5 lists the frequency of occurrence of stability classes at each station. In August, free convective conditions dominate the near shore areas (GDIL1 and CSI-3), but become less frequent offshore. This is particularly evident at CSI-6, where smaller sea-air temperature differences produce more near-neutral conditions. Free convective classes decline further at all stations in September and October.

Monthly mean mixed heights are shown in Fig. 90. Generally good agreement is found amongst all stations except CSI-6. This is found to be due to the greater observance of Class D and the relatively small mean dew point depression at this location. Station 42001 exhibits a continuous increase, again due to more numerous Class D and slightly larger dew point depression in October.

All available data from CSI-3 was combined to produce an annual distribution of stability and mixed height. From Table 6, the seasonal change of stability regime from near neutral to free convective in the summer months is clear. It should also be noted that stable conditions are observed in the winter months, but normally less than 5% of the time. Nevertheless, extremely low mixed heights can occur.

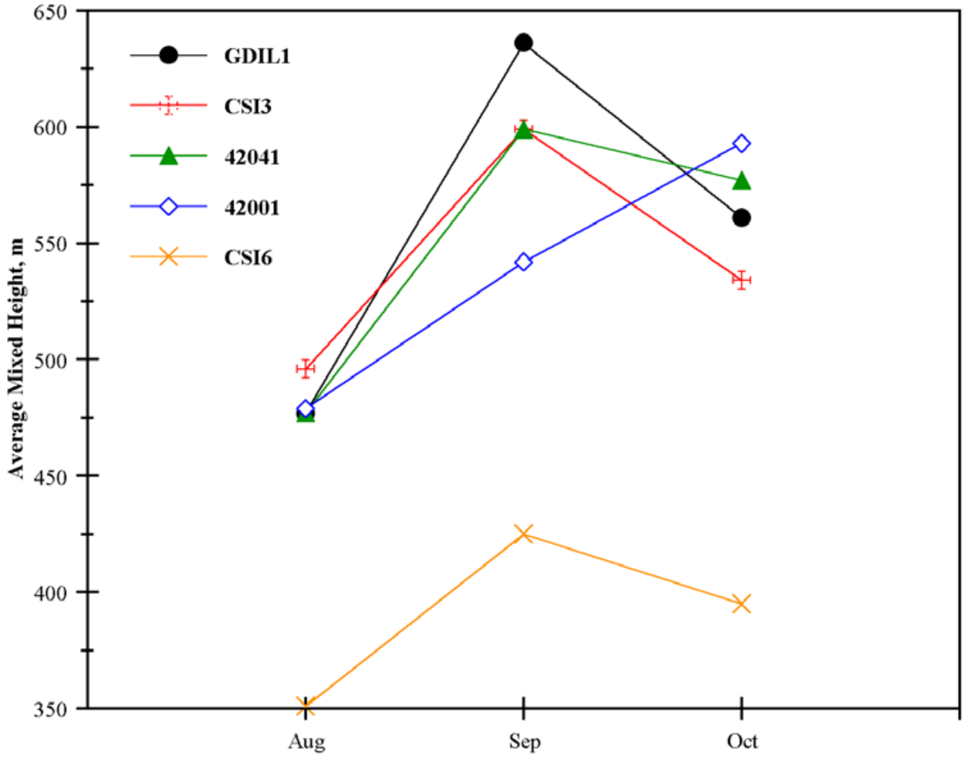

Figure 90. August to October 2003 computed mean mixed heights from the Louisiana coast to deep Gulf.

Table 5.
Frequency of occurrence (%) of stability classes, August to October 2003

Month	Category	GDIL1	CSI-3	CSI-6	42041	42001
August	<	23.7	16.4	6.9	22.2	19.8
	B	16.7	16.6	7.6	13.5	14.9
	C	30.2	31.9	15.8	20.6	22.6
	D	29.3	34.3	66.3	43.7	42.6
	E	0.1	0.1	1.1	0	0
	F	0	0.1	0.8	0	0
	>	0	0.5	1.5	0	0.1
September	<	11.0	19.0	5.6	8.6	11.1
	B	11.3	13.8	5.9	7.8	6.5
	C	20.6	28.8	14.3	13.4	15.6
	D	56.9	38.3	73.5	70.2	66.4
	E	0.3	0	0.2	0	0
	F	0	0.1	0.2	0	0
	>	0	0	0.4	0	0.4
October	<	8.9	9.3	3.7	5.9	4.9
	B	6.1	11.8	8.1	4.2	5.5
	C	21.6	27.4	18.2	20.8	16.8
	D	61.6	50.5	68.2	68.9	72.8
	E	1.2	0.3	0.9	0	0
	F	0.3	0	0.4	0	0
	>	0.3	0.7	0.6	0.1	0

Table 6.
Monthly frequency of occurrence (%) of stability class at CSI-3

Month	<	B	C	D	E	F	>
JAN	6.0	7.3	20.9	59.1	4.6	1.4	0.6
FEB	9.4	6.7	18.4	62.4	2.1	0.4	0.5
MAR	5.1	5.0	14.8	69.5	2.0	0.9	2.6
APR	5.6	5.6	21.0	66.8	0.2	0.1	0.5
MAY	6.6	7.9	26.1	59.3	0	0	0
JUN	9.5	11.6	31.4	47.3	0.1	0	0.1
JUL	16.5	15.0	36.6	31.6	0.1	0	0.1
AUG	15.8	17.2	30.7	35.8	0.1	0	0.3
SEP	13.4	9.9	23.3	52.7	0.3	0.1	0.2
OCT	9.7	11.7	27.0	50.6	0.1	0	0.3
NOV	6.8	7.4	18.3	64.7	0.8	0.7	1.3
DEC	8.1	8.3	19.4	63.0	0.1	0.4	0.5

Records from NDBC GDIL1, 42041, and 42001 are again employed to compare with CSI-3 mean annual mixed heights. Results are listed in Table 7 and depicted in Fig. 91. Mean annual mixed height at CSI-3 is 445 m with a standard deviation of 81 m. As anticipated, the near-shore stations exhibit the highest heights in summer months and lowest in winter, while the pattern for the deeper water stations is opposite.

Table 7.
Annual variation of average computed mixed height extending from shoreline to deep Gulf during the approximate period of November 2001 through October 2003.

Month	GDIL1	CSI-3	42041	42001
January	550	426	606	666
February	316	435	448	556
March	340	340	342	459
April	456	434	488	498
May	532	479	480	417
June	494	504	448	488
July	459	485	462	508
August	494	507	484	509
September	525	517	523	534
October	489	490	517	565
November	485	483	624	712
December	421	424	637	710

GDIL1	March 2002 - December 2003
42041	May 2002 - December 2003
42001	January 2002 - December 2003

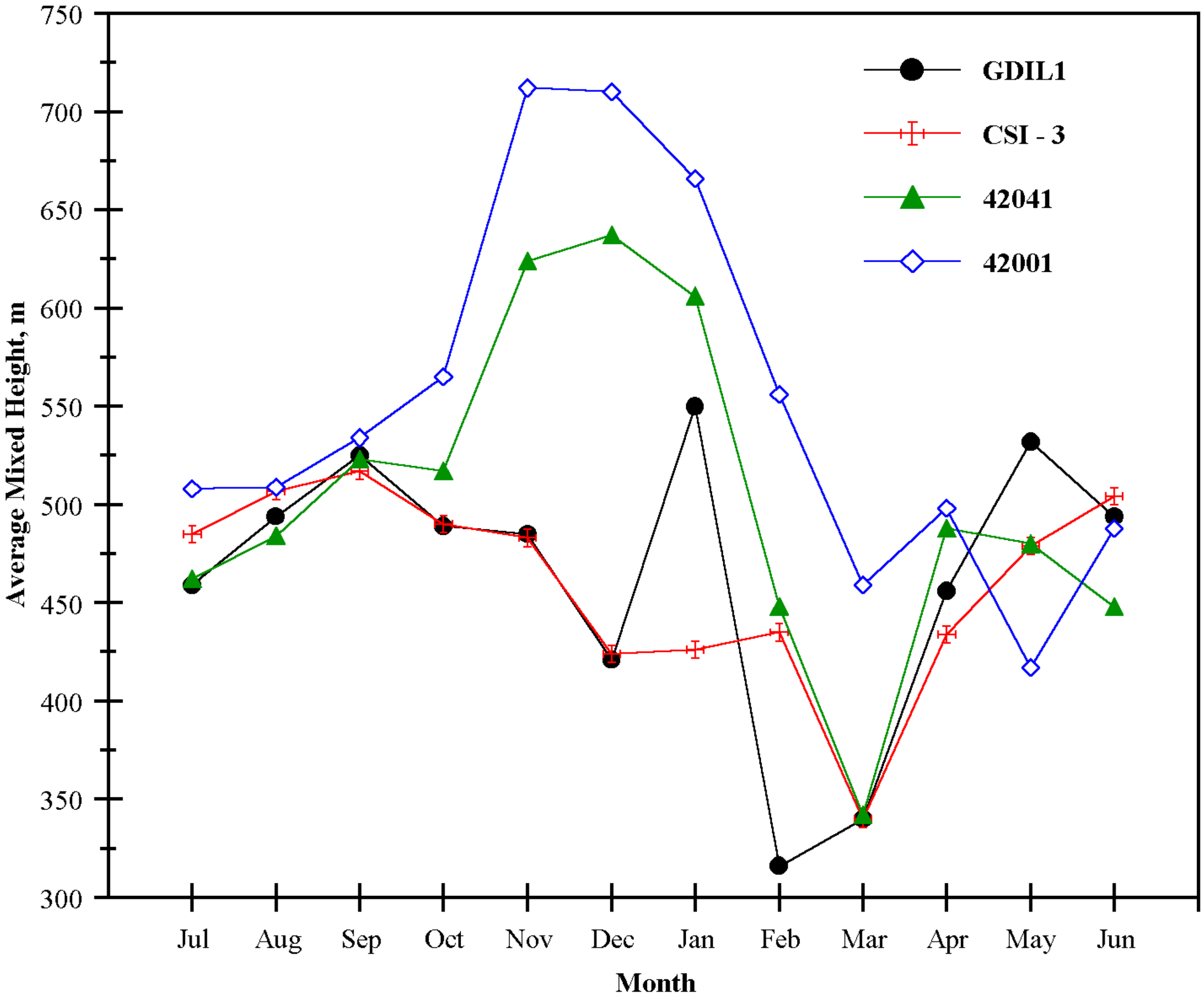

Figure 91. Annual distribution of computed mixed heights from the Louisiana coast to deep Gulf.

V. SOME CHARACTERISTICS OF FOG AND HAZE ALONG THE LOUISIANA COAST

Automated visibility sensors such as the ones deployed at CSI-3 and CSI-6 provide invaluable point measurements of visual range, however they cannot describe the conditions which may be causing a reduction of that range. To address this problem, NOAA (1998) has developed an algorithm for its Automated Surface Observing System (ASOS) stations which relies on temperature, dew point, and present weather in addition to visibility to differentiate prevailing conditions.

When the surface visibility drops below 7 statute miles, the algorithm obtains the current dew point depression to distinguish between fog, mist, or haze. If the dew point depression is less than or equal to 4°F (about 2°C), then mist is reported if the visibility is between 5/8 and 7 miles; if less than 5/8 mile, fog is reported. If these conditions are met and precipitation is occurring, fog or mist will still be reported. If the dew point depression is greater than 4°F (about 2°C) and no precipitation is observed, then haze is reported. While other sources (such as smoke, dust, or blowing sand) may certainly be the cause of reduced surface visibility, only fog, mist, or haze are indicated by the automated system.

Fog is a visible aggregate of many minute water droplets that are suspended in the atmosphere near the earth's surface. Fog differs from cloud only in that the base is at the surface, while clouds are above the surface (Huschke, 1959). According to Hsu (1988), fog can occur along the Louisiana coast in winter months when warm, moist air flows northward over the cool shelf waters. The air gives off heat to the surface waters, which eventually reduces the temperature to the dew point and condensation occurs. Due to lesser frictional effect over water, fog can occur even if winds are relatively strong. This effect is further enhanced by drainage of cold, fresh water from the Mississippi River and bays and estuaries. Due to the potential hazards to marine operations and surface traffic, the National Weather Service offices at Lake Charles and Slidell have conducted research into Louisiana coastal fog, including a sea fog forecasting decision tree (see, e.g., Erickson (2001), and National Weather Service (2003)).

Haze, on the other hand, is a suspension in the air of extremely small dry particles or aerosols invisible to the naked eye but sufficiently numerous to give the air an opalescent appearance (Byers, 1974). Growing concerns about reductions in visibility at scenic and wilderness (Class I) areas caused by haze prompted the Regional Haze Rule (Federal Register, 1999), which requires monitoring in order to track progress toward the national visibility goal. The Breton National Wildlife Refuge is a Class I area located north of the Mississippi River Delta. Since the EPA defines regional haze as "...visibility impairment that is produced by a multitude of sources and activities which emit fine particles and their precursors and which are located across a broad geographic area" (Malm et al., 2000), we extend our study westward along the Louisiana coast to incorporate available NOAA stations and our instrumented platforms. The potential for haze formation in the OCS environment may be enhanced due to the contribution of both land-based and oceanic sources. Natural and anthropogenic aerosols may drift seaward from land or from numerous production platforms. Over oceans, aerosols composed of sea salts continuously originate from drops ejected into the air when air bubbles in breaking waves burst at the ocean surface. Smaller aerosols are produced when the upper part of an air bubble film bursts. When the relative humidity rises, aerosols may increase in size, forming a haze which reduces visibility by scattering light. For example, the amount of light that sea-salt particles remove from a beam by scattering increases by about a factor of three as the relative humidity increases from 60 to 80% (Wallace and Hobbs, 1977).

A simplified version of the ASOS visibility algorithm was applied to the hourly data records from stations CSI-3, CSI-6, Boothville, and GDIL1 during the measurement period of November 2001 through October 2003. For this analysis, any hourly observation of visibility less than 7 miles was designated as "reduced" and retained. The dew point depression was then applied to separate into either fog or haze; no distinction was made for mist. Furthermore, since present weather observations are typically unavailable at most stations, no effort was made to identify or remove events associated with precipitation. Our results are shown in Figs. 92 through 98. Note that the bar graphs showing both fog and haze depict the potential occurrence of these conditions based on the criteria previously described, while the bar graphs showing visibility alone represent actual hours of severely reduced visibility recorded, regardless of cause. At each station, the potential for fog formation is most frequently observed during the winter season months of January through March. Reduced visibility due to fog can be expected from about 20 to 40% of the time (or about 6 to 12 entire days); with slightly higher frequency at the coastal stations than offshore. Surface visibility can become very restricted, being equal to or less than one mile about 7 - 10% of the time (2 - 3 entire days). Fog conditions can occur in every month.

Impaired visibility attributed to haze is also observed year round, however the frequency of occurrence is much less, generally less that 5% (about 1.5 day) per month. Peaks occur in the winter months and late summer (August - September), and more often along the coast. Reductions in surface visibility associated with haze are smaller than those that can result from fog conditions.

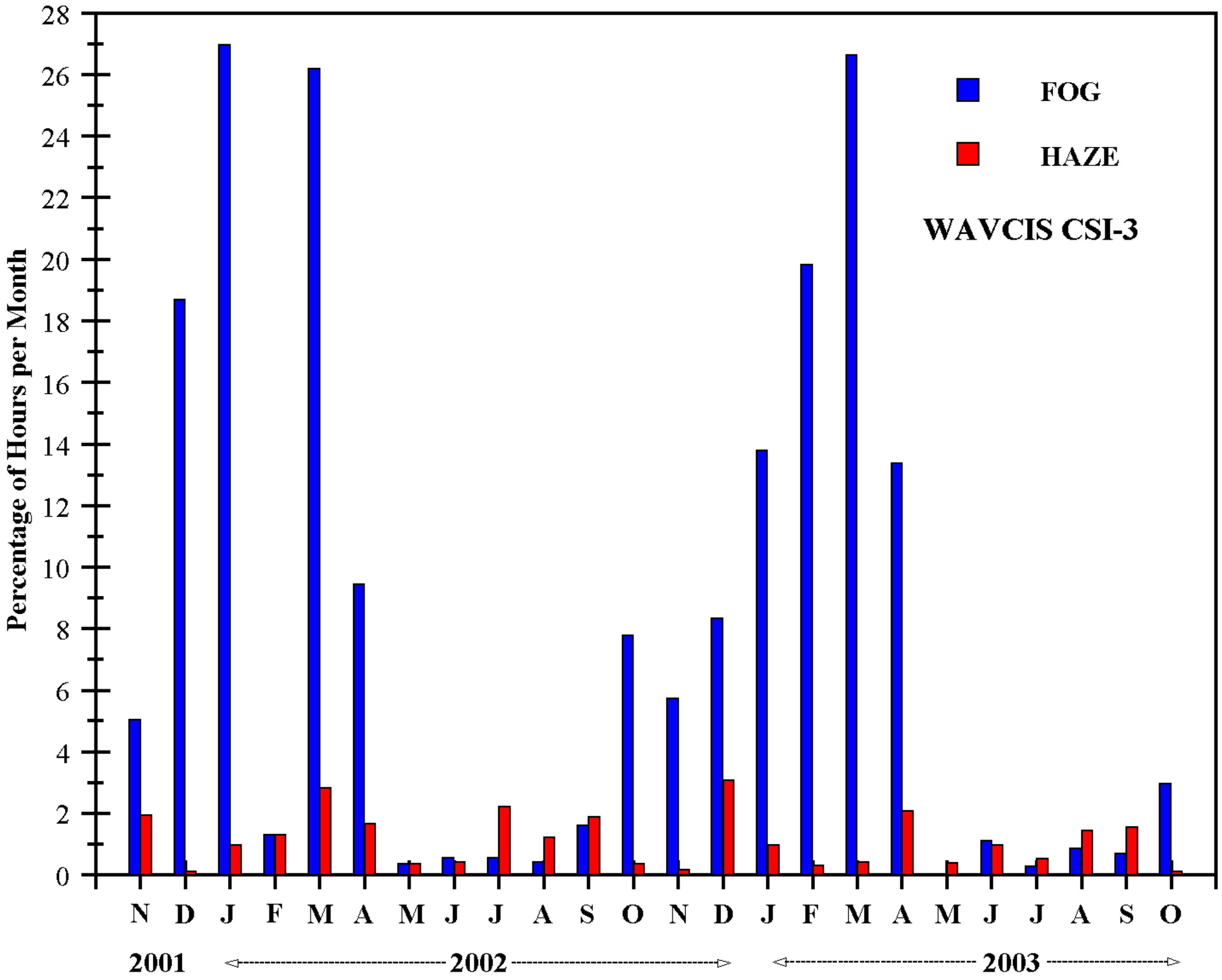

Figure 92. Frequency of occurrence of fog and haze as defined by the ASOS at CSI-3. Note that records for May and October 2002 are less than 75% complete. Fog can occur in each month.

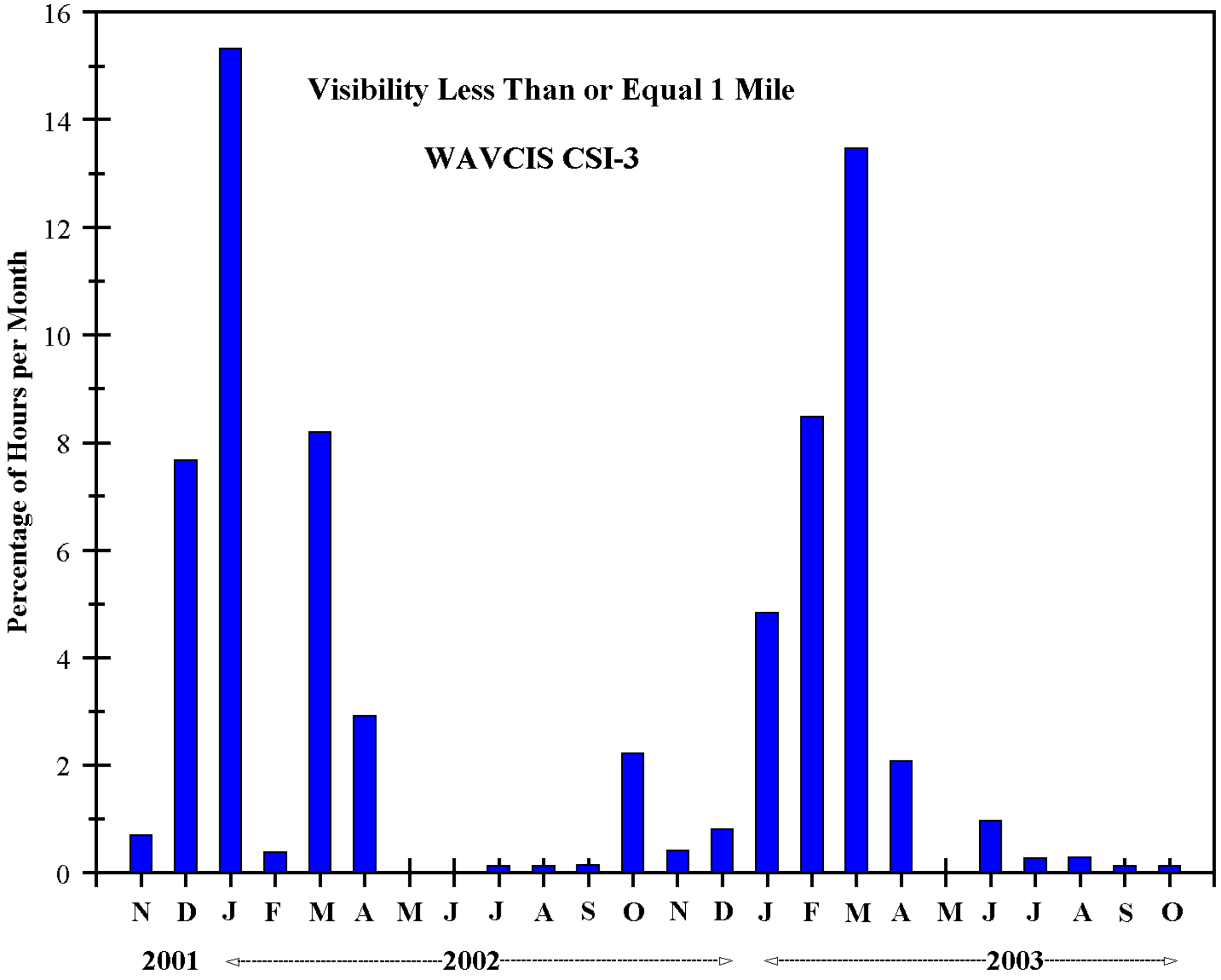

Figure 93. Frequency of occurrence of restricted visibility at CSI-3.

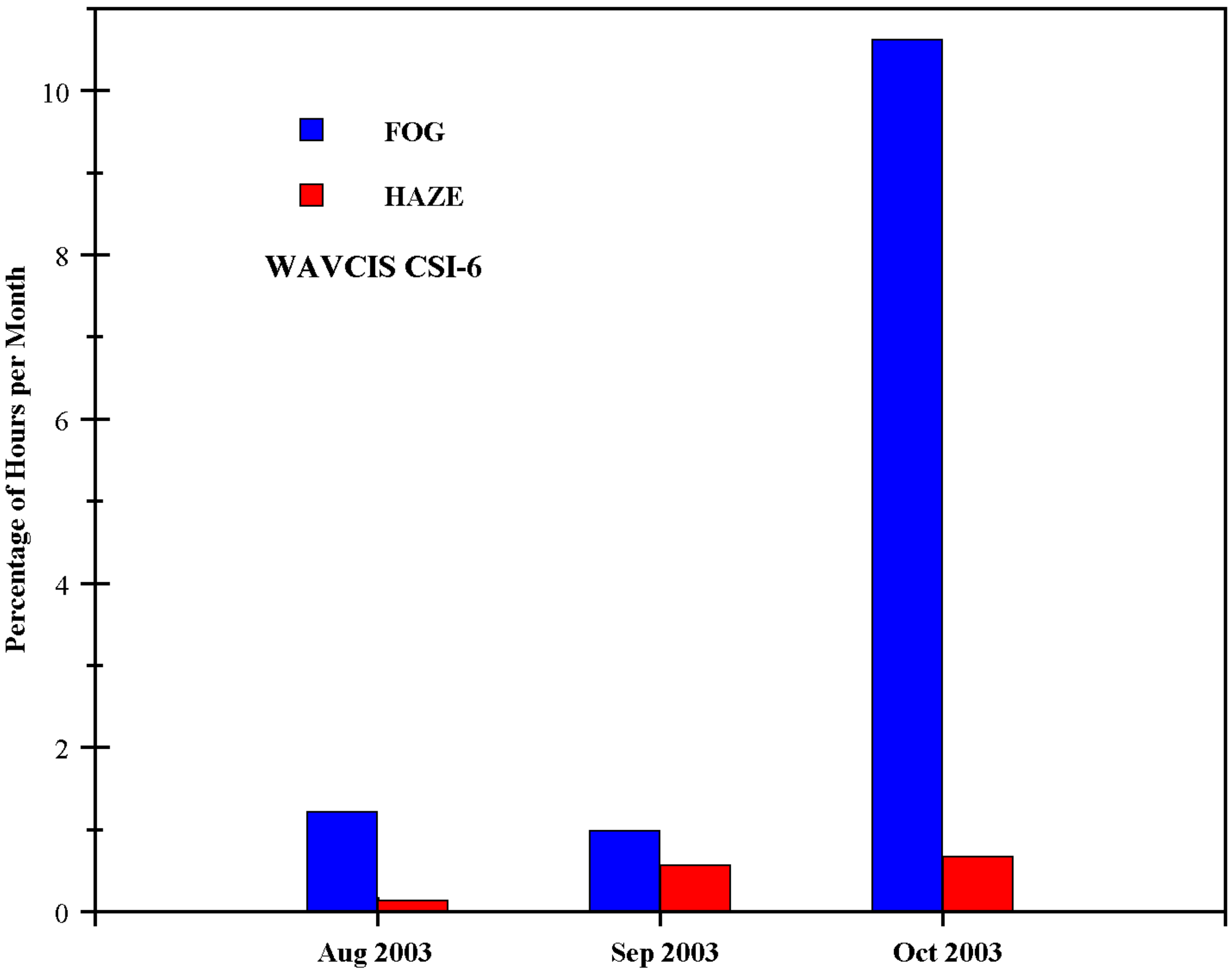

Figure 94. Frequency of occurrence of fog and haze as defined by the ASOS at station CSI-6.

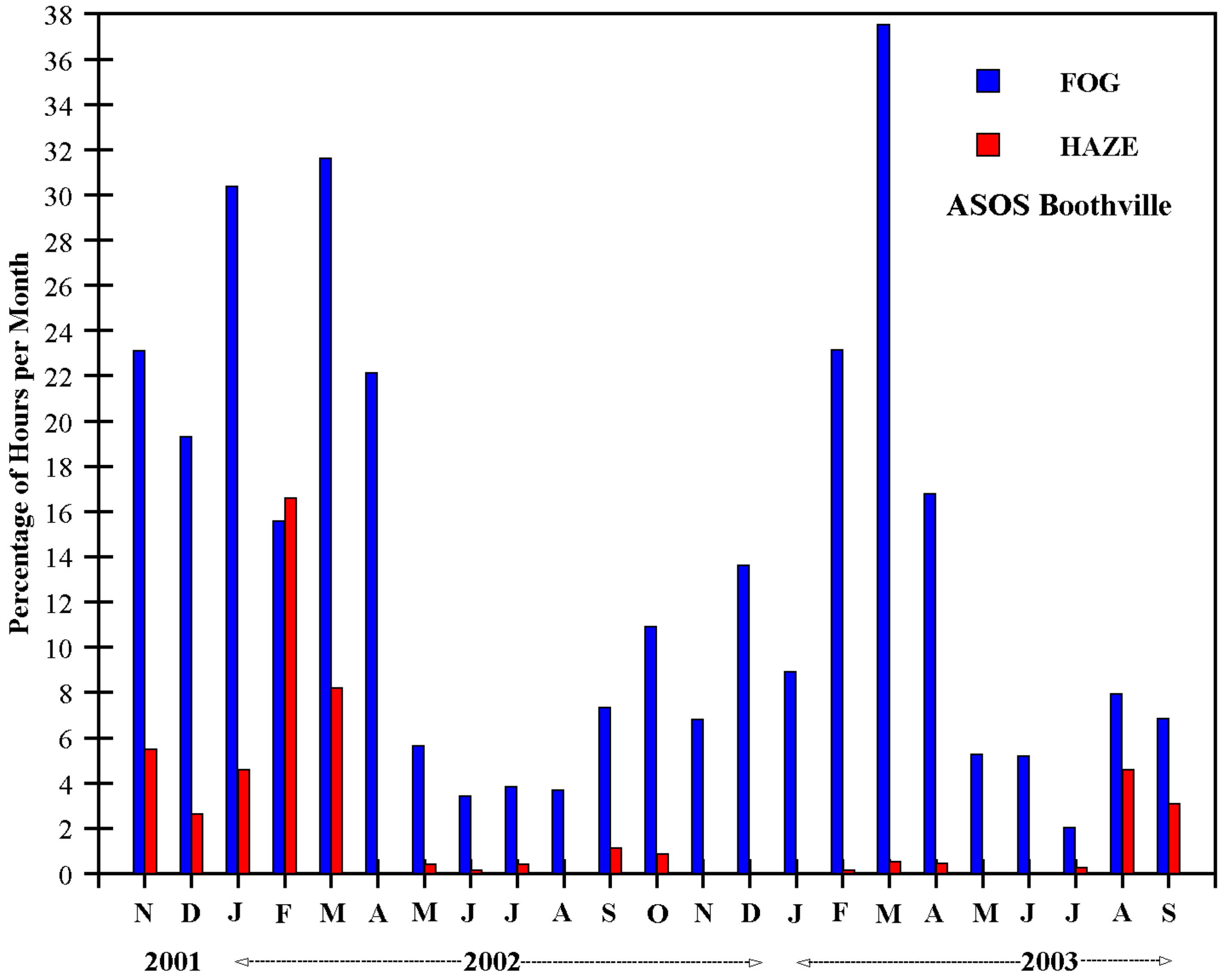

Figure 95. Frequency of occurrence of fog and haze as defined by the ASOS at the Boothville station.

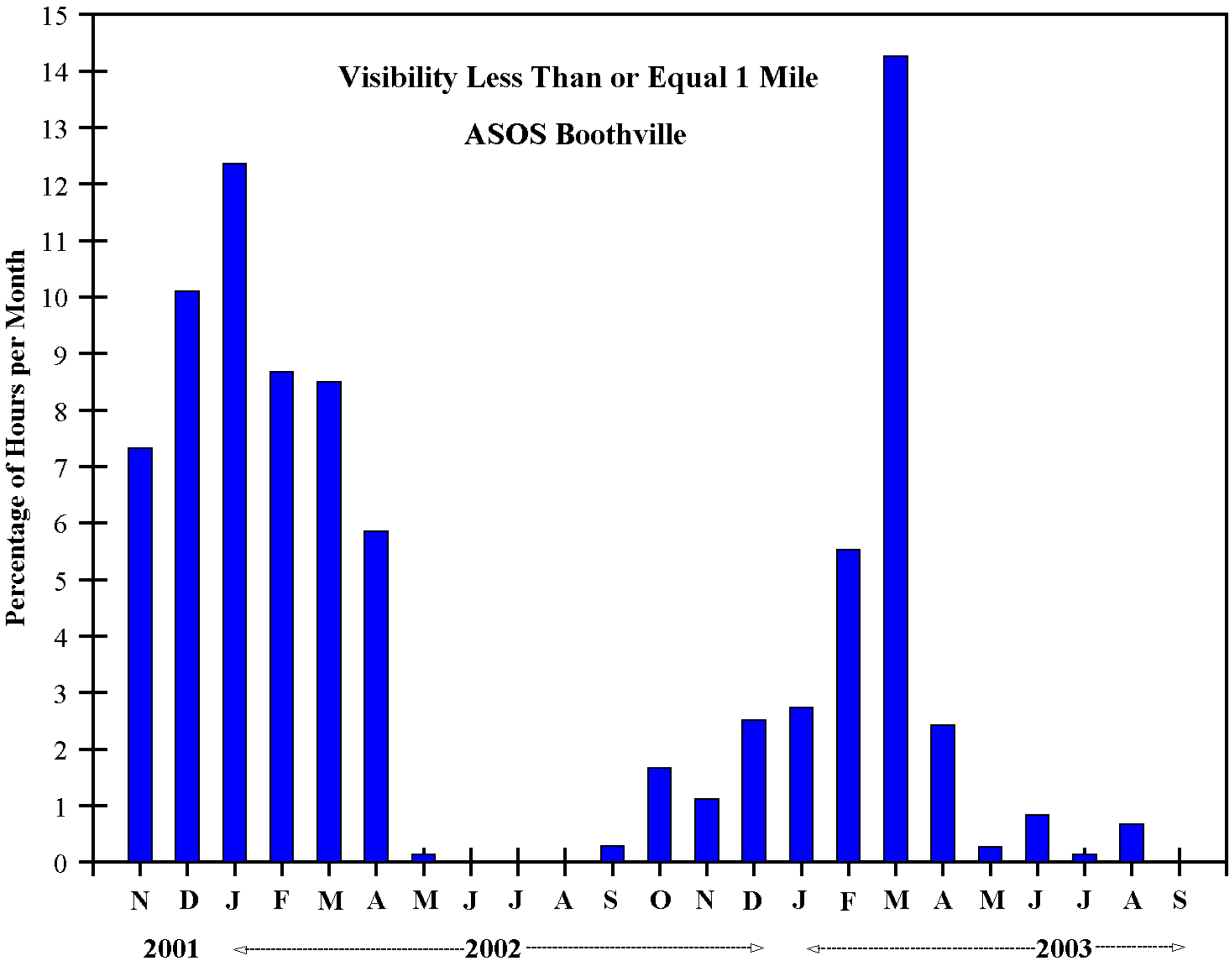

Figure 96. Frequency of occurrence of restricted visibility at the Boothville station.

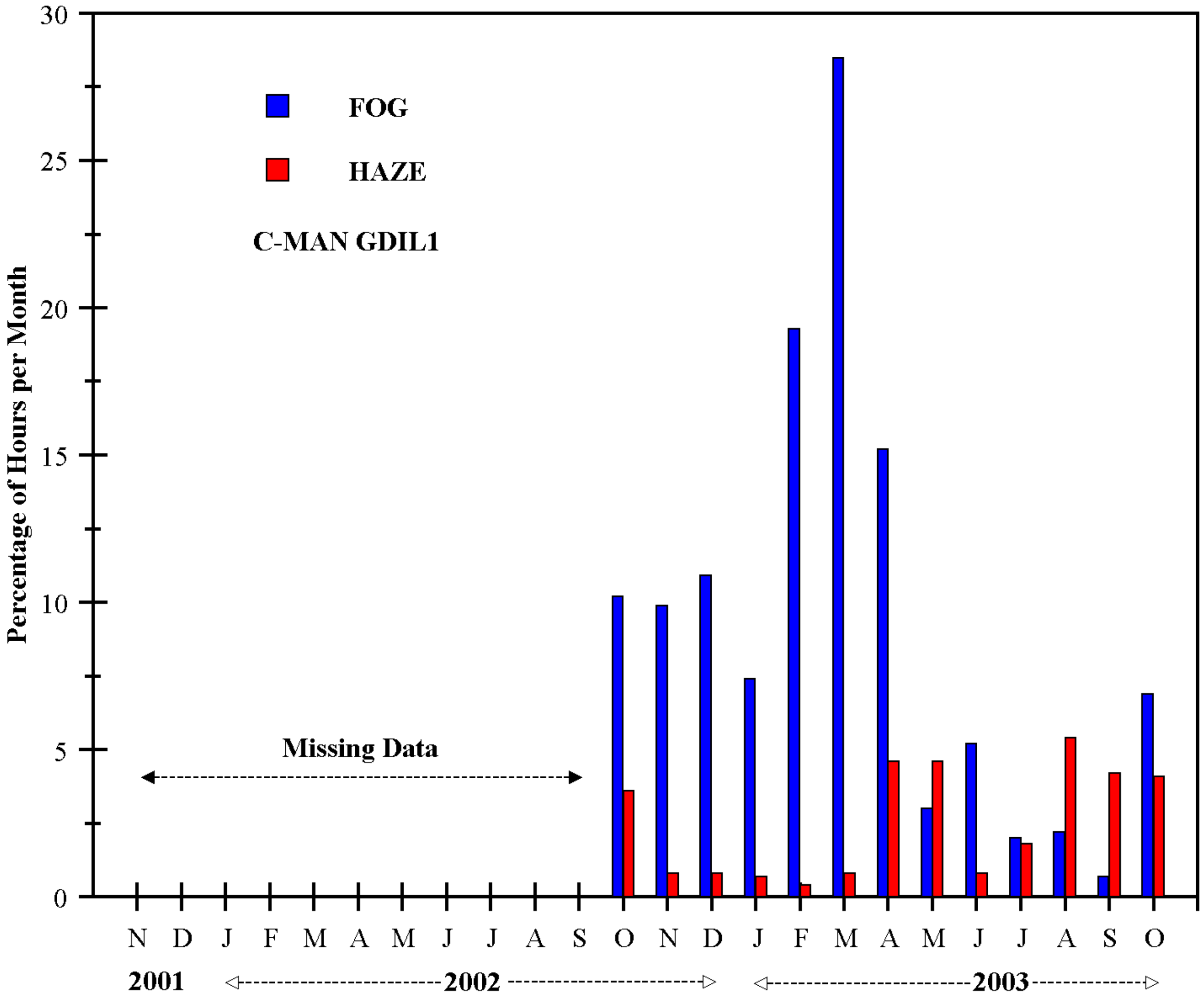

Figure 97. Frequency of occurrence of fog and haze as defined by the ASOS at NDBC GDIL1.

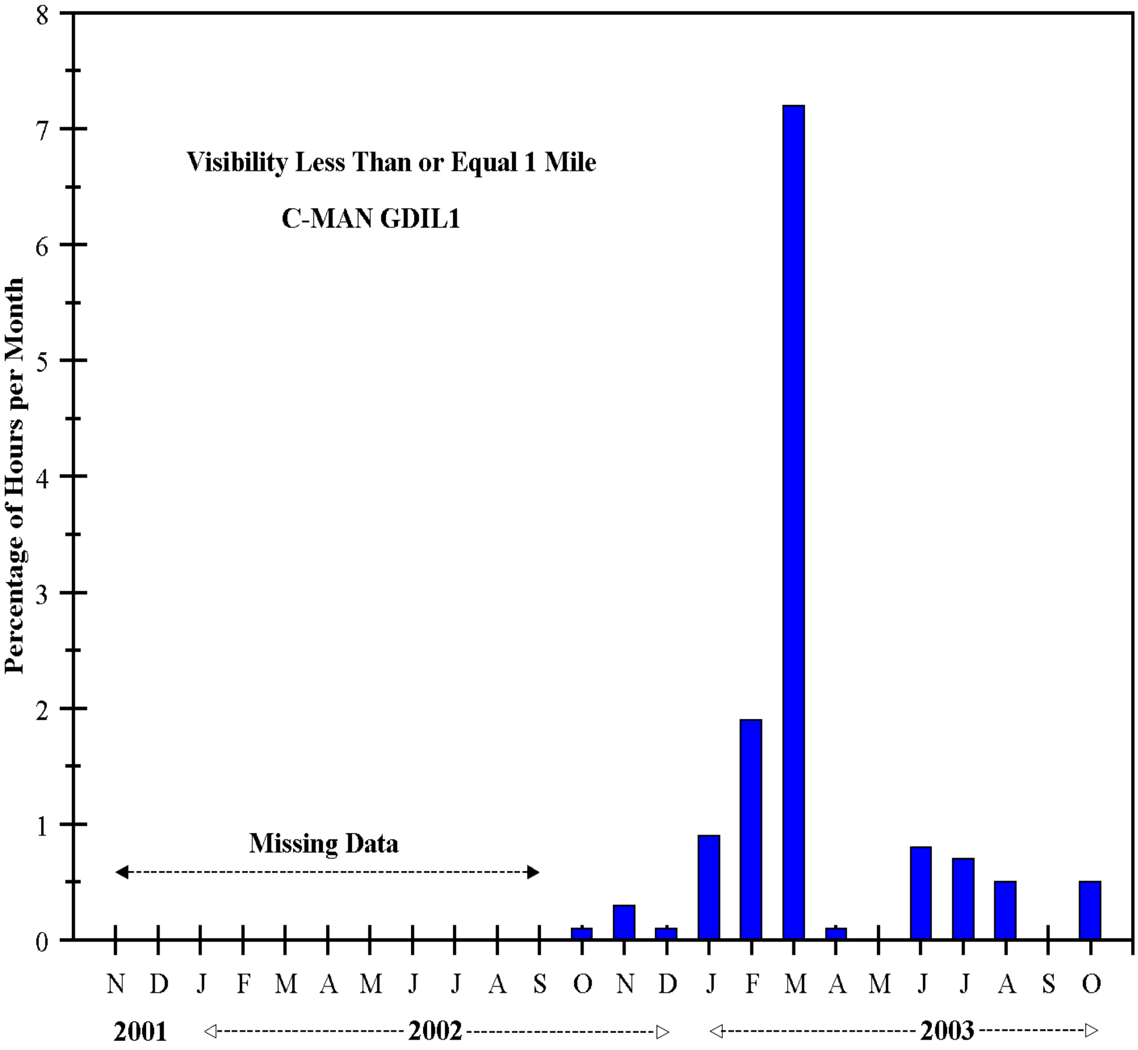

Figure 98. Frequency of occurrence of restricted visibility at NDBC GDIL1.

Monthly wind and visibility 'roses' are shown for CSI-3 and Boothville in Figs. 99 through 110. Reduced visibility at both stations is most often associated with wind flow from the east; southeast and east during January through May, and northeast to southeast during September through December. The summer months of June through August have a more even distribution with a slight westerly peak, but the frequencies are less than about 2%. Since we have shown that reduced visibility along the Louisiana coast is almost entirely caused by fog conditions, the dominance of east-southeast wind flow supports Hsu's (1988) scenario as described previously. Note that the analysis of Boothville data only considered hourly records in which both visibility and wind direction were reported; calm (no wind) reports were not included.

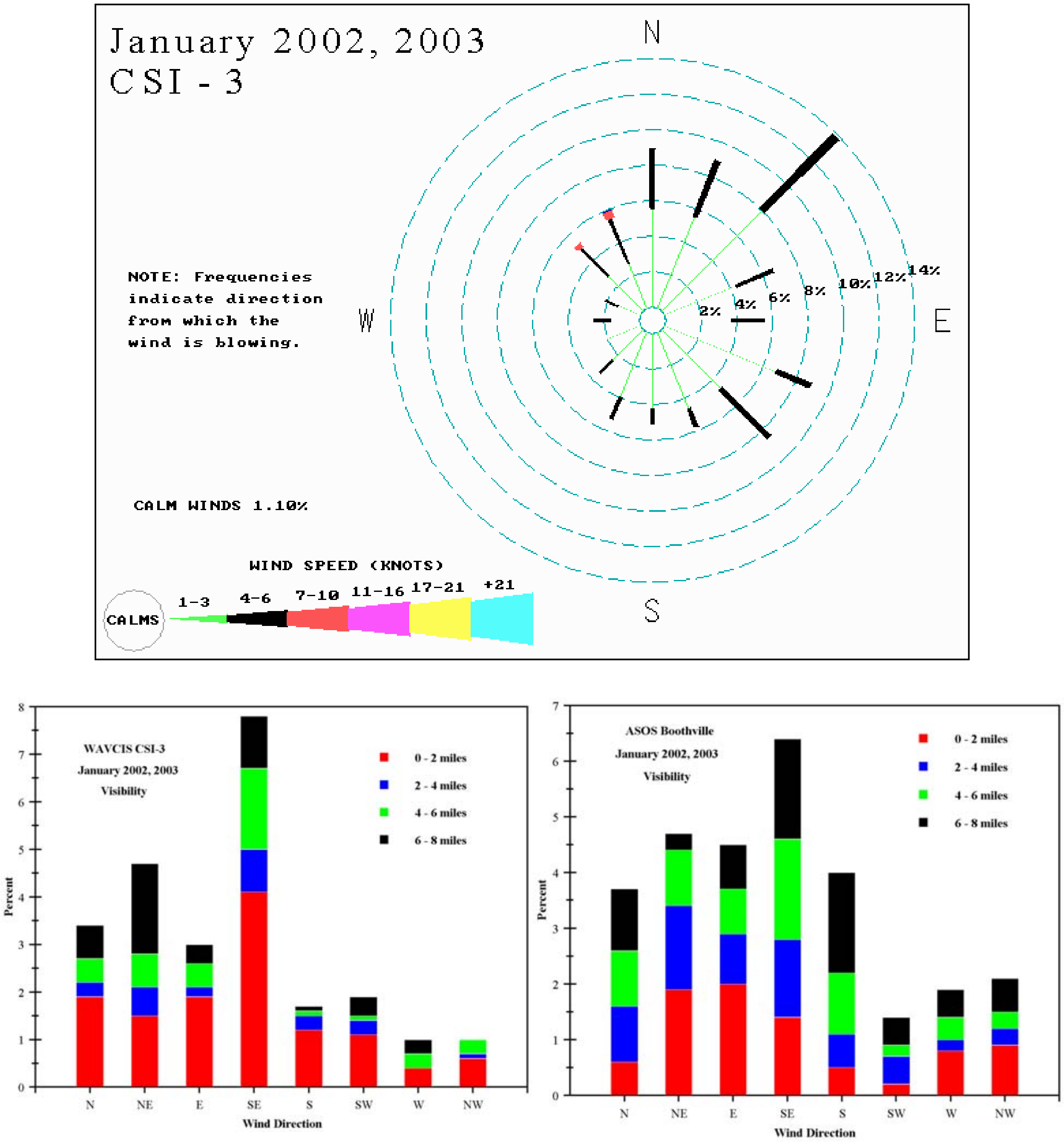

Figure 99. January wind rose for CSI-3 (top), and visibility 'roses' for the CSI-3 and Boothville stations (bottom).

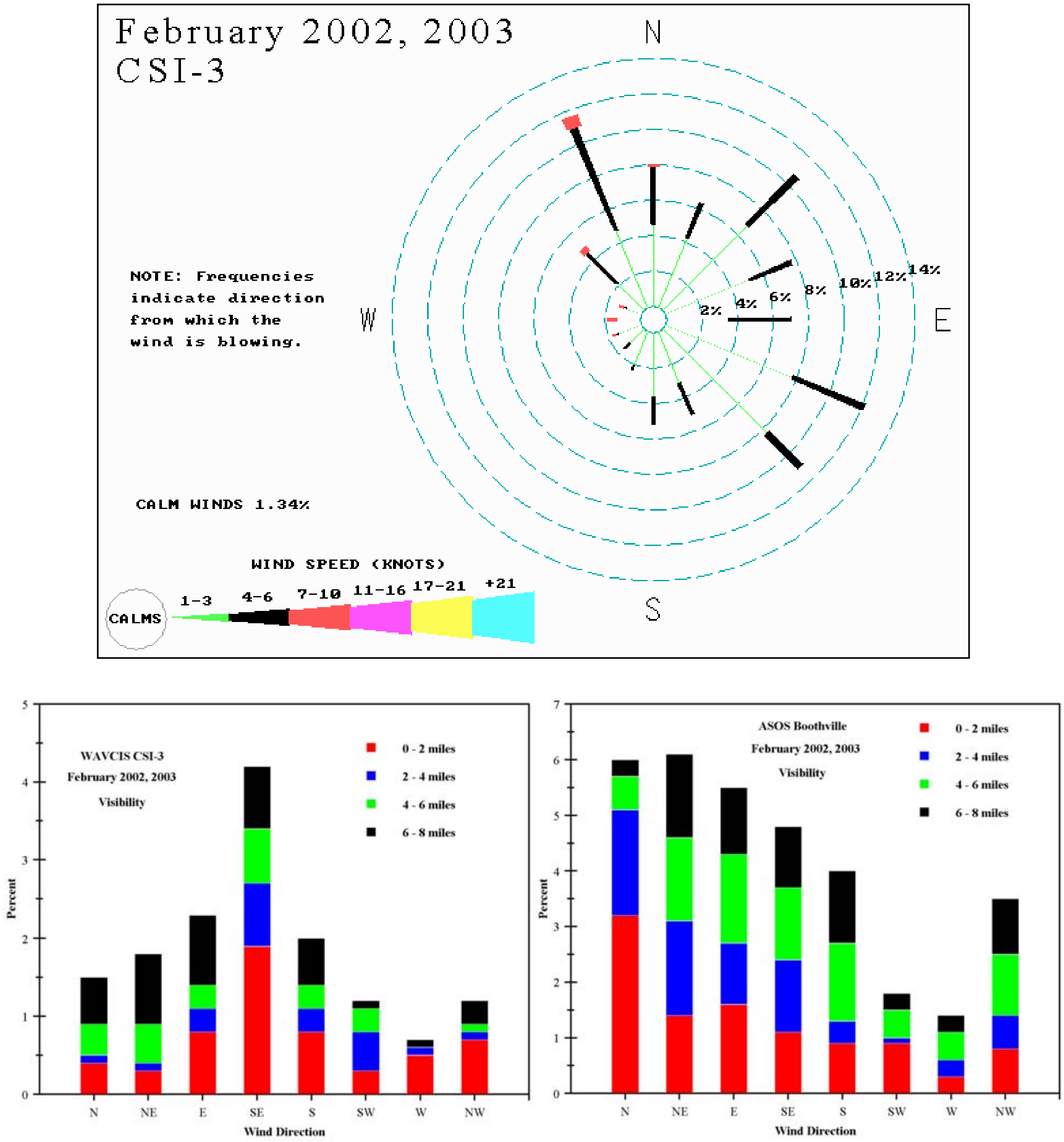

Figure 100. February wind rose for CSI-3 (top), and visibility 'roses' for the CSI-3 and Boothville stations (bottom).

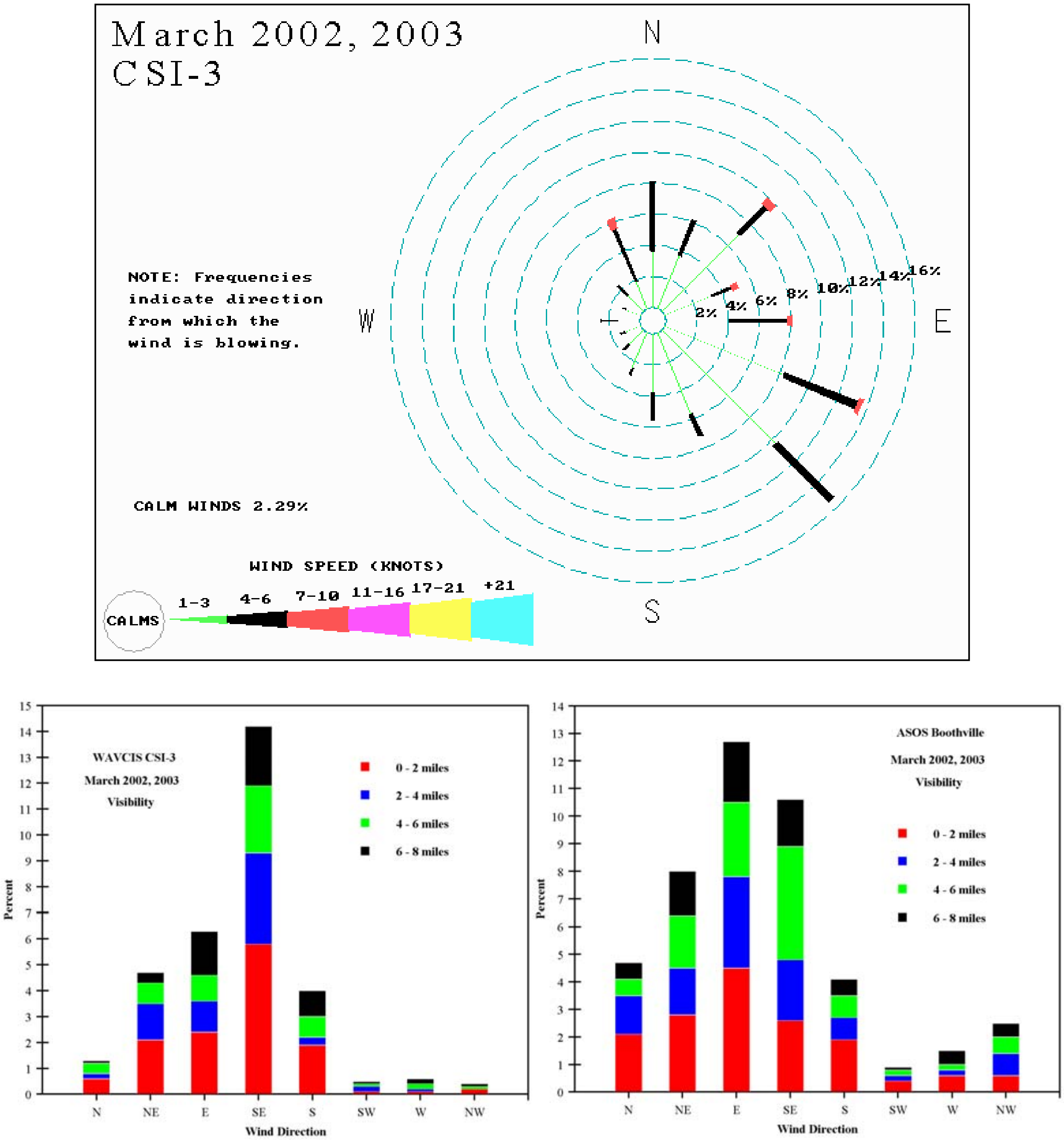

Figure 101. March wind rose for CSI-3 (top), and visibility 'roses' for the CSI-3 and Boothville stations (bottom).

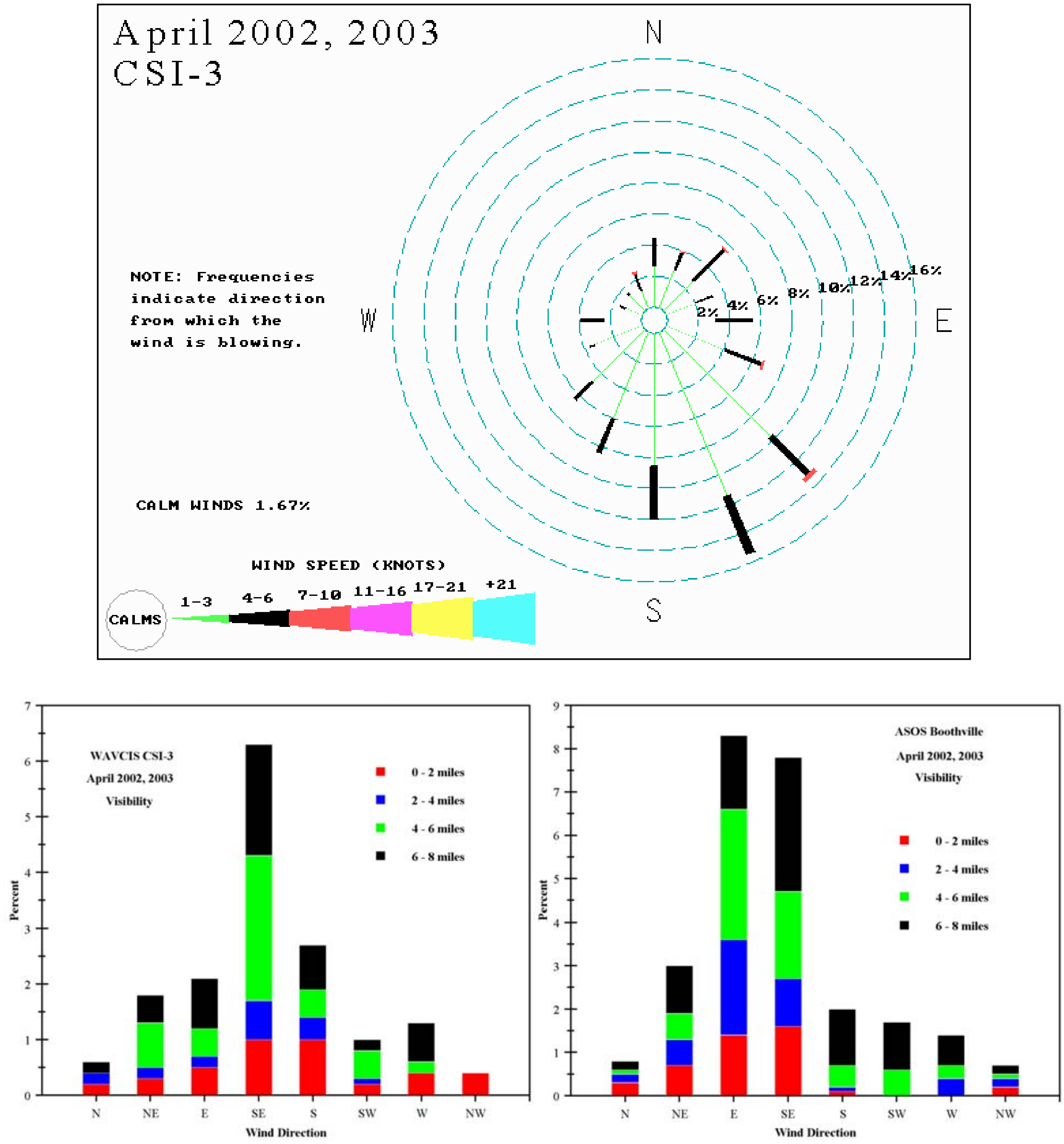

Figure 102. April wind rose for CSI-3 (top), and visibility 'roses' for the CSI-3 and Boothville stations (bottom).

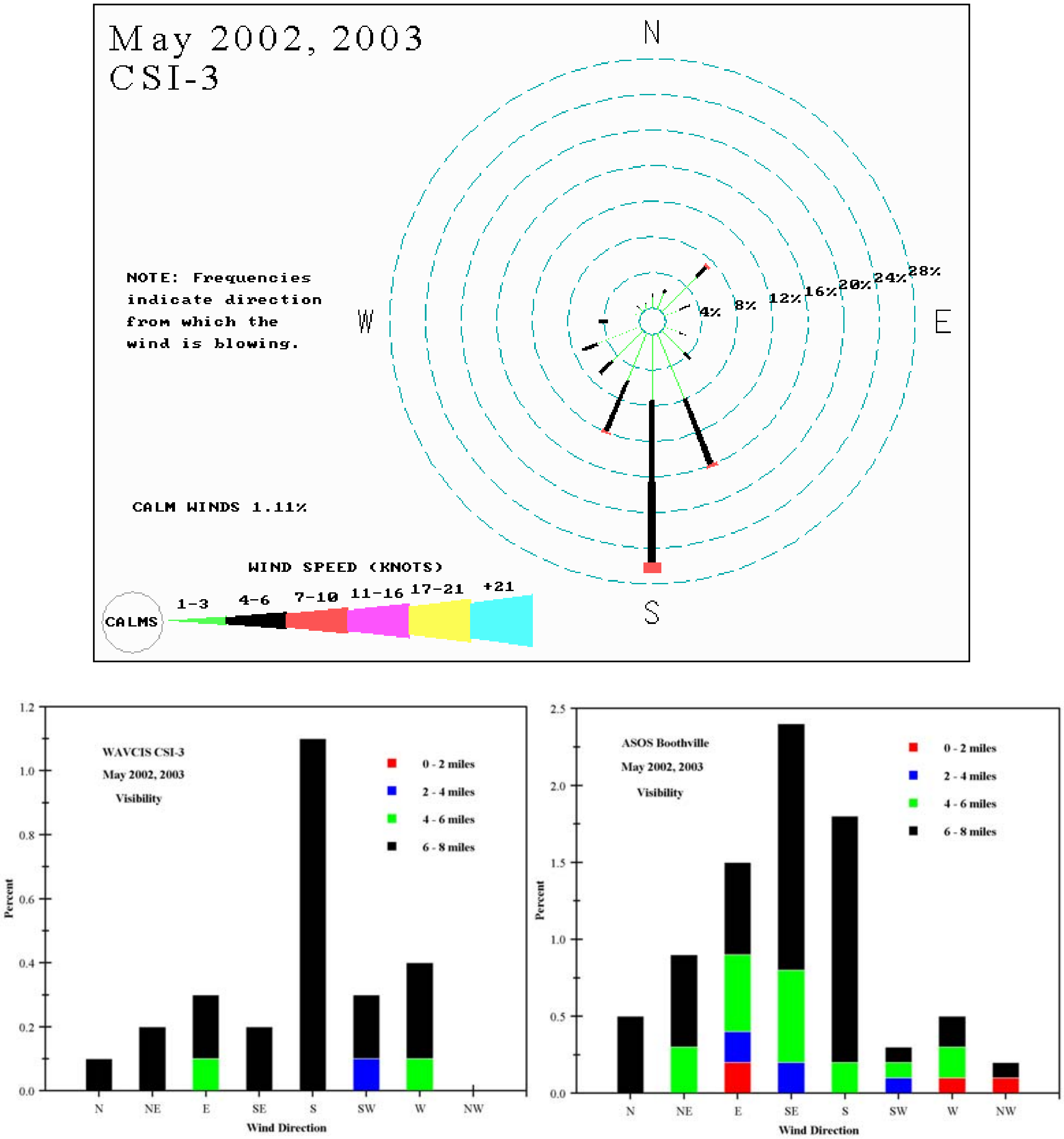

Figure 103. May wind rose for CSI-3 (top), and visibility 'roses' for the CSI-3 and Boothville stations (bottom).

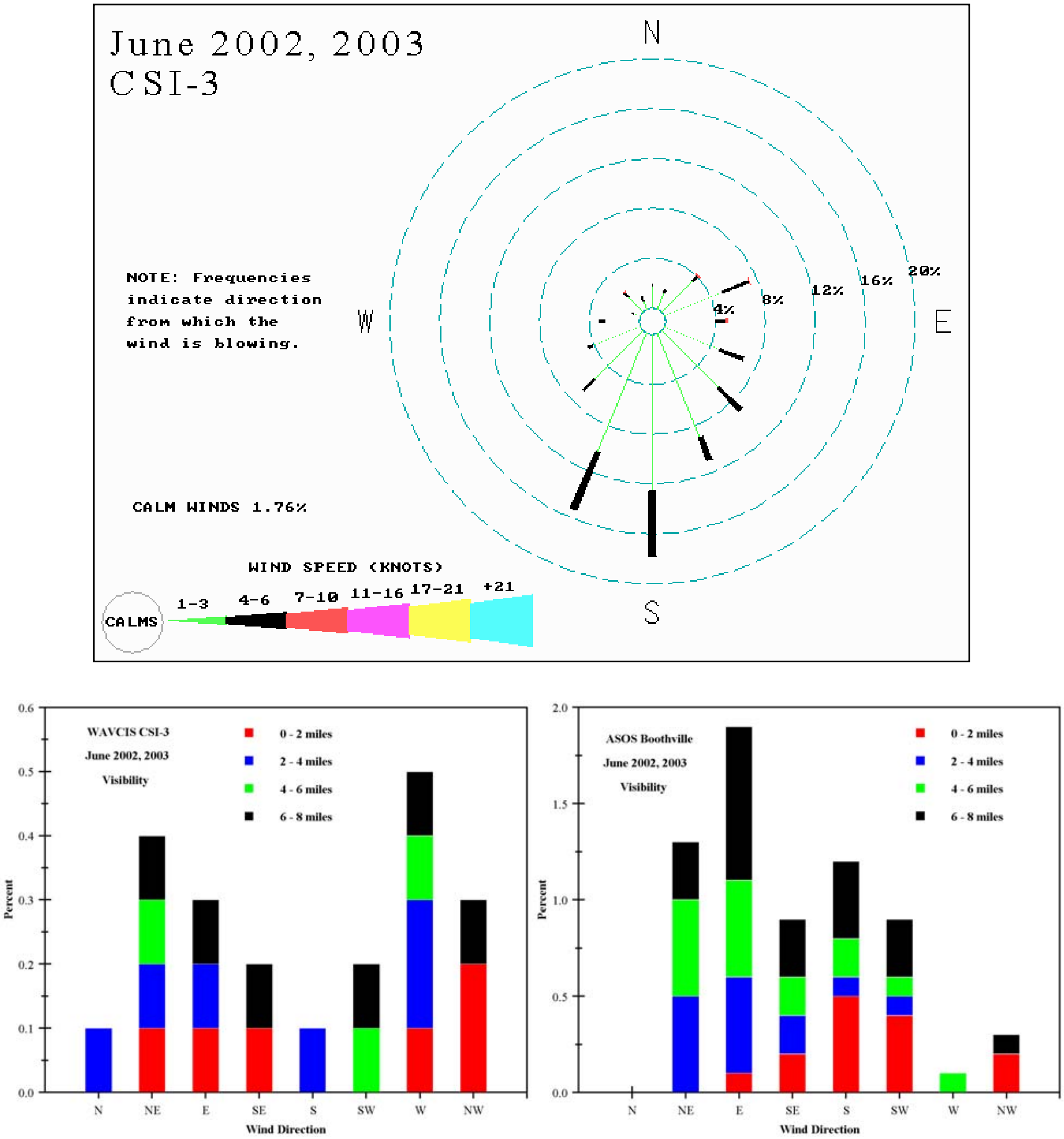

Figure 104. June wind rose for CSI-3 (top), and visibility 'roses' for the CSI-3 and Boothville stations (bottom).

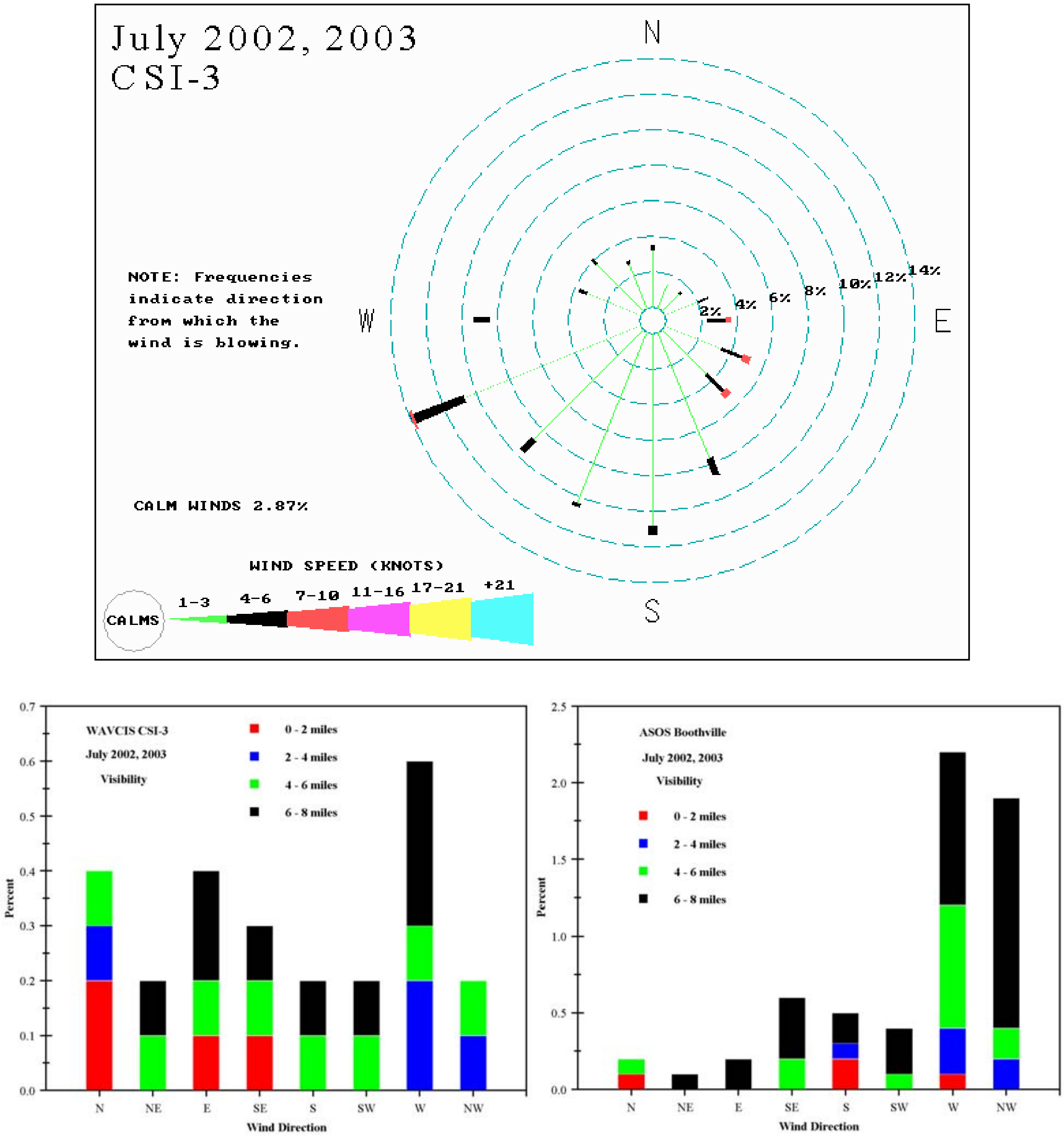

Figure 105. July wind rose for CSI-3 (top), and visibility 'roses' for the CSI-3 and Boothville stations.

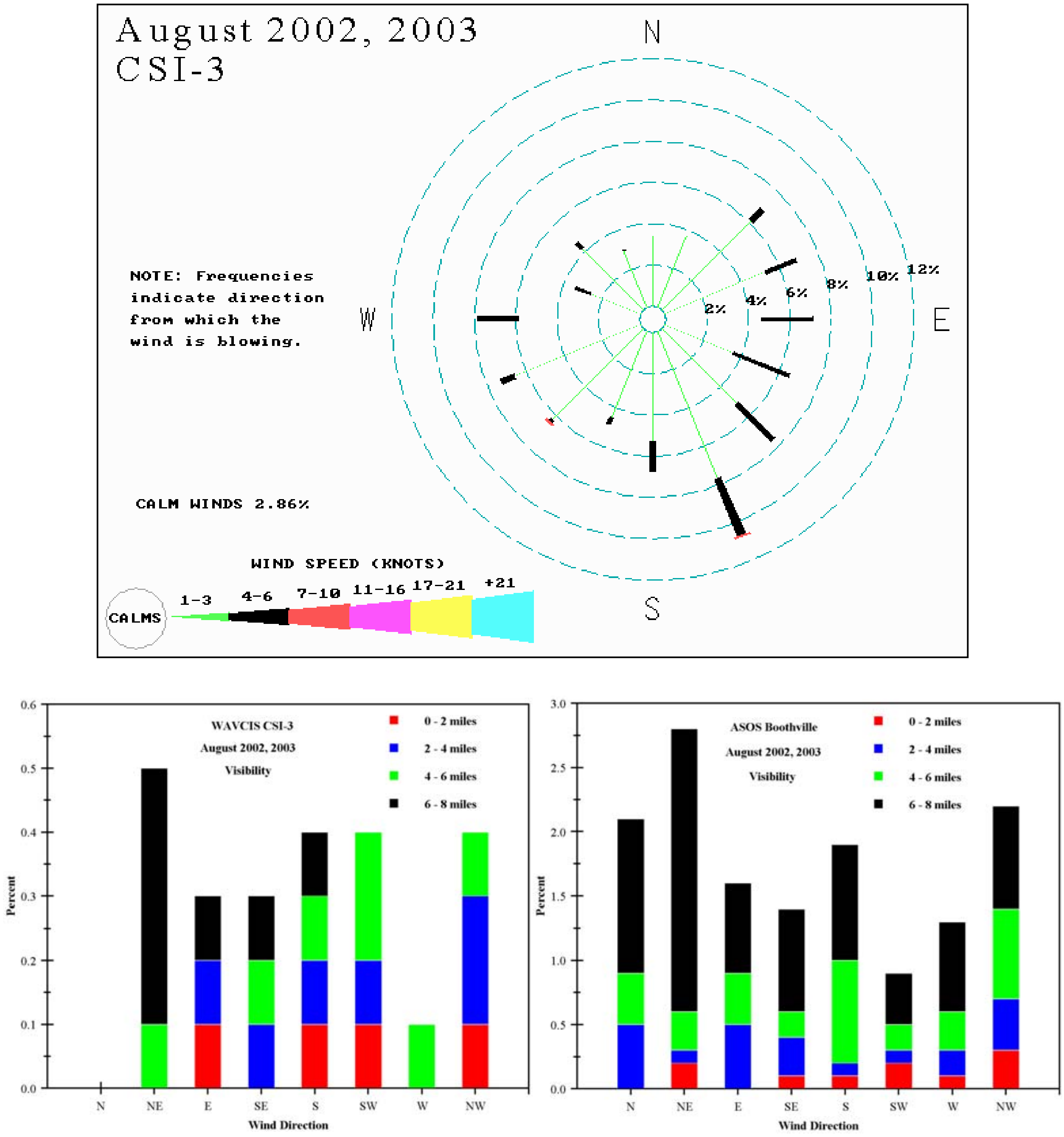

Figure 106. August wind rose for CSI-3 (top), and visibility 'roses' for the CSI-3 and Boothville stations (bottom).

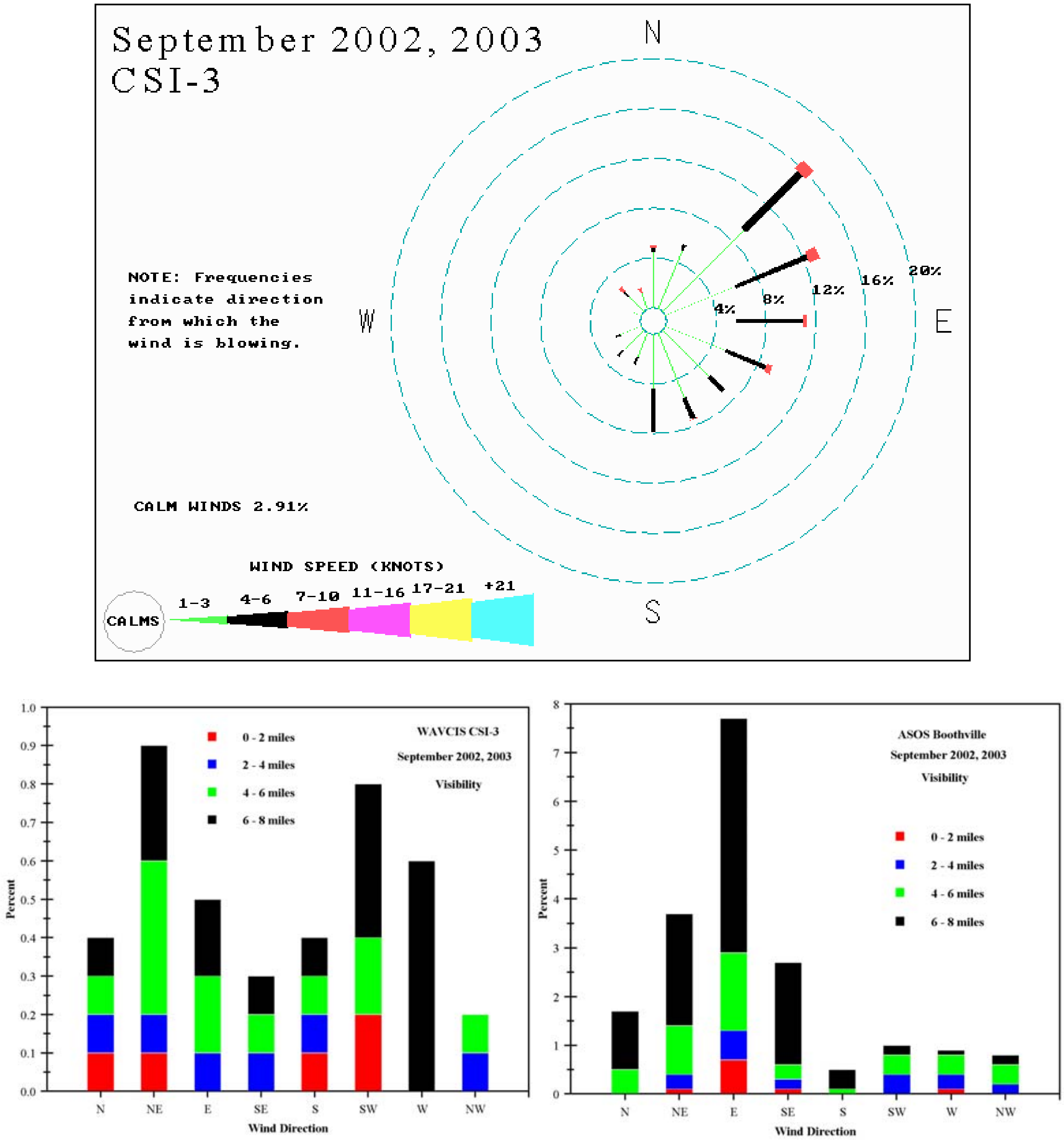

Figure 107. September wind rose for CSI-3 (top), and visibility 'roses' for the CSI-3 and Boothville stations (bottom).

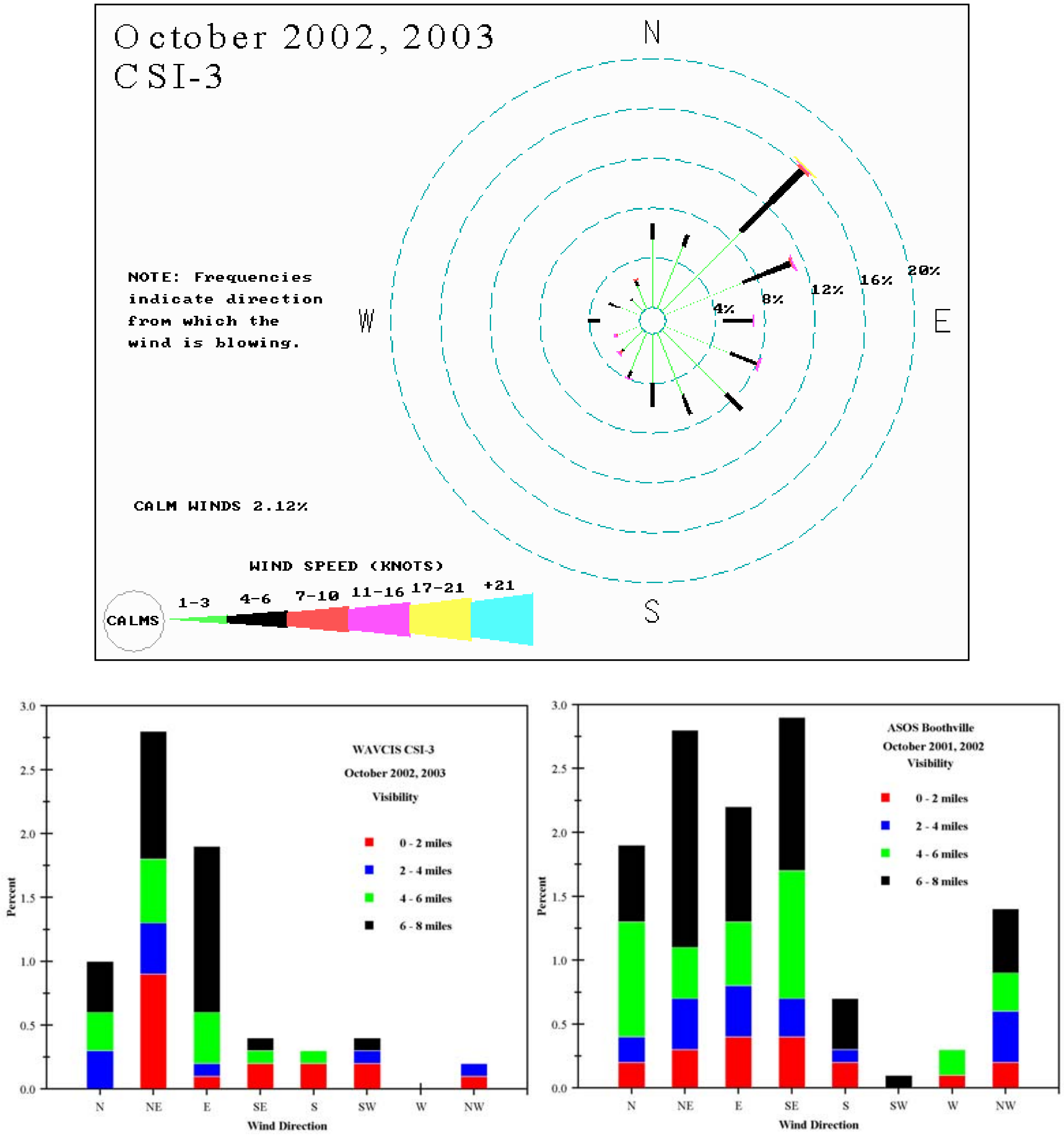

Figure 108. October wind rose for CSI-3 (top), and visibility 'roses' for the CSI-3 and Boothville station.

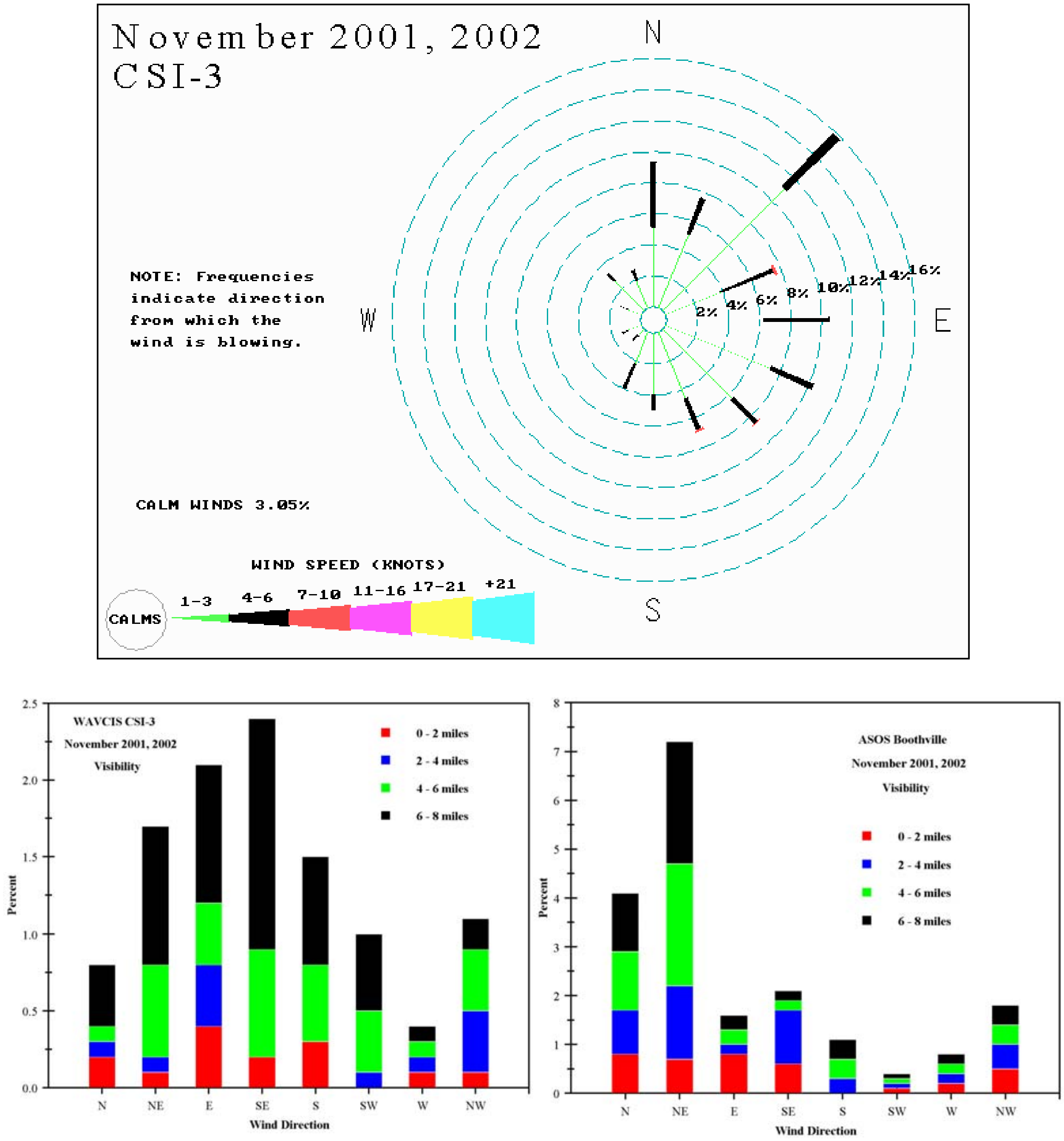

Figure 109. November wind rose for CSI-3, and visibility 'roses' for the CSI-3 and Boothville stations (bottom).

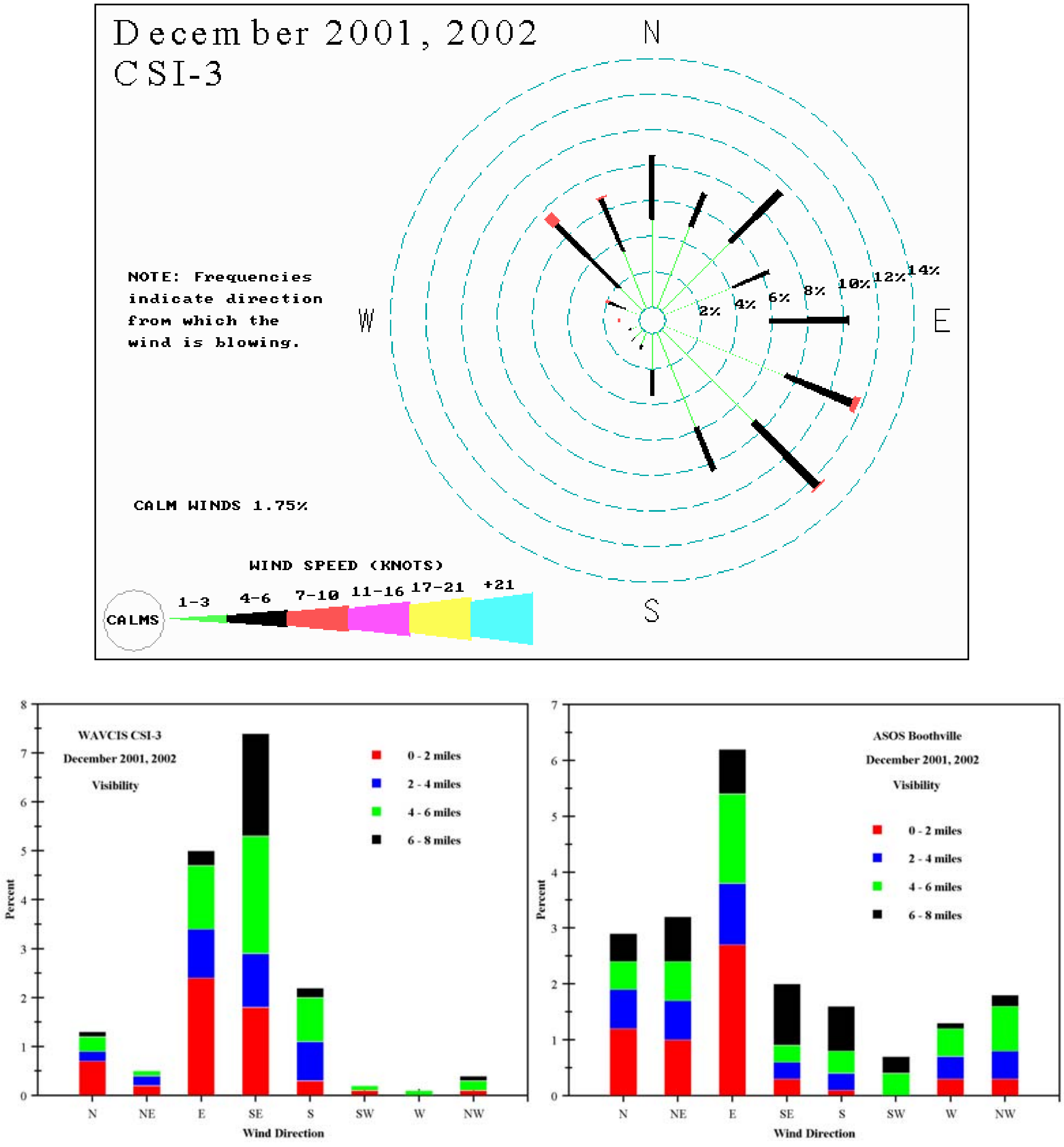

Figure 110. December wind rose for CSI-3 (top), and visibility 'roses' for the CSI-3 and Boothville stations (bottom).

VI. APPLICATIONS OF SATELLITE IMAGERY DURING PERIODS OF REDUCED VISIBILITY OVER THE NORTHERN GULF OF MEXICO

Very few surface observing stations in the Gulf of Mexico region monitor visibility. Therefore, one task of this project as originally proposed was to take advantage of satellite imagery, in particular that provided by the MODIS platform, to help differentiate natural from anthropogenic sources as well as the spatial distribution of overwater haze. Unfortunately, over the course of our measurement period, several factors were encountered which greatly limited our use of satellite data in this analysis.

As discussed in the previous section, episodes of reduced visibility attributed to haze (by ASOS definition) over the Louisiana coastal region occur fairly infrequently. In most cases, haze conditions were also of short duration, on the order of a few hours. High resolution imagery, such as provided by MODIS and other NOAA polar orbiting satellites, was only available for one or two passes per day, and rarely coincided with our identified haze times. Some of the haze cases occurred during night hours. Visual imagery, including the 250 m resolution MODIS, is not discernable at night. In many cases for which imagery was available, it was found that near-surface (low atmosphere) features over the northern Gulf were obscured by higher level cloud.

It should also be noted that the development and implementation of image processing algorithms for the MODIS data was delayed; becoming routinely available on the LSU Earth Scan system between March and June 2003. Regardless, some imagery was captured and incorporated into our analysis, and a few examples are now presented. All satellite imagery was captured, processed, and analyzed by the Earth Scan Lab, LSU. The weather charts presented were obtained via the web through the NOAA National Data Center webpage (http://nndc.noaa.gov).

In almost all of the following cases, the observed wind speeds were less than about 6 - 7 m s^{-1}. This is below the threshold necessary to produce numerous breaking waves, therefore the reduction in visibility contributed by sea spray is likely negligible.

A. November 25, 2001

A weak, stationary frontal boundary extends over the southeastern U.S. to the Mississippi River Delta during 00 - 03 UTC 26 November (Fig. 112). Surface flow over southern Louisiana and the northwest Gulf is light (about 10 kts) easterly. During the hours of 00 - 02 UTC (18 - 20 CST 25 November), visibility at CSI-3 drops to an average of 6.0 miles, while the dew point depression is 5.2°C (see Fig. 111). Areas of Marginal Visual Flight Rules (MVFR) are indicated along the Texas and Louisiana coasts (Fig. 113), and haze is indicated. GOES satellite imagery depicts a large area of low cloud extending from the Texas coastal region into southwest Louisiana and over the shelf waters (Fig. 114). Note that the earlier drop in visibility recorded at BVE (Fig. 111, 04-05 CST) was likely due to a line of precipitation which developed along the front and extended southward to the Mississippi River Delta.

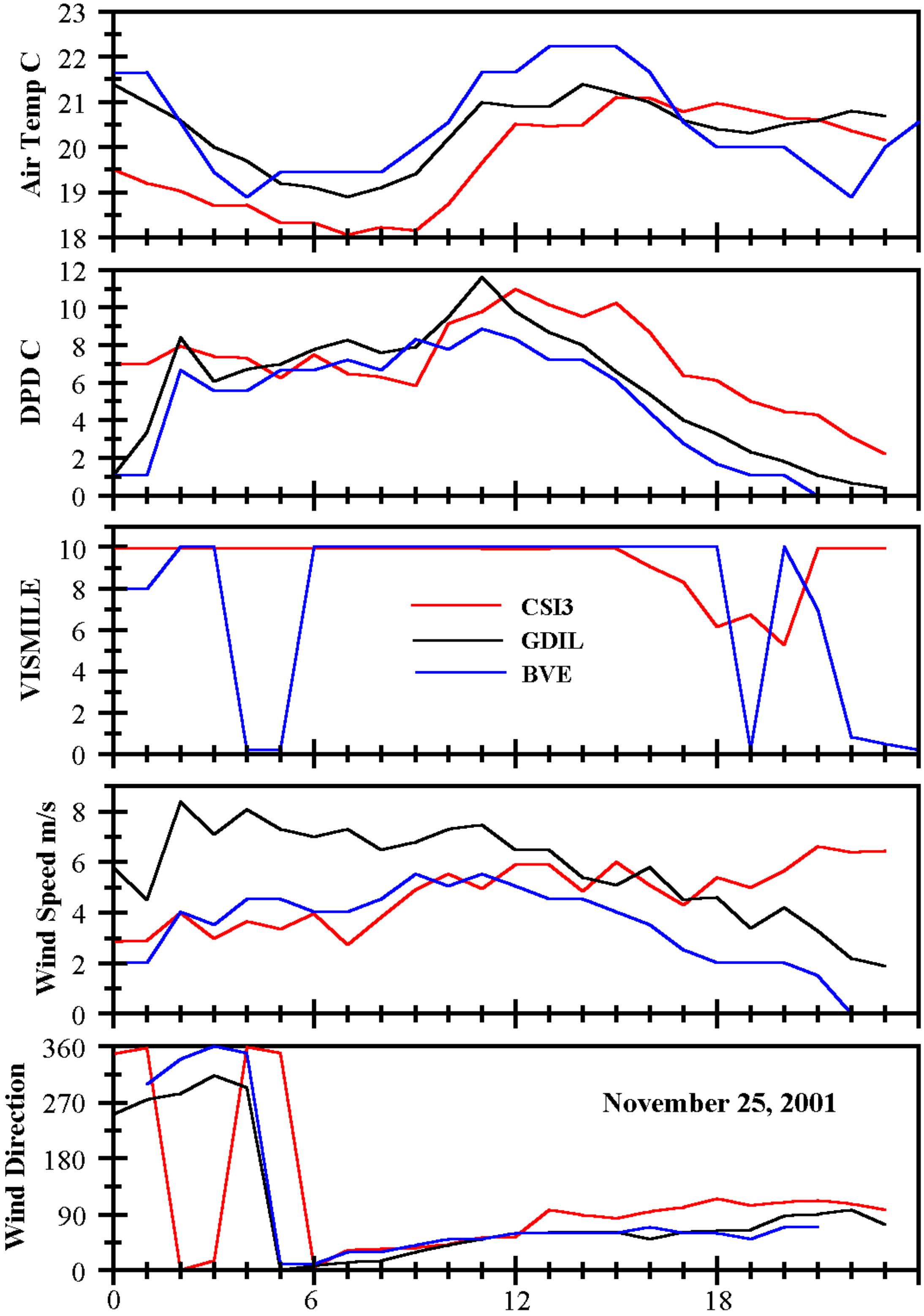

Figure 111. Time series (CST) of observed parameters on 25 November 2001.

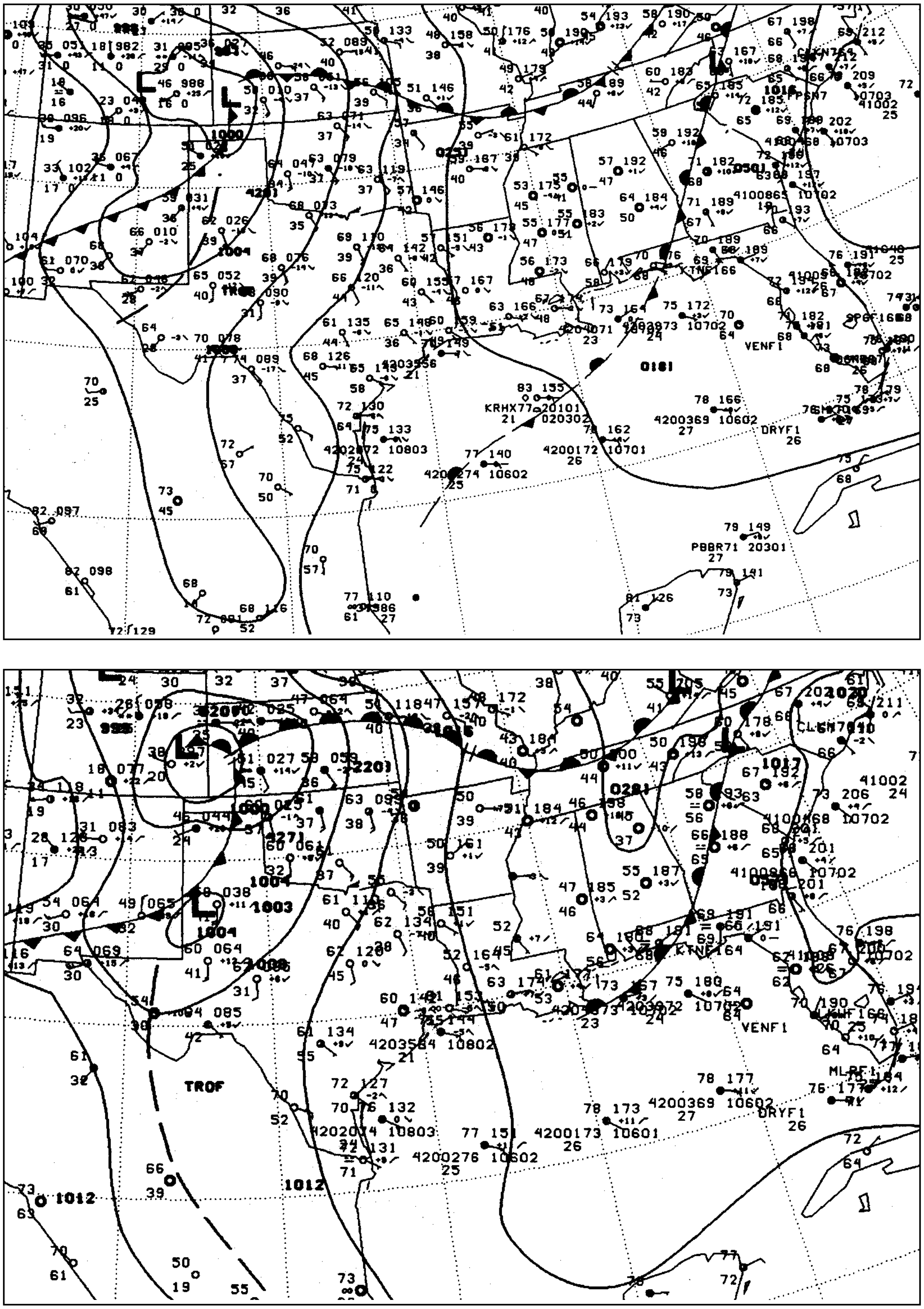

Figure 112. NWS surface weather charts for 0000Z and 0300Z 26 November 2001.

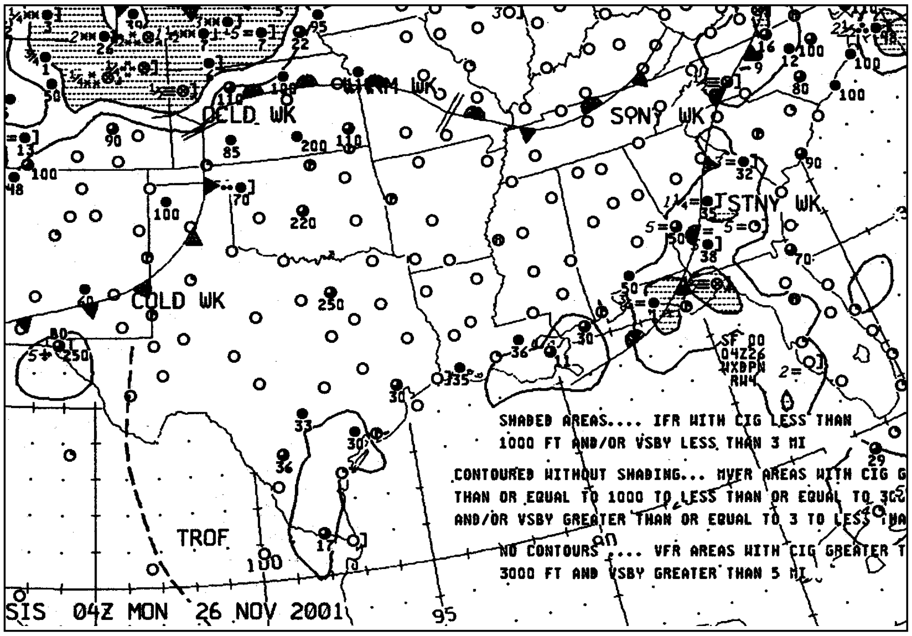

Figure 113. 0400Z 26 November 2001 NWS Weather Depiction chart.

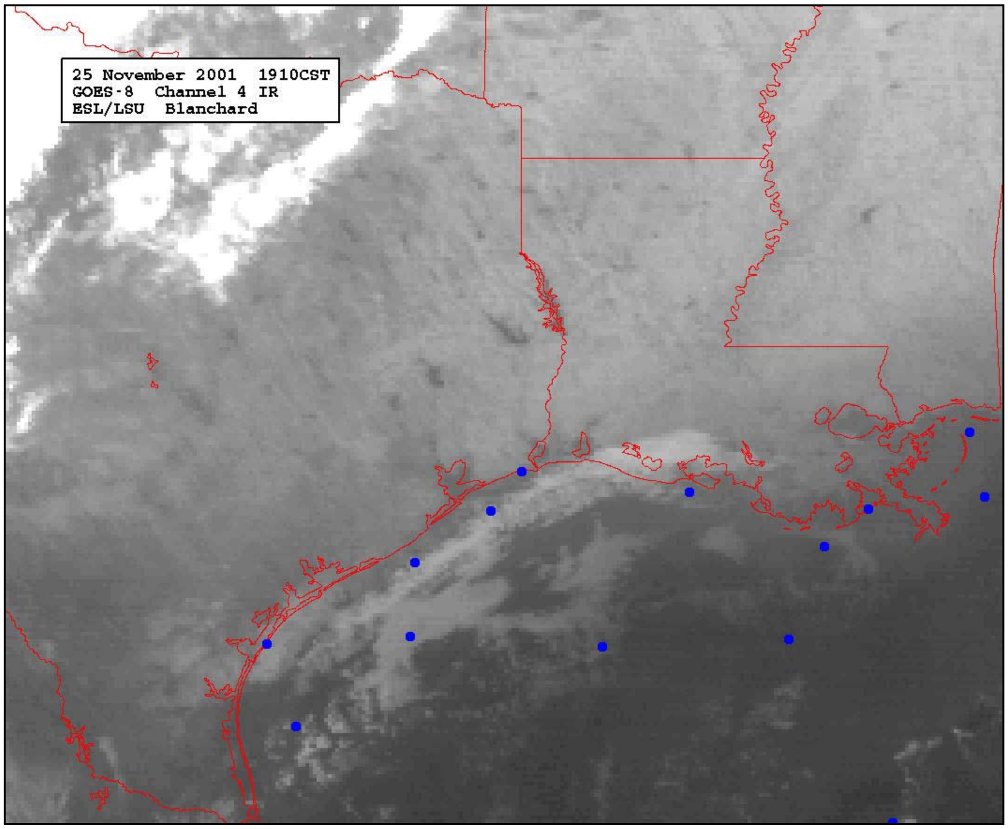

Figure 114. 1910 CST 25 November 2001 GOES-8 infrared image.

B. 4 - 5 March 2002

Weather over the northwestern Gulf of Mexico is controlled by a strong center of high pressure which migrates to the east-northeast over the period of 2100 UTC 4 March to 0600 UTC 5 March (Fig 116). Light winds and large air-sea temperature differences produce free convective conditions over the Louisiana shelf. During the hours of 01 to 06 UTC 5 March, average visibility at CSI-3 drops to 3.8 mile, while the average dew point depression is 10.0°C (Fig. 115). Computed mixed height is approximately 443 m. No restrictions are indicated on the weather charts, however patches of low cloud are seen over eastern Texas, and radar shows an area of rain (Fig. 117). No significant cloud or feature is found directly over CSI-3; on the other hand large fires on the southwest Louisiana coast and their associated smoke plumes are detected in the satellite imagery (Figs. 118 - 120). Note that the low visibility appears to coincide with a wind shift; clear with northerly flow, drops when direction becomes westerly, then clears again with shift to stronger easterly flow. Since air temperature and dew point depression remain fairly constant, the reduced visibility appears to be due to a local source

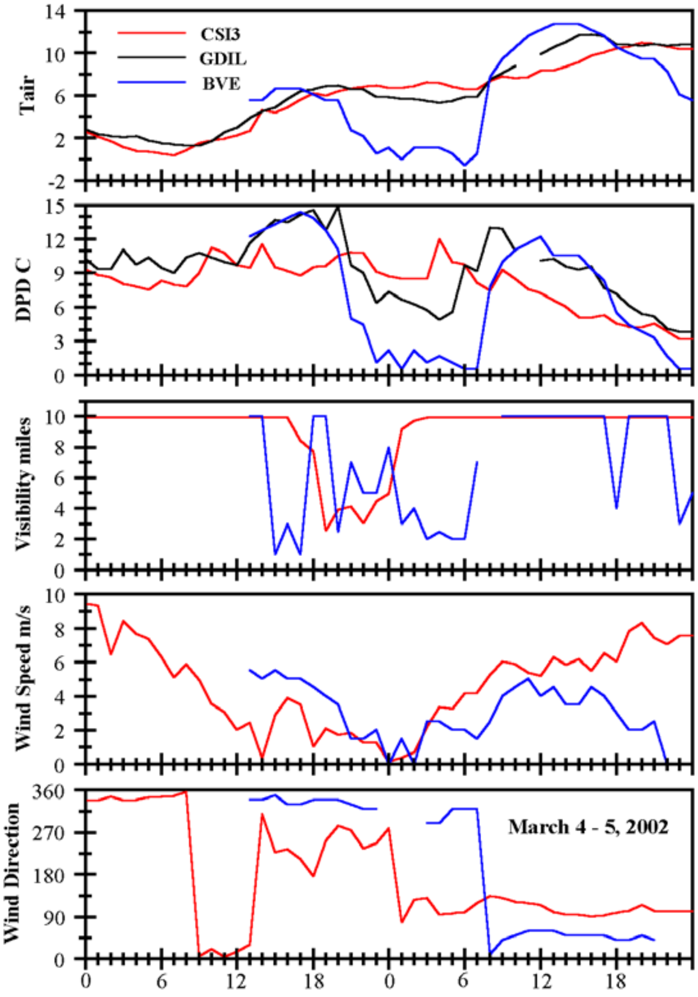

Figure 115. Time series (CST) of observed parameters on 4 - 5 March 2002.

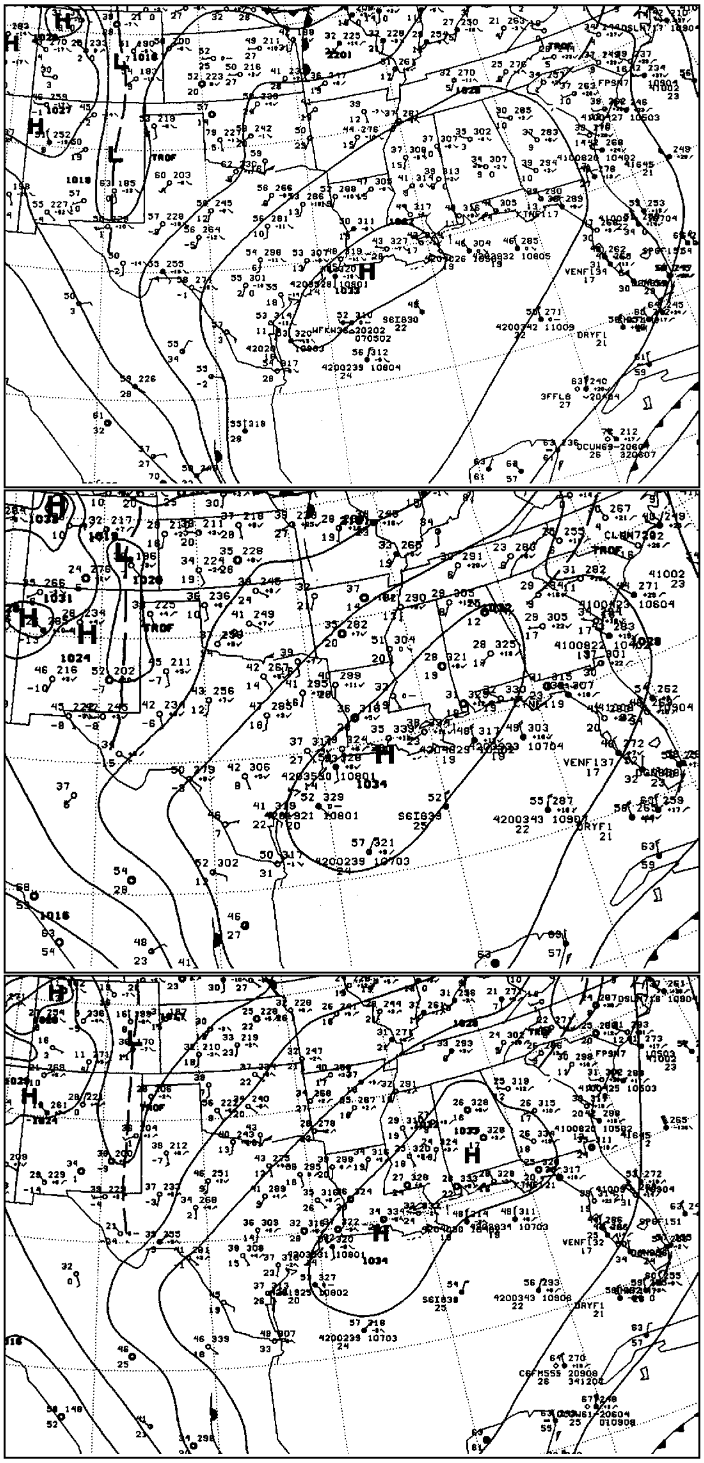

Figure 116. NWS surface weather charts for 0000, 0300, and 0600 Z 5 March 2002.

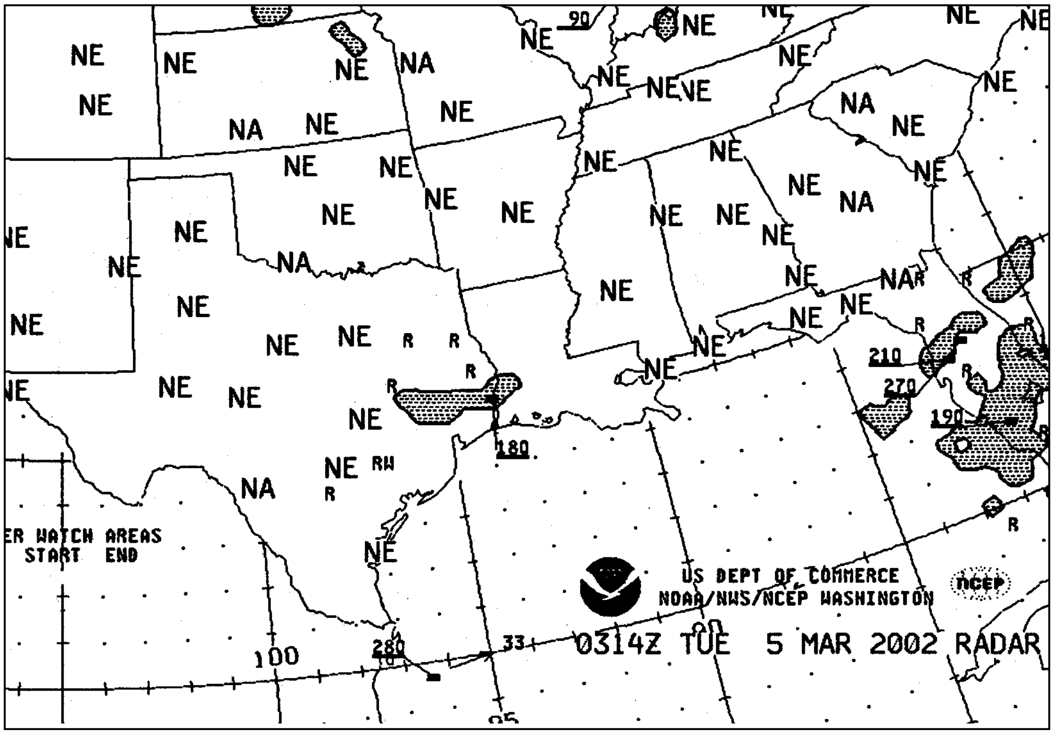

Figure 117. NWS Radar Summary chart for 0314 Z 5 March 2002.

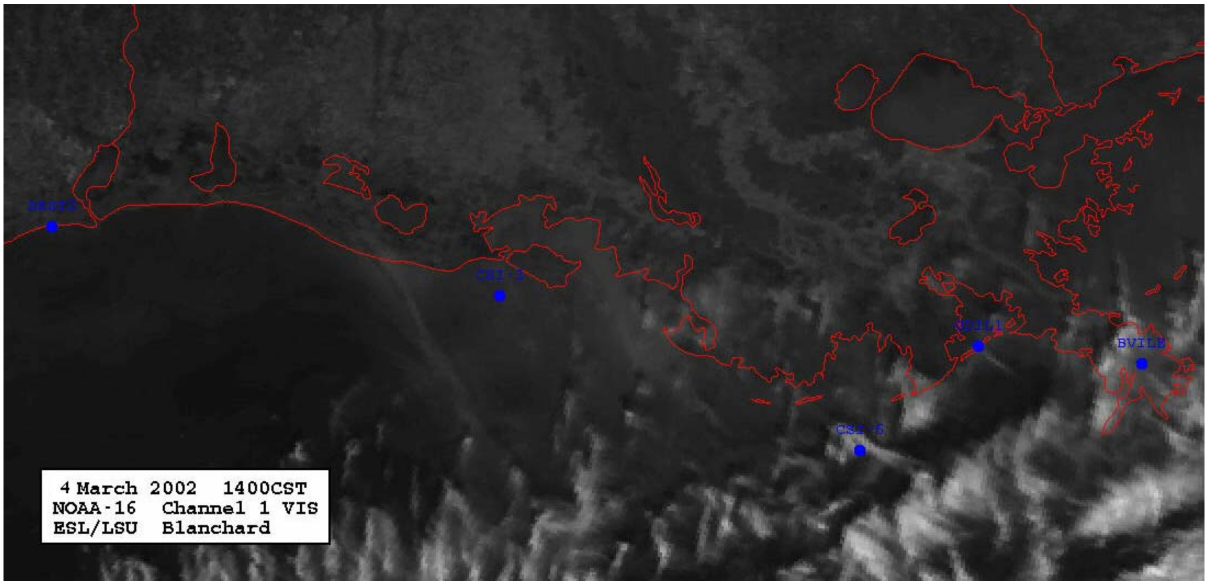

Figure 118. 1400 CST 4 March 2002 NOAA-16 visible image.

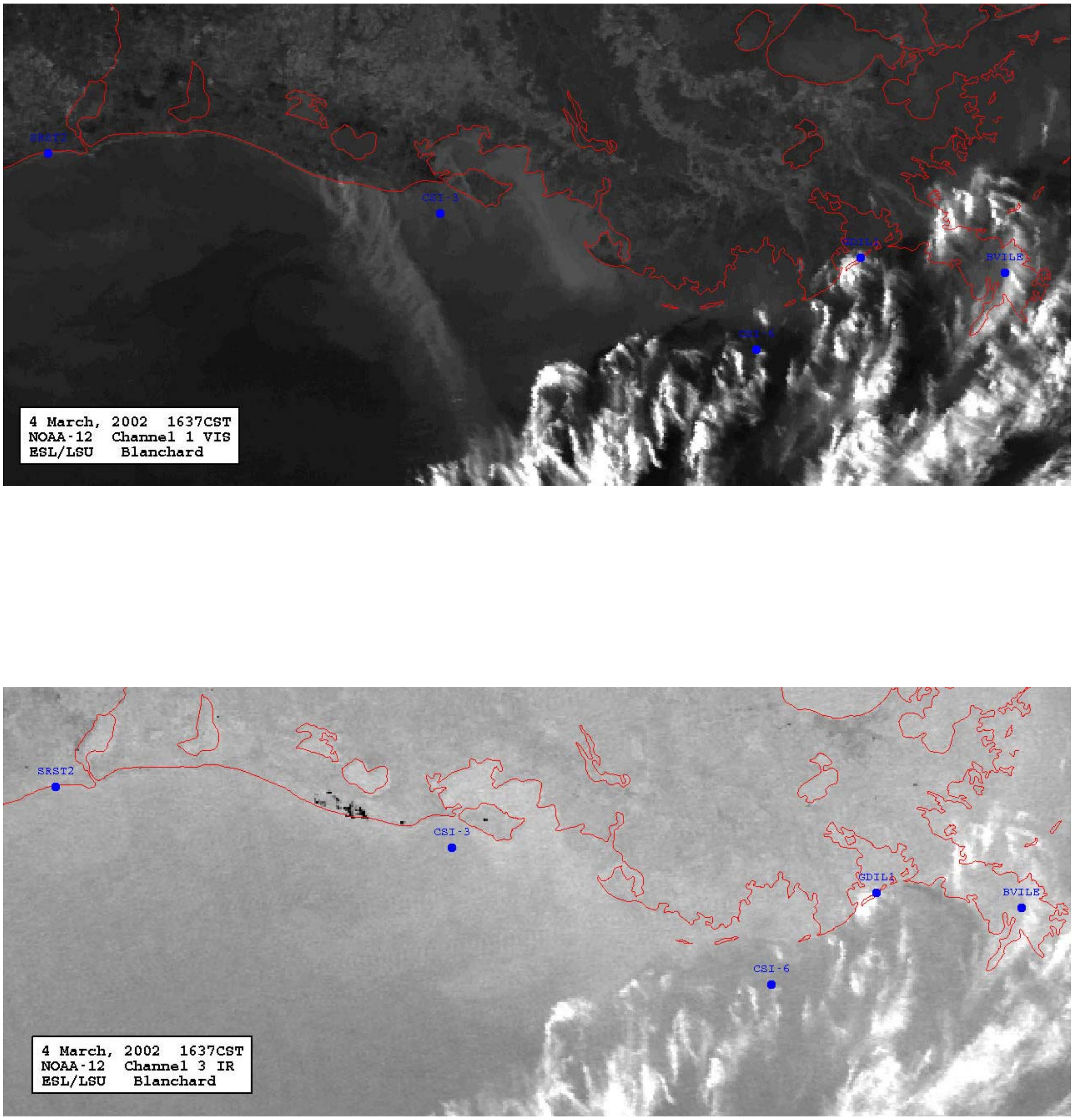

Figure 119. 1637 CST 4 March 2002 NOAA-12 visible image (top) and near-infrared image (bottom). The dark areas along the southwest Louisiana coast are fires, and a large plume is evident trailing off to the south-southeast.

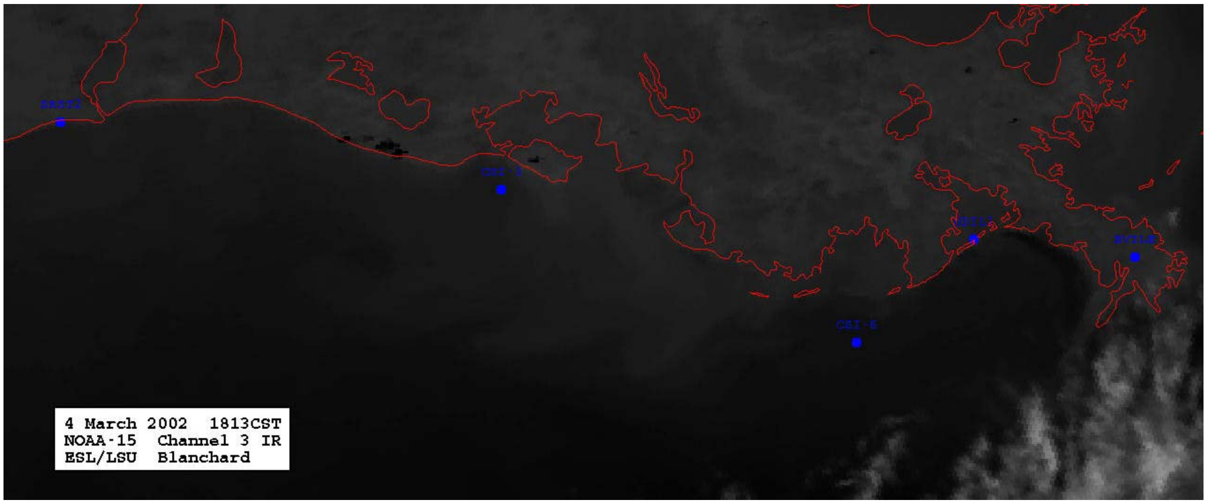

Figure 120. 1813 CST 4 March 2002 NOAA-15 near-infrared image.

C. 27 - 28 March 2002

Louisiana coastal weather is largely controlled by a high pressure ridge which extends southwestward from a center over the eastern U.S. (Fig. 122). During the period, the high moves eastward, allowing greater return flow of moist Gulf air over the state. Winds are easterly becoming more southerly, and light to nearly calm (Fig. 121). Areas of MVFR and Instrument Flight Rules (IFR) are depicted along the northwest Gulf coast (Fig. 123), attributed to fog; coastal stations become mostly overcast. Satellite imagery shows a large mass of low and high cloud progressing east-northeastward over the shelf waters (Figs. 124 - 128). Unstable conditions prevail at CSI-3, but moderate to Class C and D as winds increase and sea-air temperature difference decreases. Average computed mixed height is 403 m.

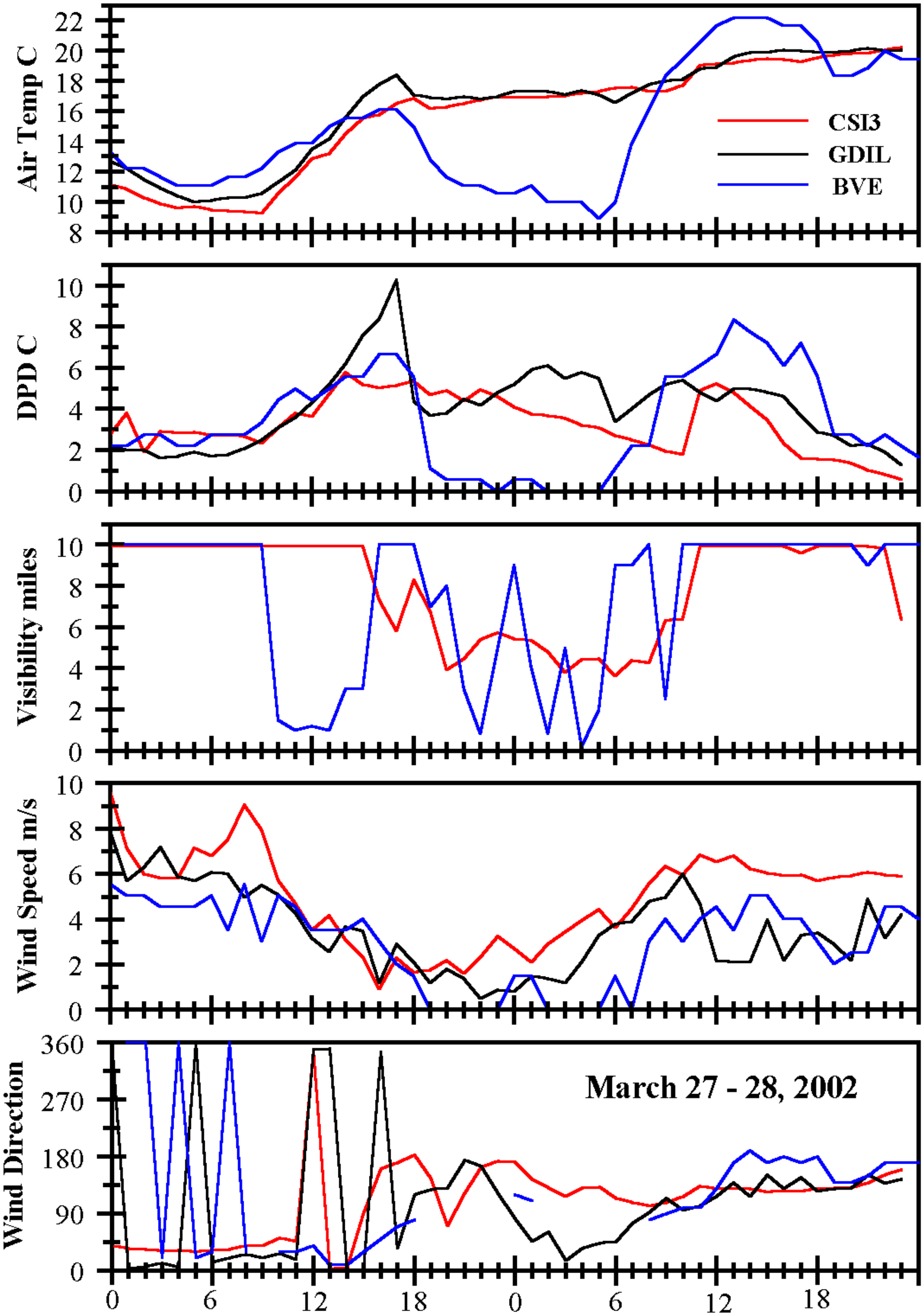

Figure 121. Time series (CST) of observed parameters on 27 - 28 March 2002.

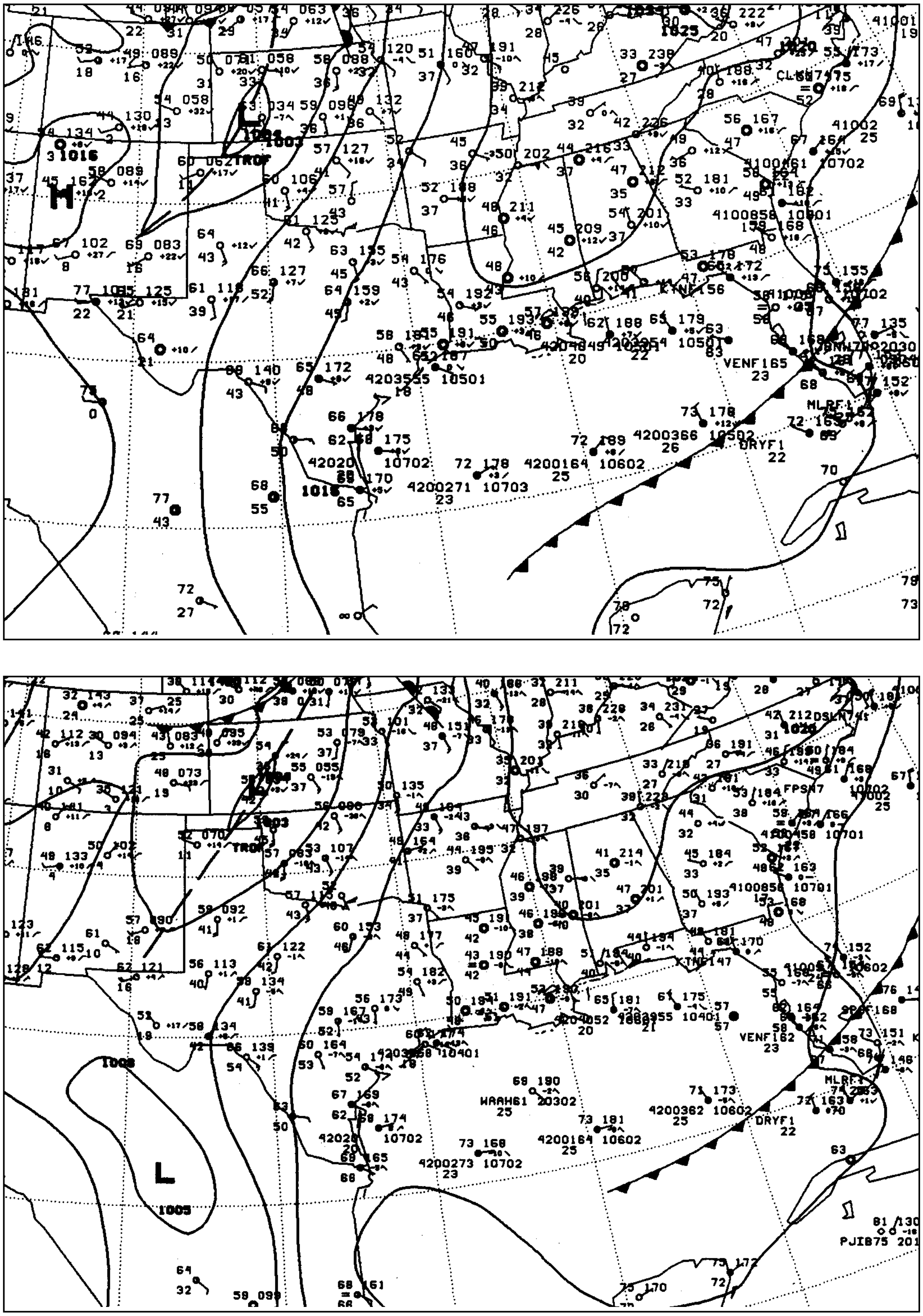

Figure 122a and b. NWS Surface Weather Charts for 0300 and 0600 Z 28 March 2002.

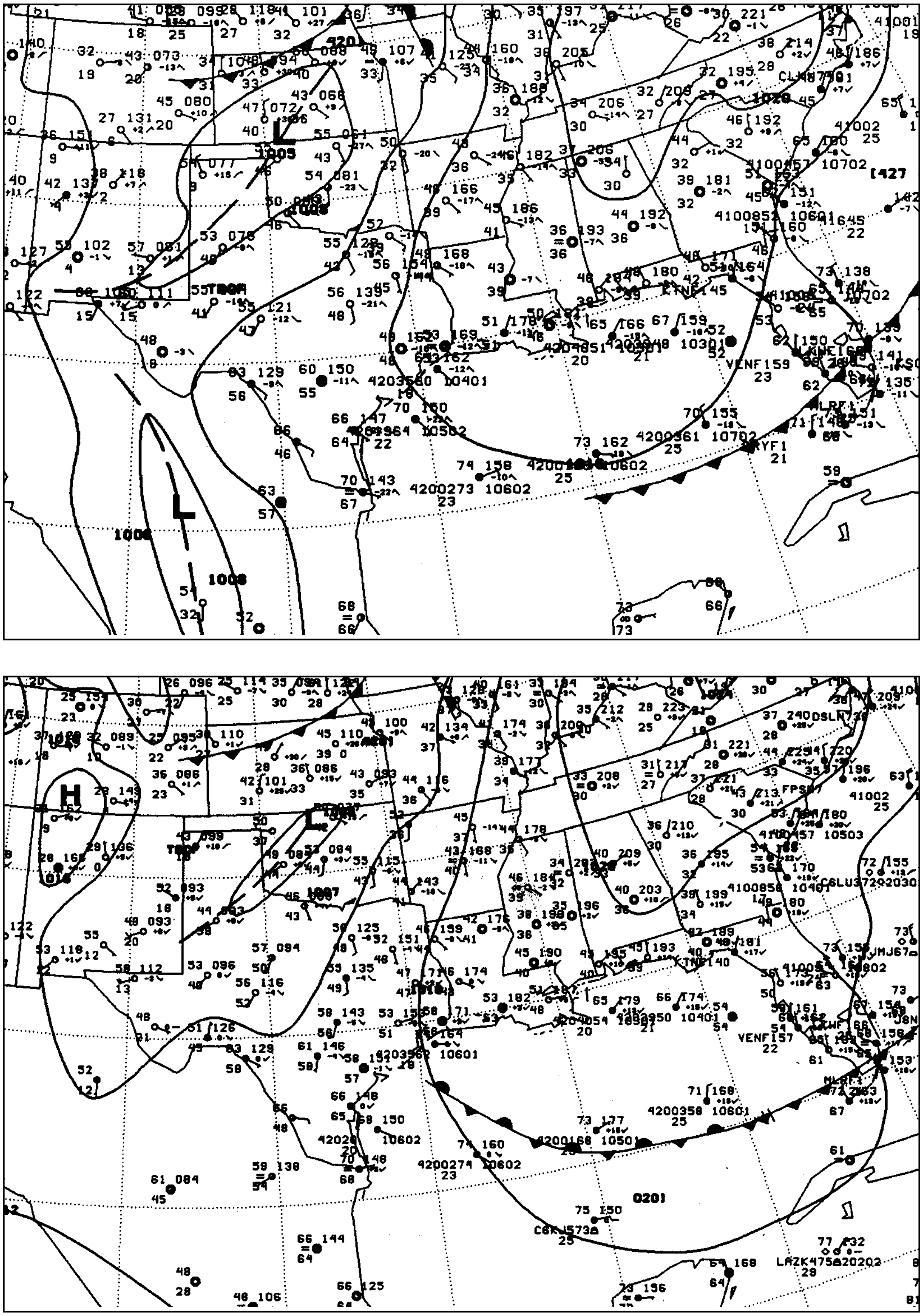

Figure 122 c and d. NWS Surface Weather charts for 0900 and 1200 Z 28 March 2002.

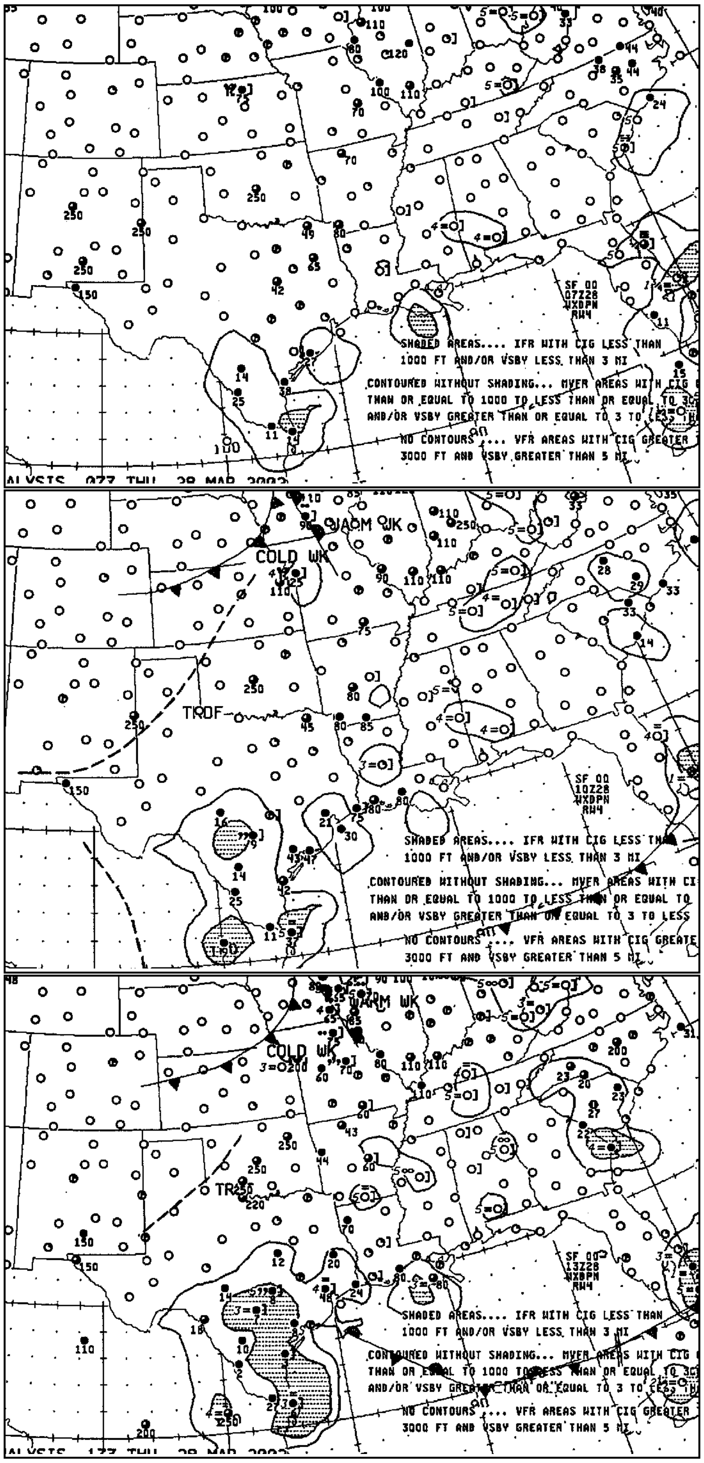

Figure 123. NWS Weather Depiction charts for 07, 10, and 13 Z 28 March 2002, top to bottom, respectively.

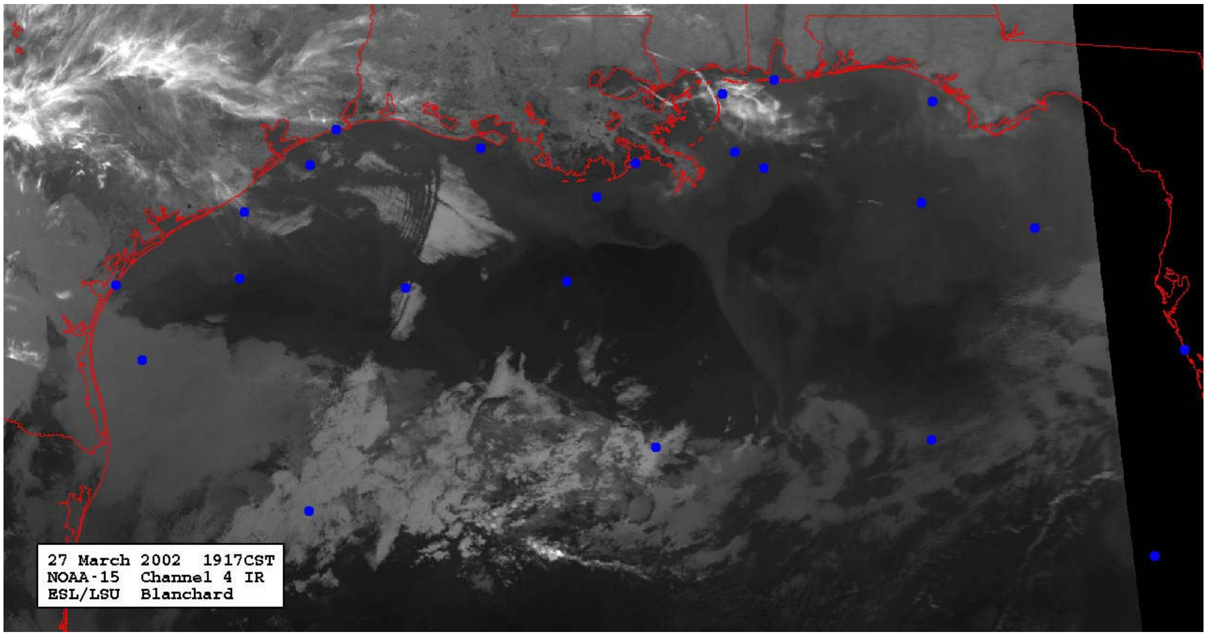

Figure 124. 1917 CST 27 March 2002 NOAA-15 infrared image.

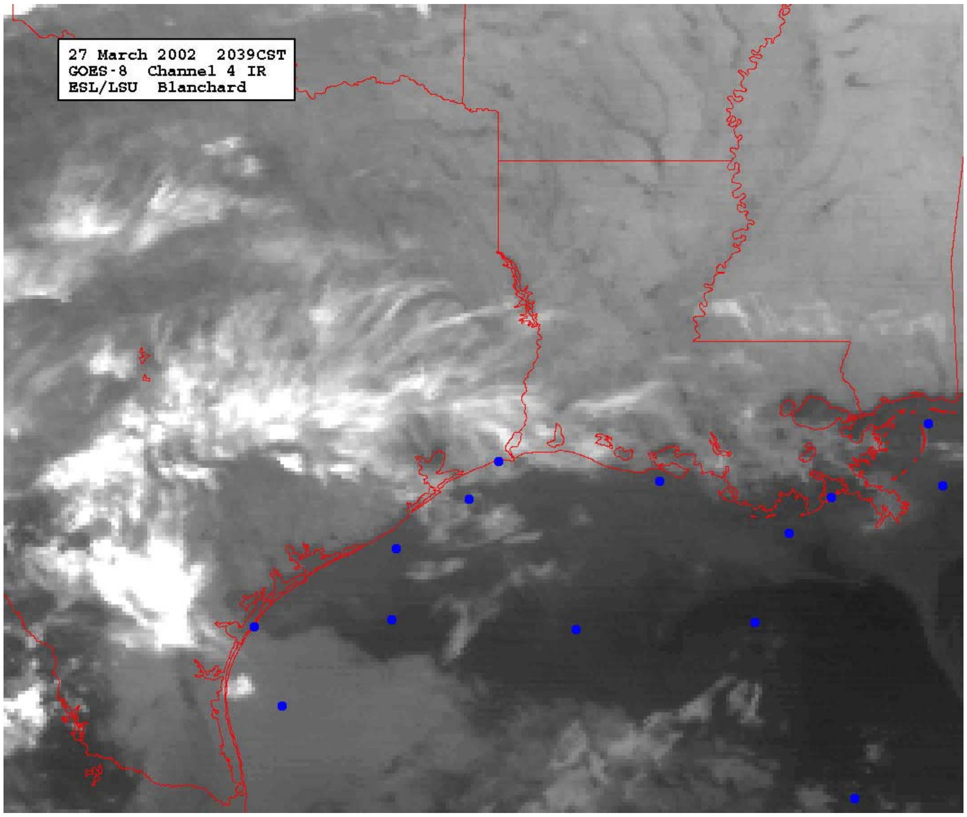

Figure 125. 2039 CST 27 March 2002 GOES-8 infrared image.

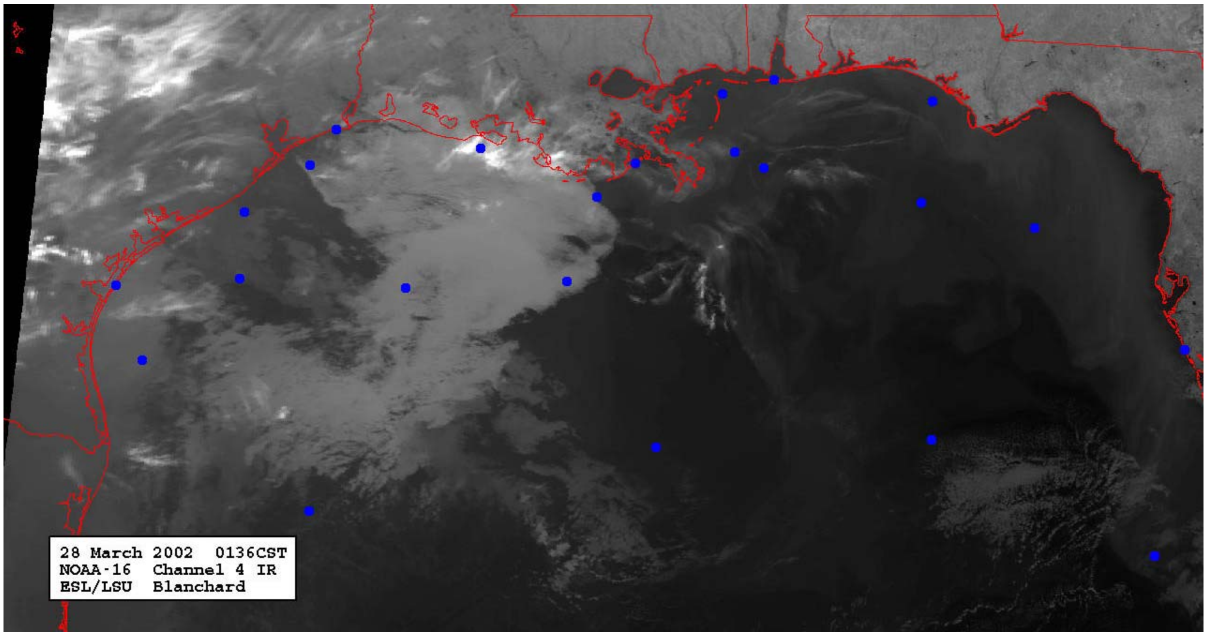

Figure 126. 0136 CST 28 March 2002 NOAA-16 infrared image.

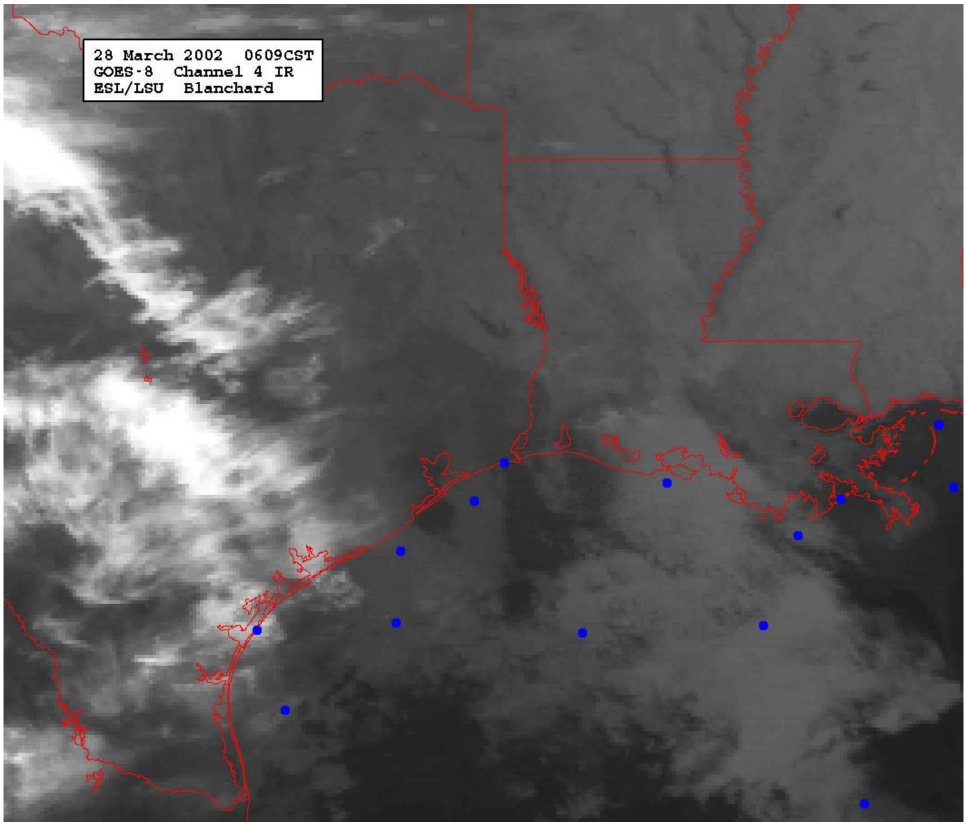

Figure 127. 0609 CST 28 March 2002 GOES-8 infrared image.

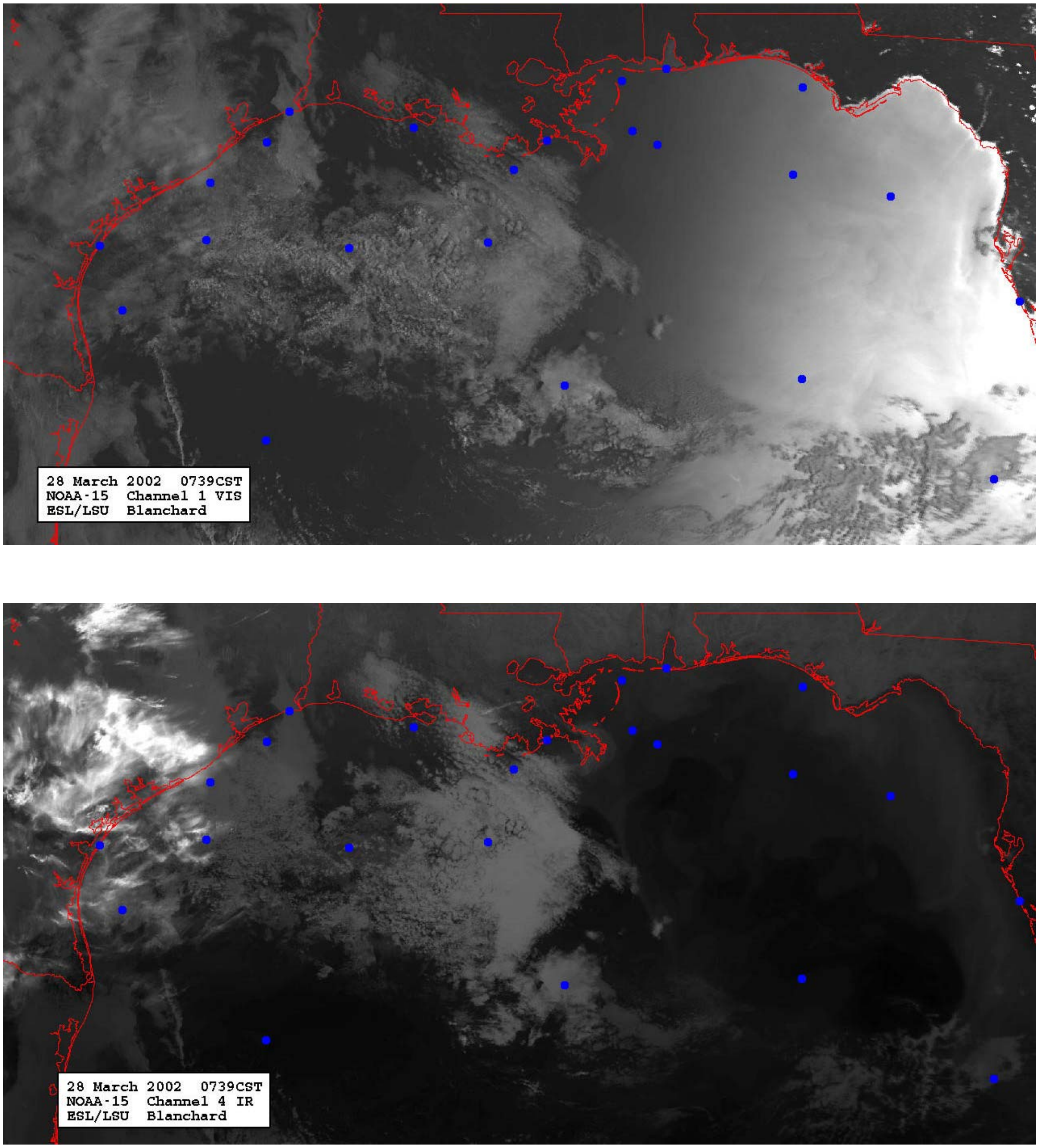

Figure 128. 0739 CST 28 March 2002 NOAA-15 visible image (top) and infrared image (bottom).

D. 10 April 2002

A stationary frontal boundary is positioned near New Orleans and extends south-southwestward into the Gulf (Fig. 130). Winds over the state are mostly light and variable to calm. An area of MVFR appears briefly along the coast; but there are no other indications of either fog or haze (Fig. 131). Considerable cloud coverage exists over the entire region (Figs. 132 - 136). Note onset of reduced visibility at CSI-3 occurs when winds shift from northeasterly to southerly and speeds decrease (Fig. 129). Unstable conditions become neutral as winds strengthen and sea-air temperature difference decreases. Average computed mixed height is 430 m.

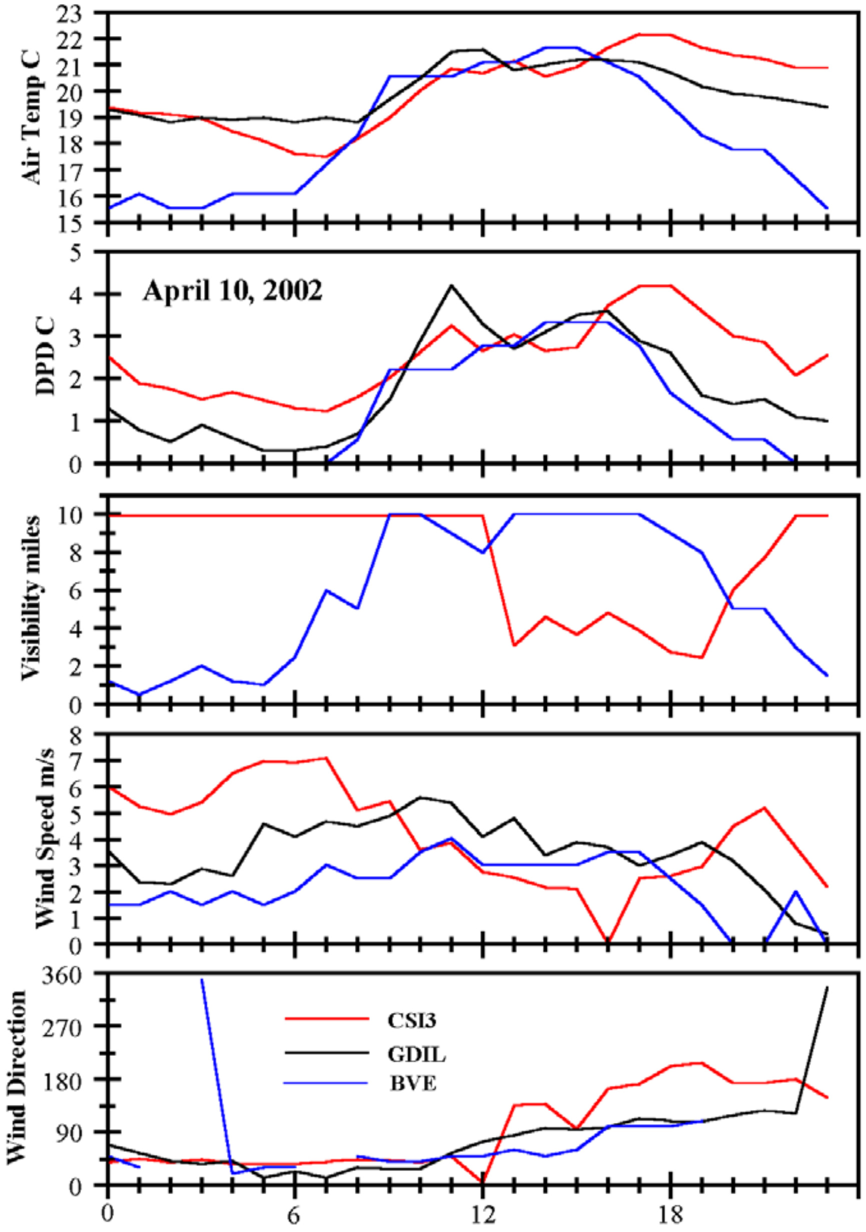

Figure 129. Time series (CST) of observed parameters on 10 April 2002.

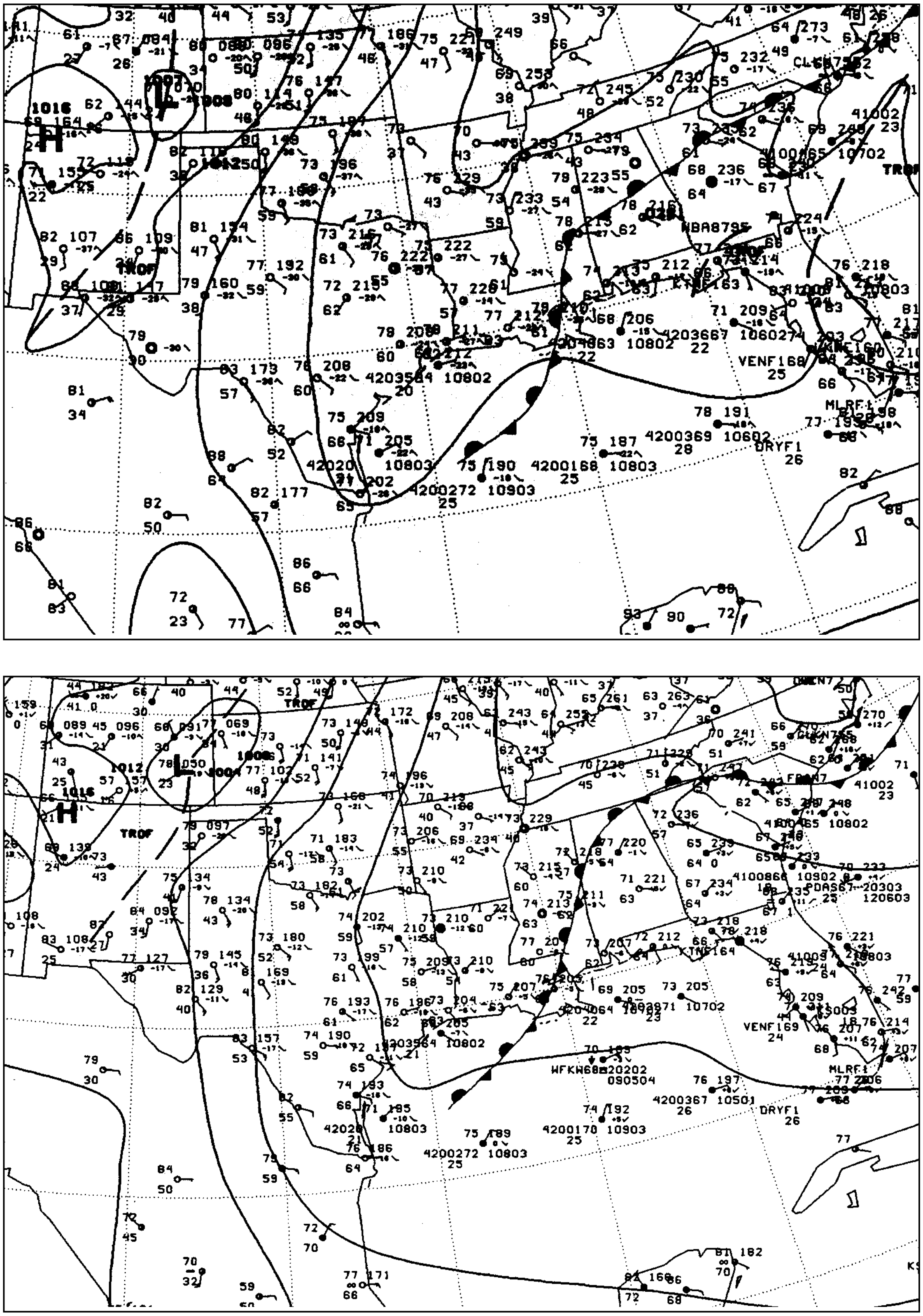

Figure 130. NWS Surface Weather charts for 21 Z 10 April (top) and 00 Z 11 April 2002 (bottom).

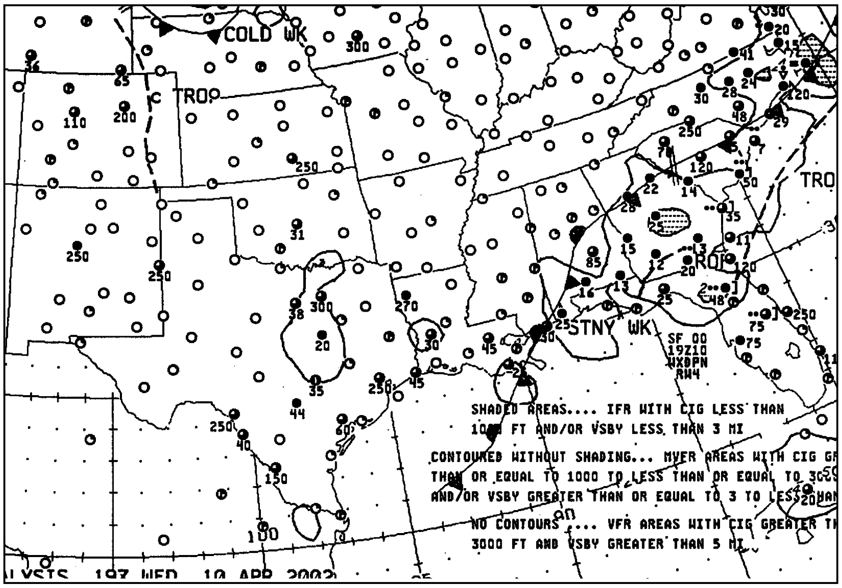

Figure 131. NWS Weather Depiction chart for 19 Z 10 April 2002.

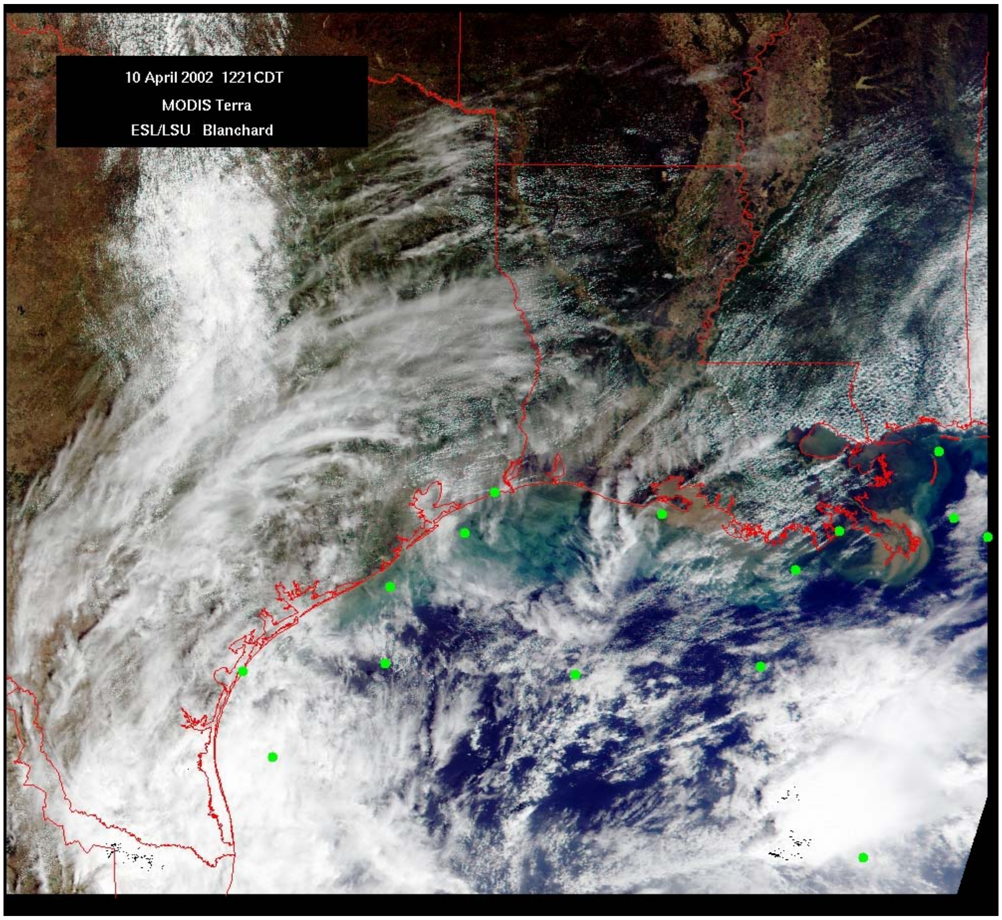

Figure 132. 1221 CDT 10 April 2002 MODIS true color image.

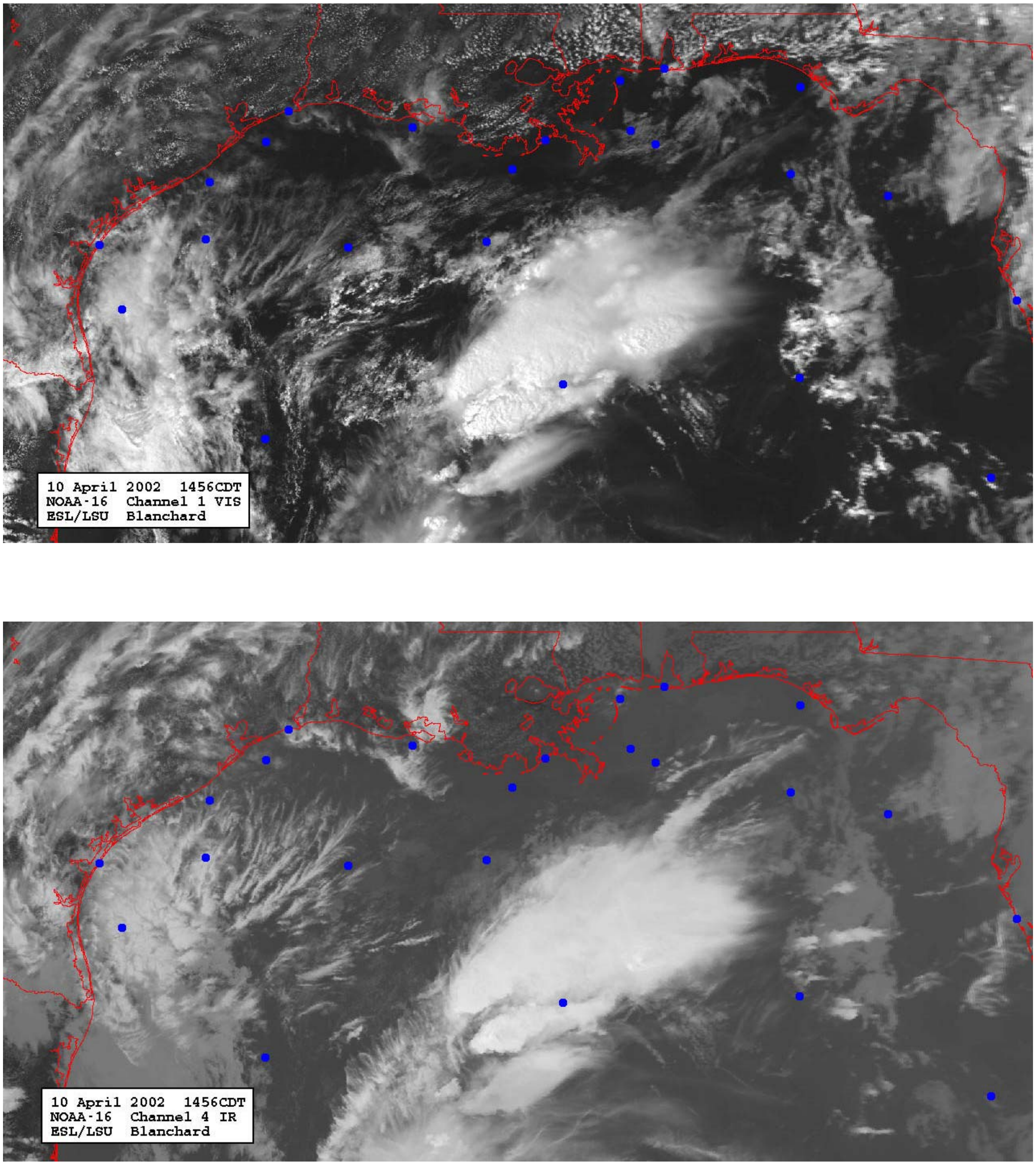

Figure 133. 1456 CDT 10 April 2002 NOAA-16 visible image (top) and infrared image (bottom).

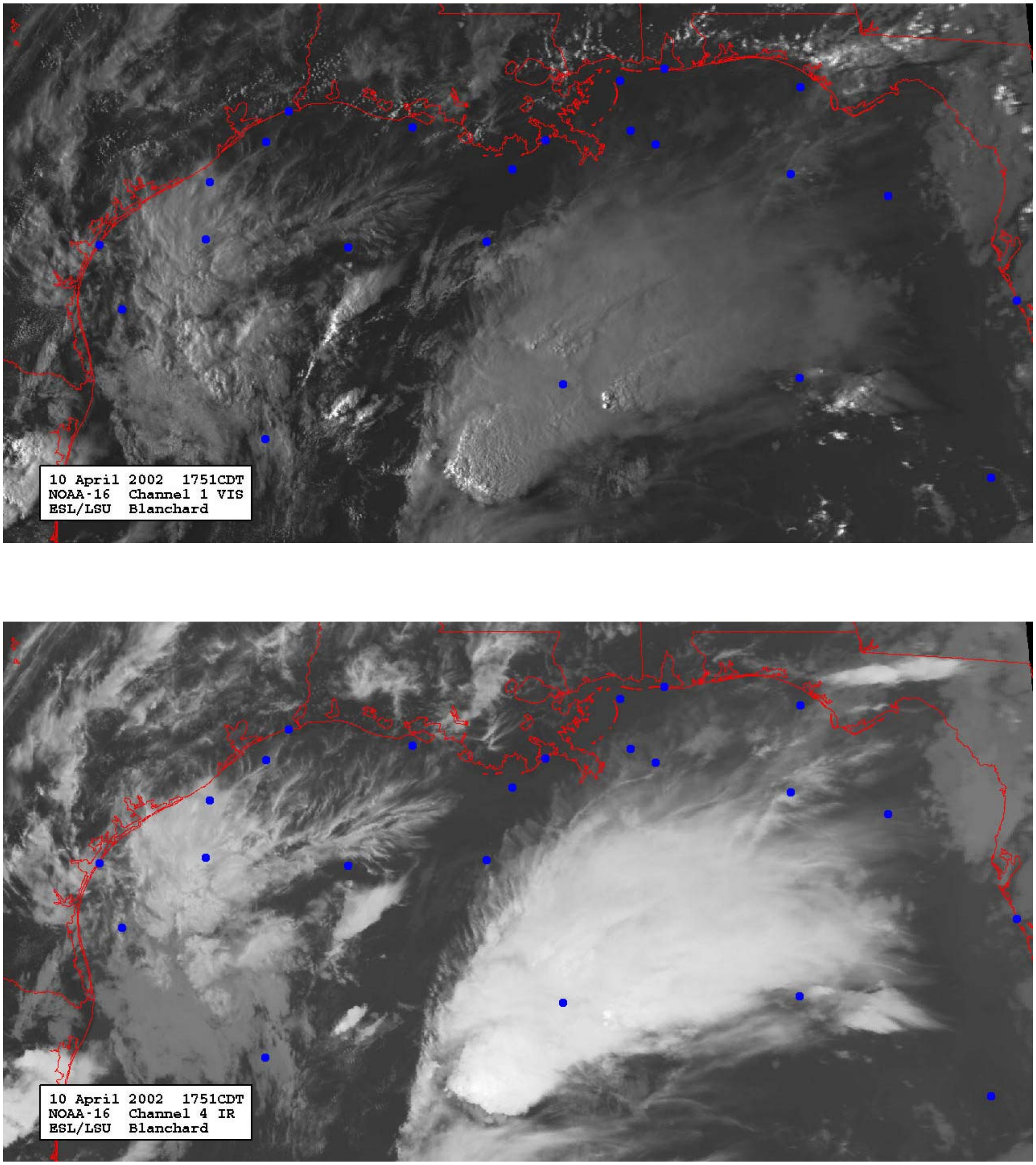

Figure 134. 1751 CDT 10 April 2002 NOAA-16 visible image (top) and infrared image (bottom).

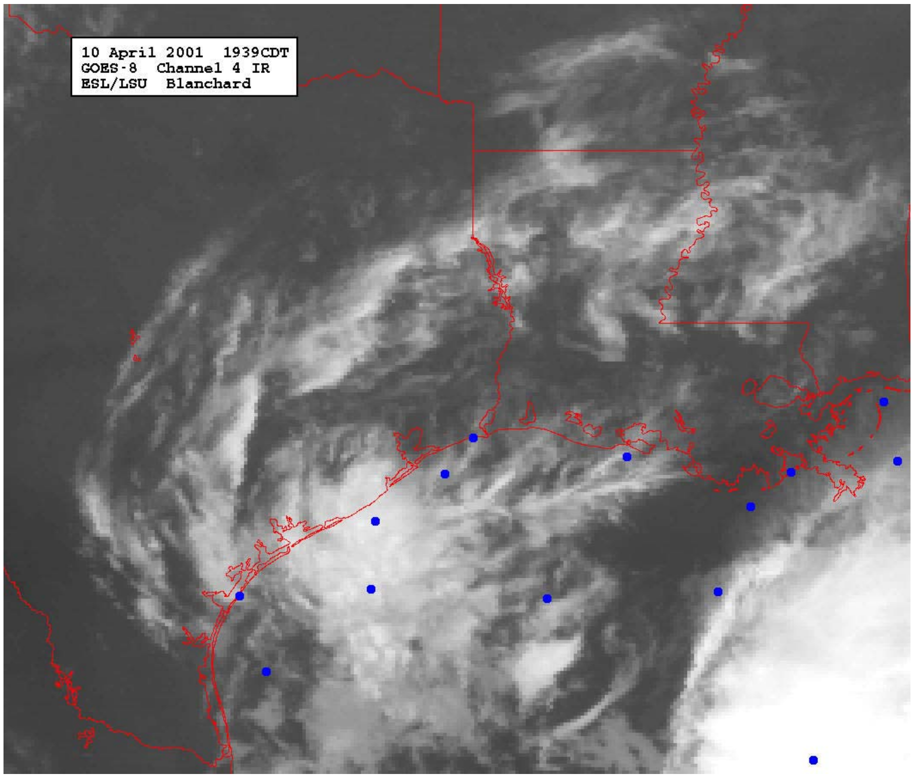

Figure 135. 1939 CDT 10 April 2002 GOES-8 infrared image.

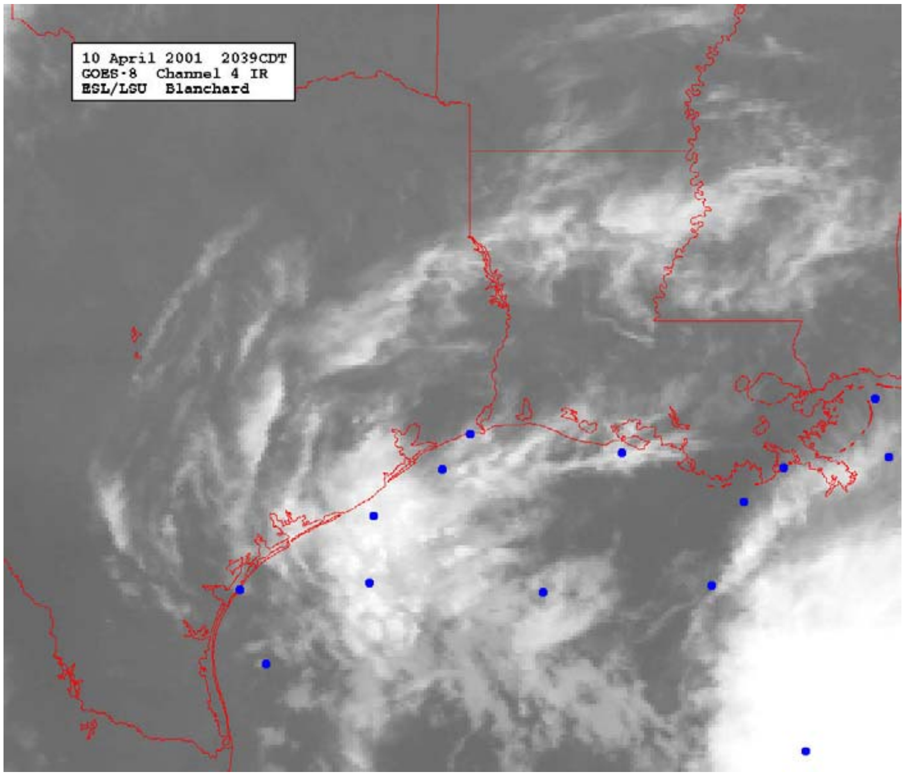

Figure 136. 2039 CDT 10 April GOES-8 infrared image.

E. 30 August 2002

A low and trough extend through the central Gulf of Mexico, but almost the entire U.S. is under the influence of high pressure (Fig. 138). Flow over Louisiana is northeast to east, and widespread haze and fog are indicated, producing MVFR and IFR over the shelf waters (Fig. 140). Scattered cloudiness appears over the Gulf, and extensive cumulus develops over land areas, however CSI-3 appears to remain mostly clear (Figs. 141 - 144). Class C conditions moderate to just barely Class D, and average computed mixed height is 531 m.

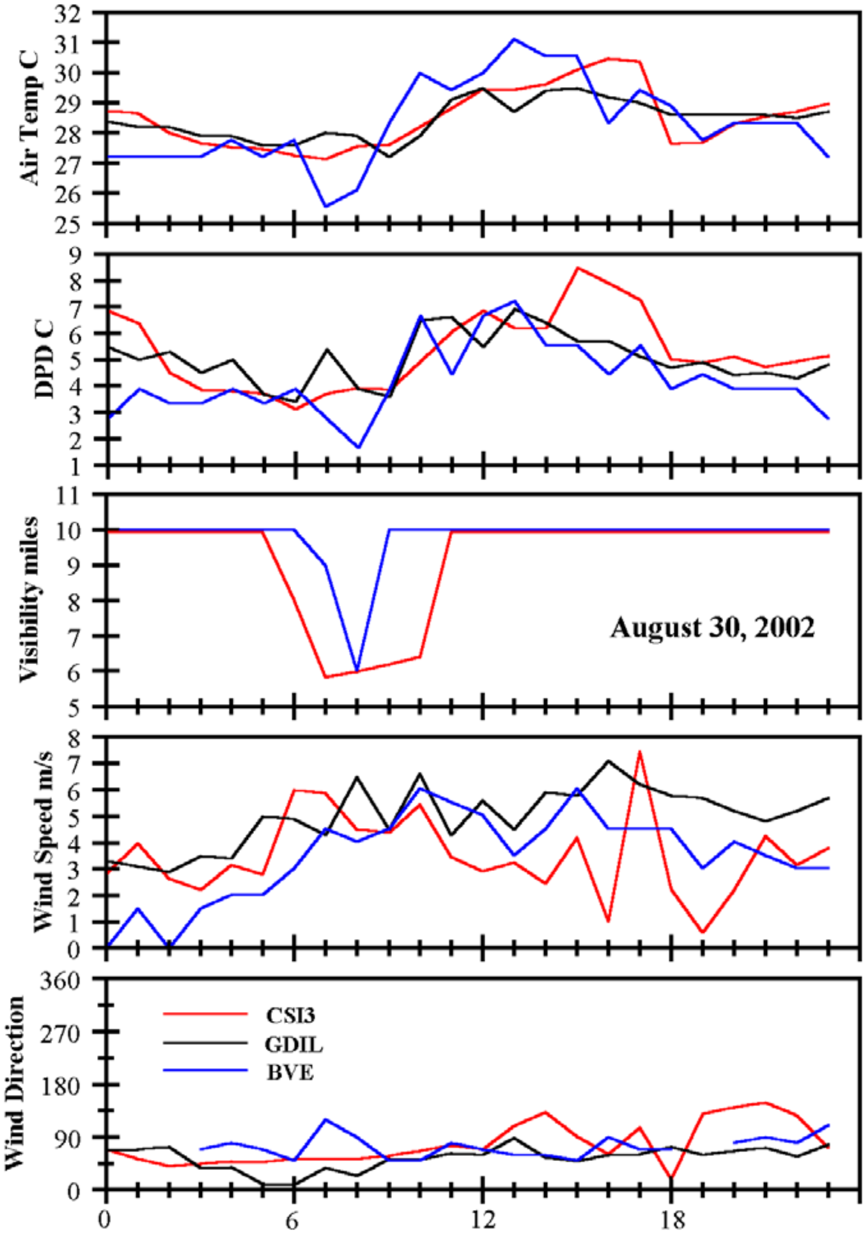

Figure 137. Time series (CST) of observed parameters on 30 August 2002.

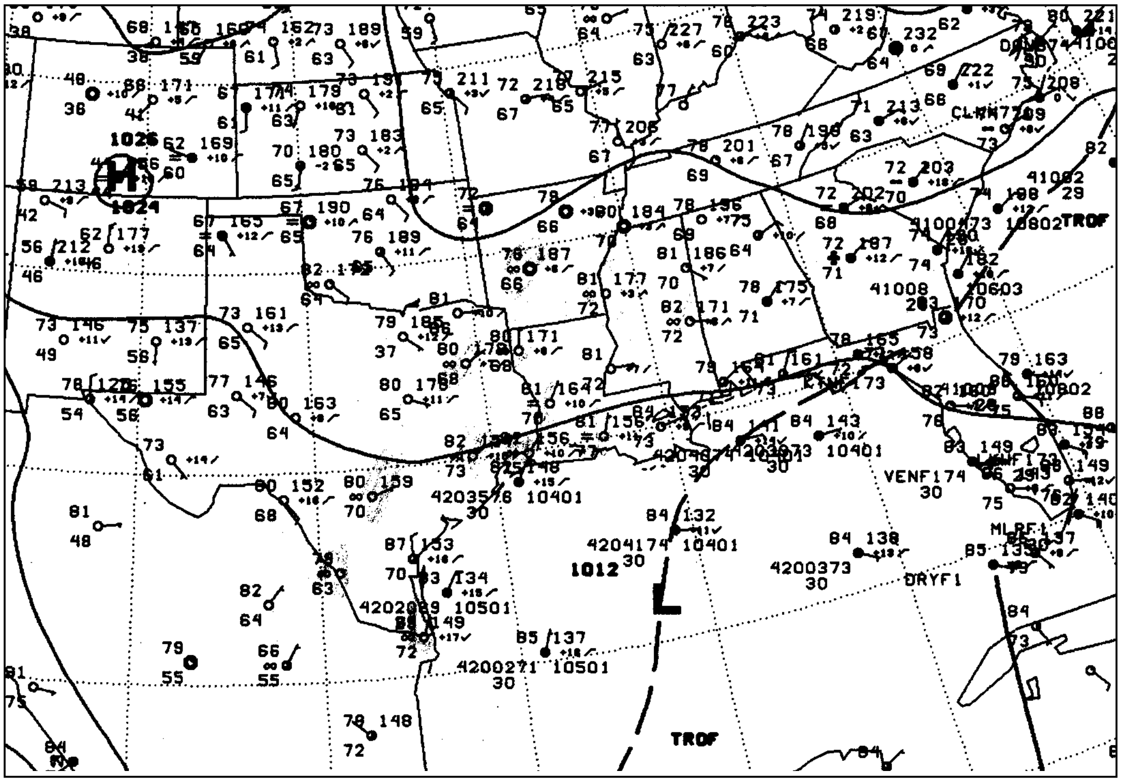

Figure 138. NWS Surface Weather chart for 1500 Z 30 August 2002.

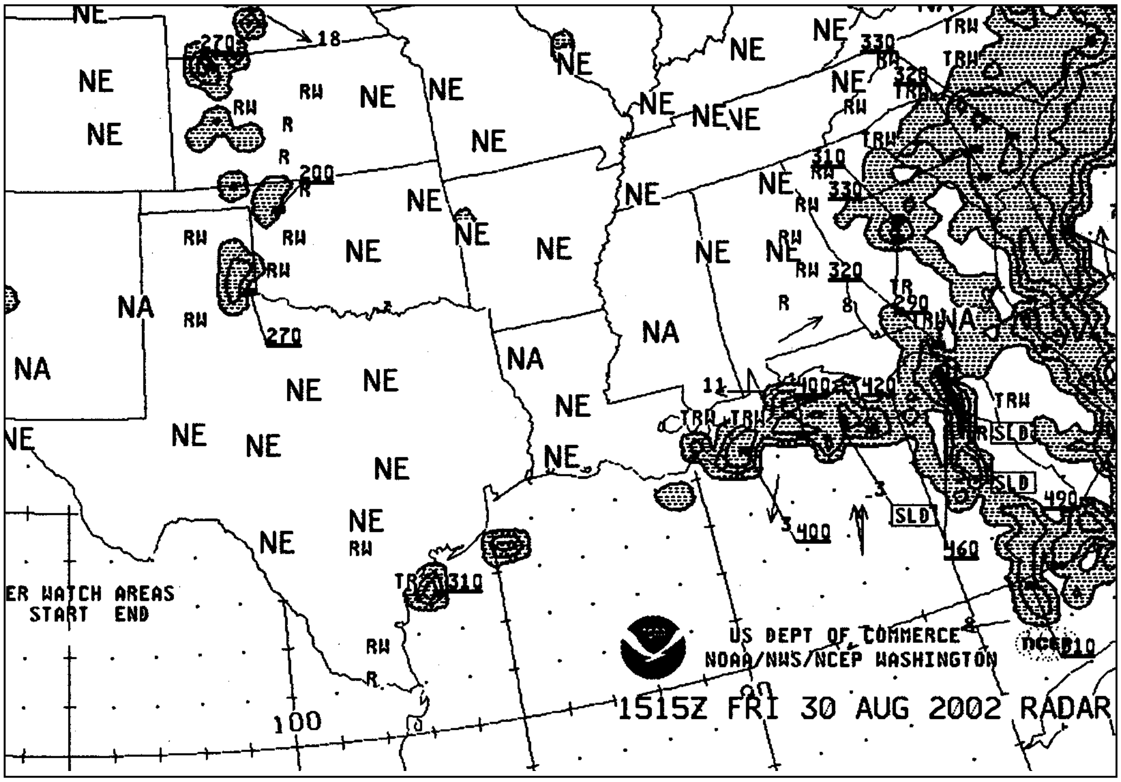

Figure 139. NWS Radar Summary for 1515 Z 30 August 2002.

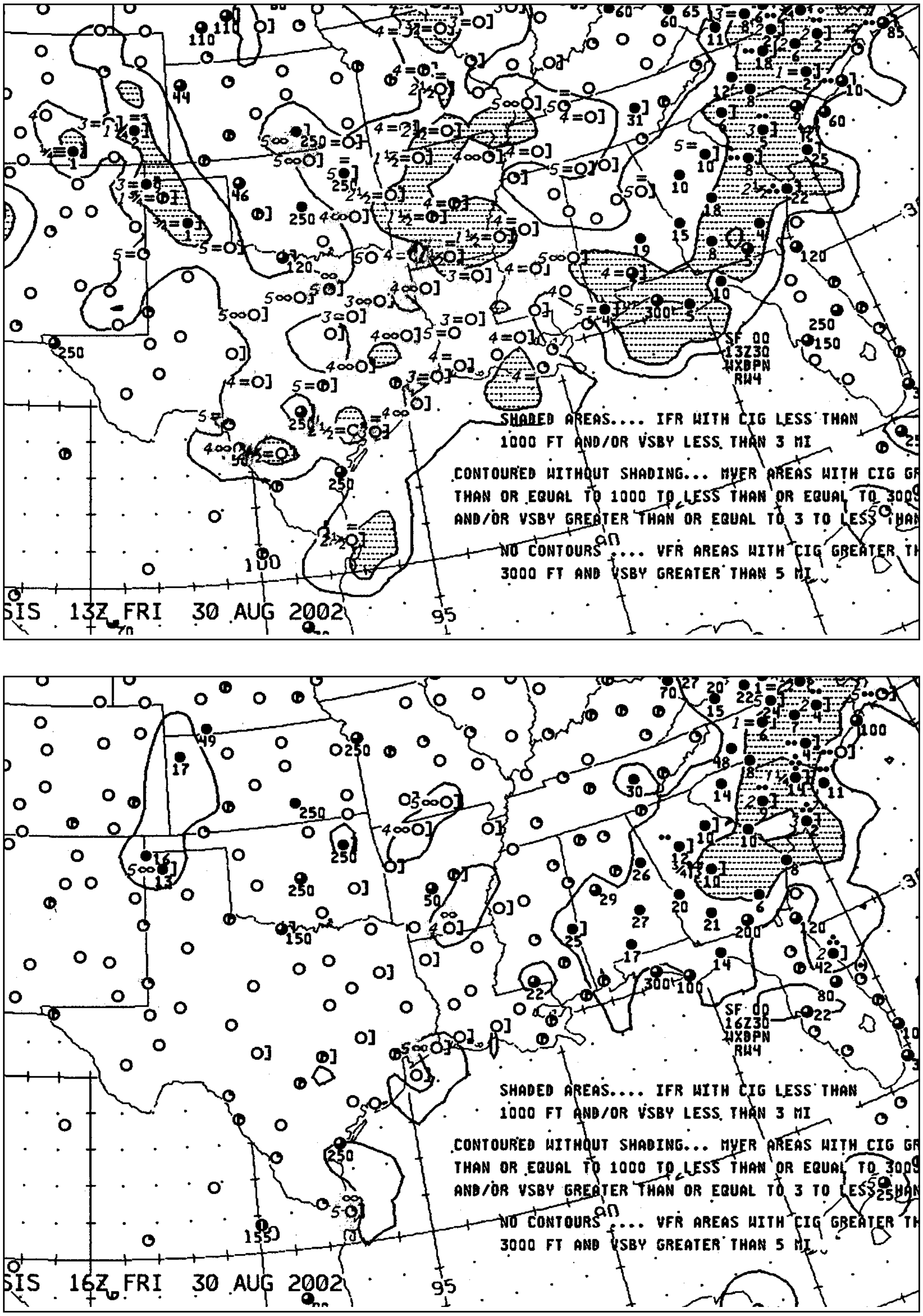

Figure 140. NWS Weather Depiction charts for 13 Z and 16 Z 30 August 2002.

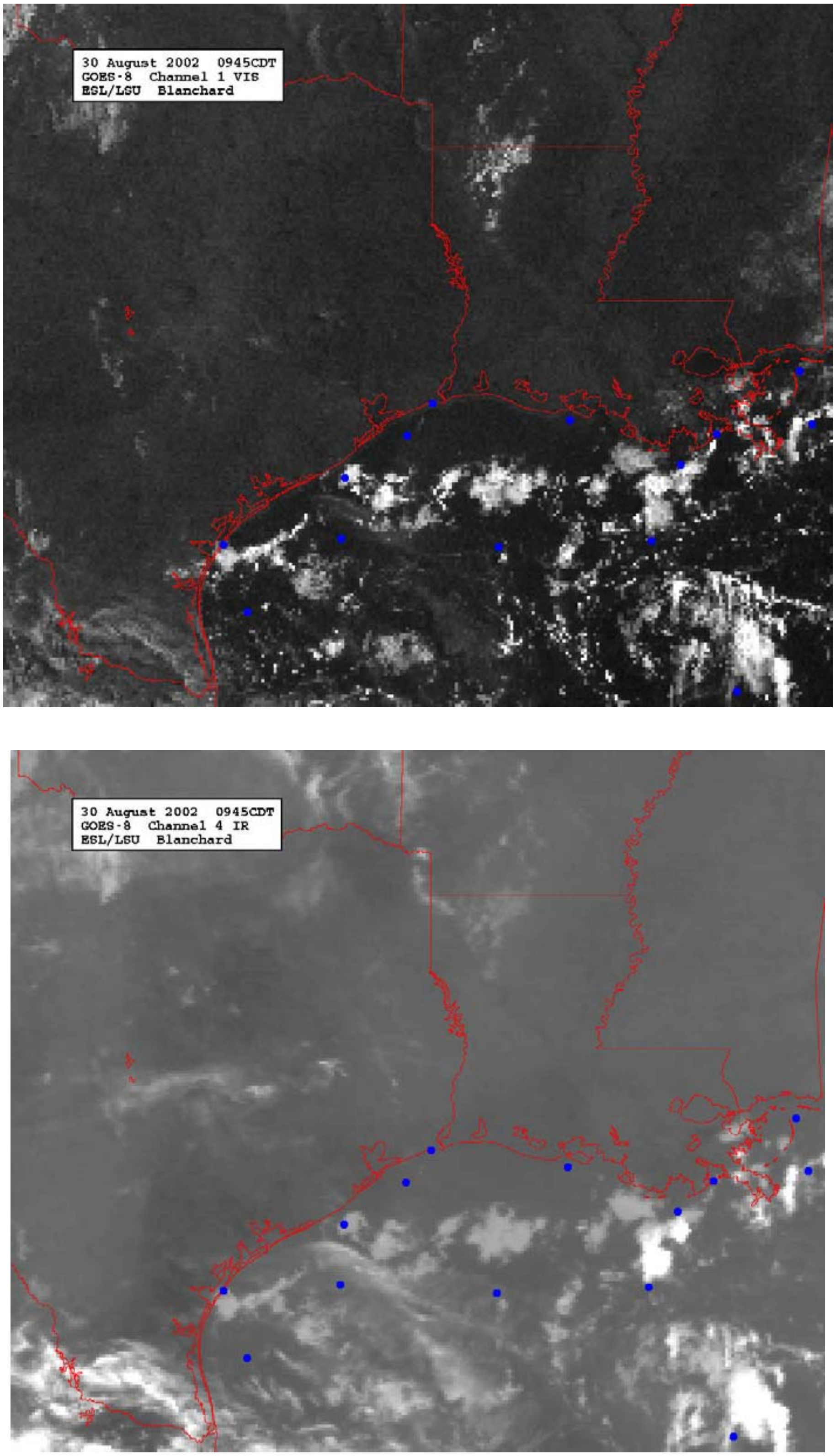

Figure 141. 0945 CDT 30 August 2002 GOES-8 visible image (top) and infrared image (bottom).

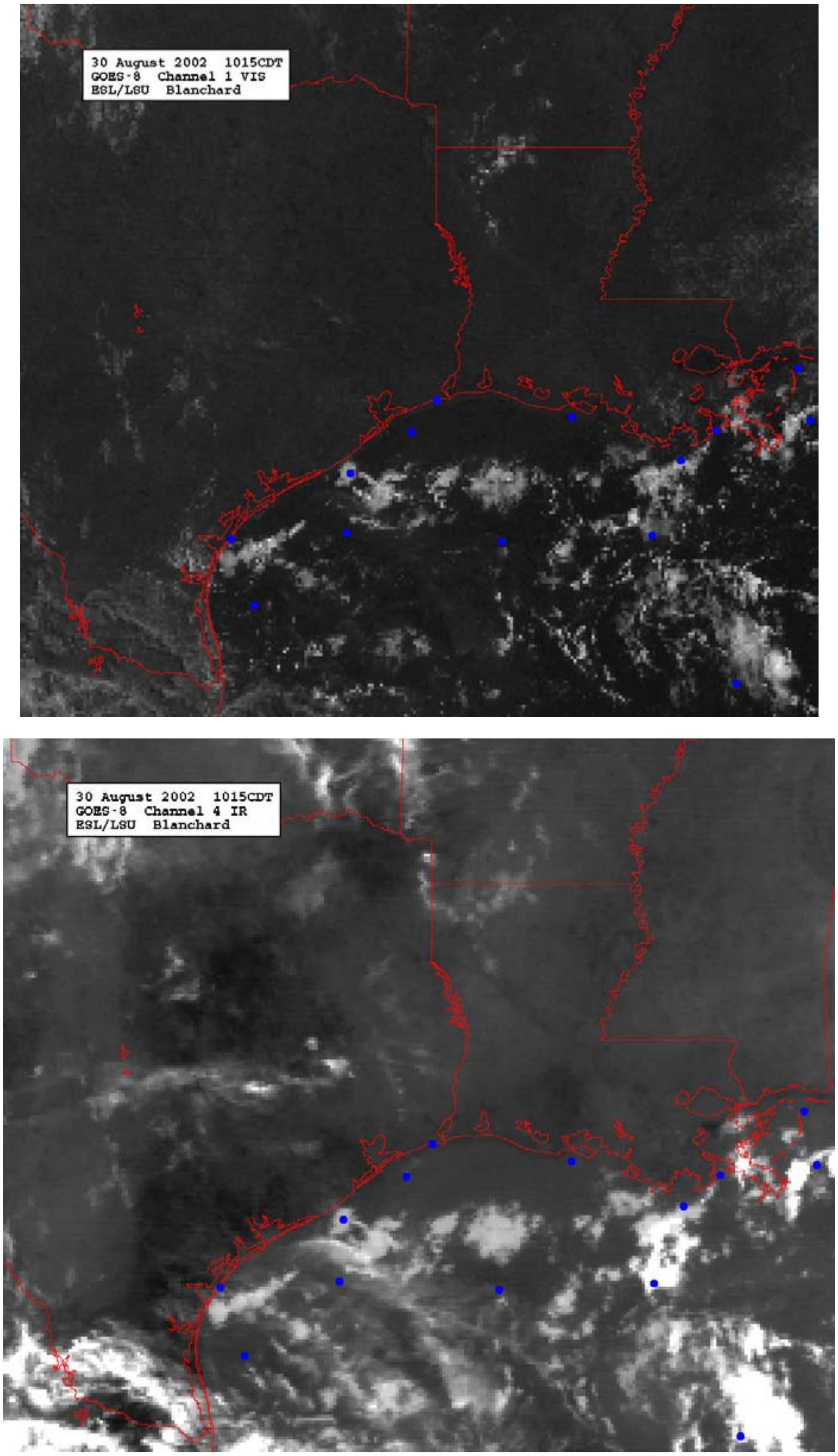

Figure 142. 1015 CDT 30 August 2002 GOES-8 visible image (top) and infrared image (bottom).

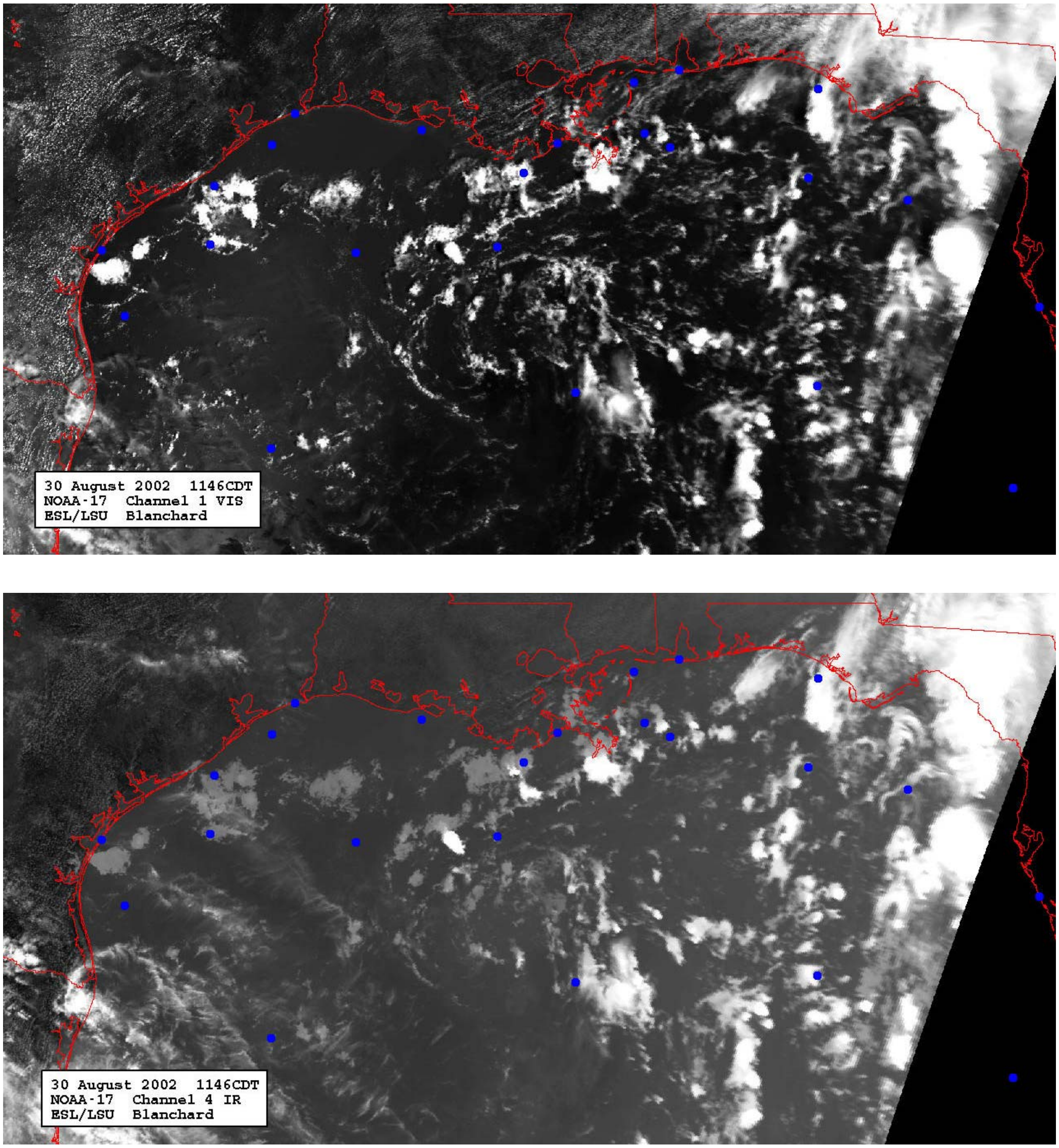

Figure 143. 1146 CDT 30 August 2002 NOAA-17 visible image (top) and infrared image (bottom).

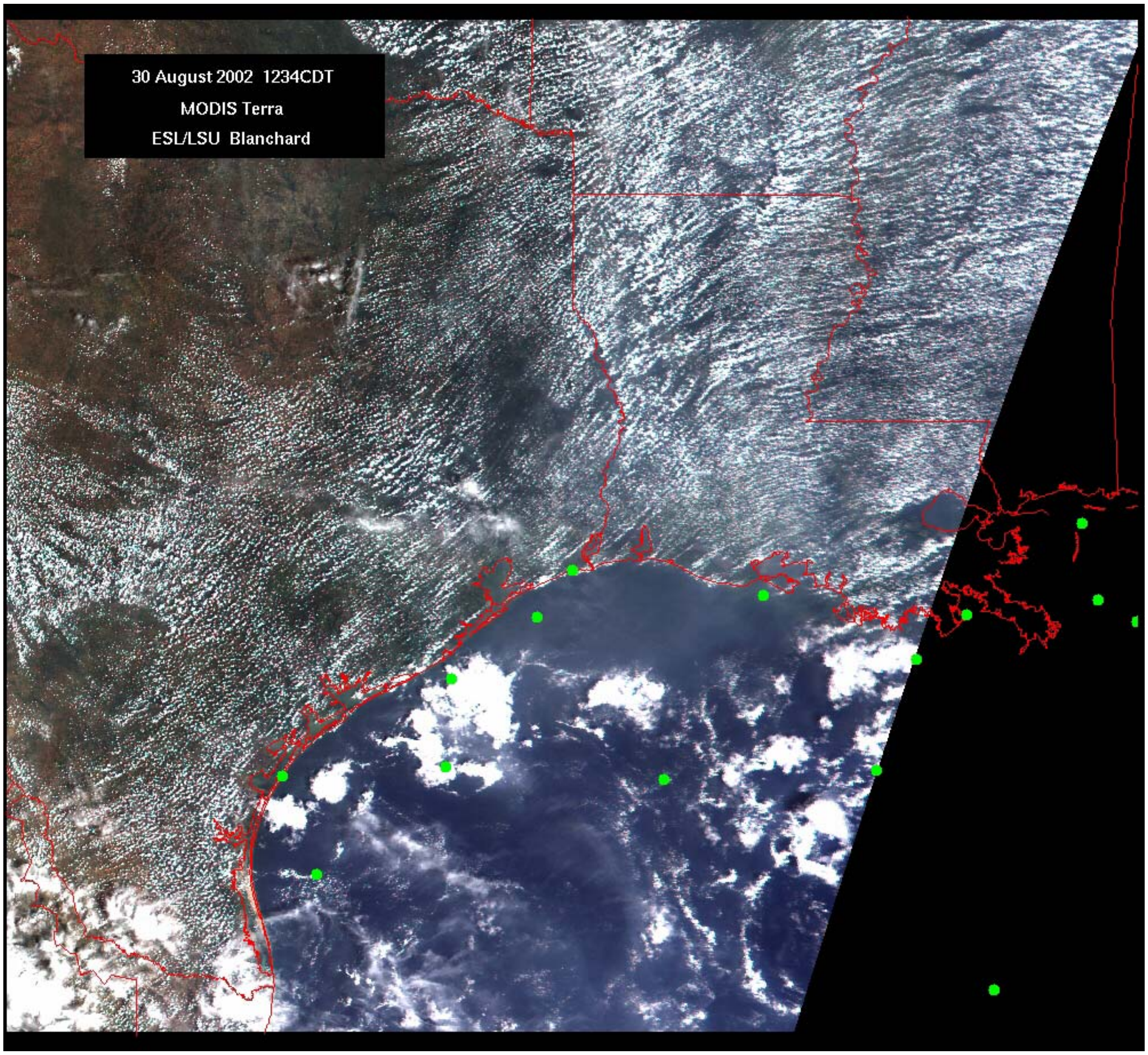

Figure 144. 1234 CDT 30 August 2002 MODIS true color image.

F. 14 - 15 September 2002

Louisiana is situated between the remnants of Tropical Depression Hanna over Alabama and an advancing low center / frontal boundary over Texas (Fig. 146). Winds are mostly westerly and light to calm (Fig. 145). There are widespread indications of haze and fog, the latter along the Louisiana coast produces MVRF and IFR restrictions (Fig. 147). There is considerable cloud cover moving into Louisiana from eastern Texas, however CSI-3 appears mostly clear during the period (Figs. 149 - 152). September 15 begins as neutral but becomes free convective as wind speeds decrease. Average computed mixed height during hours 23 - 02 CST is 536 m, lowering to 395 m during hours 07 - 09 CST.

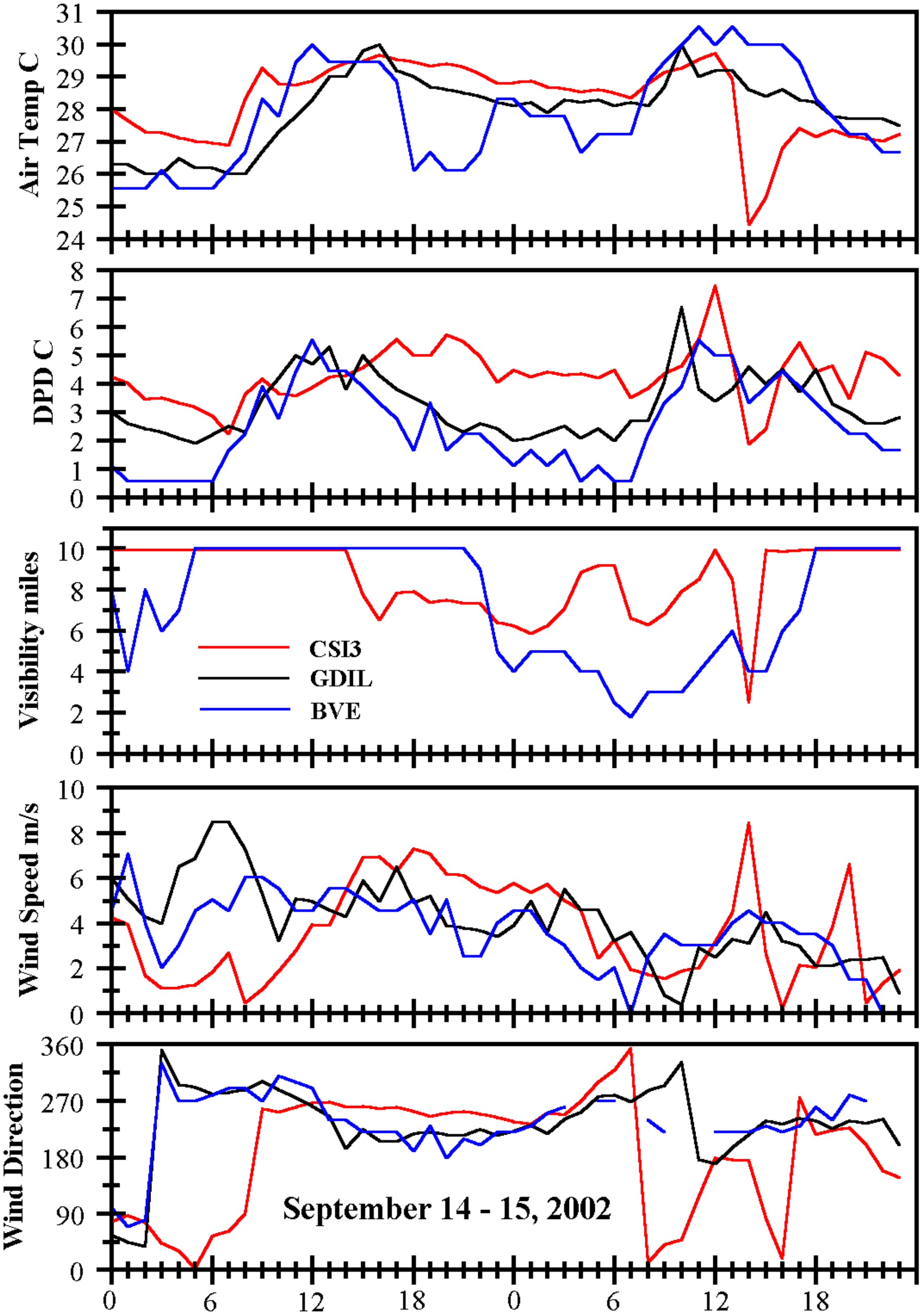

Figure 145. Time series (CST) of observed parameters on 14 - 15 September 2002.

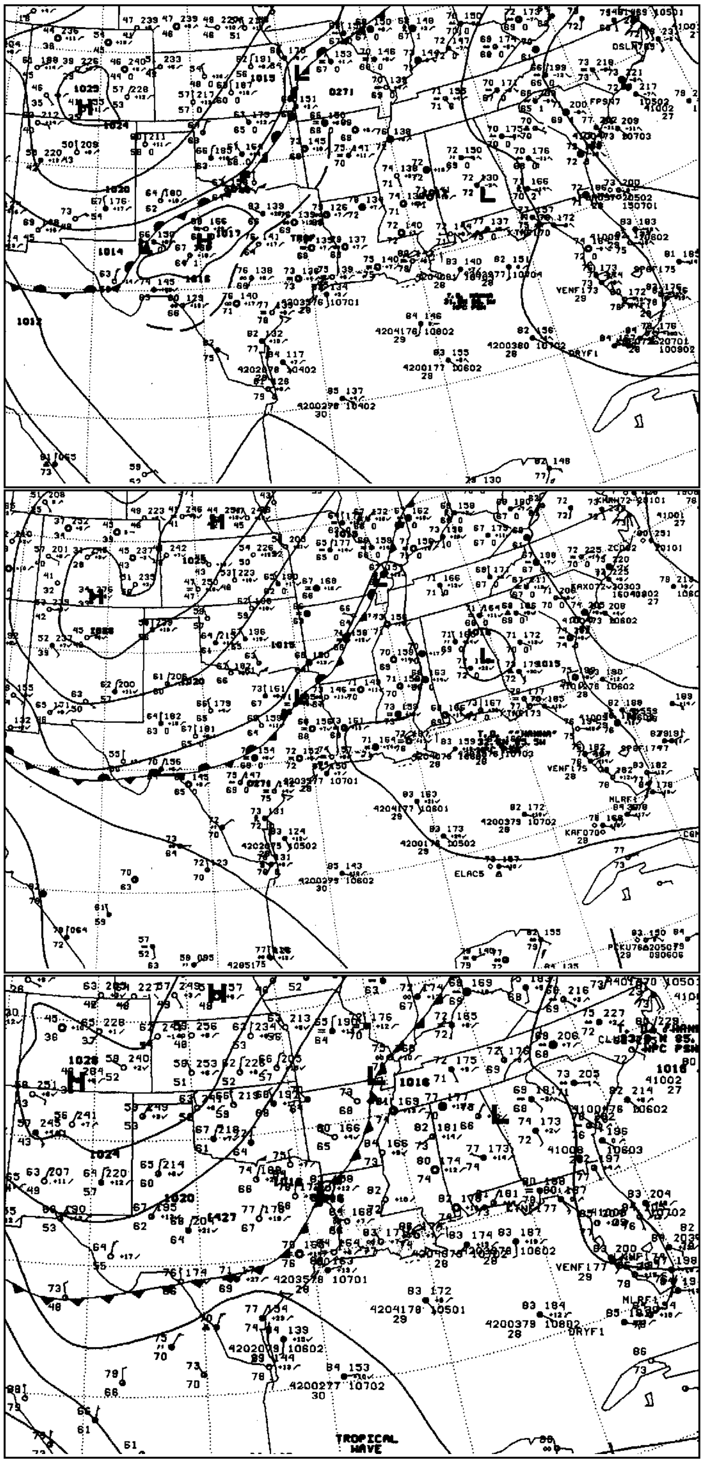

Figure 146. NWS Surface Weather Charts for 0600, 1200, and 1500 Z 15 September 2002 (top to bottom, respectively).

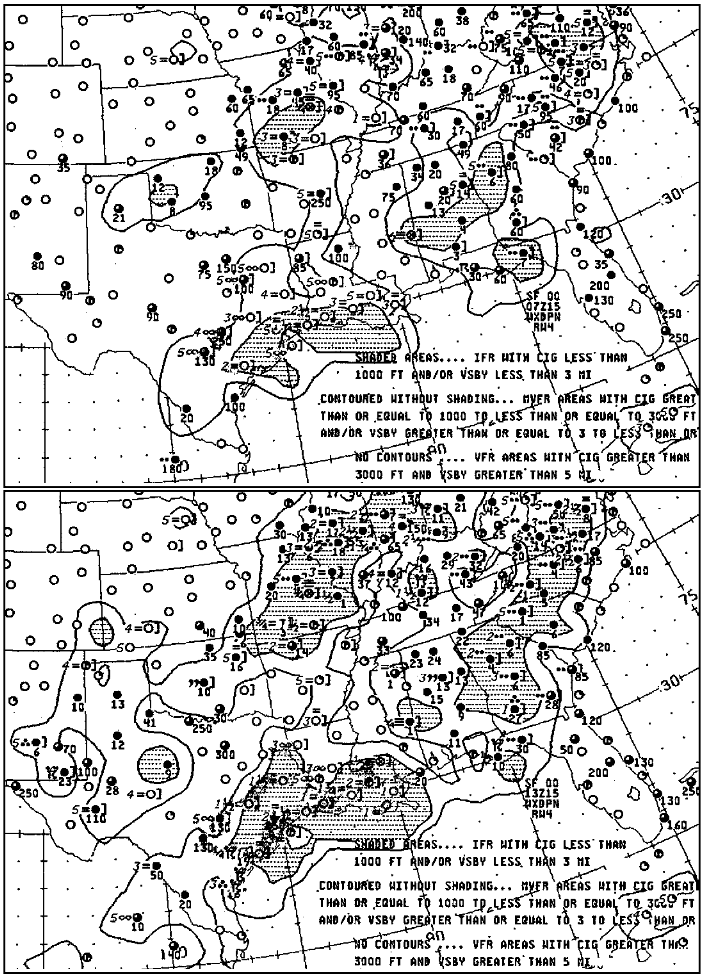

Figure 147. NWS Weather Depiction charts for 07Z (top) and 13Z (bottom) 15 September 2002.

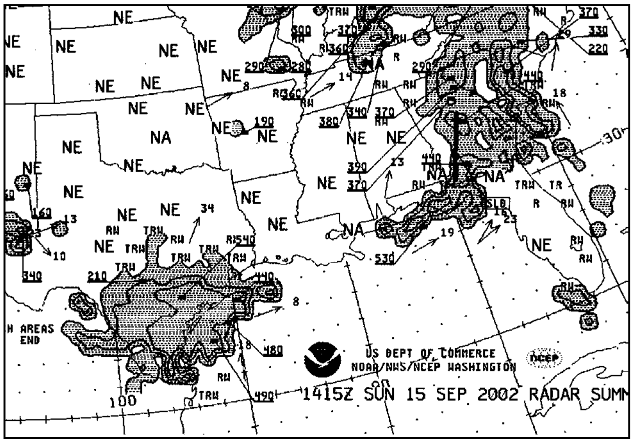

Figure 148. NWS Radar Summary chart for 1415Z 15 September 2002.

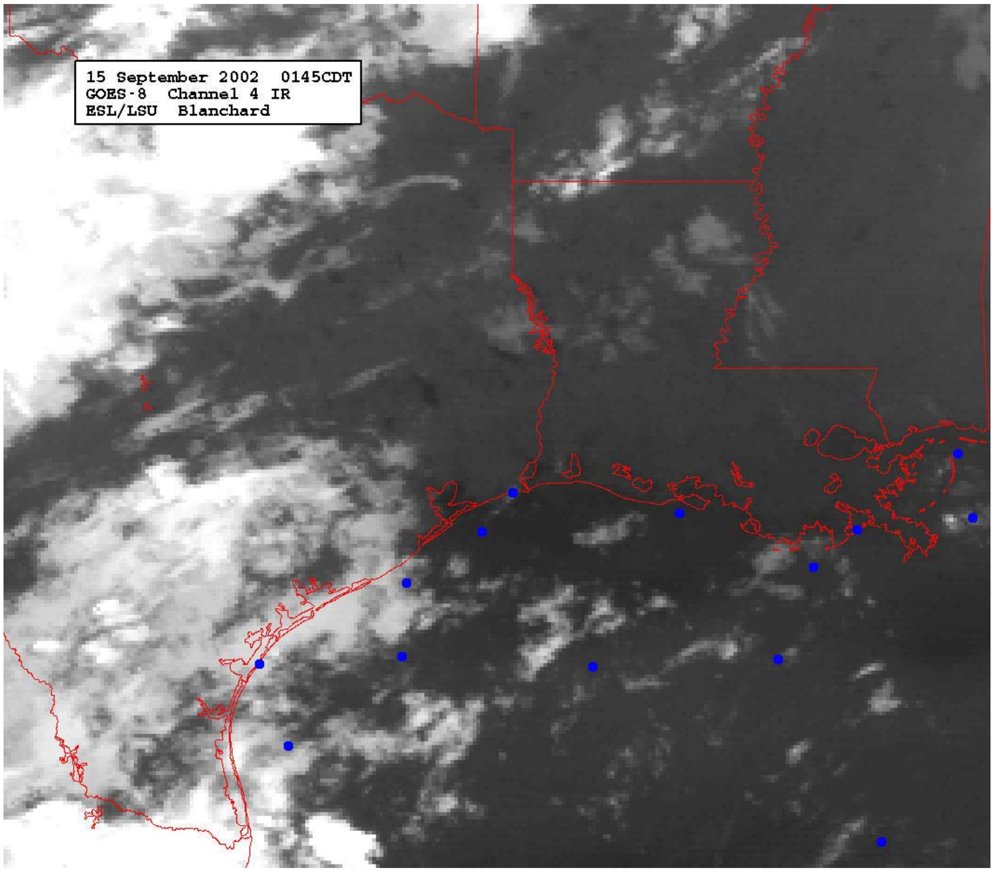

Figure 149. 0145 CDT 15 September 2002 GOES-8 infrared image.

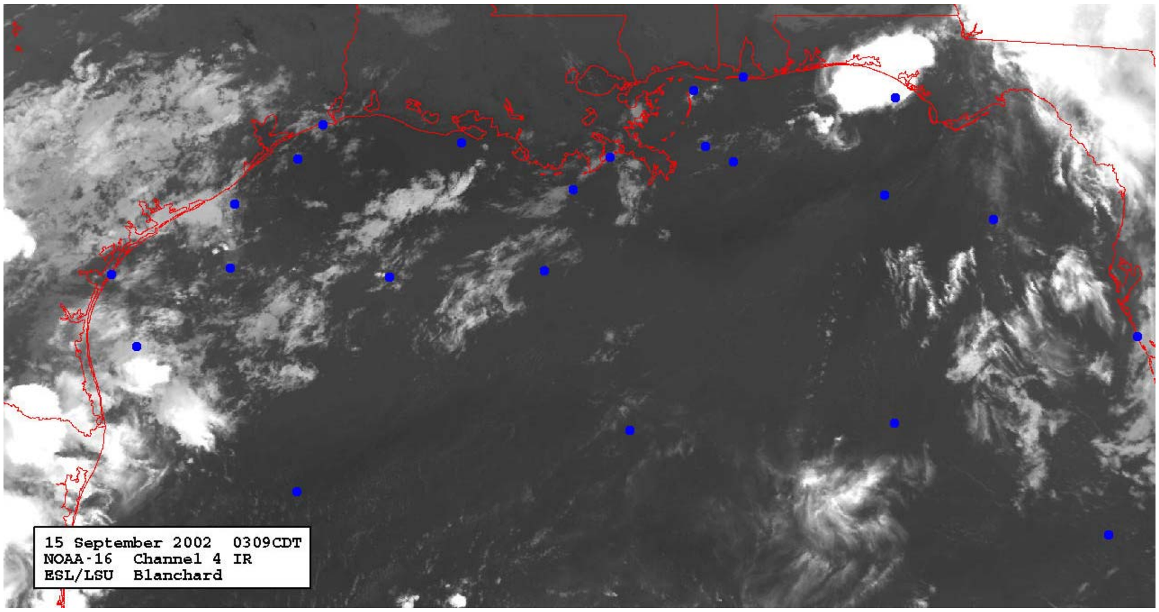

Figure 150. 0309 CDT 15 September 2002 NOAA-16 infrared image.

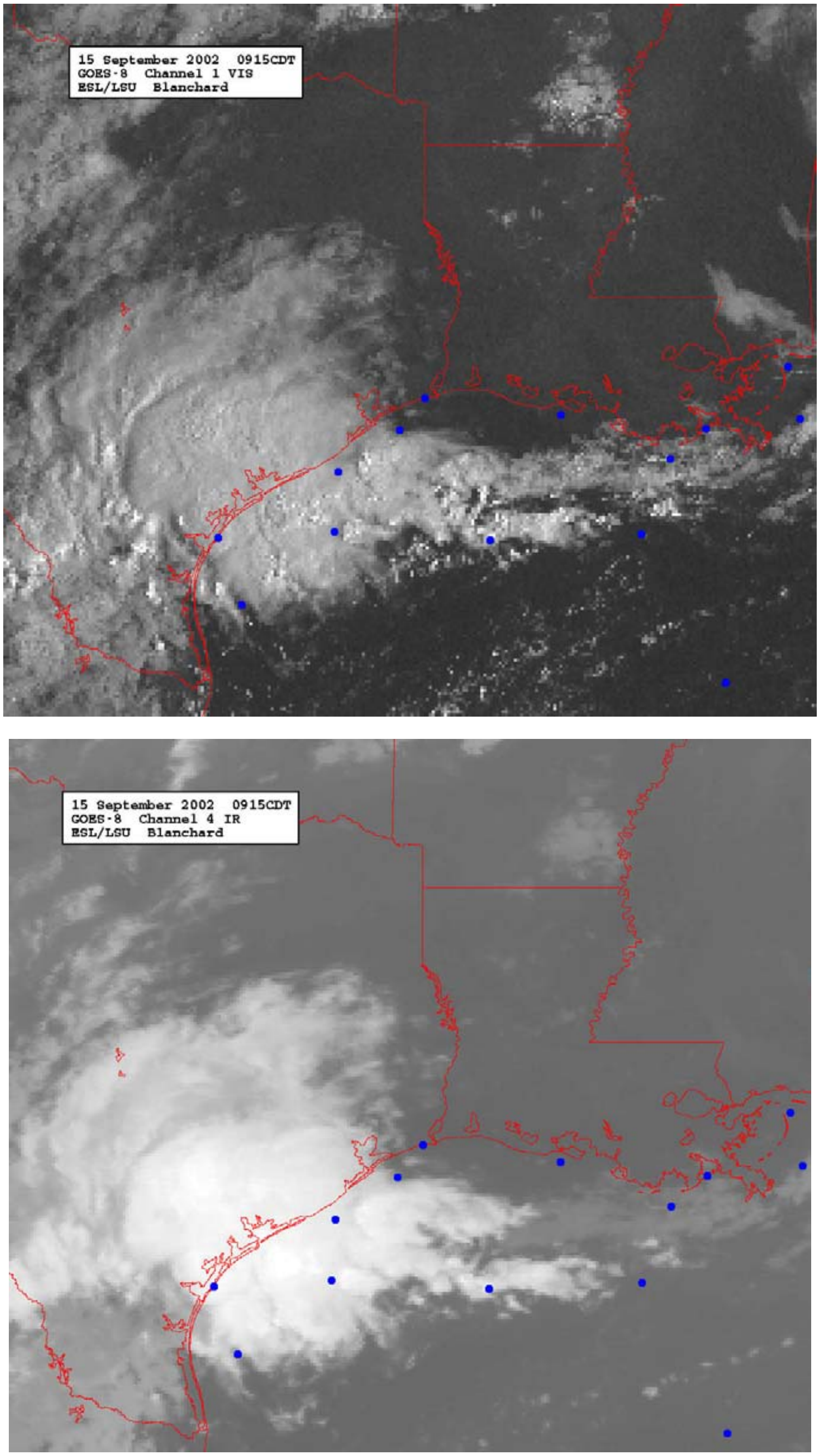

Figure 151. 0915 CDT 15 September 2002 GOES-8 visible image (top) and infrared image (bottom).

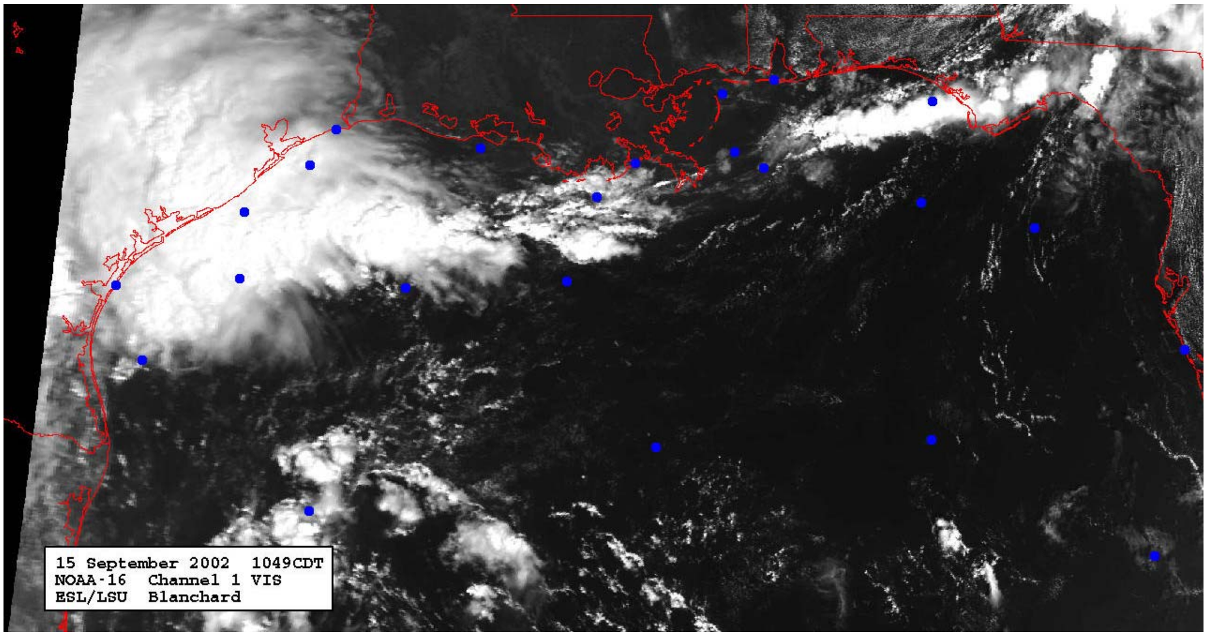

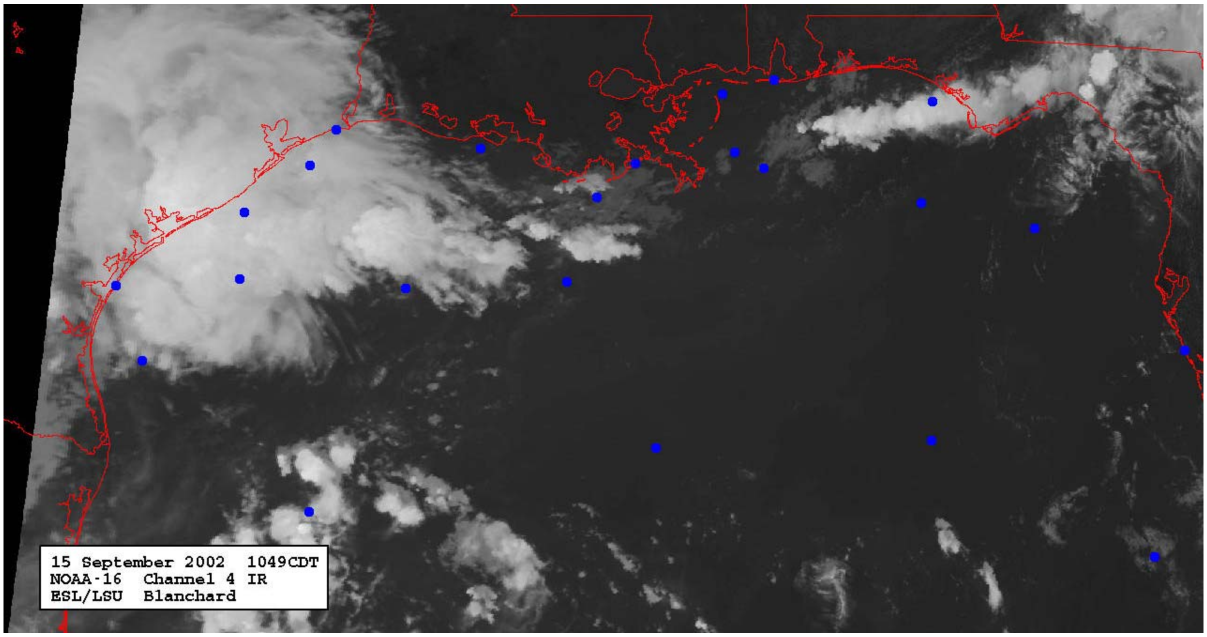

Figure 152. 1049 CDT 15 September 2002 NOAA-16 visible image (top) and infrared image (bottom).

G. 14 - 15 December 2002

High pressure is centered over the Louisiana coast. Surface winds begin light northerly and shift to southerly by the end of the period as the high moves eastward (Figs. 154 - 155). Wind speeds are extremely light and widespread dense fog is indicated along southern Louisiana (Figs 153, 156, 157). Satellite reveals patches of low cloud in the vicinity of CSI-3 (Figs. 158 - 161). Weak winds combined with large air-sea temperature differences produce unstable conditions, with average computed mixed height of 414 m.

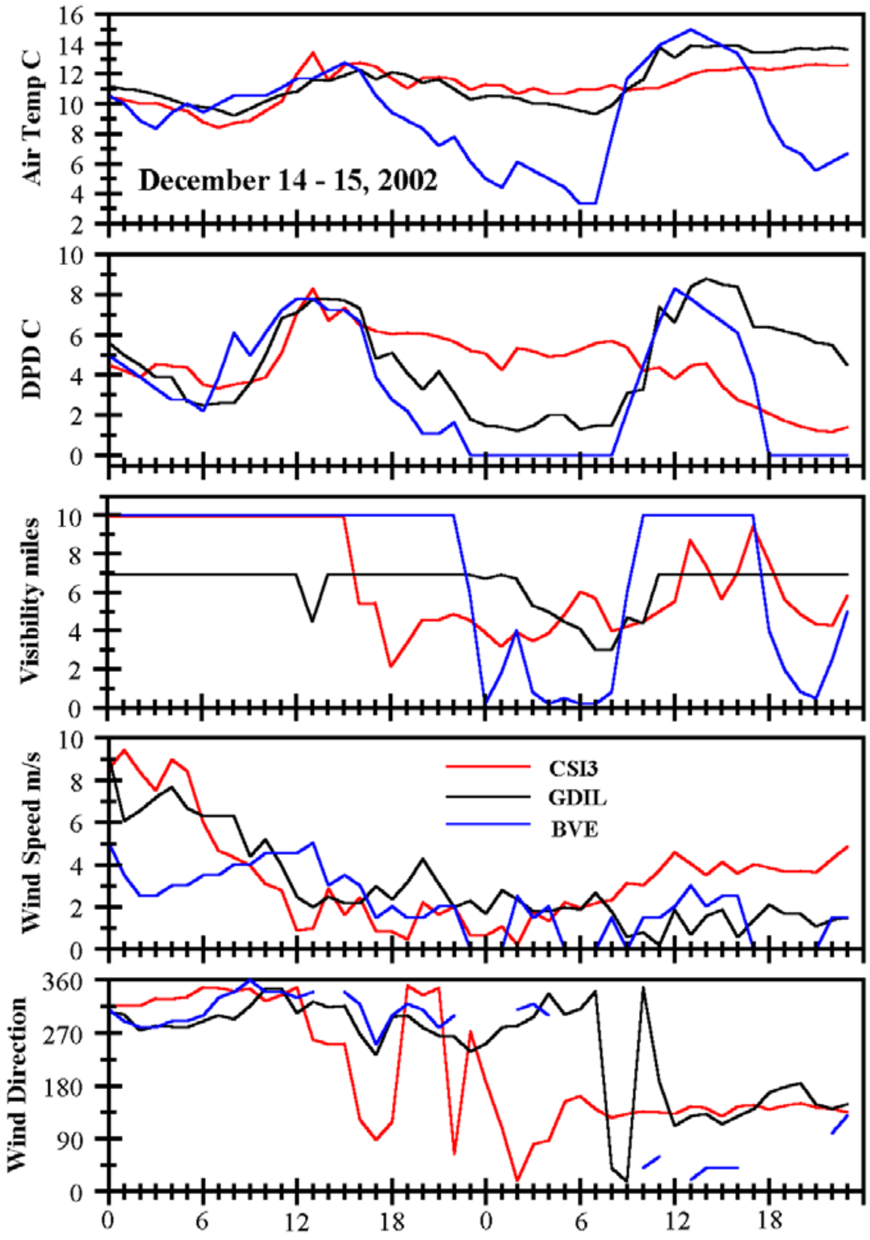

Figure 153. Time series (CST) of observed parameters on 14 - 15 December 2002.

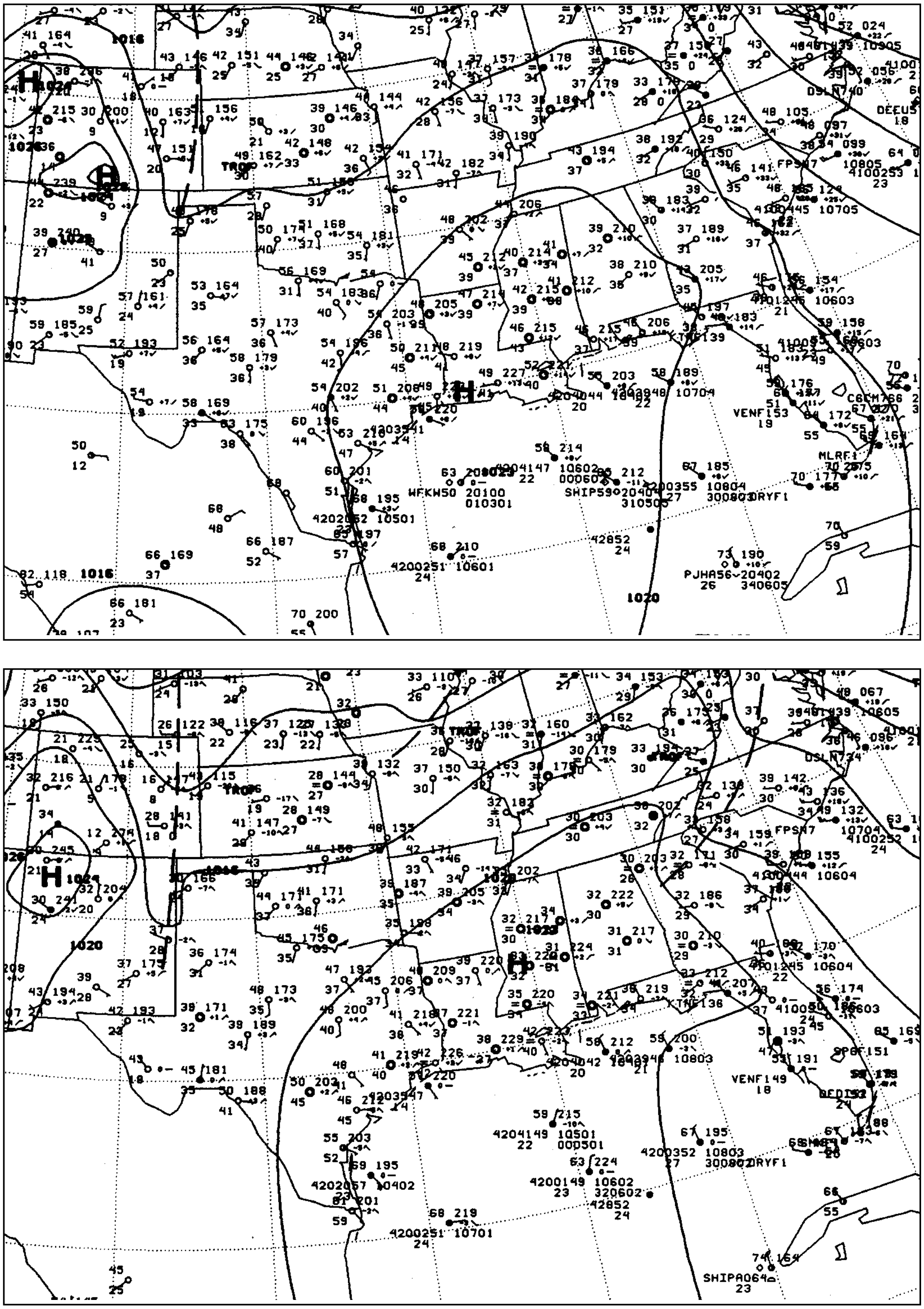

Figure 154. NWS Surface Weather charts for 0000 Z (top) and 0600 Z (bottom) 15 December 2002.

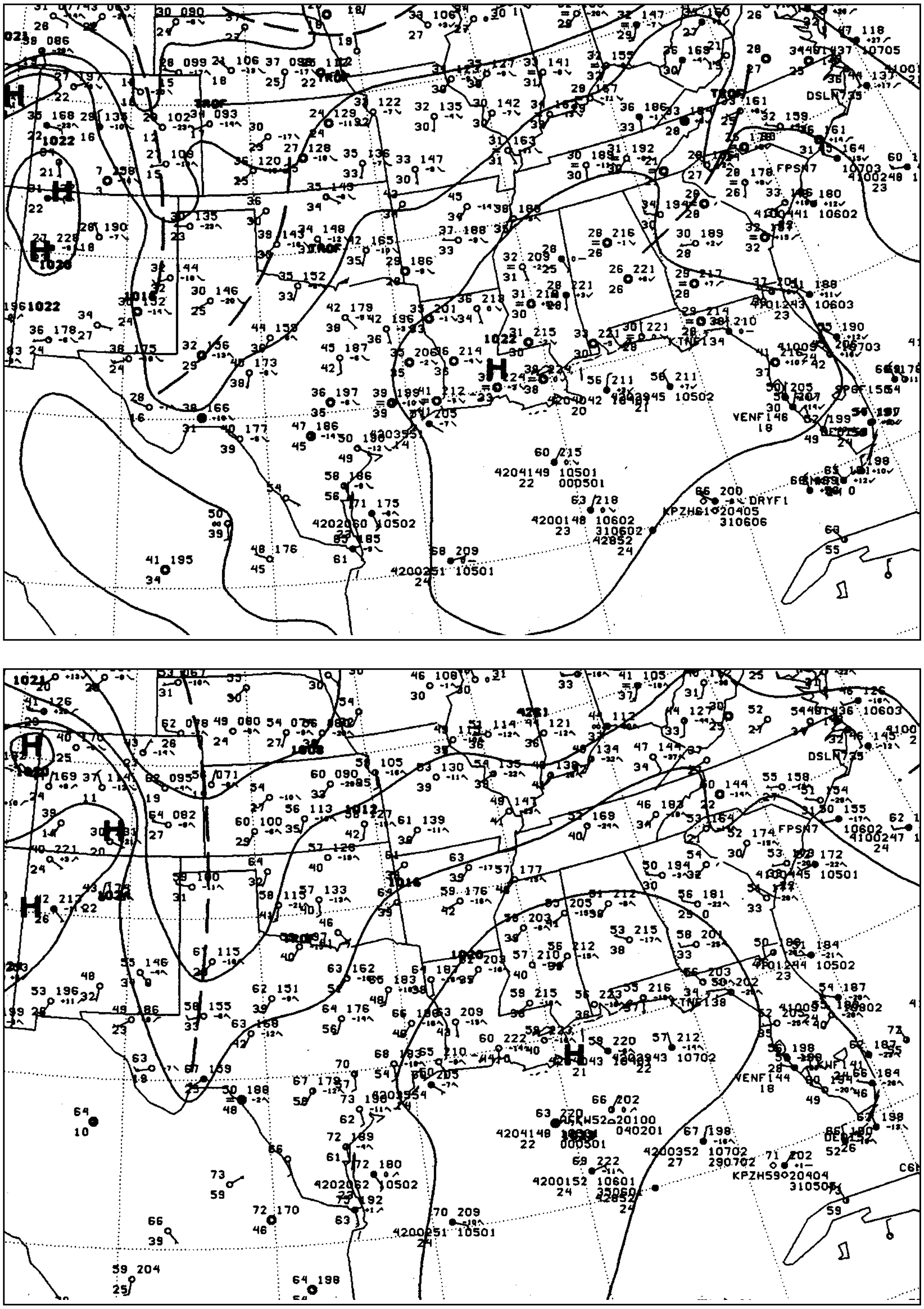

Figure 155. NWS Surface Weather charts for 1200 Z (top) and 18 Z (bottom) 15 December 2002.

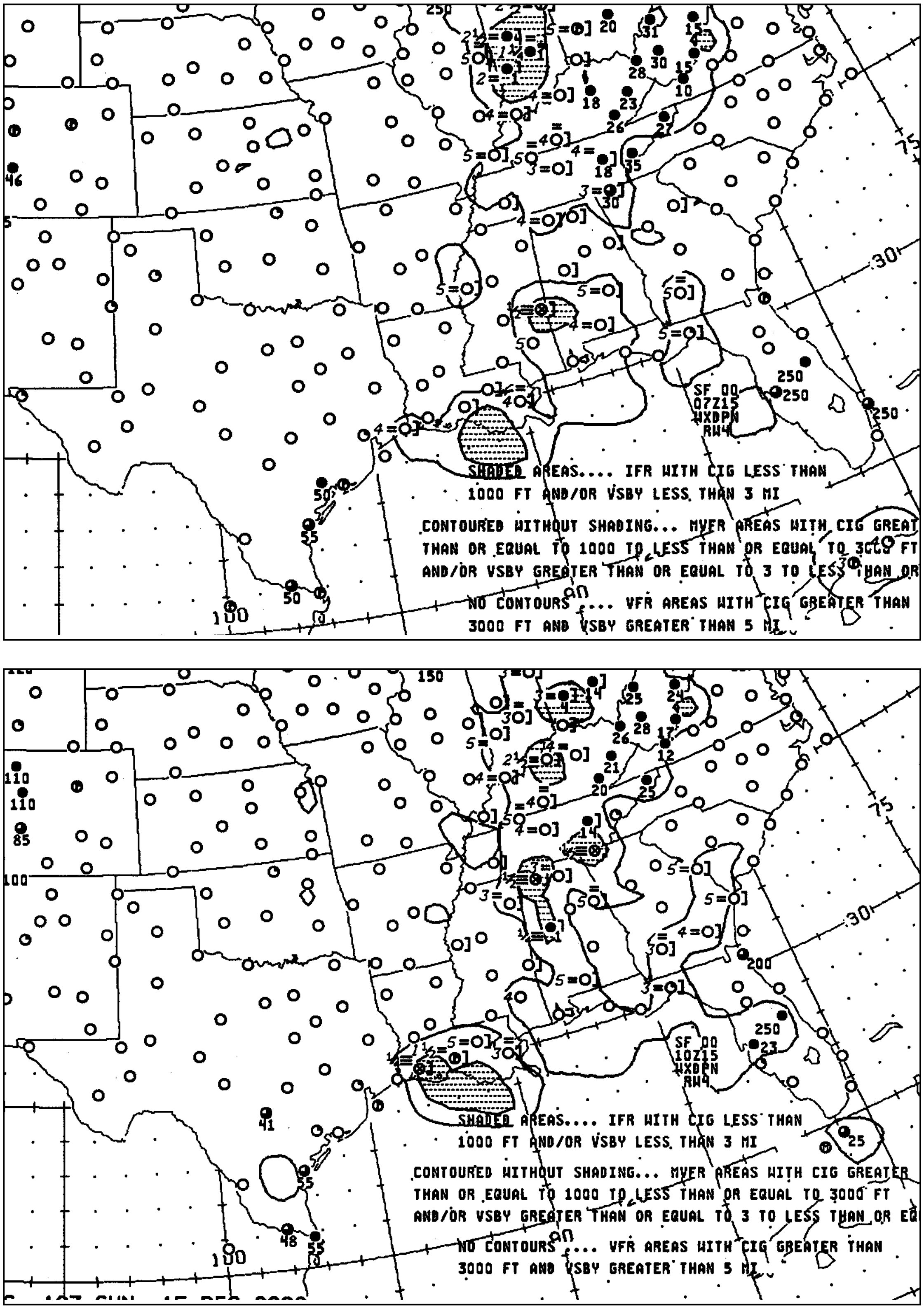

Figure 156. NWS Weather Depiction charts for 07 Z (top) and 10 Z (bottom) 15 December 2002.

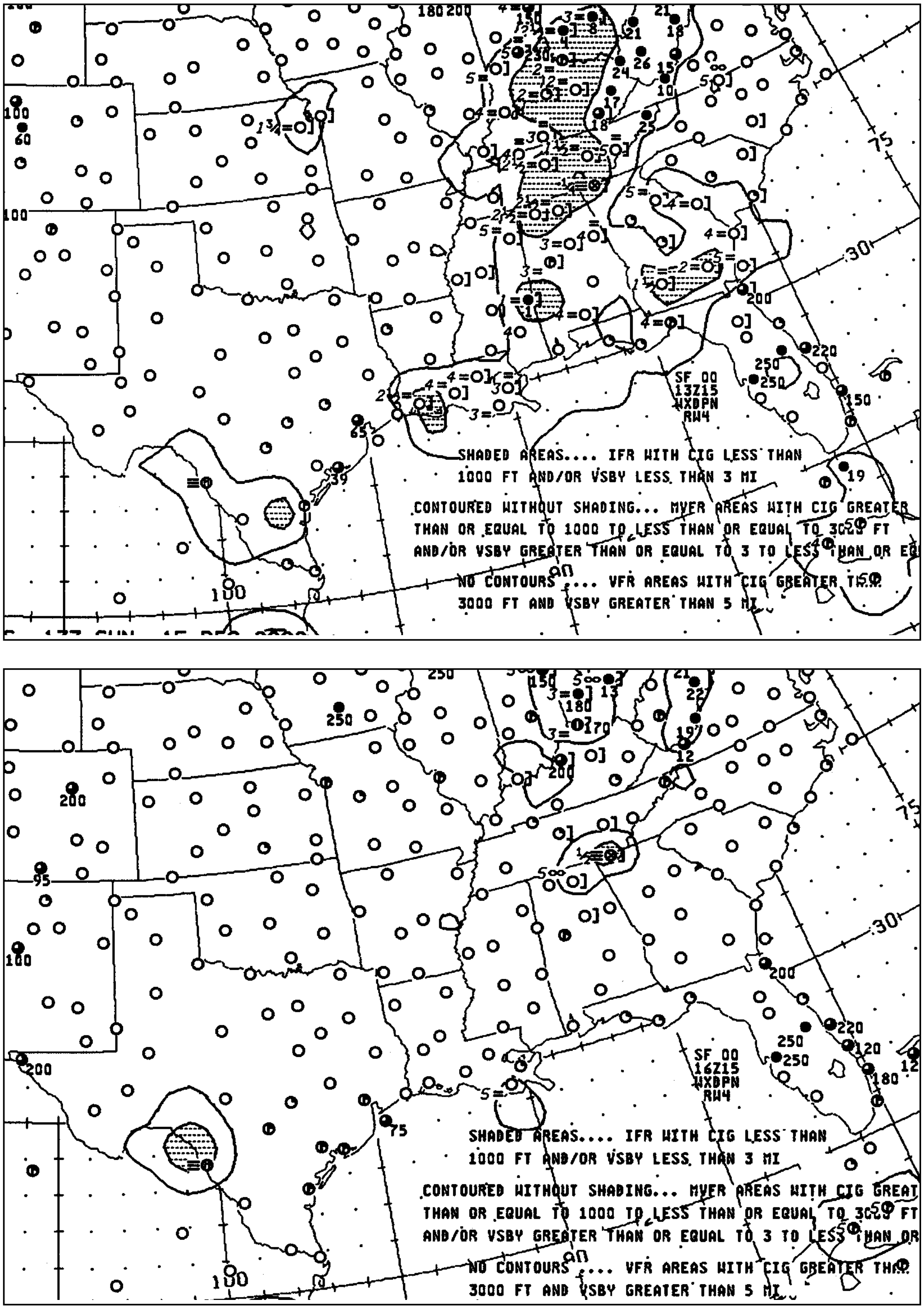

Figure 157. NWS Weather Depiction charts for 13 Z (top) and 16 Z (bottom) 15 December 2002.

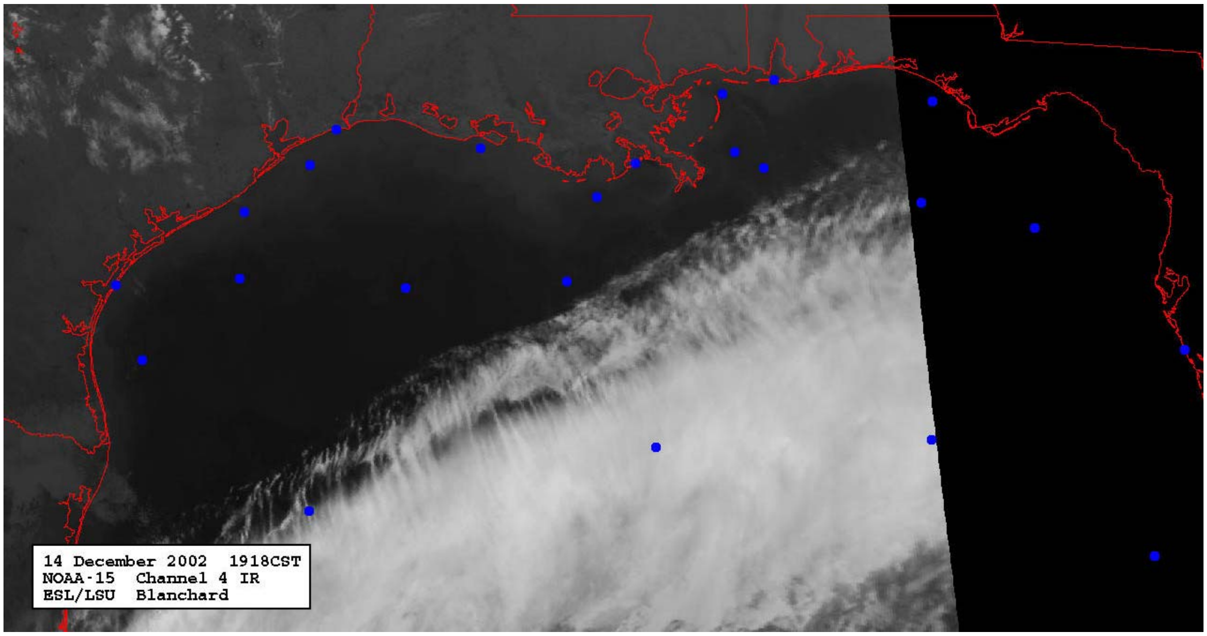

Figure 158. 1918 CST 14 December 2002 NOAA-15 infrared image.

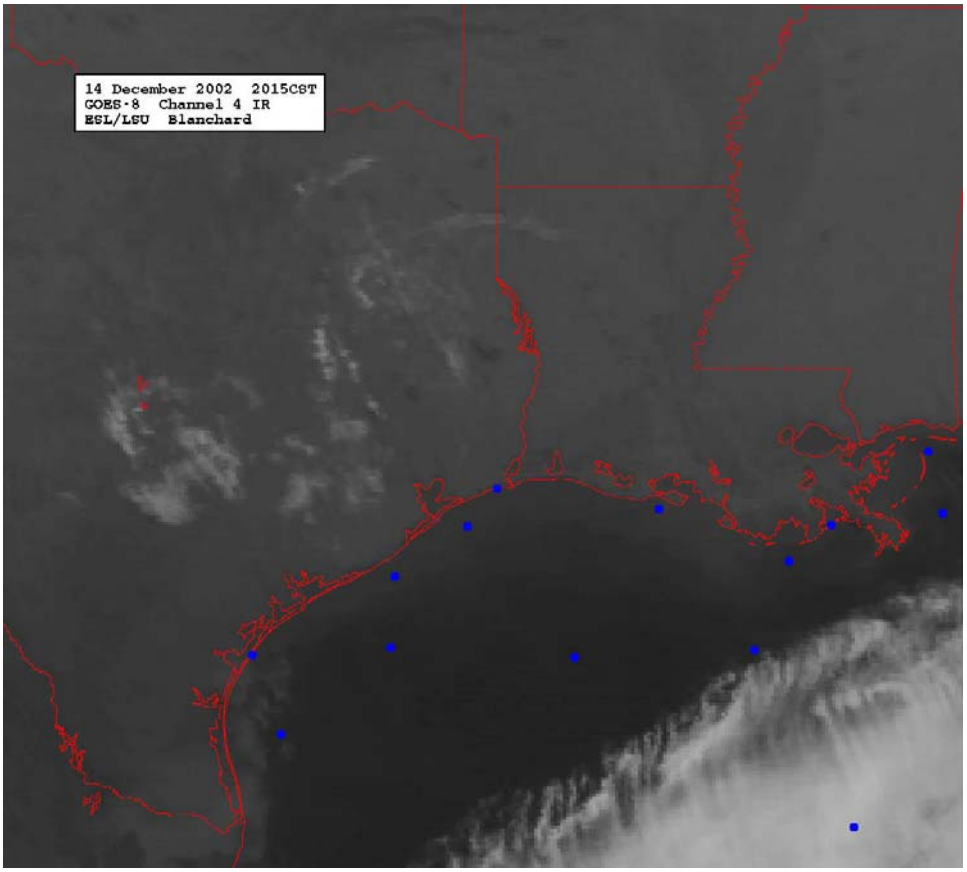

Figure 159. 2015 CST 14 December 2002 GOES-8 infrared image.

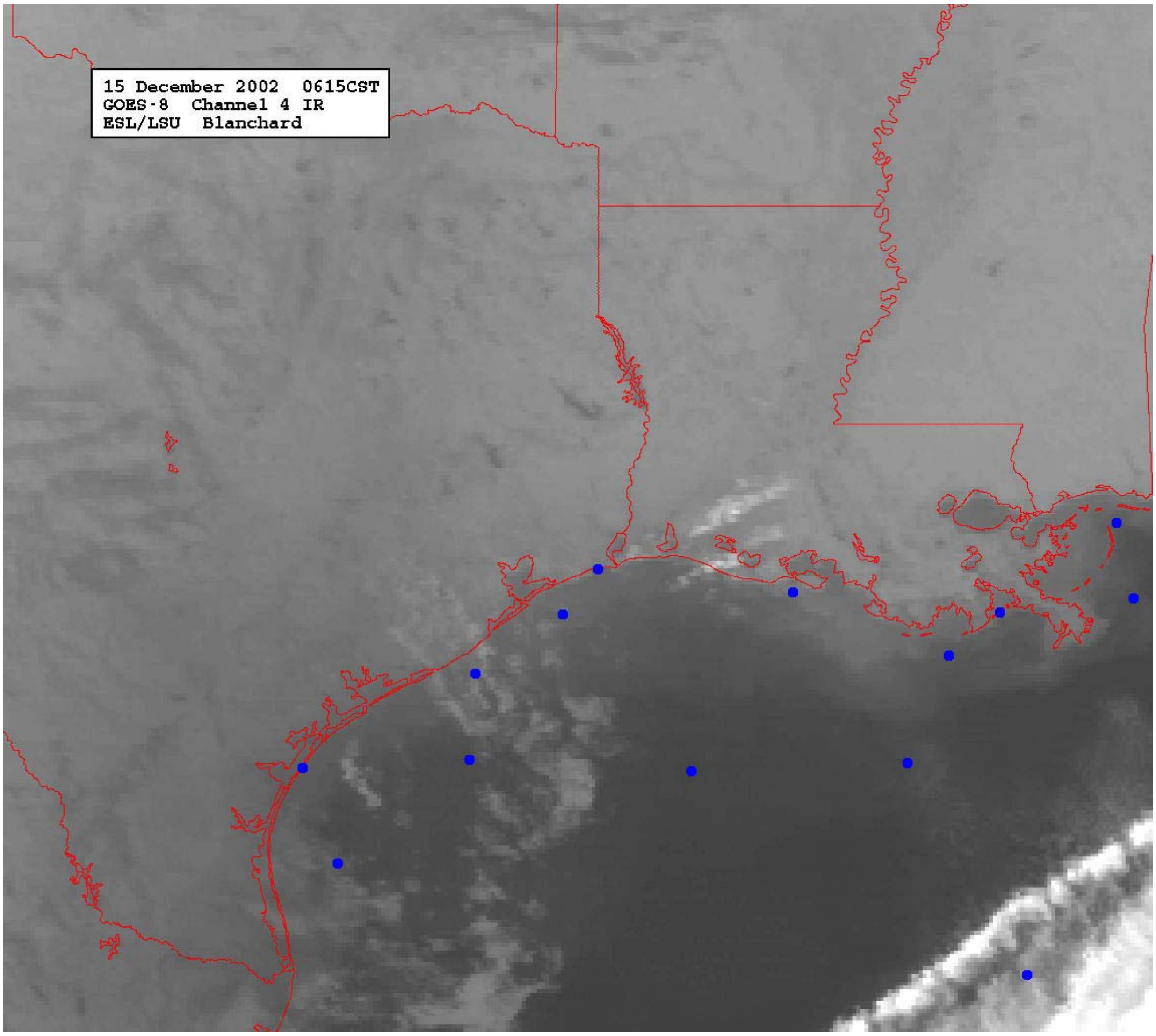

Figure 160. 0615 CST 15 December 2002 GOES-8 infrared image.

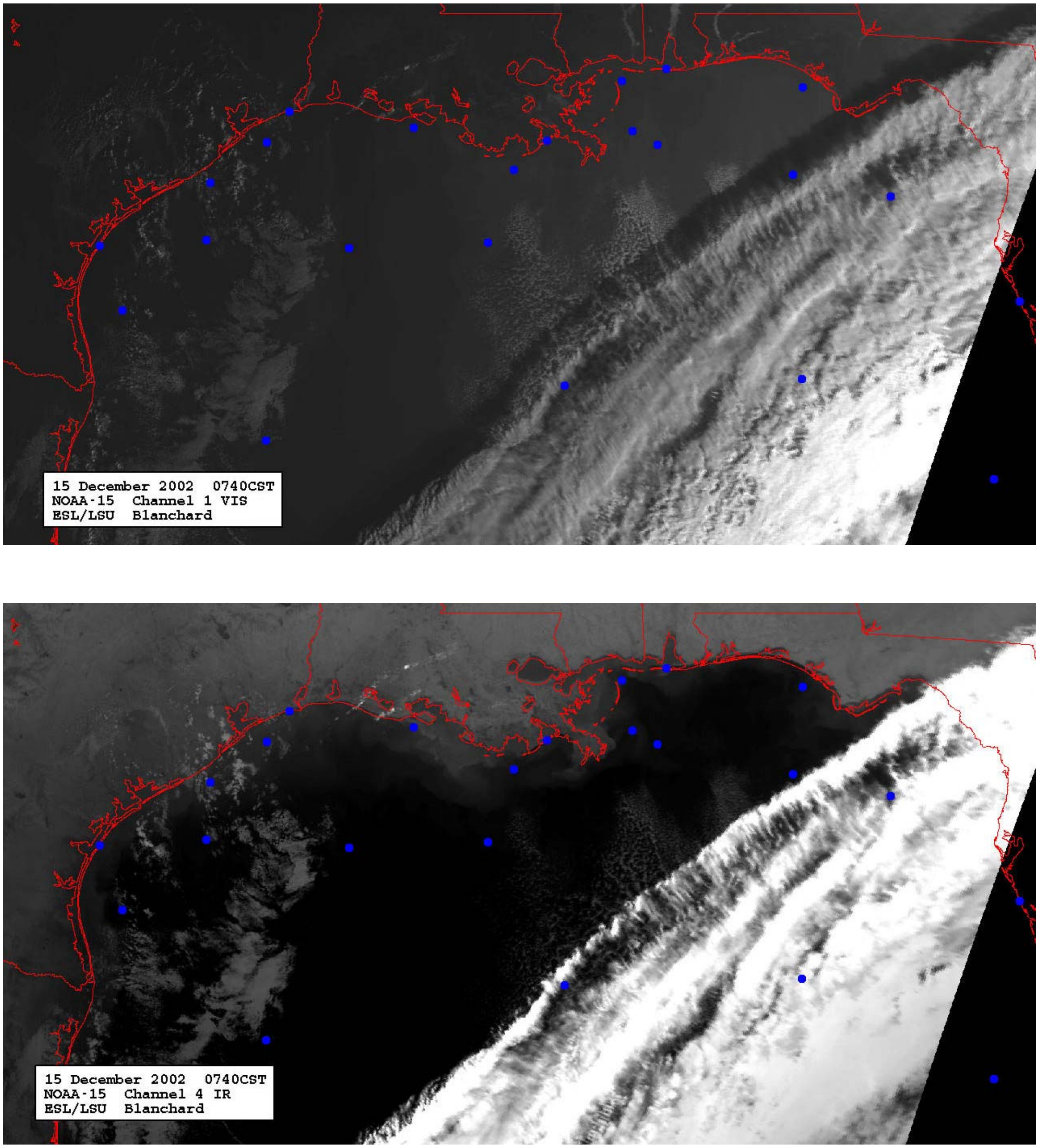

Figure 161. 0740 CST 15 December 2002 NOAA-15 visible image (top) and infrared image (bottom).

H. 26 April 2003

Weather over Louisiana is dominated by a high pressure ridge building in behind a cold frontal boundary (Figs. 163 - 164). Winds are mostly variable from north and light (Fig. 162). There are no indications of either fog or haze at any reporting stations in southern Louisiana. At CSI-3, stability improves from Class B to D, and average computed mixed height is 983 m. Satellite depicts clear skies over the northwestern Gulf of Mexico; however closer inspection reveals what appears to be marsh fires to the southeast of White Lake, with plumes extending towards CSI-3 (Figs. 165- 169). Note that when the wind shifts to the northeast and strengthens, visibility improves.

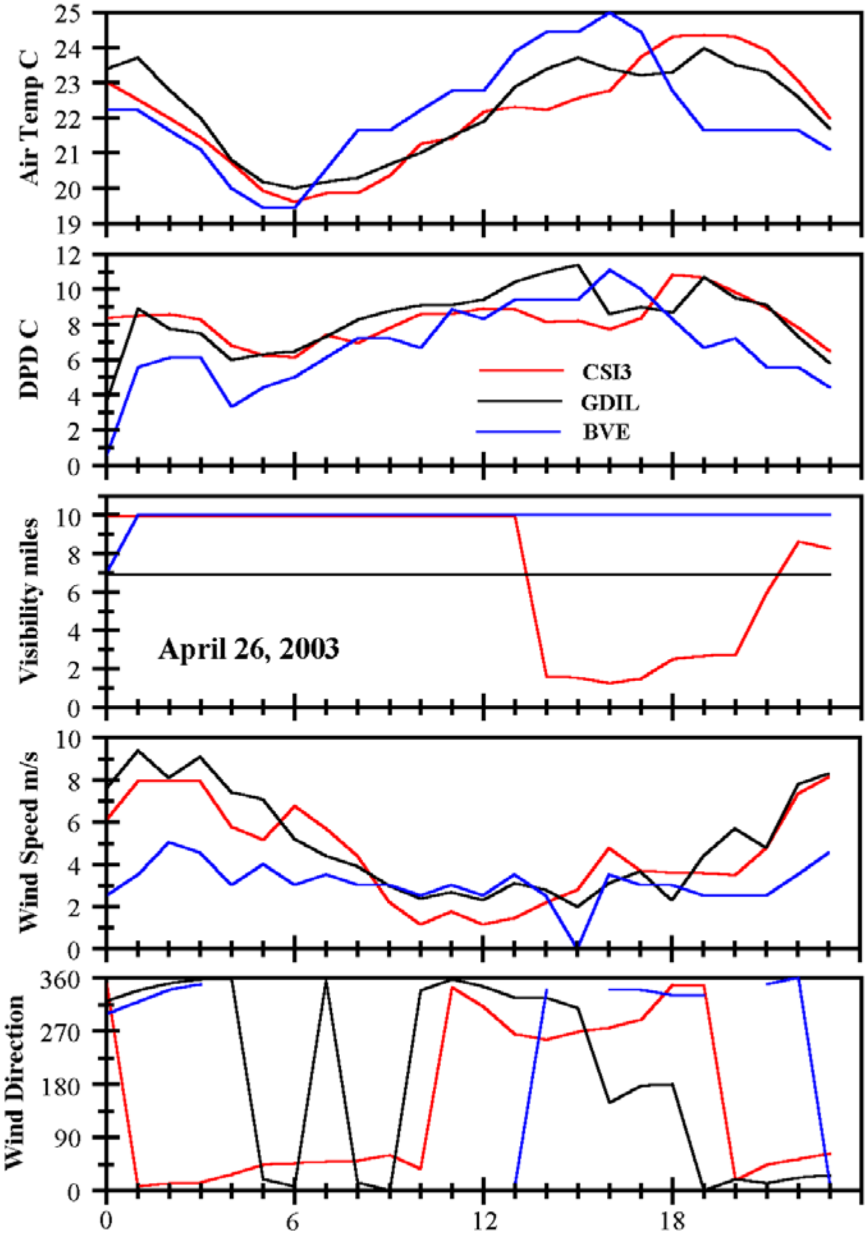

Figure 162. Time series (CST) of observed parameters on 26 April 2003.

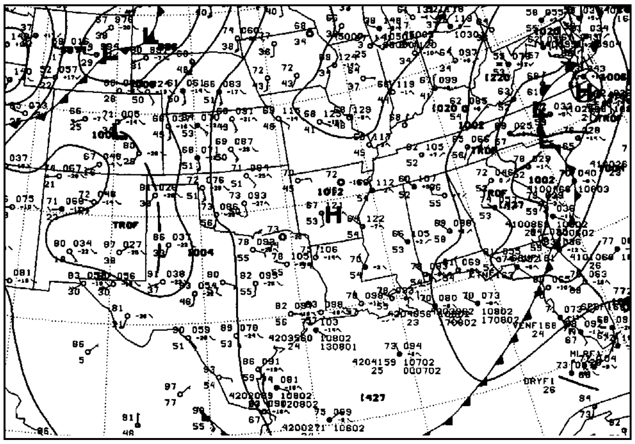

Figure 163. NWS Surface Weather Chart for 2100 Z 26 April 2003.

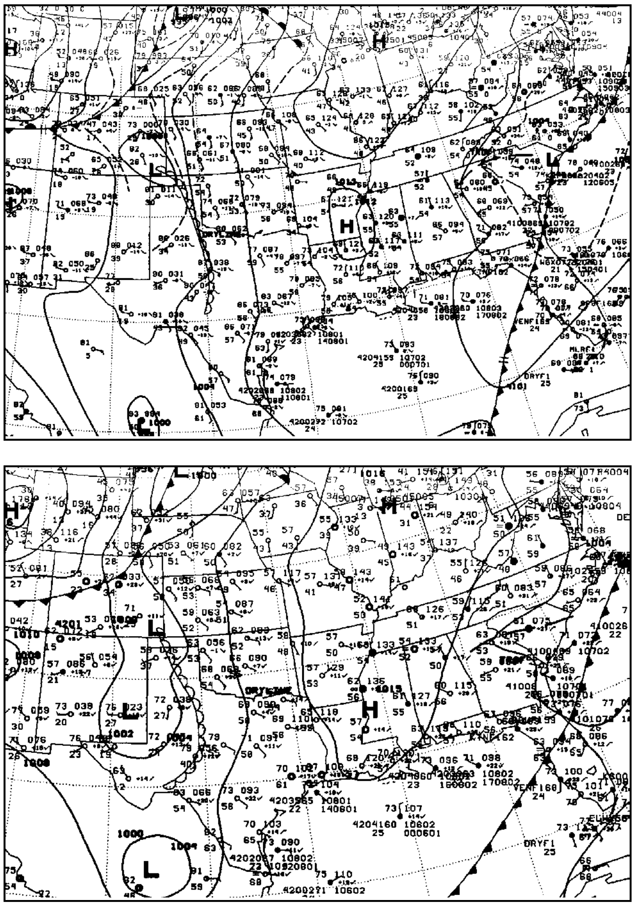

Figure 164. NWS Surface Weather charts for 0000 Z (top) and 0300 Z (bottom) 27 April 2003.

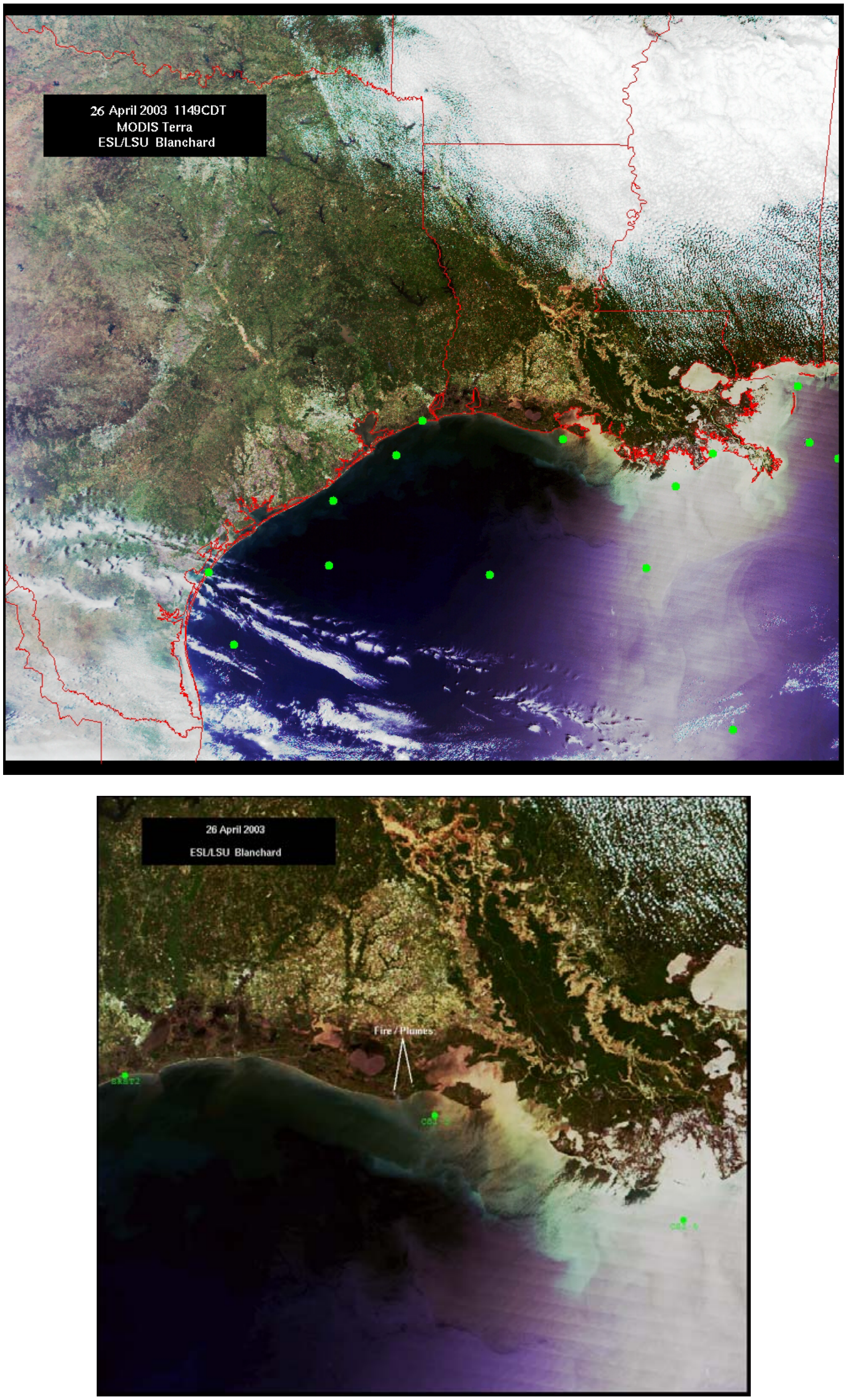

Figure 165. 1149 CDT 26 April 2003 MODIS true color image (top); close-up (bottom) identifies fires and smoke plume originating on the central Louisiana coast.

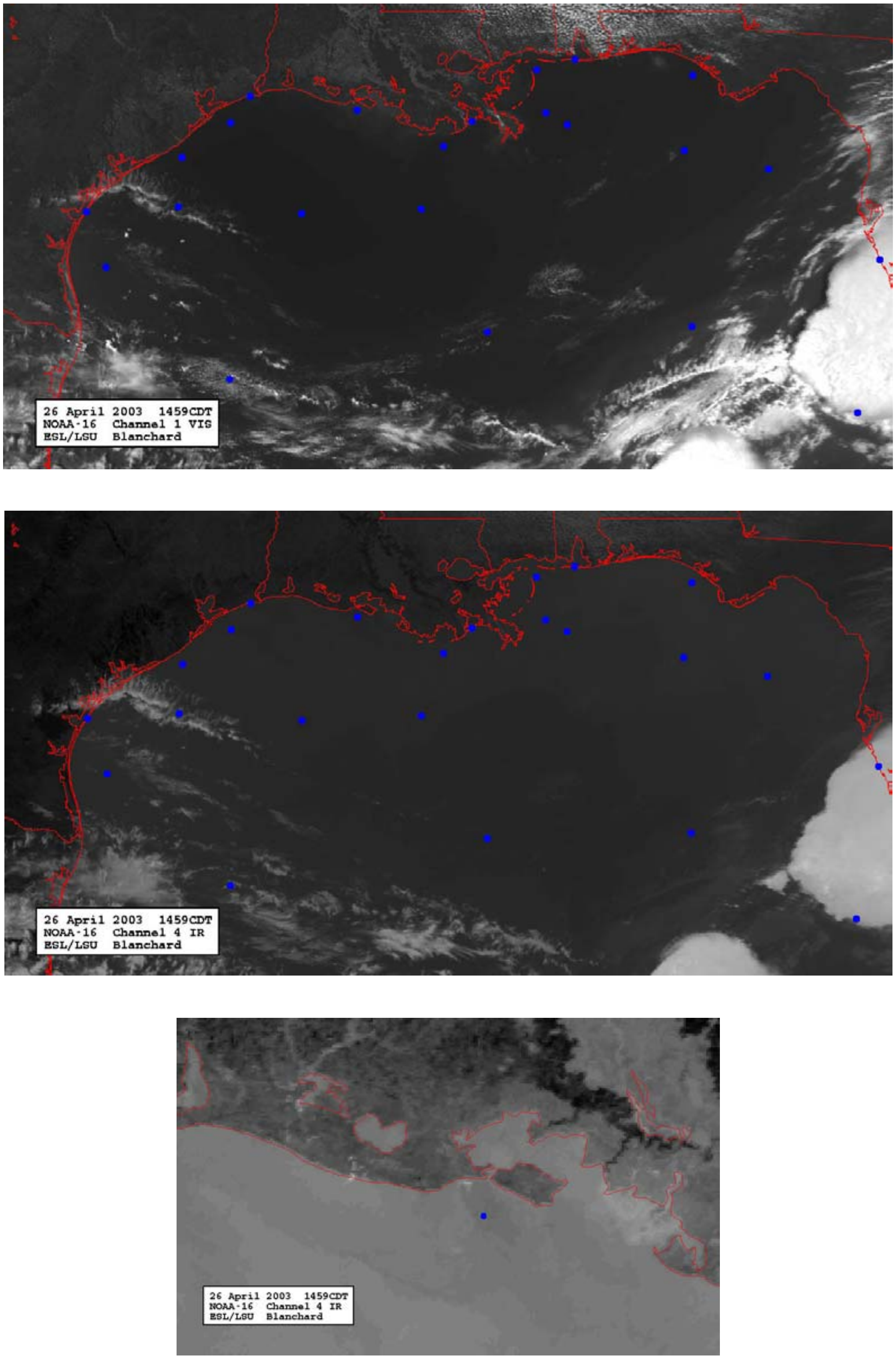

Figure 166. 1459 CDT 26 April 2003 NOAA-16 visible (top) and infrared (middle) images; bottom panel is close-up of middle IR image.

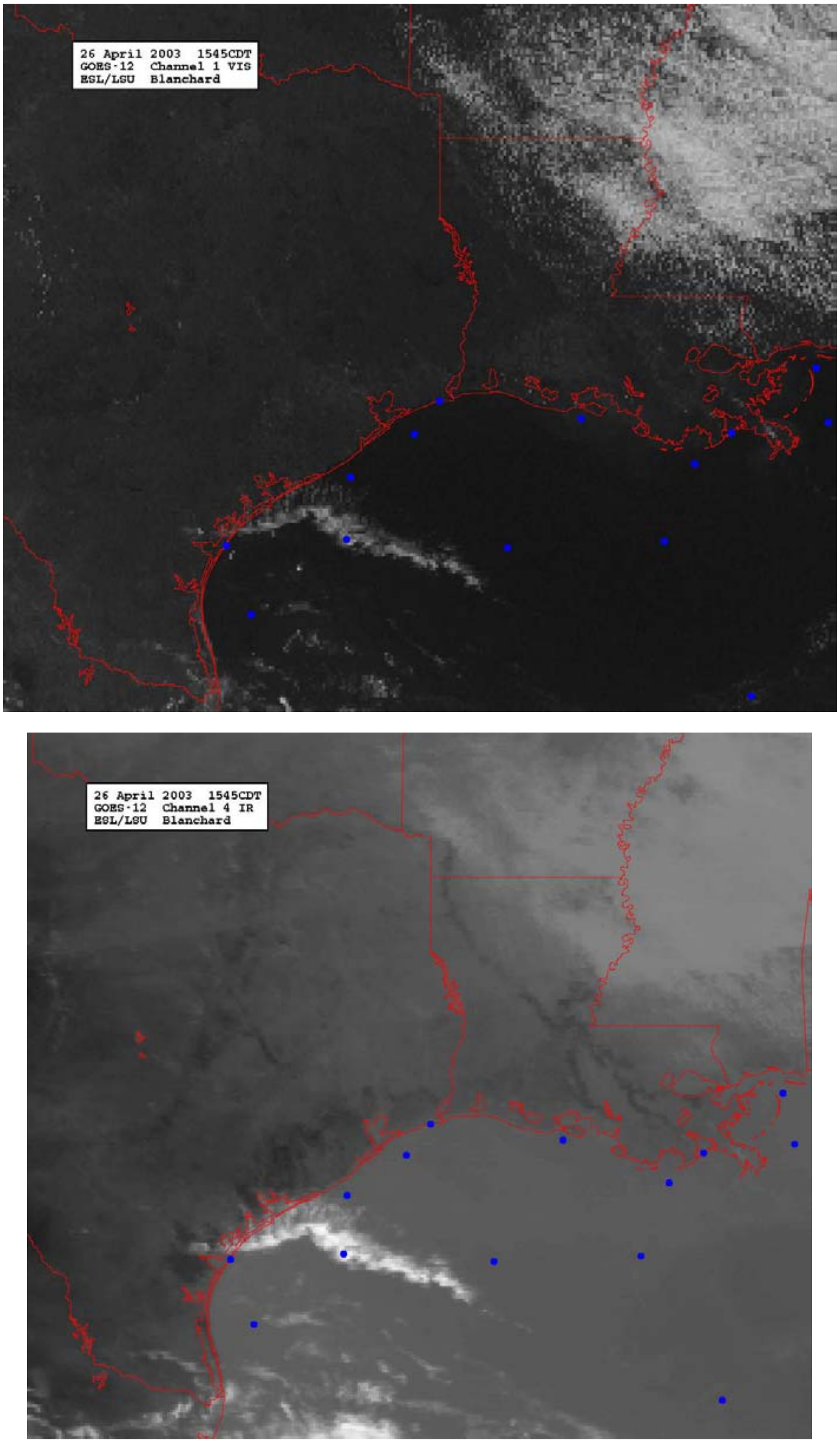

Figure 167. 1545 CDT 26 April 2003 GOES-12 visible image (top) and infrared image (bottom).

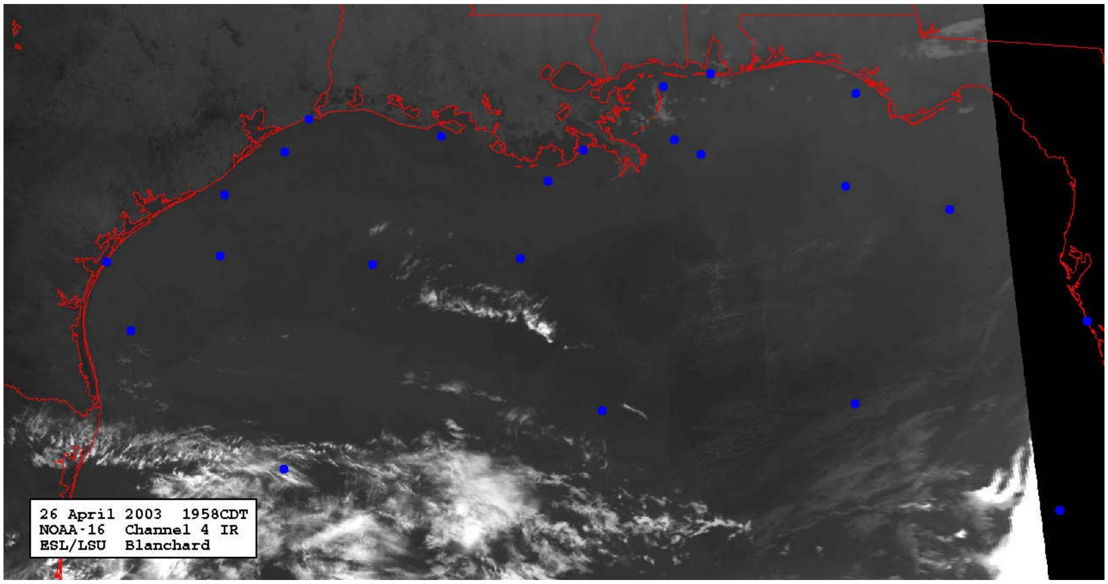

Figure 168. 1958 CDT 26 April 2003 NOAA-16 infrared image.

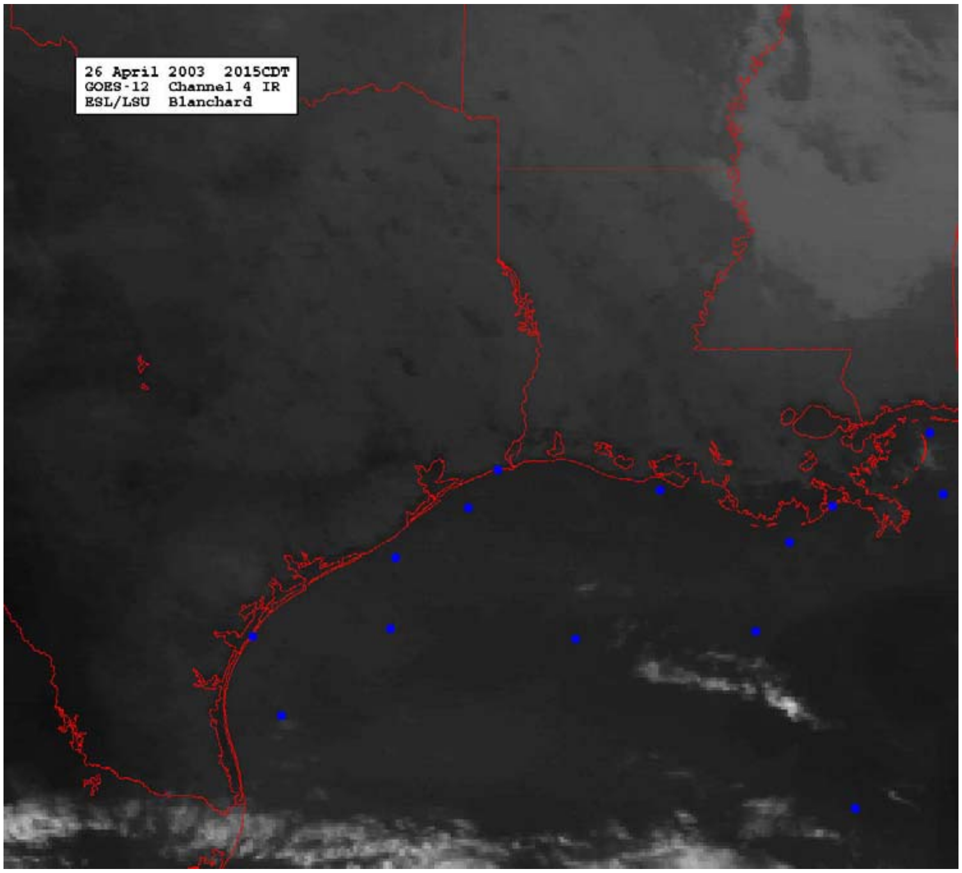

Figure 169. 2015 CDT 26 April 2003 GOES-12 infrared image.

I. Satellite Detection of Plume Geometry

Under certain conditions, the coastal and shelf waters region of the northern Gulf of Mexico can be influenced by emitting sources located further inland. This was demonstrated in two of the case studies presented, in which it appeared that offshore visibility was temporarily reduced due to smoke plume drift from an onshore fire. If the fires cover a large area (such as a controlled marsh burn) or are sustained for some time, the resultant plumes can extend a considerable distance over the shelf waters before significantly dissipating. Since such a feature can easily be detected by satellite (in the daytime), we will now show that lateral plume geometry may be determined through remotely-sensed imagery.

On 6 December, 1999 at 2134 Z (1534 CST), a large plume was detected during the overpass of the NOAA-14 satellite (Fig. 170). High pressure was centered over western Louisiana (see Figs. 171 and 172), and winds were fairly brisk out of the north-northwest. Cool, dry air prevailed as the high eventually moved northeastward and wind diminished.

Channel 2 of the NOAA-14 Advanced Very High Resolution Radiometer data was analyzed as shown in Fig. 170. Note that the pixel width and height are 1.1 km. This spectral channel was selected because it provides a measure of reflectance, hence a better contrast between the higher cloud and the water surface beneath. XVU software was used to analyze the image and find a mean, or threshold, value for the water area outside of the plume. The threshold value was input into a C program, which then examined each pixel in the image to identify the latitude and longitude of the plume boundaries (by difference from the threshold). Horizontal distances between the endpoints were computed, and the coordinates of the plume centerline position found. Finally, the distance from the fire to each point in the centerline was generated (Arnone, personal communication).

According to statistics (see, e.g., Spiegel, 1961, p. 343), the total width (i.e., 100% coverage) of the crosswind standard deviation (σ_y) is ($3.9\ \sigma_y + 3.9\ \sigma_y$) or $7.8\ \sigma_y$. Therefore,

$$\sigma_y = \frac{\text{Total Width of Plume}}{7.8}$$

From the plume analysis conducted, at 20 km downwind of the burning, the total plume width was approximately 12 km. Dividing by 7.8, one gets $\sigma_y = 1.5$ km, which is in excellent agreement with that of 1.5 km under stability C condition (after cold-air outbreak) (see, p. 2-48, Table 2.5 in Turner, 1994). Similarly, at 30 km, $\sigma_y = 2.1$ km (satellite) vs. 2.2 km (Turner), and at 40 km, $\sigma_y = 2.5$ km (satellite) vs. 2.7 km (Turner). Certainly, more cases are needed to further verify this approach.

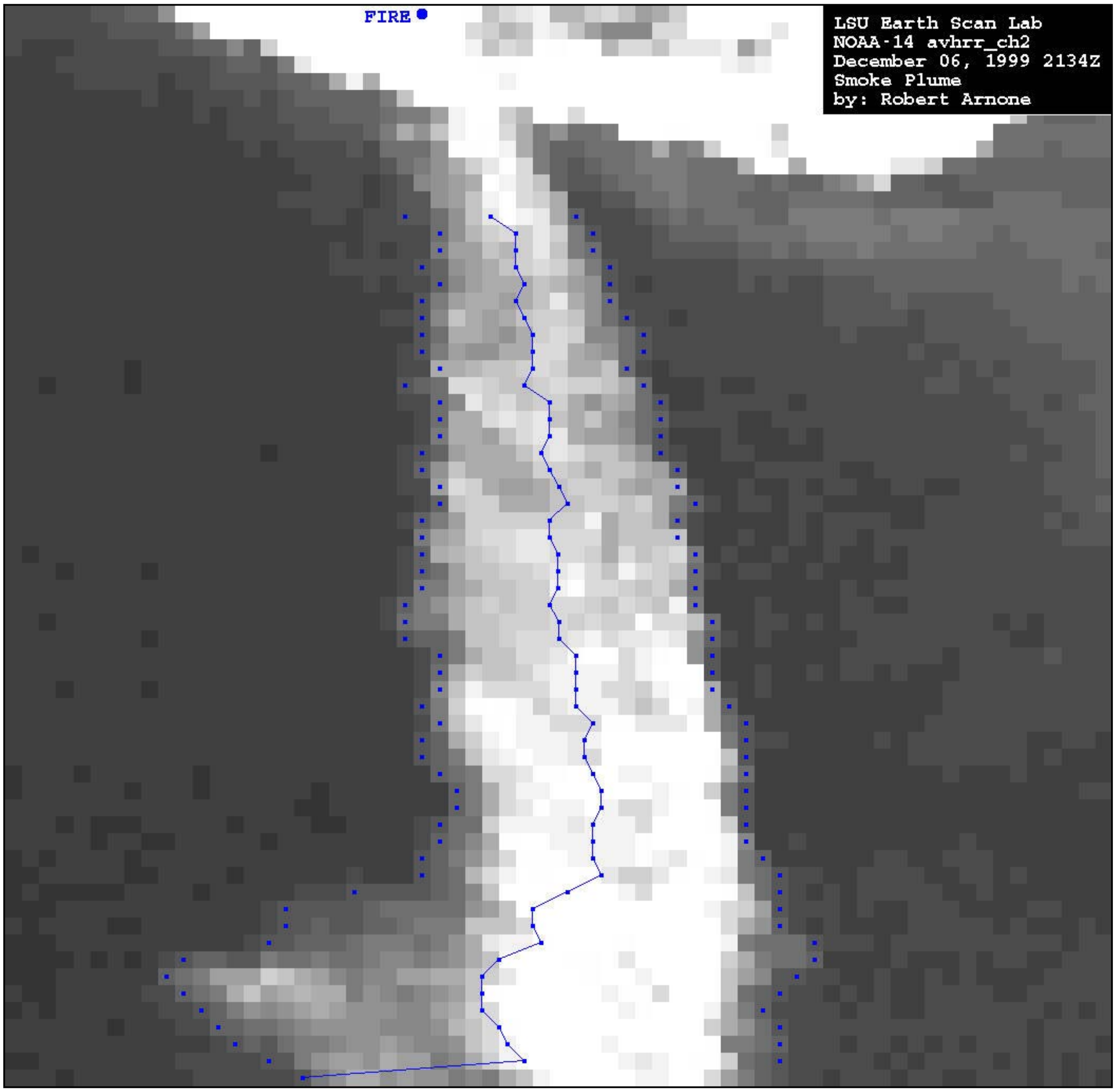

Figure 170. 2134 Z 6 December 1999 NOAA-14 near-infrared image showing a smoke plume extending from the central Louisiana coast out over the Gulf of Mexico shelf waters. Blue line is estimated center of plume, while dots are the plume crosswind boundaries (image and analysis courtesy of Robert Arnone, Earth Scan Lab, LSU).

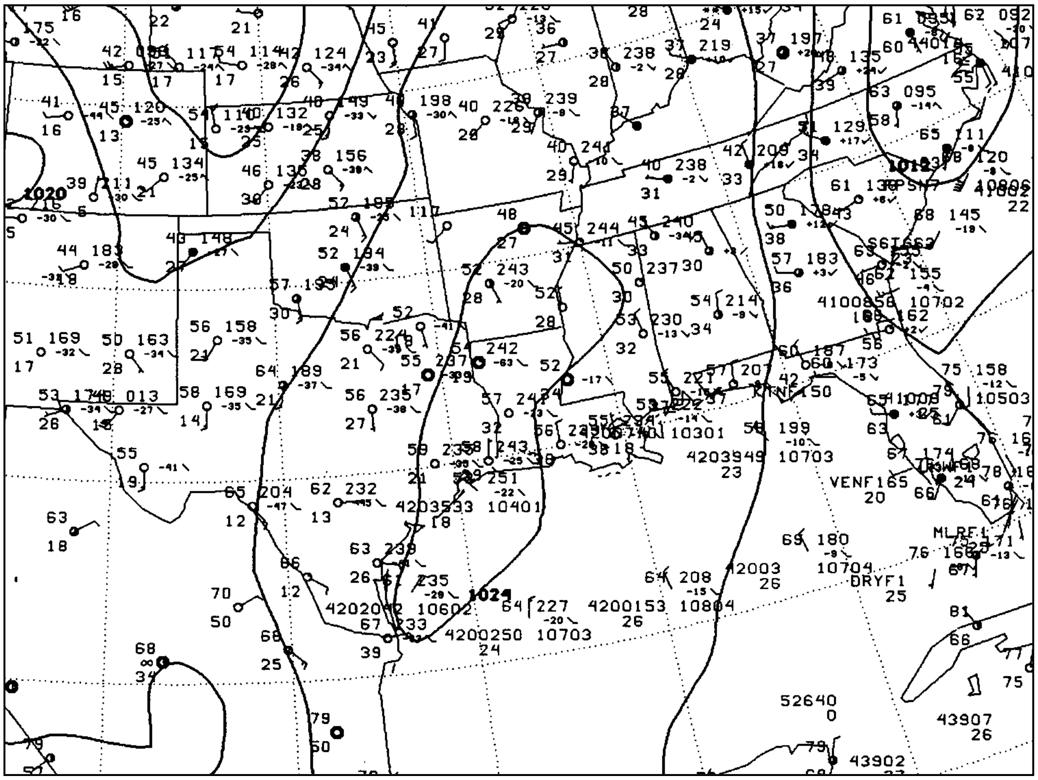

Figure 171. NWS Surface Weather chart for 2100 Z 6 December 1999.

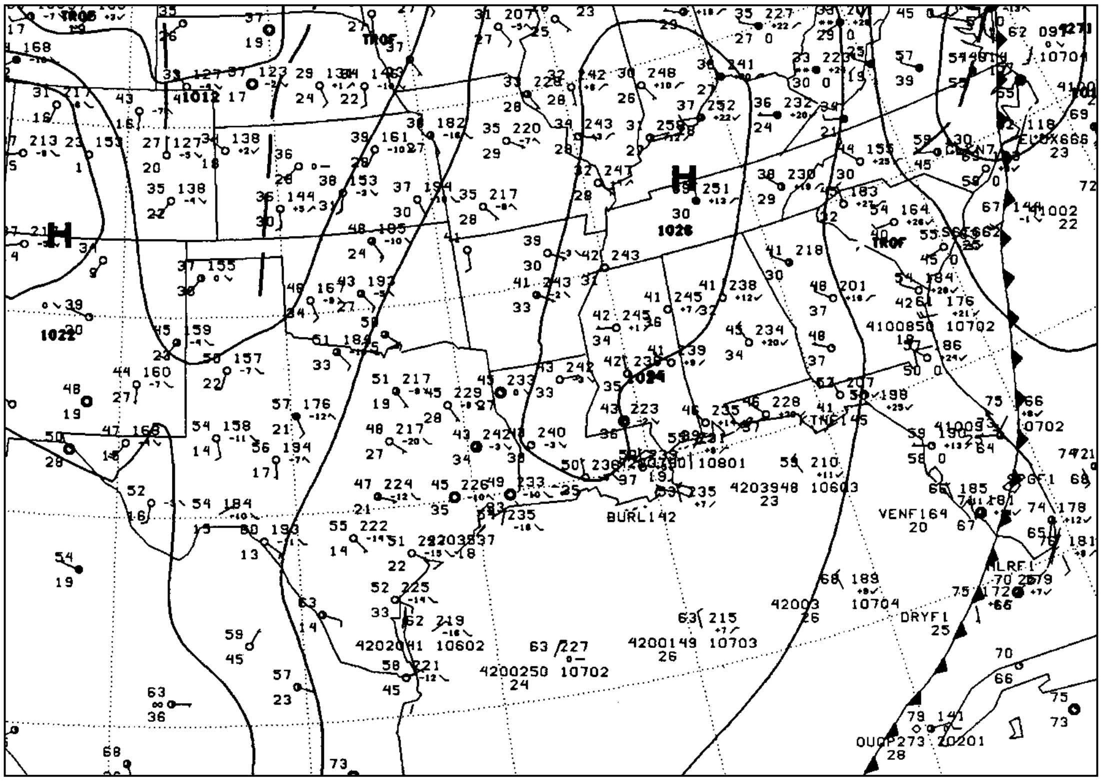

Figure 172. NWS Surface Weather chart for 0000 Z 7 December 1999.

VII. SUMMARY

Two platforms in the Louisiana coastal waters with meteorological and oceanographic monitoring capability were further outfitted with additional meteorological and visibility sensors beginning in November 2001. Hourly data recorded at these stations (part of the LSU WAVCIS chain) is available in near real time via internet; the historical archive can also be requested. This data source has been combined with that available from NDBC C-MAN stations and offshore buoys so that nearly the entire northern Gulf of Mexico is covered.

Regional visibility is influenced by the atmospheric mixed layer characteristics. Simplified air-sea interaction formulas which require only routinely observed parameters are derived for the determination of stability (M-O length), Bowen ratio, and mixed height under unstable (free convection), neutral, and stable conditions. Since very few point measurements of visibility are available over the Gulf, we employ the ventilation factor index to describe the local atmosphere dispersion capability.

Monthly mean conditions are presented for all pertinent stations in the northern Gulf. Stability Class D (neutral) is found to prevail, with Class C (free convective) occasionally observed. Sea temperatures are typically greater than air temperatures, however in winter months nearer to shore the opposite does occur with very low mixed heights resulting. On average, computed mixed heights were between 400 - 800 m, with higher values for offshore stations. Areas of poor ventilation factor index often develop near the shoreline, due to low mixed heights in winter months and low average wind speeds during the summer.

The algorithm used by the ASOS for determining whether fog or haze is impairing visibility was applied to our measurements as well as those from the NOAA Boothville and Grand Isle stations. By this definition, it is shown that fog occurs with much greater frequency than haze, and that fog can severely restrict visibility as much as 10% of the time. Haze can occur year-round, but less than about 5% per month (about 1.5 day). Episodes of haze were usually of shorter duration (several hours) than those of fog, and reductions in surface visibility were of lesser magnitude. Reductions in visibility at the Boothville and CSI-3 stations were mostly associated with winds from an easterly quadrant.

Using the record from CSI-3, several episodes of reduced visibility are identified and discussed with weather charts and satellite imagery. In two cases, it appears that smoke plumes from coastal fires may have drifted offshore and degraded surface visibility at CSI-3. A historical case is presented in which the lateral smoke plume geometry is verified through satellite imagery.

VIII. REFERENCES

Arya, S. P. 1999. Air Pollution Meteorology and Dispersion. Oxford: Oxford University Press.

Byers, H. R. 1974. General Meteorology. McGraw-Hill Book Co.

Donelan, M. A., W. M. Drennan, and K. B. Katsaros. 1997. The air-sea momentum flux in conditions of wind sea and swell. J. Phys. Oceanogr. 27:2087-2099.

Eagleman, J. R. 1996. Air Pollution Meteorology. Kansas:Trimedia Publishing Co.

Erickson, T. A. 2001. Louisiana and southeast Texas fog research and modeling. NWS Lake Charles, Louisiana. Internet website: http://www.srh.noaa.gov/lch/research/fogres.htm.

Federal Register, 1999. Regional Haze Regulations. Vol. 64, Number 126, July 1999, pp. 35713-35774.

Garratt, J. R. 1992. The Atmospheric Boundary Layer. Cambridge: Cambridge University Press.

Geer, Ira W., ed.. 1996. Glossary of Weather and Climate. Boston, MA:American Meteorological Society.

Hanna, S. R., L. L. Schulman, R. J. Paine, and J. E. Pleim. 1984. The Offshore and Coastal Dispersion (OCD) model user's guide, revised. OCS Study MMS 84-0069. Environmental Research and Technology, Inc., Concord, Massachusetts (NTIS PB86-159803).

Hsu, S. A. 1988. Coastal Meteorology. San Diego: Academic Press.

Hsu, S. A. 1992. An overwater stability criterion for the Offshore and Coastal Dispersion model. Boundary-Layer Meteorol. 60:397-402.

Hsu, S. A. 1997. Estimating overwater convective boundary layer height from routine meteorological measurements for diffusion applications at sea. J. Appl. Meteor. 36:1245-1248.

Hsu, S. A. 1998. A relationship between the Bowen ratio and sea-air temperature difference under unstable conditions at sea. J. Phys. Oceanogr. 28:2222-2226.

Hsu, S. A. 1999. On the estimation of overwater Bowen ratio from sea-air temperature difference. J. Phys. Oceanogr. 29:1372-1373.

Hsu, S. A., and B. W. Blanchard. 2003. Recent advances in air-sea interaction studies applied to overwater air quality modeling: a review. Pure and Applied Geophys. 160(2003):297-316.

Huschke, R. E., ed. 1959. Glossary of Meteorology. Boston: American Meteorological Society.

Hwang, P. A., and O. H. Shemdin. 1988. The dependence of sea surface slope on atmospheric stability and swell conditions. J. Geophys. Res. 93(C11):13903-13912.

Large, W. L., and S. Pond. 1982. Sensible and latent heat flux measurements over the ocean. J. Phys. Oceanogr. 12:464-482.

Malm, W. C.,M. L. Pitchford, M. Scruggs, J. F. Sisler, R. Ames, S. Copeland, K. A. Gebhart, and D. E. Day. 2000. Spatial and Seasonal Patterns and Temporal Variability of Haze and its Constituents in the United States, Report III. Cooperative Institute for Research in the Atmosphere, Colorado State University, Fort Collins, CO, 80523.

National Weather Service. 2003. Decision tree for forecasting sea fog in the northern Gulf of Mexico. NWS Slidell, Louisiana. Internet website: http://www.srh/noaa.gov/lix/html/seafog.htm.

NOAA. 1998. Automated Surface Observing Network (ASOS) User's Guide, March 1998.

NOAA. 2004. Climate Diagnostics Center. Internet website: http://cdc.noaa.gov.

Panofsky, H. A., and J. A. Dutton. 1984. Atmospheric Turbulence. New York:Wiley.

Roll, H. V. 1965. Physics of the Marine Atmosphere. New York: Academic Press.

Smith, S. D. 1980. Wind stress and heat flux over the ocean in gale force winds. J. Phys. Oceanogr. 10:709-726.

Smith, S. D. 1988. Coefficients for sea surface wind stress, heat flux, and wind profiles as a function of wind speed and temperature. J. Geophys. Res., 93:15467-15474.

Spiegel, M. R. 1961. Schaum's Outline of Theory and Problems of Statistics. New York: Schaum Publishing Co.

Turner, D. B. 1994. Workbook of Atmospheric Dispersion Estimates - An Introduction to Dispersion Modeling. Florida: CRC Press, Inc.

Wallace, J. M., and P. V. Hobbs. 1977. Atmospheric Science An Introductory Survey. New York: Academic Press.

Weast, R. C., S. M. Selby, and C. D. Hodgman, chief eds. 1964. Handbook of Chemistry and Physics. Ohio: The Chemical Rubber Co.

The Department of the Interior Mission

As the Nation's principal conservation agency, the Department of the Interior has responsibility for most of our nationally owned public lands and natural resources. This includes fostering sound use of our land and water resources; protecting our fish, wildlife, and biological diversity; preserving the environmental and cultural values of our national parks and historical places; and providing for the enjoyment of life through outdoor recreation. The Department assesses our energy and mineral resources and works to ensure that their development is in the best interests of all our people by encouraging stewardship and citizen participation in their care. The Department also has a major responsibility for American Indian reservation communities and for people who live in island territories under U.S. administration.

The Minerals Management Service Mission

As a bureau of the Department of the Interior, the Minerals Management Service's (MMS) primary responsibilities are to manage the mineral resources located on the Nation's Outer Continental Shelf (OCS), collect revenue from the Federal OCS and onshore Federal and Indian lands, and distribute those revenues.

Moreover, in working to meet its responsibilities, the **Offshore Minerals Management Program** administers the OCS competitive leasing program and oversees the safe and environmentally sound exploration and production of our Nation's offshore natural gas, oil and other mineral resources. The MMS **Minerals Revenue Management** meets its responsibilities by ensuring the efficient, timely and accurate collection and disbursement of revenue from mineral leasing and production due to Indian tribes and allottees, States and the U.S. Treasury.

The MMS strives to fulfill its responsibilities through the general guiding principles of: (1) being responsive to the public's concerns and interests by maintaining a dialogue with all potentially affected parties and (2) carrying out its programs with an emphasis on working to enhance the quality of life for all Americans by lending MMS assistance and expertise to economic development and environmental protection.

MMS Securing Ocean Energy & Economic Value for America